4.4 BEAM-BEAM ISSUES

As discussed in Chapter 3, the desire to achieve high luminosity leads one naturally to specify high currents and/or small beam sizes. These tend to make the beam-beam interaction stronger, which, in turn, may lead to beam blowup, coherent oscillations, or fast particle losses that could defeat the purpose of the initial specification.

If the beam-beam interaction is sufficiently weak, the beams behave as if there were no collisions, and the performance is controlled by the single-beam parameters of the two rings. This condition implies a relative simplicity in the operation of the collider, because the two beams are effectively decoupled. The price one must pay for this simplicity is that, in order to achieve a specified luminosity, the weakness of the beam-beam interaction must be compensated by using large beam currents distributed over many bunches, or over few bunches with a large beam emittance. Either of these approaches can become a problem for other aspects of the design, such as the vacuum system, RF system, etc., and can also lead to various kinds of beam instabilities.

If the beam-beam interaction is significant, the beam parameters generally are modified from their nominal values. A strong beam-beam interaction naturally tends to imply a high luminosity, but it entails the potential for the problems mentioned above. In addition, the operation becomes relatively more complicated because the two beams are effectively coupled.

Obviously the desired luminosity performance of the collider implies specifications on the dynamical quantities. The nominal quantities, on the other hand, imply specifications on the individual rings. If the beam-beam dynamics were well-understood, it would be possible to translate specifications from dynamical to nominal quantities, and then to proceed to the design of the two rings individually. Unfortunately, our understanding is incomplete. This is particularly true for asymmetric colliders, which involve the additional complication of having two separate rings. Furthermore, all beam-beam simulation tools in existence take nominal parameters as input and produce dynamical quantities as output. Therefore, the understanding obtained from beam-beam simulations proceeds, in some sense, "in reverse." In practice, therefore, the only way to arrive at a specification of nominal beam parameters is to proceed by iterations.

The basic strategy we adopt for the B Factory is to choose values for the nominal quantities (including the beam-beam parameters ξ_0) to achieve a certain (nominal) luminosity, and then to verify by simulations that the dynamical behavior is close to nominal. If the dynamical results are substantially different from the nominal expectations, we change the nominal parameters and try again until an acceptable solution is found. Ideally, we wish to obtain the highest luminosity with acceptable beam lifetime and also with the highest reliability and flexibility of operation.

In this section, we present one set of parameters that strikes a balance between these conflicting requirements. This solution is not necessarily optimal, but it is an existence proof that a luminosity of 3×10^{33} cm^{-2} s^{-1} is an achievable goal. Although substantial detailed work remains to be done, we are confident that the solution we propose will lead to a productive B Factory, and we further expect that improved solutions can be found by modest modifications of various parameters.

4.4.1 Nominal and Dynamical Beam Quantities

In the absence of the beam-beam interaction, the beam parameters are determined by the lattice, the energy, and the RF parameters of each ring. In particular, this is true of the emittances and therefore the beam sizes at the interaction point (IP). From these one can compute the beam-beam parameters and the resultant luminosity in the limit that the beam-beam interaction does not change them; the quantities calculated in this limit are referred to here as *nominal* and are indicated by a subscript 0. As an example of our notation, the nominal vertical beam size at the IP, $\sigma^*_{0y,+}$ and beam-beam parameter $\xi_{0y,+}$ of the positron beam, and the nominal luminosity $\mathcal{L}_0$ are given by

$$\sigma^*_{0y,+} = \sqrt{\varepsilon_{0y,+}\,\beta^*_{y,+}} \tag{4-36a}$$

$$\xi_{0y,+} = \frac{r_0 N_- \beta^*_{y,+}}{2\pi\gamma_+\sigma^*_{0y,-}\left(\sigma^*_{0x,-} + \sigma^*_{0y,-}\right)} \tag{4-36b}$$

$$\mathcal{L}_0 = \frac{N_+ N_- f_c}{2\pi\sqrt{\left(\sigma^{*2}_{0x,+} + \sigma^{*2}_{0x,-}\right)\left(\sigma^{*2}_{0y,+} + \sigma^{*2}_{0y,-}\right)}} \tag{4-36c}$$

where $\beta^*_{y,+}$ and $\varepsilon_{0y,+}$ are the vertical beta function at the IP and the nominal emittance of the positron beam, the $N_\pm$ are the number of particles per bunch, r_0 is the classical electron radius, and f_c is the bunch collision frequency. We assume here that the bunches collide head-on, that they have elliptical Gaussian transverse profiles with common axes, and that they have lengths comparable to or smaller than their transverse beta functions. In this case the so-called "hourglass" reduction effect is small [Furman, 1991a]. There are three more beam-beam parameters, whose expressions are obtained from the above by the replacements $x \leftrightarrow y$ and/or $+ \leftrightarrow -$. If the bunches are evenly spaced by a distance s_B, the bunch collision frequency is, in the relativistic approximation, $f_c = c/s_B$, where c is the velocity of light.

Once the beams are brought into collision, the emittances inevitably deviate from their nominal values and, as a result, so do all quantities involving the beam sizes, including the beam-beam tune shift and the luminosity. These are the *dynamical* quantities, denoted without the subscript 0; the dynamical quantities corresponding to those in Eqs. 4-36 above are given by

$$\sigma^*_{y,+} = \sqrt{\varepsilon_{y,+}\,\beta^*_{y,+}} \tag{4-37a}$$

$$\xi_{y,+} = \frac{r_0 N_- \beta^*_{y,+}}{2\pi\gamma_+\sigma^*_{y,-}\left(\sigma^*_{x,-} + \sigma^*_{y,-}\right)} \tag{4-37b}$$

$$\mathcal{L} = \frac{N_+ N_- f_c}{2\pi\sqrt{\left(\sigma_{x,+}^{*2} + \sigma_{x,-}^{*2}\right)\left(\sigma_{y,+}^{*2} + \sigma_{y,-}^{*2}\right)}} \tag{4-37c}$$

In this discussion, we assume that the beam-beam interaction does not induce coherent oscillations or a relative displacement of the closed orbits at the IP. This is discussed in greater detail when we describe our simulation results in Section 4.4.5.

4.4.2 Transparency Symmetry

The fact that an asymmetric collider necessarily consists of two rings enlarges the beam dynamics parameter space considerably relative to a single-ring, symmetric collider. The bunches in the two rings see different RF systems, different lattice functions, and different magnetic fields. Even the simplest beam-beam dynamics study requires, at a minimum, the specification of the following quantities:

- Two values for the number of particles per bunch, $N_\pm$
- Six beam sizes (two transverse and one longitudinal for each beam)
- Four beta functions at the IP (one vertical and one horizontal for each beam)
- Six tunes
- Two damping decrements

In general, the four beam-beam parameters are different, as can be seen from Eqs. 4-36.

Because no asymmetric colliders exist at present, and because the consequences of the beam-beam interaction are not completely understood for intense beams, it has been argued [Chin, 1990] that a cautious approach might be to require that the beam dynamics of an asymmetric collider resemble as closely as possible the dynamics of a symmetric one. In this way, the design can draw upon the valuable experience gained from single-ring colliders. This is the so-called "transparency symmetry" condition; it is reached by imposing constraints on the parameters of the two rings according to the following:

(i) Pairwise equality of nominal beam-beam parameters: $\xi_{0x,+} = \xi_{0x,-}$ and $\xi_{0y,+} = \xi_{0y,-}$

(ii) Pairwise equality of nominal beam sizes: $\sigma^*_{0x,+} = \sigma^*_{0x,-}$ and $\sigma^*_{0y,+} = \sigma^*_{0y,-}$

(iii) Equality of damping decrements of the two rings

(iv) Equality of the tune modulation amplitudes due to synchrotron oscillations: $(\sigma_\ell \nu_s/\beta^*_{x,y})_+ = (\sigma_\ell \nu_s/\beta^*_{x,y})_-$, where σ_ℓ is the bunch length and ν_s is the synchrotron tune

An immediate consequence of the transparency symmetry is a significant reduction in the number of free parameters, which is certainly a practical advantage for beam-beam studies. On the other hand, it has been argued on general grounds [Tennyson, 1990] that, given an asymmetric machine design, the beam-beam limit (maximum luminosity with acceptable beam lifetime), subject to certain constraints, can only be achieved with

asymmetric beam dynamics parameters. Thus, the transparency symmetry might preclude reaching the actual beam-beam limit. It is possible that the ultimate beam-beam limit in an asymmetric collider can be achieved only at the price of relinquishing too much flexibility and therefore operational reliability, or of undesirably tight tolerances. Furthermore, it is not known at present how different the luminosity at the beam-beam limit would be compared with what could be achieved in a given transparent case. These are matters that deserve careful investigation in the near future. As will be discussed in more detail in the following sections, for now we adopt an approximate transparency symmetry as a prudent starting point.

Another advantage of transparency symmetry is that the luminosity can be very simply and conveniently expressed in terms of a single beam-beam parameter. First, we note that condition (ii) above implies that there is a single nominal aspect ratio r:

$$\left(\frac{\sigma_{0y}^*}{\sigma_{0x}^*}\right)_+ = \left(\frac{\sigma_{0y}^*}{\sigma_{0x}^*}\right)_- \equiv r \tag{4-38}$$

and that the expression for the nominal luminosity simplifies to

$$\mathcal{L}_0 = \frac{N_+ N_- f_c}{4\pi\sigma_{0x}^*\sigma_{0y}^*} \tag{4-39}$$

By combining conditions (i) and (ii), we have [Chin, 1990; Furman, 1991b]

$$\frac{\beta_{x,-}^*}{\beta_{x,+}^*} = \frac{\beta_{y,-}^*}{\beta_{y,+}^*} = \frac{(EI)_-}{(EI)_+} \tag{4-40}$$

One also finds that there is a single beta-function ratio (rather than two) and a single nominal emittance ratio:

$$\frac{\beta_{y,+}^*}{\beta_{x,+}^*} = \frac{\beta_{y,-}^*}{\beta_{x,-}^*} \equiv r_\beta \quad \text{and} \quad \frac{\varepsilon_{0y,+}}{\varepsilon_{0x,+}} = \frac{\varepsilon_{0y,-}}{\varepsilon_{0x,-}} \equiv r_\varepsilon \tag{4-41}$$

so that the beam-size ratio becomes

$$r = \sqrt{r_\varepsilon r_\beta} \tag{4-42}$$

The nominal beam-beam tune shift parameters are related to r_β and r_ε by

$$\frac{\xi_{0y}}{\xi_{0x}} = \sqrt{\frac{r_\beta}{r_\varepsilon}} \tag{4-43}$$

and the nominal luminosity is

$$\mathcal{L}_0 = K(1+r)\xi_{0y}\left(\frac{EI}{\beta_y^*}\right)_{+,-} \tag{4-44}$$

where the subscript +,– means that the expression in parentheses can be taken from either beam, because of Eq. 4-40. The constant K is

$$\begin{aligned} K &= \frac{1}{2er_0mc^2} \\ &= 2.17 \times 10^{34}\ \left[\mathrm{cm^{-2}s^{-1}}\right]\cdot\left[\frac{\mathrm{cm}}{\mathrm{GeV\ A}}\right] \end{aligned} \tag{4-45}$$

where mc^2 is the rest energy of the electron and e is its charge. Therefore, if we express the energy E in GeV, the current I in A, and the beta function in cm, we obtain

$$\mathcal{L}_0 = 2.17 \times 10^{34}(1+r)\xi_{0y}\left(\frac{EI}{\beta_y^*}\right)_{+,-} \quad [\mathrm{cm^{-2}\ s^{-1}}] \tag{4-46}$$

Note that ξ_{0y} cannot be varied independently of the other parameters, since it is related to them through Eqs. 4-42 and 4-43. It is also worth commenting that Eq. 4-46 can be rewritten, if desired, in terms of horizontal, rather than vertical, parameters by making the replacements $y \rightarrow x$ and $r \rightarrow 1/r$.

In contrast, the nominal aspect ratio r, the beta function ratio r_β, and the nominal emittance ratio r_ε are free parameters, except that they are related by Eq. 4-42.

If, in addition to the transparency symmetry condition (i), we impose the extra requirement that *all four* beam-beam parameters should be equal, that is

$$\xi_{0x,+} = \xi_{0y,+} = \xi_{0x,-} = \xi_{0y,-} \equiv \xi_0$$

as we will in our simulations presented below, then one finds the additional equality $r = r_\beta = r_\varepsilon$ or, explicitly,

$$\frac{\sigma_{0y,+}^*}{\sigma_{0x,+}^*} = \frac{\sigma_{0y,-}^*}{\sigma_{0x,-}^*} = \frac{\beta_{y,+}^*}{\beta_{x,+}^*} = \frac{\beta_{y,-}^*}{\beta_{x,-}^*} = \frac{\varepsilon_{0y,+}}{\varepsilon_{0x,+}} = \frac{\varepsilon_{0y,-}}{\varepsilon_{0x,-}} = r \tag{4-47}$$

The formula for the luminosity reads the same as the previous case, Eq. 4-46, except that now the beam-beam parameter carries no index y.

4.4.3 Physics of the Simulation Codes

For our simulations, we employ two distinct codes (by H. Yokoya and J. Tennyson) that are similar, but not identical. Each of these codes represents a beam bunch by a collection of many (we have used up to 300) "superparticles." Initially, these

superparticles have a Gaussian distribution in phase space. At the IP, the rms beam sizes σ_x and σ_y are calculated from the superparticle distribution at every turn. Although the shape of the distribution deviates from Gaussian as time progresses, for the purposes of computing the beam-beam kick, it is a good approximation to retain the Gaussian shape, albeit with time-dependent σ_x and σ_y. From these distributions, the beam-beam force on each superparticle of the opposing bunch is computed by means of the well-known expression for the transverse electric field in terms of the complex error function [Bassetti and Erskine, 1980]. Deviations from a Gaussian shape are monitored; if the dynamic distribution differs substantially from Gaussian, one has reason to doubt the results, owing to the lack of self-consistency.

Each beam is transported through the rest of the machine by a linear matrix; that is, no lattice nonlinearities are considered. Synchrotron radiation and damping are included and are represented by localized kicks. The RF system is also represented by a localized kick. Typically, the beams are tracked for three to five damping times to verify that an equilibrium situation has been reached. (For the specific set of parameters studied here, we have verified that five damping times is long enough to yield stable results and that three damping times is often adequate.)

The electromagnetic fields produced by relativistic particles are Lorentz-contracted into a thin disk perpendicular to the direction of motion. As a consequence, the force on a single particle due to the opposing bunch is, to a good approximation, strictly transverse; longitudinal forces can be neglected. (Indeed, the integrated longitudinal force is *exactly* zero in the case when the beta function is constant during the collision.) What cannot be neglected, however, is the fact that the opposing bunch has a finite longitudinal extent.

Near the IP, the vertical beta function is small and the betatron phase of a particle changes rapidly. Consequently, the net force due to the opposing bunch (that is, the beam-beam interaction) is distributed over a wide range of betatron phase. Because most beam-beam limiting phenomena are resonant in nature, this feature, called phase averaging, is important and must be incorporated into beam-beam calculations and simulations. [Krishnagopal and Siemann, 1990].

Phase averaging thus emphasizes the importance of the longitudinal extent of the beam-beam interaction. A Hamiltonian analysis that includes this feature predicts resonance strengths that are smaller than those calculated by models in which the beam-beam interaction is approximated by a single kick (impulse approximation). This also implies that resonance overlap, and the stochastic motion that results from it, set in at higher currents than would be estimated in the impulse approximation.

In the simulation results presented here, we allow for phase averaging by dividing the bunch longitudinally into several slices. Typically, five slices are used, although spot-checks with nine slices have sometimes been made. Both codes distribute the slices evenly along the length of the bunch and symmetrically about its center. However, the slices farthest away from the center are located in different places in the two codes. In Yokoya's code, the outermost slice is located at a distance $s = \pm 2\sigma_\ell$ from the bunch center, regardless of the number of slices. In Tennyson's code (TRS), the corresponding outermost distance is $s = \pm[1 + (n - 3)/12]\sigma_\ell$, where n is the total number of slices. Thus, the two codes have identical slicing algorithms only when 15 slices are used; for fewer slices, Tennyson's code concentrates the slices closer to the center of the bunch than does

Yokoya's code. As the bunches pass through each other during the collision, the beta functions seen by the different slices are different, since the slices collide at points away from the IP. In the neighborhood of the IP, we take the s-dependence of the beta functions to correspond to that of a drift.

Besides the distinctions discussed above, the codes also differ in technical details having to do with the way certain quantities are averaged from turn to turn in order to smooth out statistical fluctuations associated with the relatively small number of superparticles.

The lattice design described in Section 4.1 has head-on collisions at the IP, with magnetic separation of the beams. However, the beams go into their own vacuum pipes only after traveling about 4 m away from the IP; as a result, they experience several grazing collisions on their way into and out of the IP. There are six such "parasitic" crossings on either side of the IP. These parasitic crossings couple the dynamics of all bunches, so a completely faithful simulation of the B Factory beam-beam dynamics would require 1658 bunches per ring, along with a gap equivalent to 88 bunches. Since this is an impractical requirement for any present-day simulation, we make two simplifying approximations: (i) We consider only the first parasitic crossing on either side of the IP and (ii) we use only one bunch per ring, which is "reused" (so that this bunch collides three times per turn—two parasitic crossings plus the main collision at the IP—with the same partner in the other beam).

The first approximation is quite reasonable, since, as discussed in more detail below, the effect of the first parasitic crossing overwhelms all the others. The second approximation rests on the sensible assumption that, in reality (or in a faithful simulation), the particle distributions are not expected to differ much from bunch to bunch, especially when the bunches interact at a distance, as is the case at the parasitic crossings.

Given the complicated process that is being simulated, it is natural to test the predictions of the simulation codes against known experimental results. As an example, we have studied the particular PEP configuration summarized in Table 4-22 with Yokoya's code. We find that the luminosity prediction agrees with the measured value to within 10%. In fact, the simulation result is actually slightly *pessimistic,* since it is 10% below the observed luminosity. We also predict from the simulations that there will be no saturation of the dynamic beam-beam tune-shift parameter ξ up to a beam current of 30 mA—again in agreement with experimental observations. Calculations for other PEP configurations yield more or less equivalent agreement with the observed luminosities.

We have also tested Tennyson's code for the case of PEP, for a different configuration from that above, including the effect of the parasitic crossings in the arcs. The comparison with experiment is summarized in Fig. 4-83. In this comparison, too, we find reasonable agreement with experiment. Again, we note that the code tends to underestimate the luminosity.

Insofar as the simulation results in both cases are consistent in trend with the actual PEP observations, we feel that the predictions derived from these codes are reasonable guides for the design of the B Factory. Implied in this statement is the assumption that there is no new physics that enters into the beam-beam interaction due to the asymmetric collisions. At the present time, we have every reason to believe that this assumption is valid.

Table 4-22 PEP parameters used in simulation comparison.[a]

Betatron tunes	
Horizontal	21.2962
Vertical	18.2049
Beta functions at IP	
Horizontal [m]	1.342
Vertical [m]	0.053
Dispersion at IP	
Horizontal [m]	0.00049
Emittances	
Horizontal [nm·rad]	99.6
Vertical [nm·rad]	3.96
Synchrotron tune	0.043
Beam current [mA]	18.85
Nominal beam-beam parameter, ξ_0	
Horizontal	0.04653
Vertical	0.04653
Luminosity	
Nominal [$cm^{-2}\ s^{-1}$]	5.07×10^{31}
Observed [$cm^{-2}\ s^{-1}$]	4.80×10^{31}
Simulation [$cm^{-2}\ s^{-1}$]	4.34×10^{31}

[a]Data from E. Bloom and M. Donald

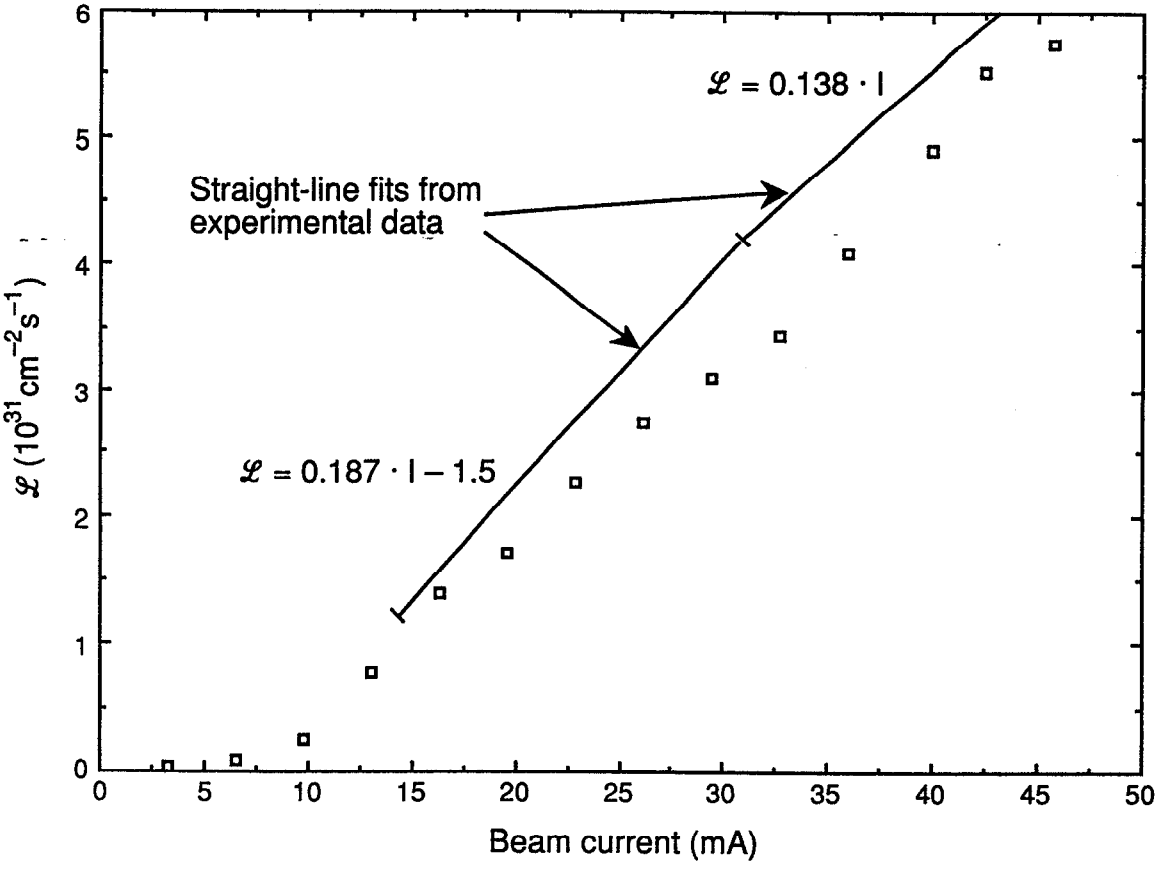

Fig. 4-83. Plot of observed luminosity at PEP and the simulation results from Tennyson's code. The tune values used in the simulation were slightly different from those used in the experiment itself; preliminary results show that the agreement improves when the tunes are the same.

4.4.4 Beam Dynamics Studies

The primary parameters that determine the strength of the beam-beam interaction are the four nominal beam-beam parameters, $\xi_{0x,\pm}$ and $\xi_{0y,\pm}$. If these are small enough, and if the working point of the ring is not too close to the integer tunes, ξ_0 is equal to the nominal tune spread induced by the beam-beam interaction. We adopt, as a starting point, the fully symmetric condition

$$\xi_{0x,+} = \xi_{0y,+} = \xi_{0x,-} = \xi_{0y,-} = 0.03 \tag{4-48}$$

The specification of $\xi_0 = 0.03$ is intended to be conservative, insofar as existing machines have already achieved substantially higher values of ξ_0 [Rice, 1989 and 1990; Seeman, 1985]. As mentioned, this strategy of setting the beam-beam interaction to be reasonably weak has the desirable consequence that the beam behavior will be close to nominal. This has the advantage of preserving operational flexibility, because the closer to nominal the beam-beam dynamics is, the more controllable is the machine

performance. (Clearly, in an operating collider, the machine parameters will be adjusted to maximize the luminosity. The idea here is not to limit the machine performance, but rather to leave room for subsequent improvements.)

Our basic strategy is first to choose nominal parameters, and then to verify that the beam-beam interaction does not cause significant deviations from them. If the beam dynamics is substantially different from nominal (for example, if beam blowup is too large or beam lifetime too short), we change the nominal parameters and try again until an acceptable solution is found. In more detail, this strategy is divided into several steps:

(*i*) *Set nominal parameters.* Our design goal is to reach a nominal luminosity of $\mathscr{L}_0 = 3 \times 10^{33}\ \mathrm{cm^{-2}\ s^{-1}}$. From this requirement and other considerations, a complete set of parameters for both rings can be derived (see Appendix A). For the purposes of this section, however, we show only an abbreviated list in Table 4-23. Further, because the collider design has evolved in parallel with the simulation study, some of the final parameters in Appendix A differ slightly from those in this section. The parameters indicated in Table 4-23, however, are the values used in the simulation study.

In Table 4-23, E is the beam energy, s_B is the bunch spacing, and f_c is the bunch collision frequency at the IP ($f_c = c/s_B$); V_{RF}, f_{RF}, and ϕ_s are the RF voltage, frequency, and synchronous phase, respectively; α is the momentum compaction factor; ν_s is the synchrotron tune; σ_ℓ is the rms bunch length; and τ_x and τ_y are the horizontal and vertical damping times, respectively. The other parameters are the emittances ε, beta functions β, and nominal rms beam sizes σ_0 at the IP.

The above parameters are consistent with Eq. 4-48 and our stated luminosity goal, as can be easily verified. Their values do not, however, correspond exactly to the requirements of transparency symmetry, on account of the difference in the amplitudes of the tune modulation:

$$\left(\frac{\sigma_\ell \nu_s}{\beta_x^*}\right)_+ = 1.07 \times 10^{-3}\ , \qquad \left(\frac{\sigma_\ell \nu_s}{\beta_x^*}\right)_- = 6.93 \times 10^{-4}$$

$$\left(\frac{\sigma_\ell \nu_s}{\beta_y^*}\right)_+ = 2.69 \times 10^{-2}\ , \qquad \left(\frac{\sigma_\ell \nu_s}{\beta_y^*}\right)_- = 1.73 \times 10^{-2} \tag{4-49}$$

(*ii*) *Select a working point.* Only the primary collisions at the IP are considered in this step. The choice of tunes can be made quite effectively with "weak-strong" beam-beam simulations, in which the high-energy beam is forced to remain undisturbed while the low-energy beam is studied dynamically. (For the B Factory, we are confident that this approximation is reasonable, because more realistic "strong-strong" simulations show that there is little or no beam blowup for the high-energy beam in our design.) This more approximate type of simulation has the advantages that it is relatively fast and that the effects of resonances, such as synchrotron sidebands, are clearly seen (thus allowing, in principle, a theoretical understanding of the underlying beam dynamics). The main figure-of-merit that we use in this study is the beam blowup factor of the low-energy beam.

In general, the resonance density in the tune diagram is lowest close to the integer tune, so we have begun by performing a tune scan close to the lower left corner of the

Table 4-23. Main B Factory parameters used in the beam-beam simulation studies.

	LER (e^+)	HER (e^-)
E [GeV]	3.1	9
s_B [m]	1.26	1.26
f_c [MHz]	238	238
V_{RF} [MV]	8.0	18.5
f_{RF} [MHz]	476.0	476.0
ϕ_s [deg]	170.6	168.7
α	1.15×10^{-3}	2.41×10^{-3}
ν_s	0.0403	0.0520
σ_ℓ [cm]	1	1
N_b	5.61×10^{10}	3.88×10^{10}
ε_{0x} [nm·rad]	92	46
ε_{0y} [nm·rad]	3.6	1.8
β_x^* [cm]	37.5	75.0
β_y^* [cm]	1.5	3.0
σ_{0x}^* [μm]	186	186
σ_{0y}^* [μm]	7.4	7.4
τ_x [turns]	4400	5014
τ_y [turns]	4400	5014

tune plane. The beam-beam interaction causes a tune spread because particles of different betatron amplitude experience different tune shifts. This causes the beam to have a characteristic "footprint" that extends diagonally upward from the working point. Figure 4-84 shows the vertical and horizontal blowup factors of the low-energy beam for each working point scanned. Figure 4-85 shows the same portion of the tune plane, with even-order resonance lines through sixth order. The results in Fig. 4-84 can be interpreted by assuming that the large blowup points, indicated by darker shading, are caused by synchrotron sidebands of the fourth order and the integer resonances.

While a comprehensive scan of the entire tune square remains to be carried out, for the present limited purpose of studying the beam-beam dynamics, we selected the fractional tunes to be $\nu_x = 0.09$ and $\nu_y = 0.05$ (both beams). For these tunes, the blowup factor is 10% or less, as can be seen from Fig. 4-84. Other considerations, such as dipole error sensitivity, may well dictate working points further away from the integer.

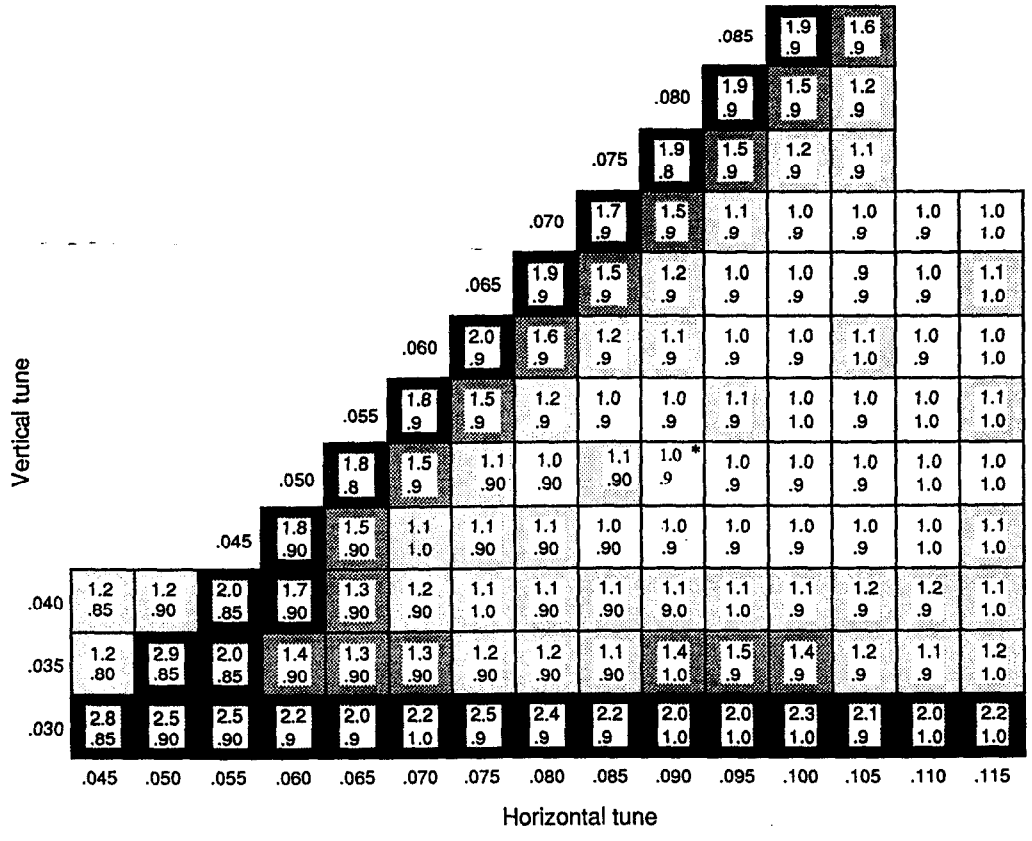

Fig. 4-84. Low-energy beam blowup factors (σ/σ_0) for various working points. The numbers in each box are the vertical and horizontal blowup factors at that particular working point. Our choice at (0.09, 0.05) is indicated by an asterisk. The shading in each box is indicative of the blowup: the darker the shading, the larger the vertical blowup.

Nevertheless, at least some existing machines [Rice, 1989 and 1990; Seeman, 1985] operate in this general area of the tune plane. Figure 4-86 shows the beam footprint extending away from this working point.

(*iii*) *Verify the behavior of the beam-beam interaction.* The next step is to check that the beam-beam interaction remains reasonably weak in the fully coupled beam-beam calculations. This is done with "strong-strong" simulations, in which both beams are allowed to vary dynamically according to their mutual beam-beam interaction. At this stage, the study is still done with only the primary collisions at the IP. This type of simulation is time-consuming, but it is necessary because it is the only way to compute dynamical quantities, such as actual beam blowup and luminosity, and because it can reveal coherent oscillations, closed-orbit distortion, and particle losses. As a check on the robustness of our chosen parameters and working point, we have considered values of ξ_0 much higher than the nominal value of 0.03 in the simulations. This is shown in Fig. 4-87, which gives the calculated blowup factors of all four beam sizes vs ξ_0, and Fig. 4-88, showing the corresponding luminosities. In both Figs. 4-87 and 4-88, we maintain the equality of all four ξ_0 values (which are varied by simply increasing the number of

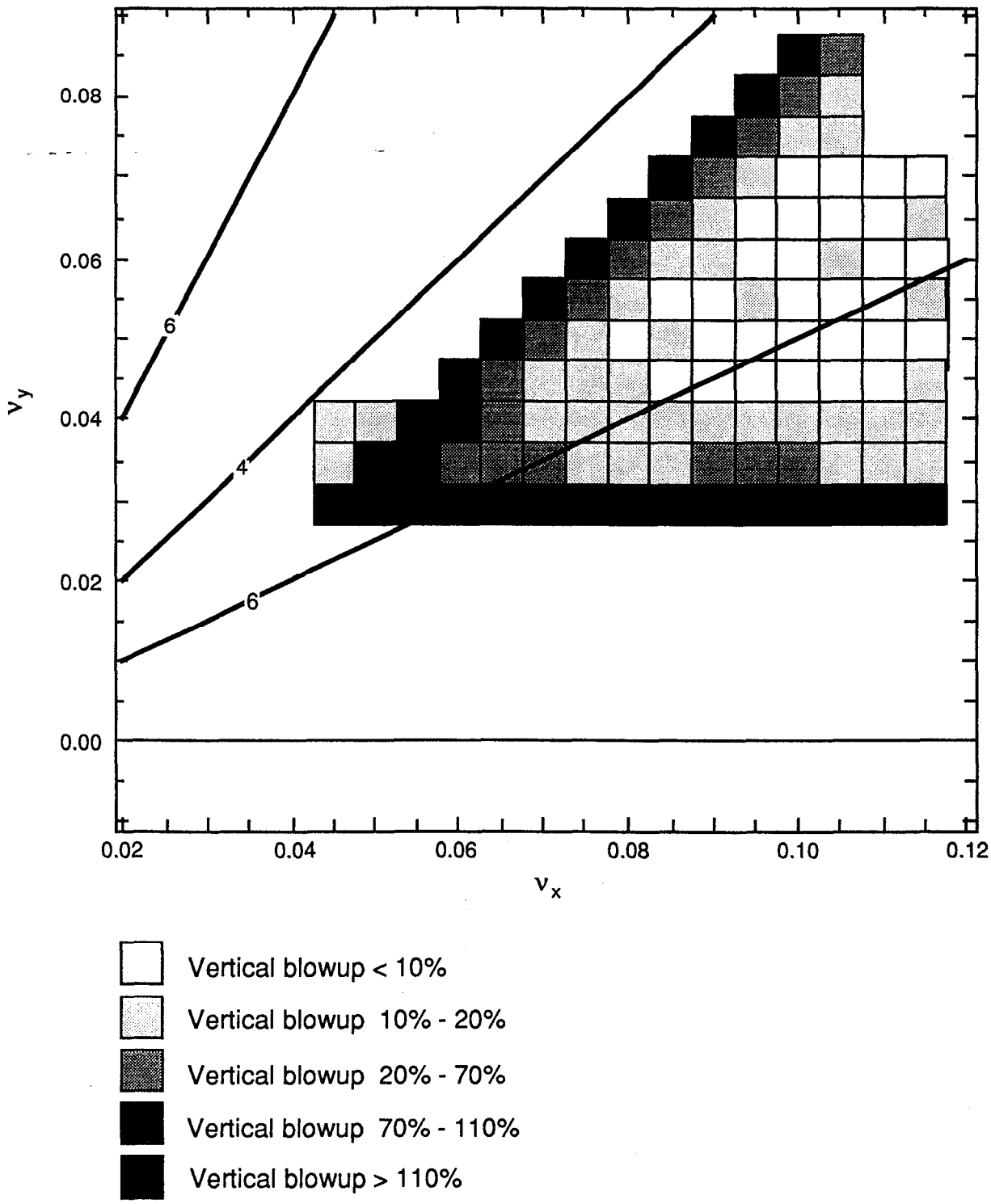

Fig. 4-85. Tune plot with even-order resonance lines through sixth order. This is the same portion of the tune plane as in the previous figure.

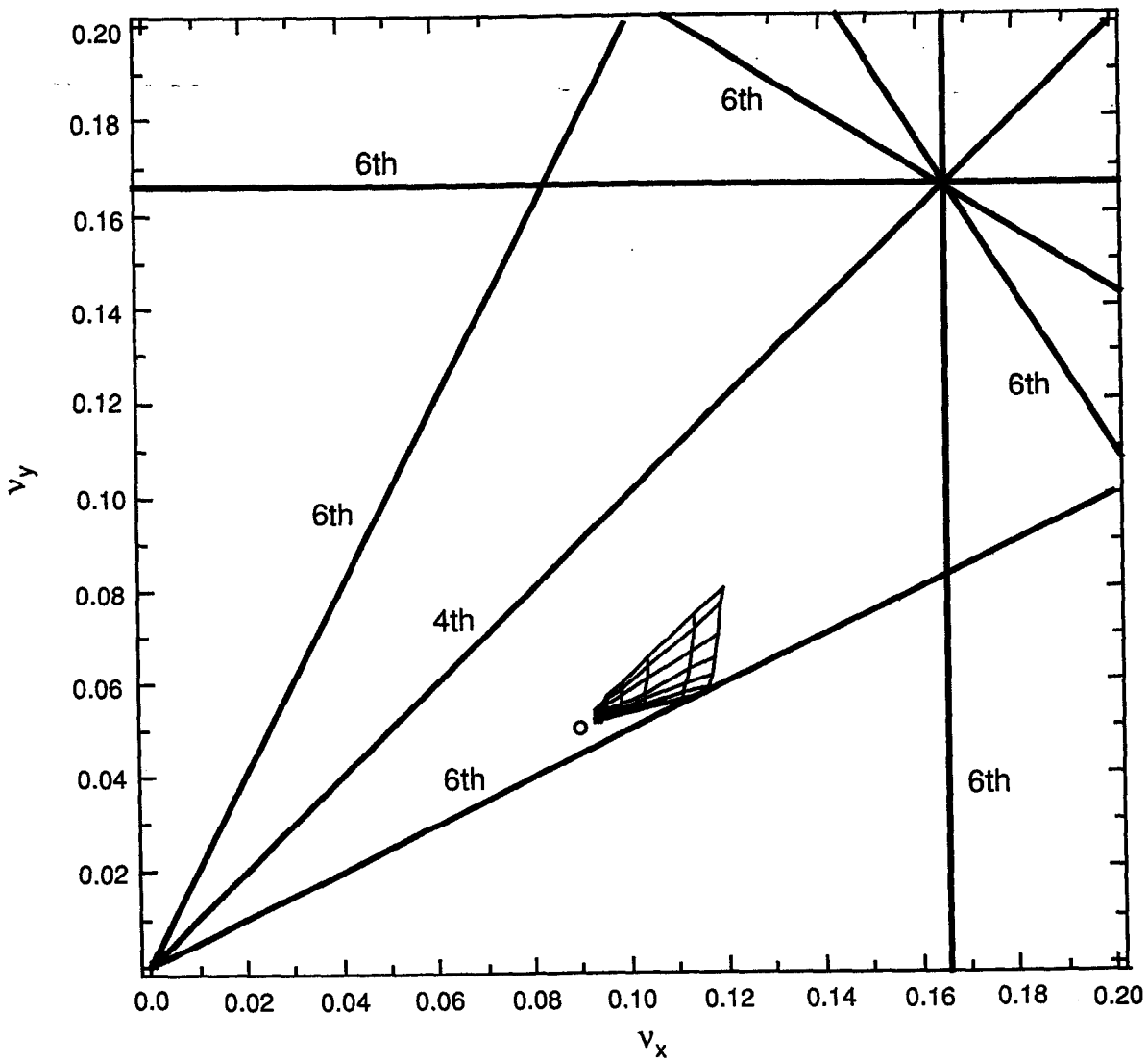

Fig. 4-86. Tune plot and beam footprint. The tune plane shows the working point (circle) and the beam footprint caused by the beam-beam tune spread. The lines in the footprint correspond to particles with amplitudes with constant σ_x or constant σ_y, from 0 to 7σ in steps of 1σ. The particle closest to the working point has the largest amplitude, 7σ_x and 7σ_y. The particle furthest away is at the center of the bunch.

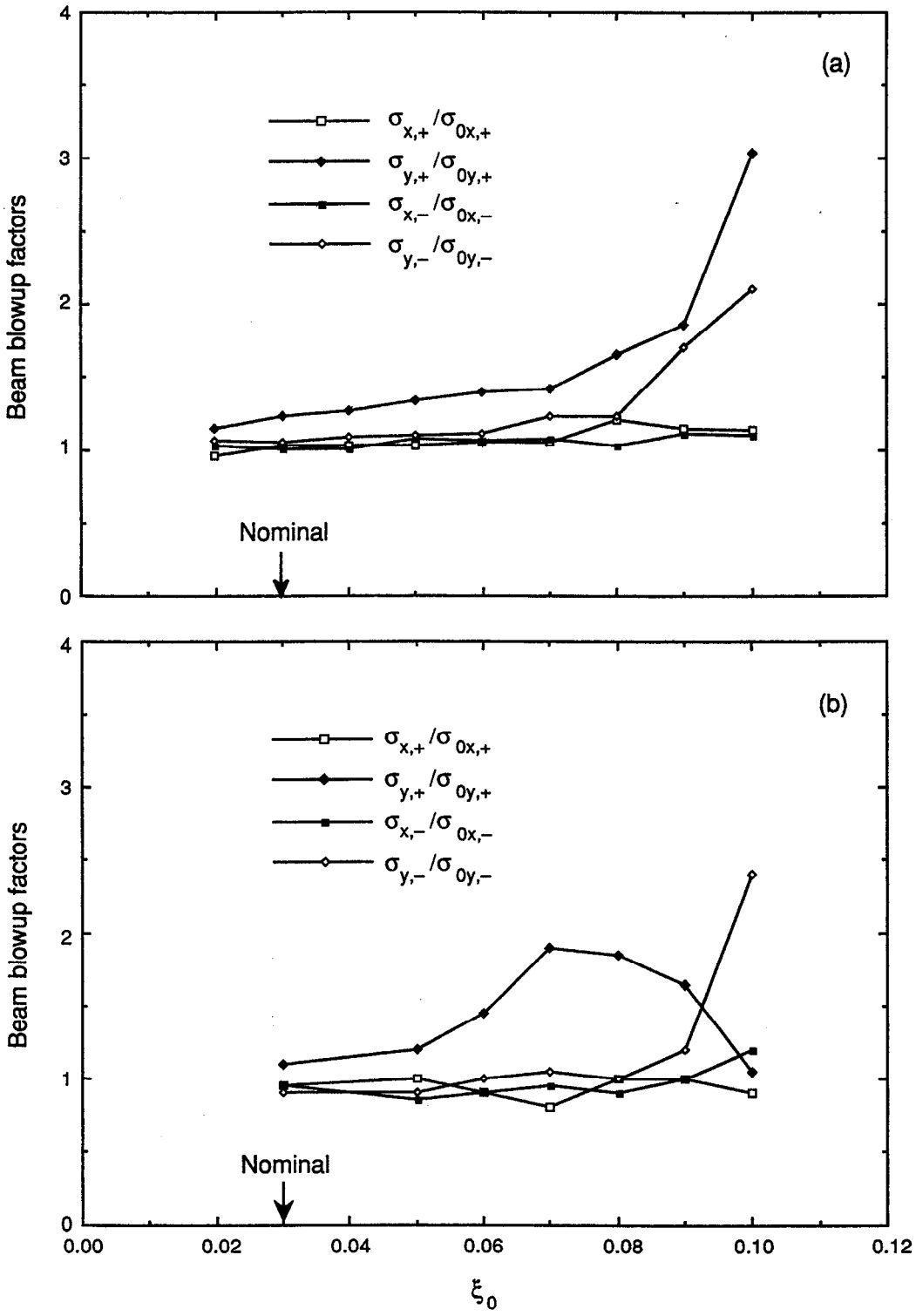

Fig. 4-87. Beam blowup factors vs ξ_0. These are the results for the dynamical beam size over nominal beam size for both beams, from both simulation codes: (a) Yokoya's and (b) TRS. The parameter ξ_0 is increased by increasing the number of particles per bunch in both beams, with fixed nominal emittance.

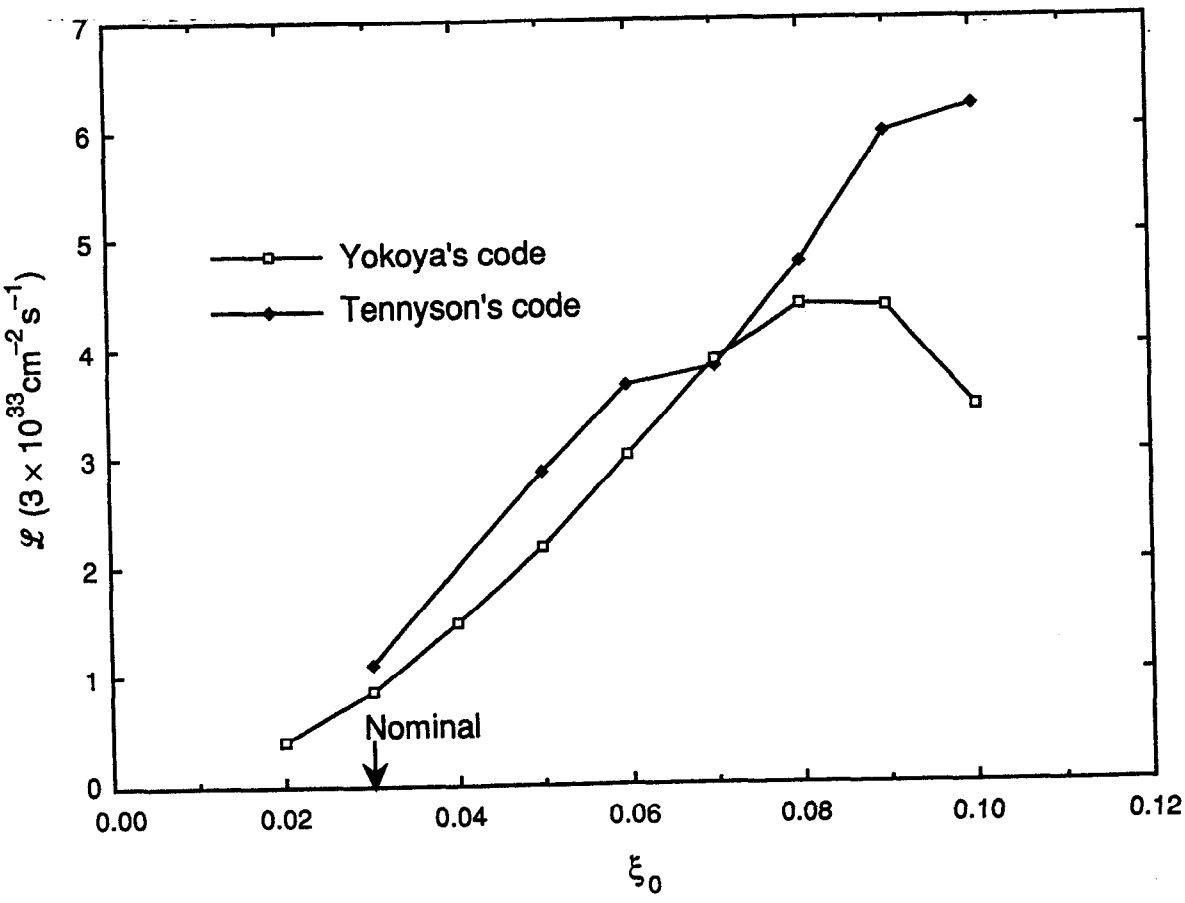

Fig. 4-88. Luminosity vs ξ_0 corresponding to the blown-up beam sizes in Fig. 4-87.

particles per bunch). In general, the two codes predict reasonably similar dynamical behavior.

Because the various beam sizes change differently, the dynamical beam-beam parameters also become different from each other. This means that the transparency symmetry is inherently broken by the dynamics, although not to a great extent. This is shown in Fig. 4-89.

- - *(iv) Verify that the results are maintained when parasitic crossings are included.* Although the beams collide head-on at the IP, the bunches experience grazing collisions on their way into and out of the region within ±4 m of the IP, where both beams travel in a common pipe. We must assess the effect of these parasitic crossings on the performance. This is done with strong-strong simulations. Parasitic crossings have a potentially detrimental effect on beam blowup, because they induce odd-order resonances and because the vertical beta function is sufficiently high at the crossing points that the long-range tune shift is comparable to the head-on tune spread at the IP. This also means that the parasitic crossings induce significant horizontal-vertical coupling. Taken together, these effects make it harder to find an optimum working point in the tune plane.

There are six parasitic crossings symmetrically located on either side of the IP. For the purposes of studying the beam-beam dynamics, the first parasitic crossing (that is, the one closest to the IP on either side) overwhelms the others on account of the small separation, together with the large vertical beta function. The strength of the long-range beam-beam kick at this first parasitic crossing is much greater than those of all the remaining crossings combined. This justifies our considering only this first parasitic crossing in our present calculations. Table 4-24 shows the relevant parameters for the primary and the first parasitic crossing for the B Factory.

In Table 4-24, Δs is the distance from the IP to the parasitic crossing point along the beam trajectory; $2\pi\Delta\nu_x$ and $2\pi\Delta\nu_y$ are the phase advances from the IP to the parasitic crossing; d is the separation between the two closed orbits at the parasitic crossing; and d/σ_{0x} is a measure of the extent of the overlap between the two bunches at the parasitic crossing point. The nominal emittances and number of particles per bunch are listed in Table 4-23. The parasitic crossings induce a tune shift and an amplitude-dependent tune spread in the particles due to the mutual interaction of the two bunches. It can be shown that the incoherent tune shifts experienced by a particle at the center of the positron bunch from a single parasitic interaction point are, to lowest-order approximation, given by [Tennyson, 1991a]

$$\Delta\nu_{x,+} = -\frac{r_0 N_- \beta_{x,+}}{2\pi\gamma_+ d^2}$$

$$\Delta\nu_{y,+} = +\frac{r_0 N_- \beta_{y,+}}{2\pi\gamma_+ d^2} \qquad (4\text{-}50)$$

with the corresponding expressions for the electron bunch obtained by exchanging the indices + and − in Eq. 4-50. In these expressions, $\beta_{x,y}$ are the beta functions at the parasitic crossing location. The negative sign in $\Delta\nu_x$ arises from the fact that the horizontal force is a decreasing function of separation at the parasitic crossing (the

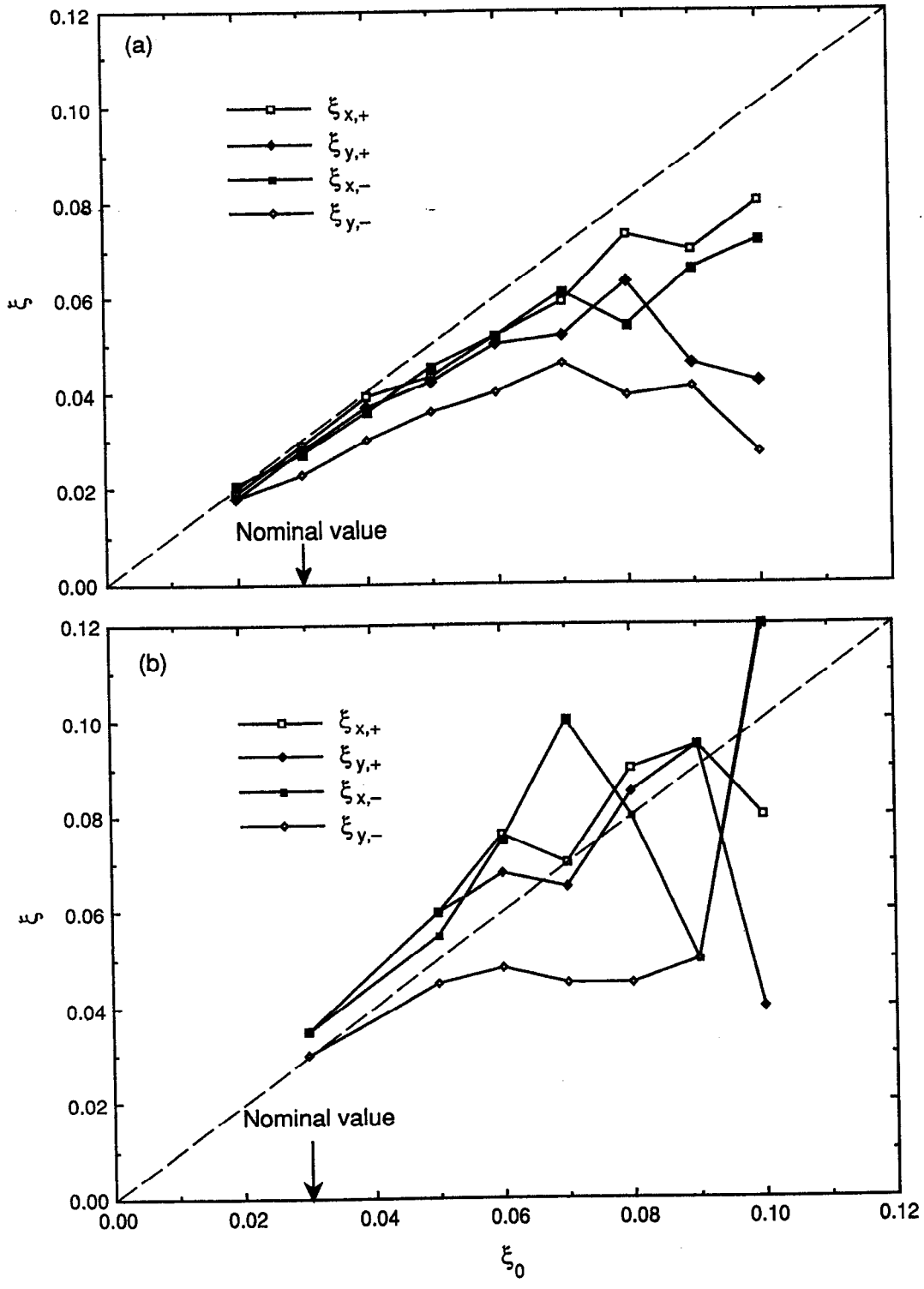

Fig. 4-89. Dynamical beam-beam parameters ξ vs ξ_0 corresponding to the blown-up beam sizes of Fig. 4-87: (a) Yokoya's code and (b) TRS. If the behavior were nominal, all four lines would coincide with the dashed main diagonal.

Table 4-24. B Factory nominal parameters at the IP and first parasitic crossing.

	LER (e^+)		HER (e^-)	
Δs [cm]	63			
d [mm]	2.82			
	IP	1st PC	IP	1st PC
$\Delta\nu_x$	0	0.1643	0	0.1111
$\Delta\nu_y$	0	0.2462	0	0.2424
β_x [cm]	37.5	151	75	130
β_y [cm]	1.5	2,523	3	1,301
α_x	0	–2.42	0	–1.06
α_y	0	–29.25	0	–18.74
σ_{0x} [μm]	186	373	186	245
σ_{0y} [μm]	7.4	302	7.4	153
d/σ_{0x}	—	7.56	—	11.5

"background" force induced by the closed-orbit separation is subtracted out in arriving at the above expressions). Using the numerical values for the parameters given in Table 4-24, we obtain

$$\begin{aligned} \Delta\nu_{x,+} &= -0.001, \qquad \Delta\nu_{x,-} = -0.0002 \\ \Delta\nu_{y,+} &= +0.009, \qquad \Delta\nu_{y,-} = +0.002 \end{aligned} \tag{4-51}$$

which shows that each of the first parasitic crossings contributes a vertical tune shift of almost one-third of the nominal IP tune shift of 0.03 in the positron beam. The remaining parasitic crossings contribute negligibly to the tune shifts.

A tune shift by itself is not detrimental, since it can be compensated by a shift in the working point. However, as mentioned above, the amplitude dependence causes a tune spread, which is more problematic. This spread, which can be calculated by appropriate numerical integration [Tennyson, 1991a], causes a distortion of the beam footprint, as shown in Fig. 4-90. Such a distortion makes it more difficult to find a good working point; for our present simulation purposes, we have maintained the original working point, $\nu_x = 0.09$, $\nu_y = 0.05$.

As implied by the above, the parasitic crossings produce horizontal-vertical coupling that can cause beam blowup. Obviously if the separation d were large enough, all effects of the parasitic crossings would disappear altogether. To assess this effect, we have carried out simulations in which we vary the separation d and keep all other parameters fixed. Figure 4-91 shows the beam blowup factors vs $d/\sigma_{0x,+}$ for $\xi_0 = 0.03$ and 0.05. Figure 4-92 shows the corresponding luminosity vs $d/\sigma_{0x,+}$ for $\xi_0 = 0.03$ and 0.05.

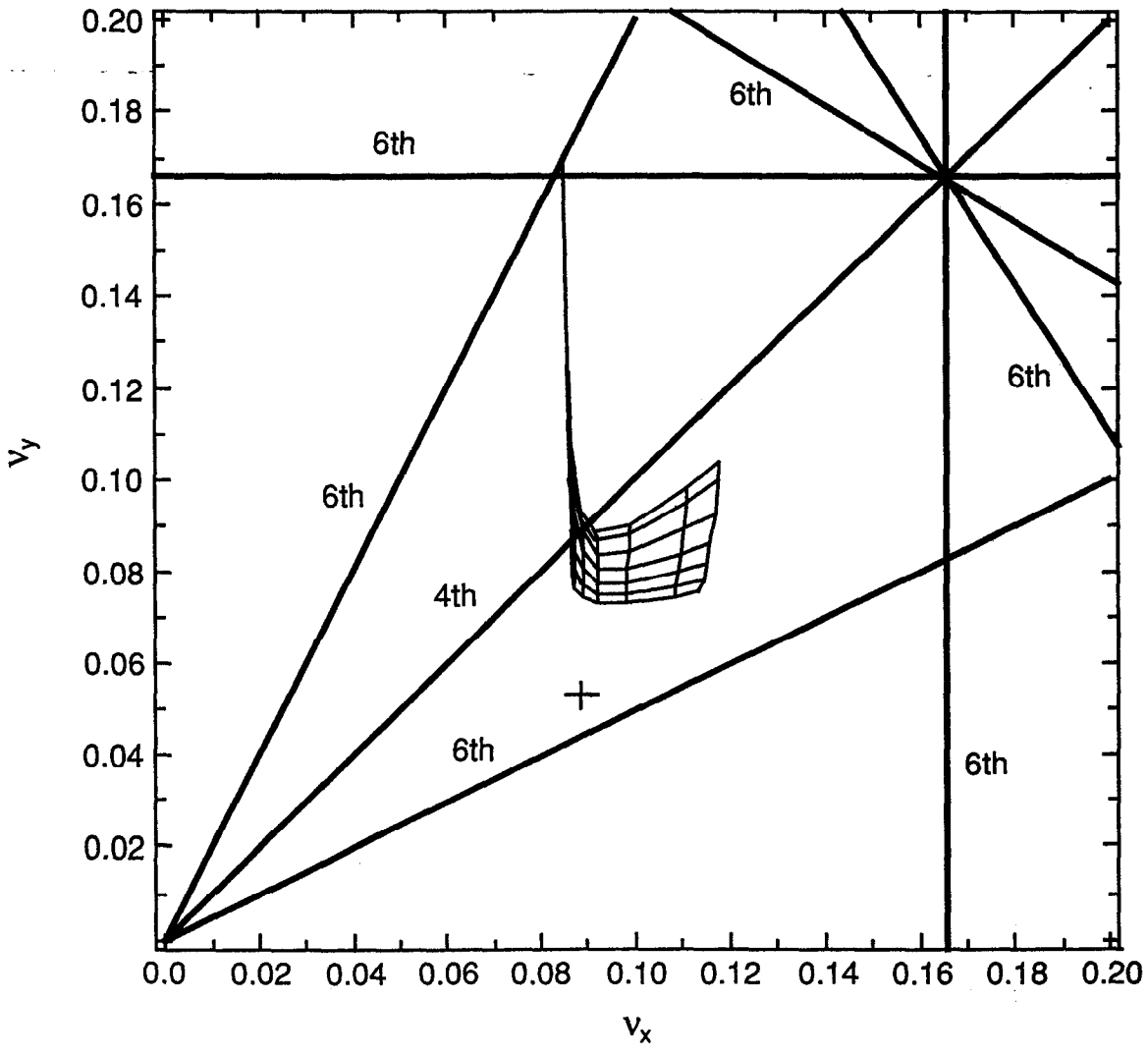

Fig. 4-90. Beam footprint, including the effect of the parasitic crossings. The large-amplitude distortion of the footprint produced by the long-range collision is apparent (see Fig. 4-86 for a comparison).

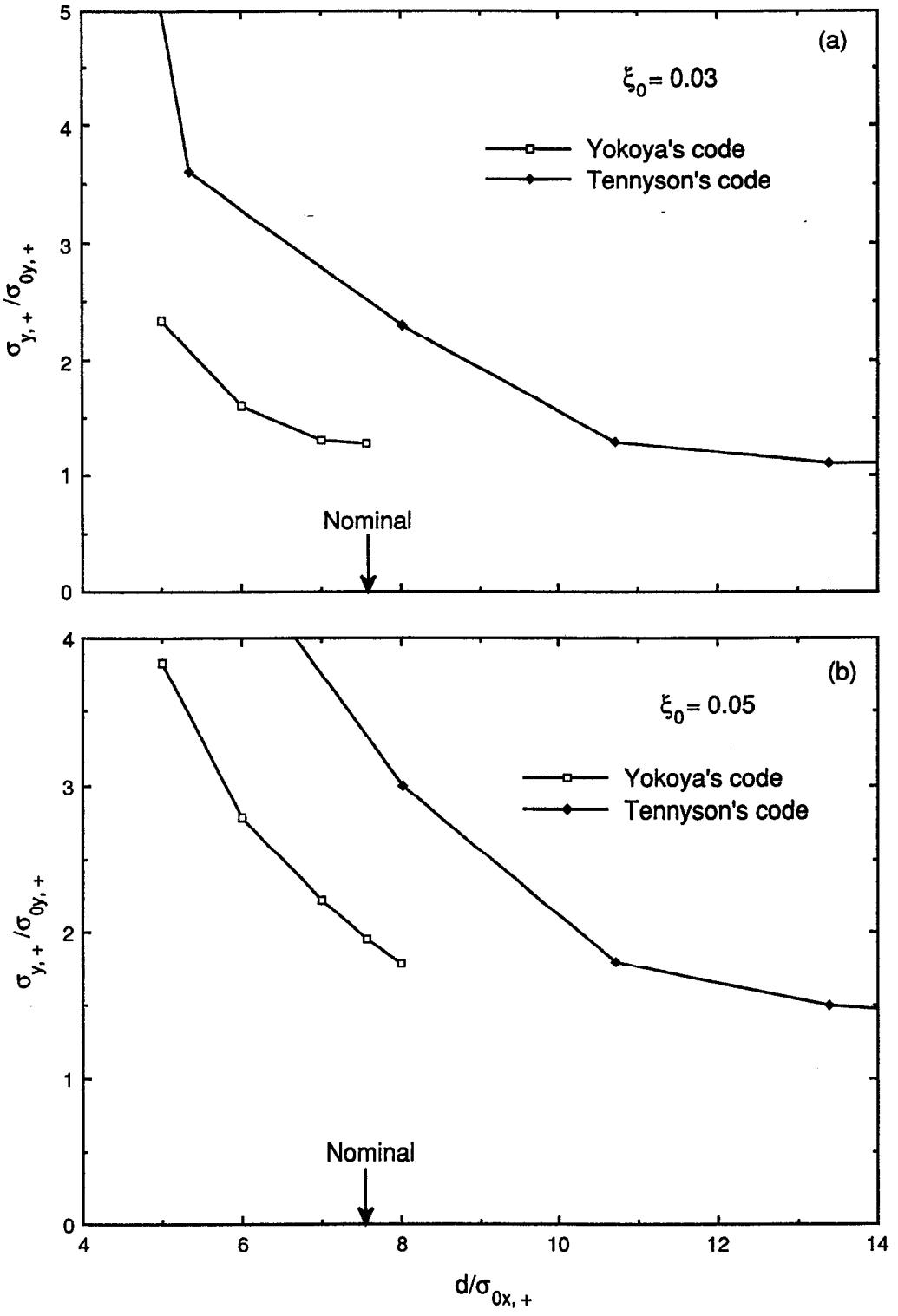

Fig. 4-91. Vertical beam blowup factor for the low-energy (positron) beam vs $d/\sigma_{0x,+}$ for the B Factory design, for (a) $\xi_0 = 0.03$ and (b) $\xi_0 = 0.05$. The nominal beam separation at the parasitic crossing, indicated by the arrow, corresponds to $d/\sigma_{0x,+} = 7.56$. The remaining three beam sizes are not shown because they exhibit blowup (or contraction) factors of 10% or less in all cases, except at very low values of $d/\sigma_{0x,+}$. This feature is qualitatively similar to what is shown in Fig. 4-87.

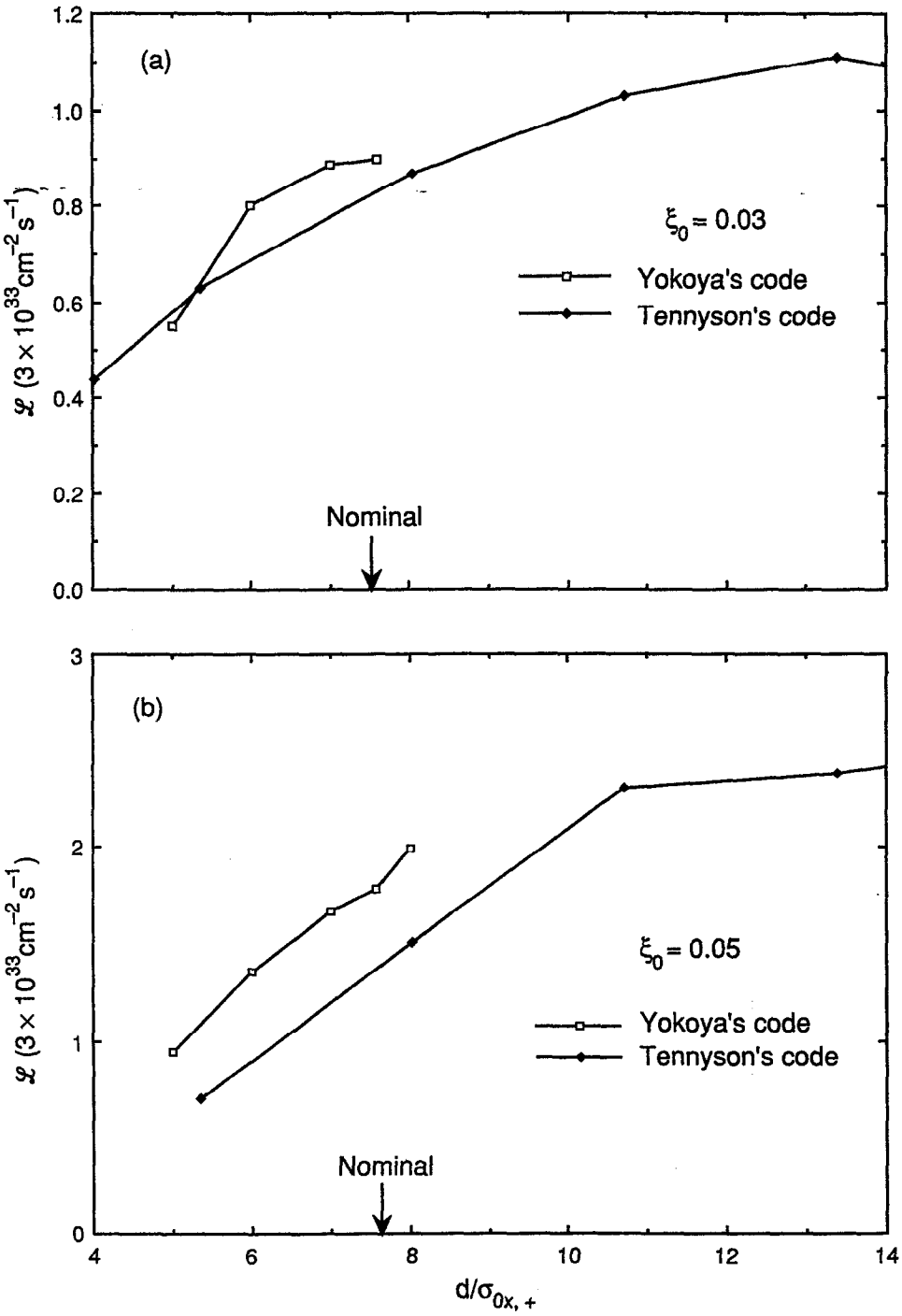

Fig. 4-92. Luminosity vs $d/\sigma_{0x,+}$ for the B Factory design, for (a) $\xi_0 = 0.03$ and (b) $\xi_0 = 0.05$, corresponding to the blown-up beam sizes shown in Fig. 4-91. Note that, for $\xi_0 = 0.05$, the nominal value of the luminosity is 8.3×10^{33} cm^{-2} s^{-1}.

4.4.5 Discussion

Figure 4-88 shows that, if only the IP were considered, nominal behavior for the working point chosen would persist up to values of ξ_0 much larger than 0.03. However, the parasitic crossings induce significant blowup in the vertical size of the low-energy beam. Even so, Fig. 4-92a shows that the luminosity is only reduced by about 15% from its design value for $\xi_0 = 0.03$. For the higher value of $\xi_0 = 0.05$, the luminosity degradation from its nominal value ($\mathscr{L}_0 = 8.3 \times 10^{33}$ cm^{-2} s^{-1}) is more significant, but the absolute luminosity still increases roughly linearly with beam current.

Although the two codes show good agreement in the absence of parasitic crossings, the agreement is less good when the parasitic crossings are included, especially for the larger value of ξ_0. We have not yet resolved this discrepancy. Qualitatively, however, both codes show the same features. For example, both indicate that it is the low-energy beam vertical blowup that is responsible for the luminosity degradation. This result means that the transparency symmetry is broken substantially by the dynamics.

The asymmetric behavior in the simulations suggests two approaches to try to improve the situation: Either make the nominal design truly conform to transparency symmetry or abandon the transparency symmetry approach altogether. The fact that the low-energy beam blows up suggests that, in the latter approach, one should probably lower its specified tune-shift value and raise the values of the other three beam-beam parameters. It is worth exploring the consequences of both routes in the future, as part of an expanded exploration of parameter space.

For now, however, we have adopted a more limited approach in order to examine other possibilities for luminosity improvement, by changing the nominal parameters slightly from those specified above, a few at a time. The first such exploration is to see the effect of a larger $\beta^*_{x,+}$ and $\beta^*_{y,+}$. The idea is to try to make the tune modulation amplitude closer to the transparency condition, as defined in Eq. 4-49. In order that the nominal luminosity and the four nominal beam-beam parameters remain constant at their original values, this change in $\beta^*_{x,+}$ and $\beta^*_{y,+}$ requires an increase in the emittances of the high-energy beam, $\varepsilon_{0x,-}$ and $\varepsilon_{0y,-}$, and in the number of particles per bunch of the low-energy beam, N_+, all in the same proportion as the increase in $\beta^*_{x,y,+}$. The result of the simulation, which does not include parasitic crossings, is shown in Figs. 4-93 and 4-94, where we compare the old result, corresponding to $\beta^*_{x,+} = 37.5$ cm, $\beta^*_{y,+} = 1.5$ cm, with the result for a new set of values, 33% larger, $\beta^*_{x,+} = 50$ cm, $\beta^*_{y,+} = 2$ cm. We see that the behavior is better in the sense that the luminosity is closer to its nominal value.

The penalty in this case is a larger low-energy beam current, which approaches 3 A on account of the increase in N_+. However, a beneficial effect of increasing the beta function at the IP is that the beta function at the first parasitic crossing decreases. This serves to make the bunches smaller, therefore increasing $d/\sigma_{0x,+}$, and also to reduce the tune shift produced at the parasitic crossing. At present, simulations including the parasitic crossings have not been done to test the effect of this reduction.

Another way of making the tune-modulation-amplitude parameters closer to the transparency condition is by decreasing the bunch length $\sigma_{\ell,+}$ of the low-energy beam in such a way that the synchrotron tune ν_s remains constant (see Eq. 4-49). This requires changing the momentum compaction factor α and the RF voltage V_{RF}. The result of the

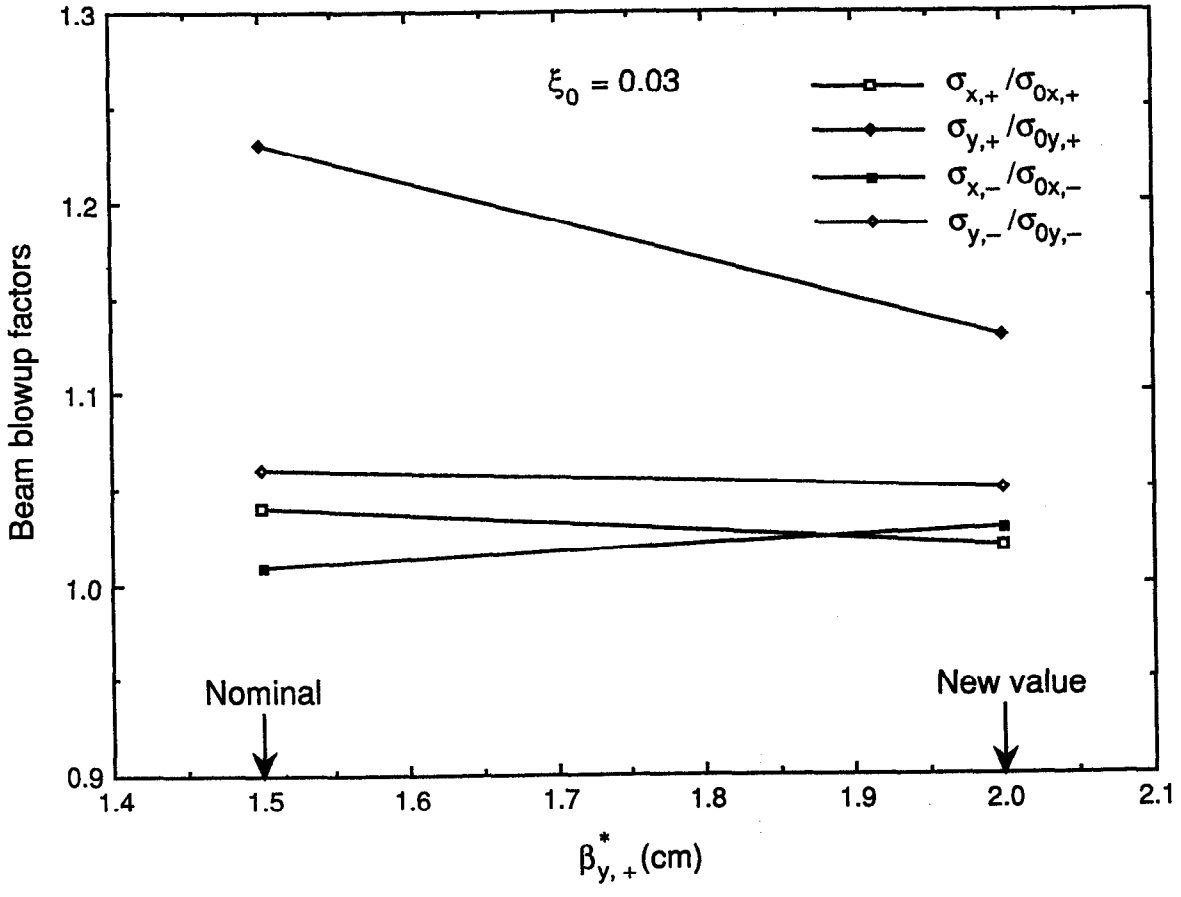

Fig. 4-93. Beam blowup factors vs $\beta^*_{y,+}$ for the B Factory design. Only the IP collision is considered ($\xi_0 = 0.03$, Yokoya's code). Other parameters were changed along with the beta function; see text.

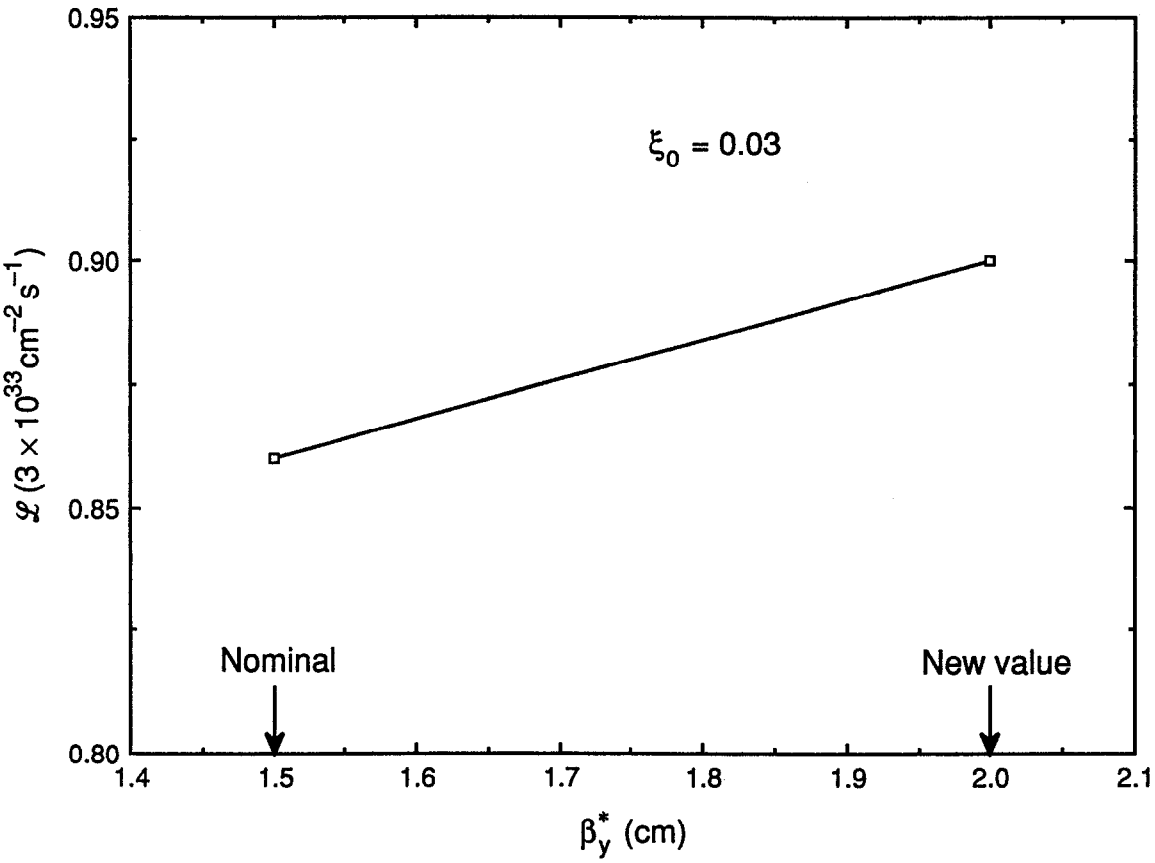

Fig. 4-94. Luminosity vs $\beta^*_{y,+}$ for the B Factory design. This corresponds to the blown-up beams of Fig. 4-93.

simulation, which again does not take into account parasitic crossings, is shown in Figs. 4-95 and 4-96. We see that the beam blowup is smaller and that the luminosity loss is quite small.

Finally, a third approach to making the beam dynamics closer to nominal is to increase the bunch spacing s_B by 50%, from 1.26 m to 1.89 m, by filling the rings with bunches every third RF bucket rather than every second bucket. The idea is to push the parasitic crossings farther away from the IP, so that the bunch separation is

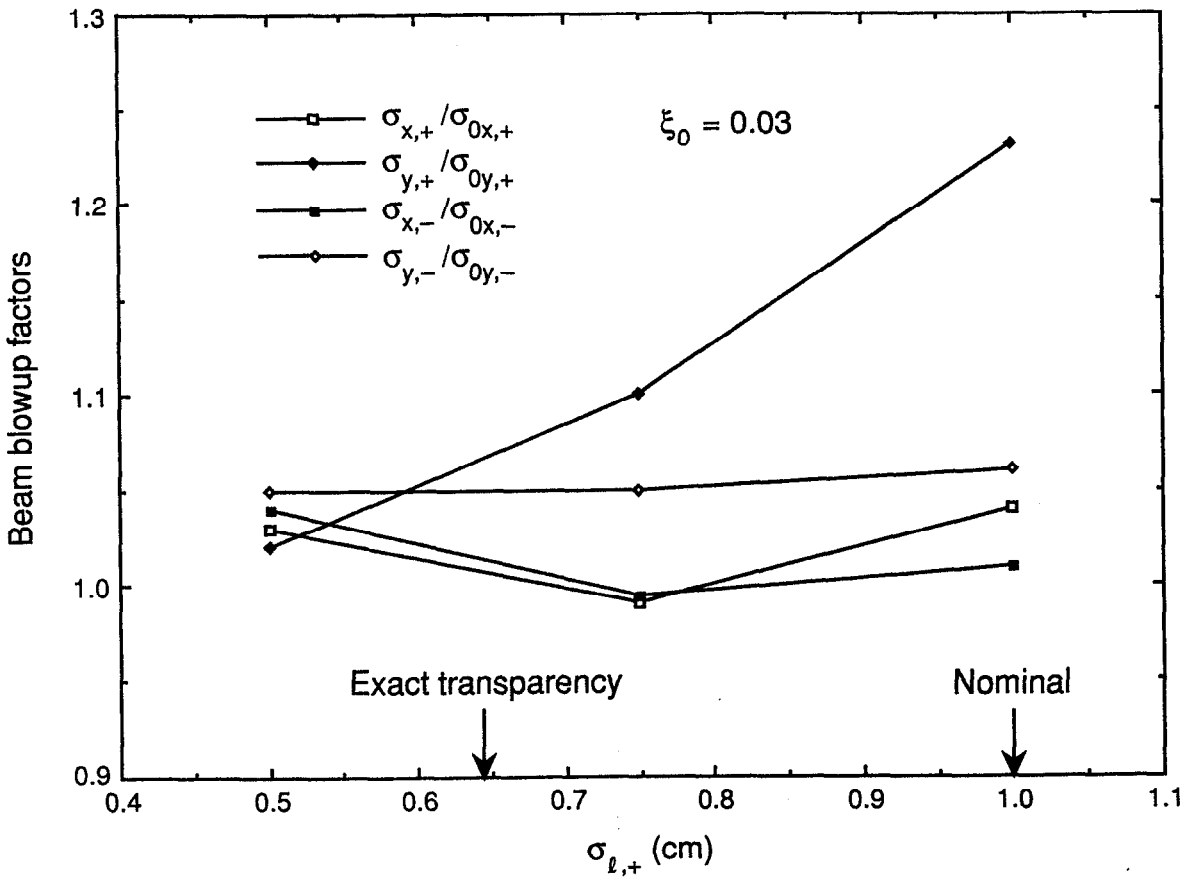

Fig. 4-95. Beam blowup factors vs $\sigma_{\ell,+}$. Only the IP collision is considered (ξ_0 = 0.03, Yokoya's code). The arrow labeled "exact transparency" indicates the value of $\sigma_{\ell,+}$ for which the amplitudes for the tune modulation due to synchrotron oscillations are the same in both beams. Other parameters are changed along with the bunch length; see text for details.

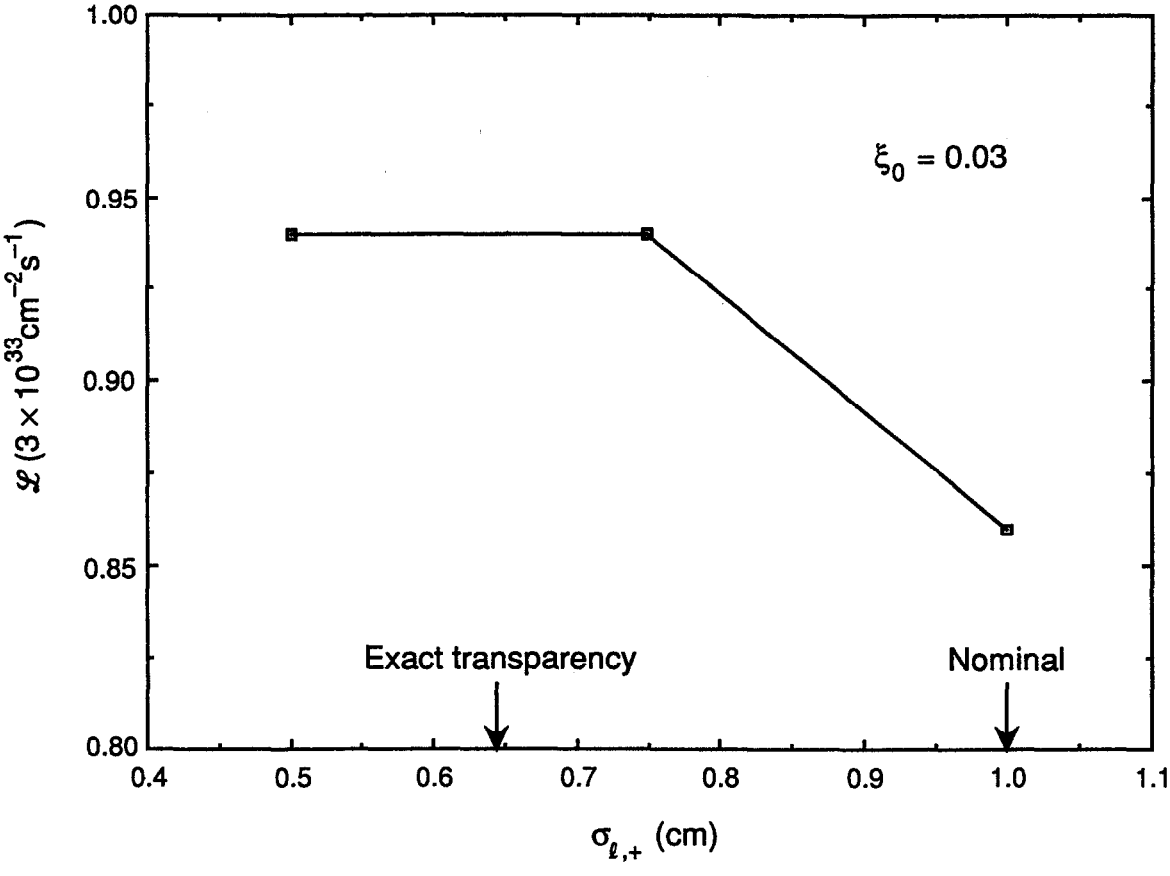

Fig. 4-96. Luminosity vs $\sigma_{\ell,+}$ for the B Factory design. This corresponds to the blown-up beams of Fig. 4-95.

correspondingly larger. In order to maintain ξ_0 and $\mathcal{L}_0$ at their original values of 0.03 and 3×10^{33} cm^{-2} s^{-1}, respectively, we require that the numbers of particles per bunch and the emittances also be increased by 50%. The resulting lattice parameters and nominal beam parameters are listed in Table 4-25.

Note that the bunch separation d at the first parasitic crossing is now 7.41 mm rather than the old value of 2.82 mm. The parameter $d/\sigma_{0x,+}$ is now a more comfortable 9.16 instead of the original value of 7.56. The resulting simulation results are shown in Figs. 4-97 and 4-98.

By comparing Fig. 4-97 with the previous case, Fig. 4-91, we can see a substantial improvement. The behavior is now very close to nominal.

Table 4-25. B Factory nominal parameters at the IP and the first parasitic crossing with increased bunch separation (every third bucket filled).

	LER (e^+)		HER (e^-)	
Δs [cm]	94			
d [mm]	7.41			
N_B	8.42×10^{10}		5.82×10^{10}	
ε_{0x} [nm·rad]	138		69	
ε_{0y} [nm·rad]	5.4		2.7	
	IP	1st PC	IP	1st PC
$\Delta\nu_x$	0	0.1844	0	0.1403
$\Delta\nu_y$	0	0.2478	0	0.2453
β_x [cm]	37.5	474	75	241
β_y [cm]	1.5	3,265	3	2,449
α_x	0	–9.20	0	–2.60
α_y	0	8.68	0	–15.95
σ^*_{0x} [μm]	228	809	228	408
σ^*_{0y}[μm]	9.00	420	9.00	257
d/σ_{0x}	0	9.16	0	18.2

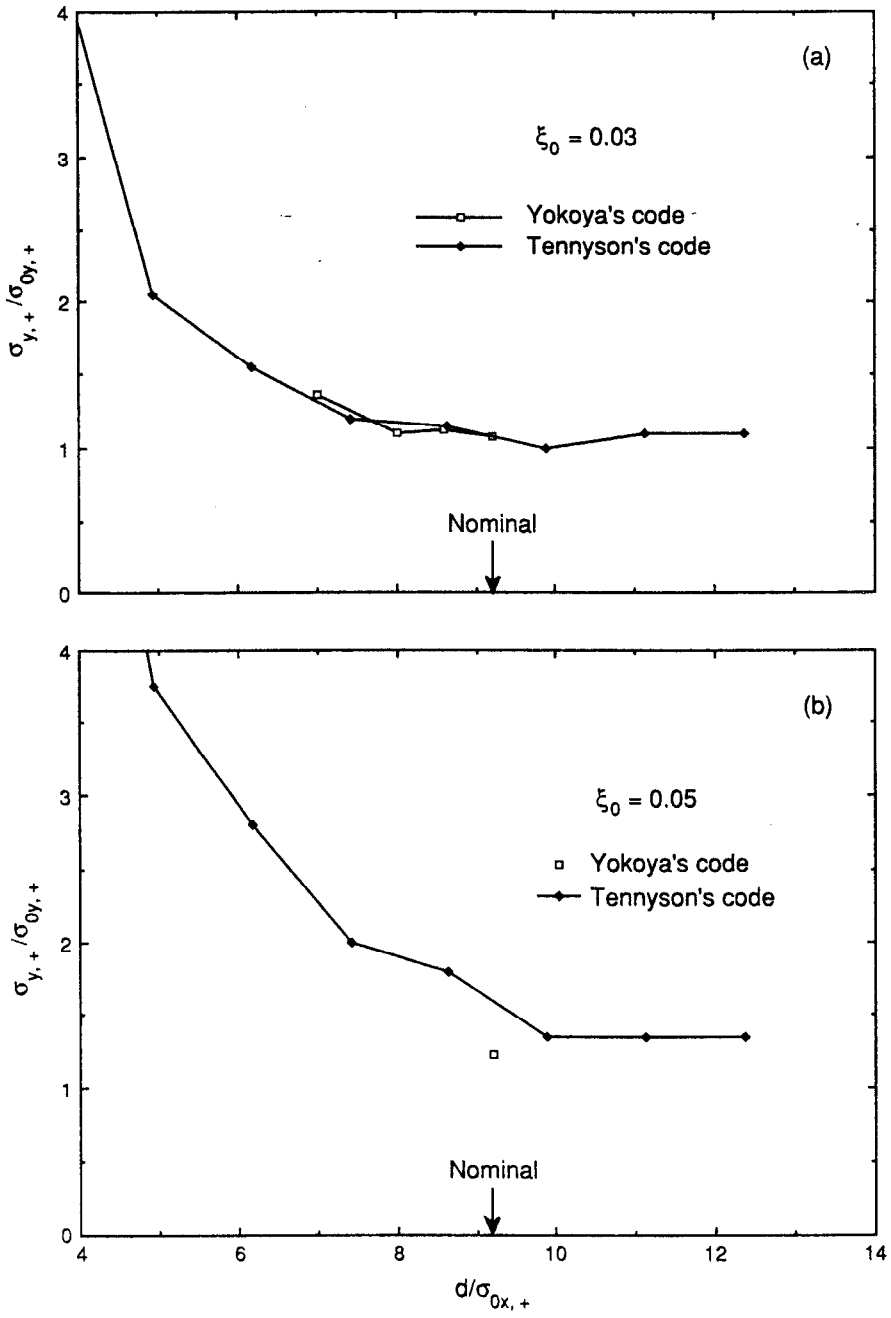

Fig. 4-97. Vertical beam blowup factor for the low-energy (positron) beam vs $d/\sigma_{0x,+}$ for the B Factory design, in the case where the bunches are filled every third bucket instead of every second bucket, for (a) $\xi_0 = 0.03$ and (b) $\xi_0 = 0.05$. The nominal beam separation at the parasitic crossing, indicated by the arrow, corresponds now to $d/\sigma_{0x,+} = 9.16$. The bunches have 50% more particles and 50% larger emittances than in the every-second-bucket filling scheme so that the nominal luminosity and beam-beam parameters retain their original values. The remaining three beam sizes are not shown, because they exhibit blowup (or contraction) factors of 20% or less in all cases, except at very low values of $d/\sigma_{0x,+}$. This feature is qualitatively similar to what is shown in Fig. 4-91.

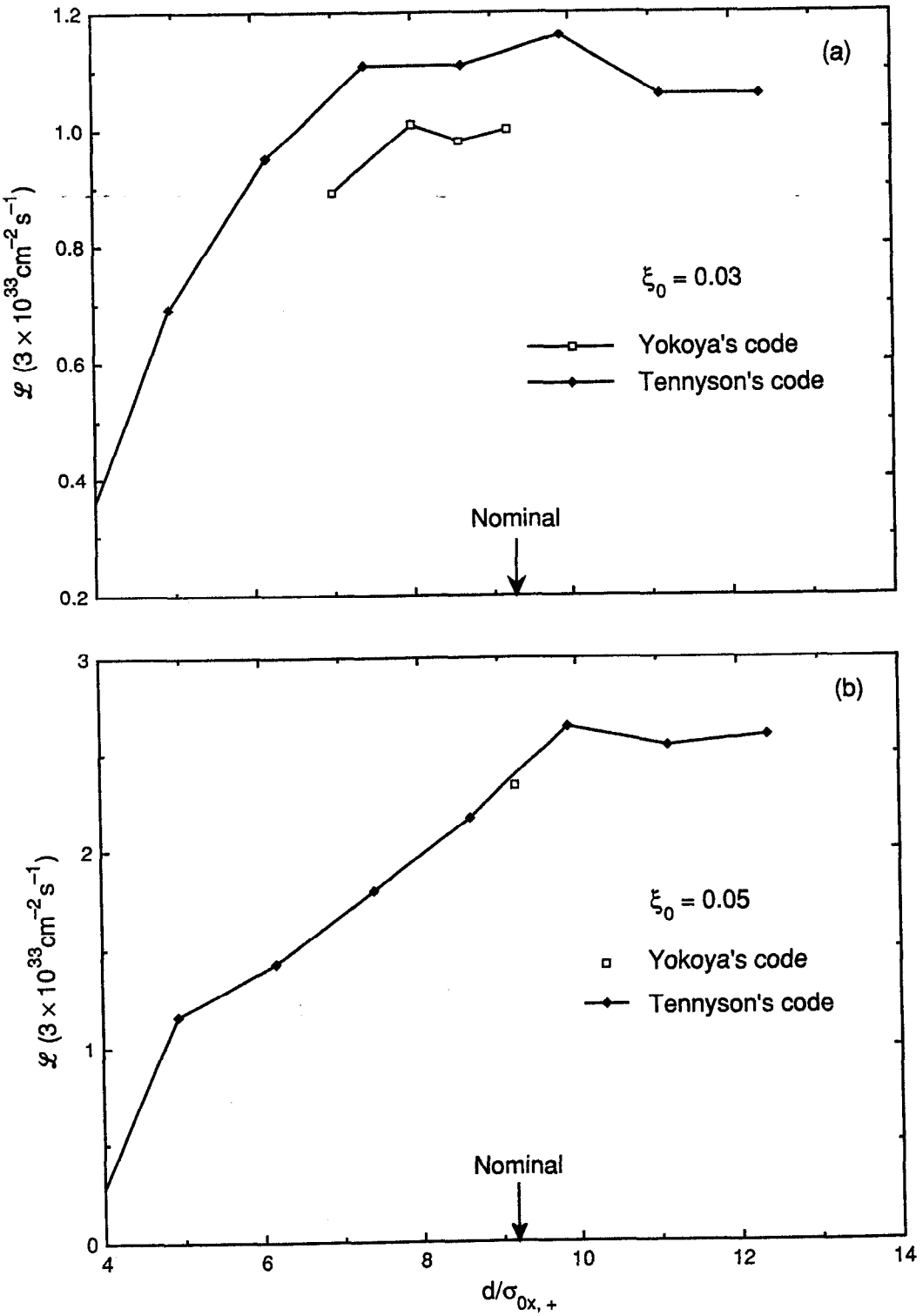

Fig. 4-98. Luminosity vs $d/\sigma_{0x,+}$ for the B Factory design, in the case where the bunches are filled every third bucket instead of every second bucket, for (a) ξ_0 = 0.03 and (b) ξ_0 = 0.05, corresponding to the blown-up beam sizes of Fig. 4-97.

4.4.6 Conclusions

Our results to date show that, without the parasitic crossings, the beam dynamics performance of the machine is quite close to nominal, up to values of ξ_0 substantially higher than the design specification of 0.03. Although we have shown this to be the case only for a working point just above the integer, we have preliminary evidence that this feature remains qualitatively valid for other working points as well [Tennyson, 1991b]. Another important issue that we are beginning to study in detail is that of beam lifetime. This is the most expensive and difficult part of beam-beam simulations; for this reason, we have concentrated our effort thus far on finding solutions with acceptable luminosity.

The parasitic crossings introduce a substantial horizontal-vertical coupling due to the large value of the vertical beta function. This has the effect of increasing the vertical size of the low-energy beam substantially, with a corresponding lowering of the luminosity. However, because the other three transverse beam sizes are not changed much, the luminosity degrades no more than 15% from its nominal value for $\xi_0 = 0.03$. For $\xi_0 = 0.05$, the relative degradation is larger, of the order of 40–50%; however, since the nominal luminosity is larger in this case ($\mathscr{L}_0 = 8.3 \times 10^{33}$ cm^{-2} s^{-1}), the *absolute* value of the luminosity is about 5×10^{33} cm^{-2} s^{-1}, which exceeds the nominal specification. Although the resultant performance is still deemed completely acceptable, we intend to seek improvements by exploring alternative parameters that entail less blowup at the larger value of ξ_0. Some possibilities, which are either in progress or as yet untried, are

- Make the machine designs more symmetric from the point of view of tune modulation due to synchrotron motion (for example, increase $\beta^*_{x,y,+}$, or decrease the bunch length $\sigma_{\ell,+}$)
- Leave the design of the collider as it is (slightly asymmetric), but introduce a slight asymmetry in the nominal beam parameters in such a way as to compensate the asymmetry (for example, increase $\xi_{0,-}$ and decrease $\xi_{0,+}$)
- Increase the bunch spacing from $2\lambda_{RF} = 1.26$ m to $3\lambda_{RF} = 1.89$ m, with a concomitant increase in emittances and numbers of particles per bunch, so that the total beam current, nominal beam parameters, and nominal luminosity remain unchanged
- Introduce a slight horizontal crossing angle, so that the beams are farther apart at the first parasitic crossing

So far we have tried only the first and third possibilities in any detail, with encouraging preliminary results that show dynamical behavior noticeably closer to nominal.

Because of this, and because of the other possibilities for improvement mentioned above, we are confident that a solution with a luminosity of 3×10^{33} cm^{-2} s^{-1} is entirely feasible. While many issues remain to be studied in much more detail, such as beam lifetimes, choice of working point, effect of magnet errors on beam dynamics performance, etc., it seems clear that a more comfortable, even conservative, solution is possible with relatively modest changes to the present design. Even without these improvements, the B Factory will be able to meet its luminosity goals with the addition of slightly more beam current in each ring.

5.

COLLIDER COMPONENTS

In Chapter 4 we presented the physics design of the Asymmetric B Factory. The parameters we have adopted to achieve a luminosity of 3×10^{33} cm^{-2} s^{-1}, and the beam separation scheme we have arrived at (driven mainly by background considerations), impose many requirements on the various technical components of the project. In this chapter, we describe these technical components, paying particular attention to those aspects that are most crucial to reaching the high luminosity we have specified. In general, the challenges to be met are associated with the high beam currents that must be stored in the two rings, 1.48 A in the high-energy ring (HER) and 2.14 A in the low-energy ring (LER). In all cases, we have designed the hardware to have adequate operating margin to ensure reliability, and we have employed proven design concepts wherever possible.

In Section 5.1 we describe the magnets and supports. In the case of the HER, nearly all of these magnets are existing PEP magnets, but we describe them briefly for completeness. Though the LER magnets will be newly constructed, they are based in large measure on proven PEP designs and are therefore straightforward to design and build. Magnets in the interaction region (IR), however, are technically quite challenging and are the key to the successful implementation of the beam separation scheme; these are described in Section 5.1.3.

The vacuum systems for the two rings are described in Section 5.2. The design challenges here are to provide a low background gas pressure in the face of copious synchrotron-radiation-induced photodesorption and to manage the high thermal loads associated with many megawatts of synchrotron radiation power. We have adopted a copper chamber for our design, based on its desirable properties in both these regards. In this section, we also describe the design and cooling for the various IR hardware components, such as the synchrotron radiation masks, the beam dumps, and the vertex detector beam pipe.

The other technically challenging aspects of the B Factory design include the RF cavities (Section 5.5) and the feedback system (Section 5.6). The RF cavities must be designed to dissipate approximately 150 kW of power and to permit the effective damping of dangerous higher-order modes (HOMs) to Q values of about 70. This

damping is accomplished with an innovative design in which three waveguides are attached to the body of the room-temperature cavity to remove the HOM power. The feedback system utilizes a bunch-by-bunch approach that is designed to handle the full bunch repetition rate of 238 MHz; the system employs a novel digital processing scheme that is very flexible and can accommodate both injection and colliding-beam conditions. Detailed simulations of system performance have demonstrated the efficacy of the design.

The remaining design aspects covered in Chapter 5—survey and alignment (Section 5.3), power supplies (Section 5.4), instrumentation (Section 5.7), and control system (Section 5.8) are relatively straightforward. Here too we have paid attention to providing flexibility and reliability in all components to ensure that the B Factory will indeed function as a "factory."

5.1 MAGNETS AND SUPPORTS

The magnet system in the B Factory provides the guide fields that bend and focus the charged particles, electrons in the HER and positrons in the LER. In the case of the HER, the lattice is designed to make use of most of the existing PEP magnets. The LER is an entirely new ring for which all magnets must be newly constructed.

Because PEP was designed to operate at 18 GeV, whereas the B Factory HER need operate at only 9 GeV, the PEP magnets are very conservatively designed for their new function. As discussed in Section 7.2, it is prudent to inspect the magnets when they are removed from the tunnel; as needed, the magnet coils will be refurbished to ensure their reliability for long-term B Factory service. In addition, the magnets will be measured after reassembly to ensure that their fields remain the same.

We plan to reuse all of the PEP dipoles and quadrupoles for the B Factory HER. Because the HER lattice uses more quadrupoles than did PEP, additional magnets must be fabricated. In the case of the dipoles, we need 192 regular bending magnets and an additional 16 PEP low-field bending magnets, for a total of 208 PEP dipoles; four short LER-style dipoles will also be used, making a grand total of 212 dipoles for the HER. All 144 sextupoles are available from PEP. For completeness, however, we describe the existing PEP magnets briefly in Section 5.1.1.

The quadrupole and sextupole magnets for the LER are designed to have the same aperture as the present PEP magnets. This is justified because the required beam-stay-clear aperture in the LER is almost identical to that of the HER, as discussed in Section 5.2.1. Basing the LER designs on PEP magnets minimizes the engineering and design efforts required, because the already-optimized pole profiles of the PEP magnets can be used without modification. The LER dipoles are much shorter than the PEP dipoles (1 m compared with 5.4 m for PEP) but can nevertheless make use of the same pole profile. Design details for the LER magnets are presented in Section 5.1.2.

5.1.1 HER Magnets

As mentioned above, most of the magnets for the HER are existing PEP magnets. The only exception is the quadrupoles. Additional quadrupoles are needed for the HER

because the FODO focusing structure (see Section 4.1) will be maintained throughout the straight sections, except the IR-2 straight that houses the detector.

5.1.1.1 Dipoles. The main parameters of the laminated PEP dipoles are summarized in Table 5-1 for conditions corresponding to the nominal B Factory operating energy of 9 GeV. Physical dimensions of the magnet are shown in Fig. 5-1. Each magnet has a magnetic length of 5.4 m (212.607 in.) and weighs 7.4 tons. The coils, located above and below the midplane, are constructed of water-cooled aluminum, insulated with Mylar and fiberglass tape and vacuum potted in an alumina-based epoxy. All dipoles will be disassembled and will have their coil insulation inspected and refurbished to ensure reliable service in the B Factory. After reassembly, a sample of magnets will be remeasured to ensure the constancy of their magnetic properties. To provide horizontal orbit correction, backleg windings are employed. Windings from a pair of dipoles on either side of a focusing quadrupole will be ganged together to form a single corrector.

5.1.1.2 Quadrupoles. As with the dipole magnets, all existing PEP quadrupoles will be reused for the HER. Altogether, 272 magnets are required for the B Factory HER, of which 204 are available from PEP. The additional magnets will be fabricated using the same pole-tip profile developed for PEP, thus avoiding the need to develop a new design. Dimensions of a typical quadrupole magnet are shown in Fig. 5-2. The electrical characteristics of the existing quadrupoles, together with the new magnets, are summarized in Table 5-2. As is the case for the dipoles, the conductor for the quadrupoles is an aluminum extrusion. The insulating procedure used for the dipoles, employing Mylar, fiberglass tape, and alumina-loaded epoxy, will also be used for the quadrupole magnets.

5.1.1.3 Sextupoles. For chromaticity correction in the B Factory HER, 144 sextupoles are required; all are available from PEP. The nominal operating point of the HER is quite similar to that of PEP, and since the sextupoles were designed for 18-GeV operation, they have ample margin for any reasonable HER operating parameters. The dimensions of the sextupole are shown in Fig. 5-3, and the electrical characteristics for the various sextupole types at the nominal HER energy are summarized in Table 5-3. Coil design and insulation are the same as for the dipoles and quadrupoles, discussed above.

5.1.2 LER Magnets

All magnets for the LER will be newly constructed. However, the beam-stay-clear aperture requirements for the LER are sufficiently similar to those of the HER (and PEP) that it is justifiable to use the same magnet aperture dimensions. (It is worth noting here that a review of the anticipated gas loads in both the HER and the LER indicates very little difference between the two; this argues for the choice of a vacuum chamber of similar cross section in the two rings.)

The main benefit of keeping the same magnet aperture is that the new LER magnets can take advantage of the well-proven pole-tip profiles developed for PEP and PETRA (using the computer program POISSON); that is, the magnets can be very similar to PEP magnets, with only the external dimensions changed to reflect the lower field

Table 5-1. HER dipole parameters. All are refurbished PEP dipoles.

Magnet designation	2.8C212	2.8C40	5.25C80	5.25C80
Number of magnets	192	4	8	8
Field @ 9 GeV [T]	0.1819	0.0356	0.0166	0.0214
Integrated field @ 9 GeV [T·m]	0.9824	0.0356	0.0332	0.0428
Pole width [in.]	8.425	7.5	5.9	5.9
Gap height [in.]	2.787	2.787	5.276	5.276
Core length [in.]	209.820	36.583	73.622	73.622
Magnetic length [in.]	212.607	39.370	78.740	78.740
Width of useful field, 0.1% [in.]	4.725	4.00	3.15	3.15
Lamination height [in.]	15.433	16	13.38	13.38
Lamination width [in.]	18.19	17.8	10.47	10.47
Packing factor, minimum [%]	96	96	NA	NA
Core weight [lb]	14,168	2,000	1,500	1,500
Amp turns per pole @ 9 GeV	5,279	1,007	469	605
Turns per pole	8	15	1	1
Pancakes per pole	1	1	1	1
Conductor dimensions [in.]	2.4 × 0.7	2.0 × 0.3125	2.4 × 0.7	2.4 × 0.7
Cooling hole diameter [in.]	0.25	0.1875	0.25	0.25
Conductor cross section [in.^{2}]	1.59	0.60	1.59	1.59
Current @ 9 GeV [A]	659.9	67.1	469.4	605.2
Resistance @ 40°C [mΩ]	5.5	7.2	0.362	0.362
Power @ 9 GeV [kW]	2.39	0.03	0.08	0.13
Voltage drop @ 9 GeV [V]	3.63	0.48	0.17	0.22
Coil weight [lb]	585	200.00	40.00	40.00
Number of water circuits	2 @ 0.6 gpm	2 @ 0.6 gpm	2 @ 0.6 gpm	2 @ 0.6 gpm
Water flow rate [gpm]	1.2	1.20	1.20	1.20
Water pressure drop [psi]	50	100	50	50
Temperature rise [°C]	7.6	0.1	0.3	0.4
Total power, magnets and buss [kW]	545.5	0.1	0.6	1.1
Total voltage, magnets and buss [V]	736.4	1.9	1.4	1.8
Total system water requirements [gpm]	230.4	4.8	9.6	9.6

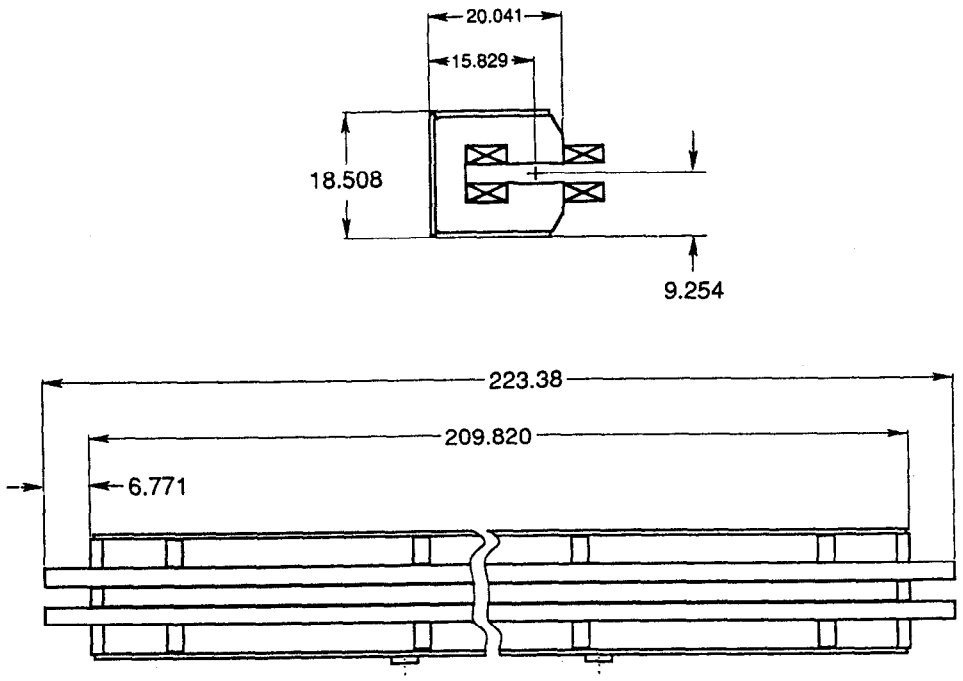

Fig. 5-1. End and side views of the HER bending magnet. Dimensions are given in inches.

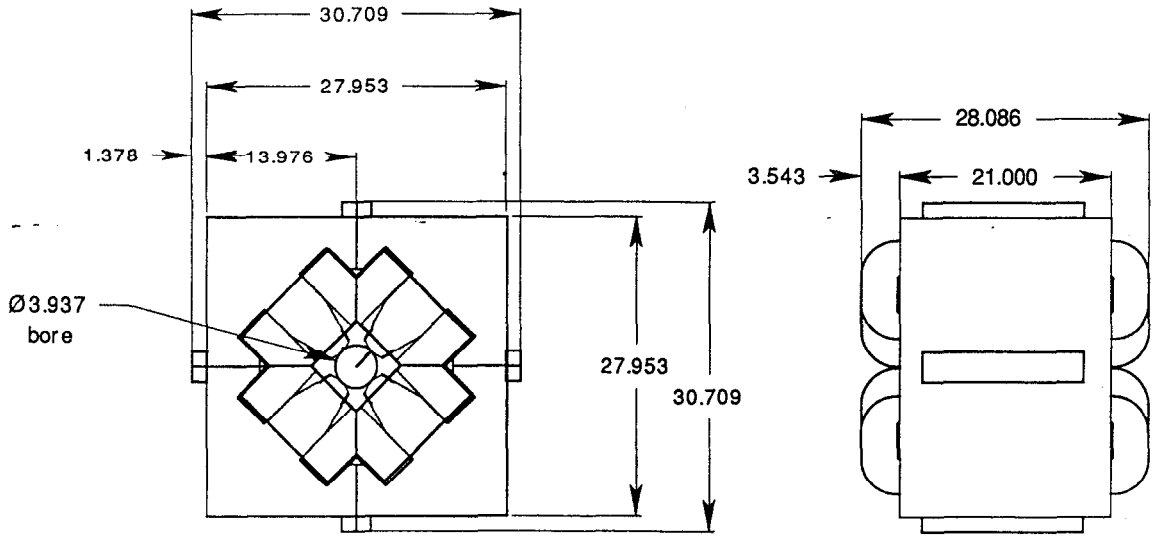

Fig. 5-2. End and side views of an HER quadrupole magnet. Dimensions are given in inches.

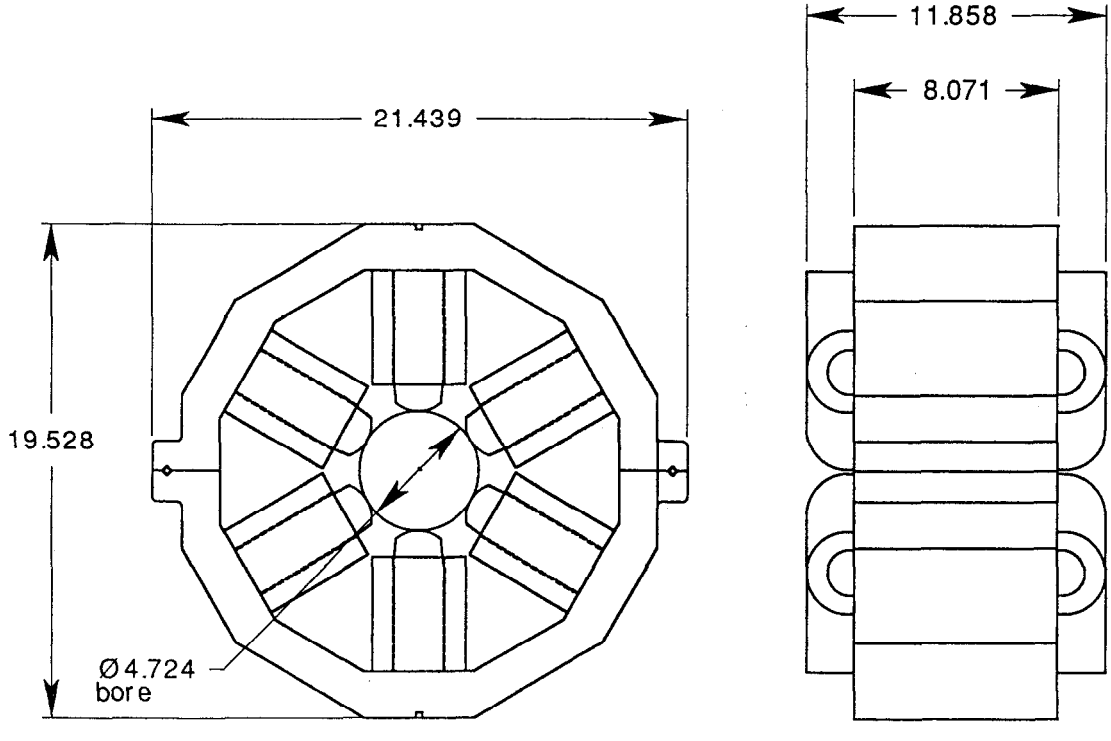

Fig. 5-3. End and side views of a PEP/HER sextupole magnet. Dimensions are given in inches.

Table 5-2a. HER quadrupole parameters. The column heads indicate whether the magnets are refurbished PEP quadrupoles or newly constructed magnets.

	PEP	PEP	PEP	New	PEP	PEP
Magnet designation	4Q21	4Q29	4Q39	4Q39L	4Q21	4Q29,
Location in ring	QD Sup	QD Sup	QF Sup	Straights	QD arc	QF arc
Number of magnets	24	12	24	60	66	72
Operating gradient [T/m]	7.99	5.59	5.39	4.05	7.29	5.58
Pole tip field @ operating gradient [T]	0.399	0.279	0.270	0.203	0.364	0.279
Gradient length product [T]	4.460	4.095	5.386	4.053	4.070	4.090
Inscribed radius [in.]	1.968	1.968	1.968	1.968	1.968	1.968
Minimum gap [in.]	1.457	1.457	1.457	1.457	1.457	1.457
Core length [in.]	21.00	27.87	38.35	38.39	21.00	27.86
Magnetic length [in.]	21.98	28.85	39.33	39.37	21.98	28.85
Lamination height [in.]	13.98	13.98	13.98	10.50	13.98	13.98
Lamination width [in.]	13.35	13.35	13.35	10.50	13.35	13.35
Packing factor, minimum [%]	98	98	98	98	98	98
Core weight [lb]	2882	3825	5264	3455	2882	3824
Amp turns per pole @ 9 GeV	7937	5552	5357	4027	7243	5546
Turns per pole	56	56	56	37	56	56
Pancakes per pole	1	1	1	1	1	1
Conductor cross-sectional area [in.^{2}]	0.197	0.197	0.197	0.197	0.197	0.197
Conductor dimensions [in.]	0.5×0.5	0.5×0.5	0.5×0.5	0.5×0.5	0.5×0.5	0.5×0.5
Cooling hole diameter [in.]	0.25	0.25	0.25	0.25	0.25	0.25
Current @ 9 GeV [A]	142	99	96	109	129	99
Resistance @ 40°C [mΩ]	72.7	91.8	121.45	80.24	72.7	91.8
Power @ 9 GeV [kW]	1.46	0.90	1.11	0.95	1.22	0.90
Voltage drop @ 9 GeV [V]	10.30	9.10	11.62	8.73	9.40	9.09
Coil weight [lb]	233	308	396	396	233	308
Number of water circuits	1	1	1	1	1	1
Water flow rate [gpm]	0.65	0.55	0.50	0.50	0.65	0.55
Water pressure drop [psi]	150	150	150	150	150	150
Temperature rise [°C]	8.5	6.2	8.4	7.2	7.1	6.2
Total power (magnets and buss) [kW]	35.1	10.8	26.7	57.0	80.3	64.8
Magnet system water requirements [gpm]	15.6	6.6	12	30	42.9	39.6

Table 5-2b. HER special quadrupoles.

	NEW	NEW	PEP	PEP	PEP	NEW	NEW
Magnet designation	4Q39	4Q39	6Q60	6Q60	6Q60	4Q39	4Q39
Transport name	QFi1	QDi2	QFi3	QDi4	QFi5	Qd6	Qf7
Location in ring	Inj	Inj	Inj	Inj	Inj	IR	IR
Number of magnets	2	2	2	2	2	2	2
Operating gradient [T/m]	3.43	3.96	0.86	2.52	3.14	5.16	4.04
Pole tip field @ operating gradient [T]	0.172	0.198	0.069	0.201	0.251	0.258	0.202
Gradient length product [T]	3.431	3.962	1.309	3.833	4.784	7.871	6.155
Inscribed radius [in.]	1.968	1.968	3.1496	3.1496	3.1496	1.968	1.968
Minimum gap [in.]	1.457	1.457	1.457	1.457	1.457	1.457	1.457
Core length [in.]	38.39	38.39	58.43	58.43	58.43	59.02	59.02
Magnetic length [in.]	39.37	39.37	60.00	60.00	60.00	60.00	60.00
Lamination height [in.]	10.50	10.50	13.98	13.98	13.98	10.50	10.50
Lamination width [in.]	10.50	10.50	13.35	13.35	13.35	10.50	10.50
Packing factor, minimum [%]	98	98	98	98	98	98	98
Core weight [lb]	2882	2882	16148	16148	16148	2882	2882
Amp turns per pole @ 9 GeV	3409	3937	2186	6401	7989	5132	4013
Turns per pole	37	37	13	13	13	37	37
Pancakes per pole	1	1	1	1	1	1	1
Conductor cross-sectional area [in.^{2}]	0.197	0.197	0.197	0.197	0.197	0.197	0.197
Cooling hole diameter [in.]	0.25	0.25	0.25	0.25	0.25	0.25	0.25
Conductor dimensions [in.]	0.5 × 0.5	0.5 × 0.5	0.5 × 0.5	0.5 × 0.5	0.5 × 0.5	0.5 × 0.5	0.5 × 0.5
Current @ 9 GeV [A]	92	106	168	492	615	139	108
Resistance @ 40°C [mΩ]	72.7	72.7	72.7	72.7	72.7	72.7	72.7
Power @ 9 GeV [kW]	0.62	0.82	2.06	17.62	27.45	1.40	0.86
Voltage drop @ 9 GeV [V]	6.70	7.73	12.22	35.79	44.67	10.08	7.88
Coil weight [lb]	233	233	955	955	955	233	233
Number of water circuits	1	1	1	1	1	1	1
Water flow rate [gpm]	0.65	0.65	0.65	0.65	0.65	0.65	0.65
Water pressure drop [psi]	150	150	150	150	150	150	150
Temperature rise [°C]	3.6	4.8	12.0	103.0	160.5	8.2	5.0
Total power (magnets and buss) [kW]	1.2	1.6	4.1	35.2	54.9	2.8	1.7

Table 5-3. HER sextupole parameters.

Magnet designation	10 D	10 F	10D1	10 F1	10 D2	10 F2
Number of magnets	56	64	8	4	8	4
Operating gradient [T/m^2]	73.04	44.67	104.41	66.57	33.61	22.81
Pole tip field @ operating gradient [T]	0.131	0.080	0.188	0.120	0.060	0.0411
Integrated strength @ 9 GeV [T/m]	18.63	11.39	26.63	16.98	8.57	5.817
Aperture inscribed radius [in.]	2.362	2.362	2.362	2.362	2.362	2.362
Core length [in.]	8.071	8.071	8.071	8.071	8.071	8.071
Magnetic length [in.]	10.041	10.041	10.041	10.04	10.041	10.041
Core weight [lb]	170.	170.	170.	170.	170.	170.
Amp turns per pole	2081	1273	2974	1896	957	650
Turns per pole	24	24	24	24	24	24
Pancakes per pole	1	1	1	1	1	1
Square conductor dimensions [in.]	0.375	0.375	0.375	0.375	0.375	0.375
Cooling hole diameter [in.]	0.125	0.125	0.125	0.125	0.125	0.125
Conductor cross-sectional area [in.^{2}]	0.127	0.127	0.127	0.127	0.127	0.127
Current @ 9 GeV [A]	–86.7	–53.0	–123.9	–79.0	–39.9	–27.1
Coil length/pole [ft]	70.0	70.0	70.0	70.0	70.0	70.0
Resistance @ 40°C [mΩ]	44.25	44.25	44.25	44.25	44.25	44.25
Power @ 9 GeV [kW]	0.33	0.12	0.68	0.28	0.07	0.03
Voltage drop @ 9 GeV [V]	3.84	–2.35	5.48	–3.50	1.77	–1.20
Coil weight [lb]	200	200	200	200	200	200
Number of water circuits	2	2	2	2	2	2
Water flow rate [gpm]	0.25	0.25	0.25	0.25	0.25	0.25
Water pressure drop [psi]	150	150	150	150	150	150
Temperature rise [°C]	5.1	1.9	10.3	4.2	1.1	0.5
Total magnet power [kW]	18.6	8.0	5.4	1.1	0.6	0.1
Total voltage [V]	214.8	–150.2	43.9	–14.0	14.1	–4.8
Total system water requirements [gpm]	14.0	16.0	2.0	1.0	2.0	1.0

requirements at the nominal 3.1-GeV operating point. In this way, we substantially reduce our R&D and engineering costs.

The design of the new magnets will be optimized by minimizing the sum of the installed capital cost plus ten years of operating cost at the design energy. This means that prudent attention is paid to reducing power consumption. Despite this, the LER magnets use proportionately more power than the PEP/HER magnets. This comes about because the PEP magnets were optimized for 18-GeV operation, where the operating costs are higher than at 9 GeV.

5.1.2.1 Dipoles. The design of the LER dipoles was dictated by several considerations. First, the LER magnets must be mounted above the HER. To minimize the weight that must be rigidly supported, it is important to reduce the size of the dipoles considerably, compared with the PEP design. Second, the problems with synchrotron-radiation-induced gas desorption are eased considerably if the dipole is kept short enough to permit its synchrotron radiation fan to exit the magnet completely (as discussed in detail in Section 5.2). Finally, the lattice parameters of the LER call for a relatively high emittance and short damping times, compared with what would result from a low-field bending magnet lattice. Although we have chosen to provide wigglers to adjust these parameters, the choice of a short, higher-field dipole helps to reduce the demands on the wigglers and to spread the synchrotron radiation power around more of the ring.

The LER arc dipole magnet physical dimensions are shown in Fig. 5-4. The key dimensions are the length of 36.583 in. and the gap of 2.787 in. The electrical properties of the LER dipole at its nominal operating energy of 3.1 GeV are summarized in Table 5-4.

To reduce production costs and to maximize magnet-to-magnet uniformity, the main ring magnets for the LER are of laminated construction. The dipole magnets will be constructed of one-piece laminations, 1/16-in. thick, punched from a decarburized, annealed, low-carbon steel sheet, such as Armco special magnet steel. This material—which has been used successfully for many accelerator applications, including those at PEP and Fermilab—exhibits high saturation induction, modest coercive force, and low remanent field. The estimated steel weight to manufacture the required 208 bending magnets is 350 tons.

Laminations will be punched with built-in fiducials to provide convenient external references for alignment, as discussed in Section 5.3. In addition, for reasons explained below, new witness marks will be introduced into the die at each heat-change to ensure magnet uniformity. Particular attention will be paid to the wear on the die. The vendor will be required to keep track of the number of laminations punched between die sharpenings and to provide SLAC with sample laminations on a regular basis, so that in-house inspections can be made to ensure that undue wear (>0.0005 in.) has not taken place on the critical surfaces (thereby producing out-of-tolerance laminations).

The vendor responsible for stacking the laminations will be required to deburr and then stack them, using laminations from consecutive heats. If this is done, the pattern generated by the witness marks will be obvious upon visual inspection. If the observed pattern is regular, the core will be acceptable, whereas an irregular pattern will indicate a lack of quality control on the part of the manufacturer and will be sufficient cause for rejecting the magnet core.

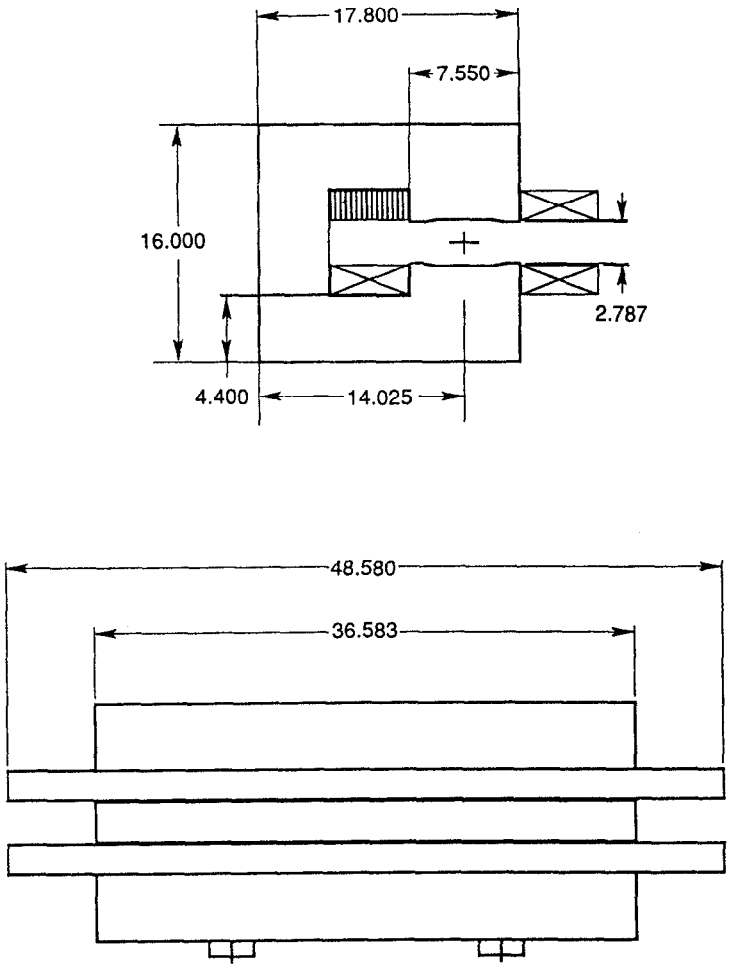

Fig. 5-4. End and side views of the LER bending magnet. Dimensions are given in inches.

Table 5-4. LER dipole parameters.

Magnet designation	2.8C40	2.8C20	2.8C20	2.8C40	2.8C40	2.8C40	2.8C80
Bending angle [deg]	1.875	1.300	0.750	2.5	1.078	0.176	3.000
Location in ring	Arc	Vert bend	Vert bend	IR	IR	IR	Wiggler
Number of magnets	192	4	4	2	1	1	4
Field [T]	0.33948	0.47074	0.27158	0.45264	0.19518	0.03187	0.27158
Integrated field [T·m]	0.33948	0.23537	0.13579	0.45264	0.19518	0.03187	0.54317
Pole width [in.]	7.5	7.5	7.5	7.5	7.5	7.5	7.5
Gap height [in.]	2.787	2.787	2.787	2.787	2.787	2.787	2.787
Core length [in.]	36.583	16.898	16.898	36.583	36.583	36.583	75.953
Magnetic length [in.]	39.370	19.685	19.685	39.370	39.370	39.370	78.740
Width of useful field, 0.1% [in.]	4.00	4.00	4.00	4.00	4.00	4.00	4.00
Lamination height [in.]	16	16	16	16	16	16	16
Lamination width [in.]	17.8	17.8	17.8	17.8	17.8	17.8	17.8
Packing factor, minimum [%]	96	96	96	96	96	96	96
Core weight [lb]	2,000	1,000	1,000	2,000	2,000	2,000	3,000
Amp turns per pole	9,600	13,313	7,680	12,801	5,520	901	7,680
Turns per pole	15	15	15	15	15	15	15
Pancakes per pole	1	1	1	1	1	1	1
Conductor dimensions [in.]	2.0×0.3125	2.0×0.3125	2.0×0.3125	2.0×0.3125	2.0×0.3125	2.0×0.3125	2.0×0.3125
Cooling hole diameter [in.]	0.1875	0.1875	0.1875	0.1875	0.1875	0.1875	0.1875
Conductor cross section [in.^{2}]	0.60	0.60	0.60	0.60	0.60	0.60	0.60
Conductor length/pole [ft]	150	150	150	150	150	150	150
Current [A]	640.03	887.51	512.02	853.37	367.97	60.08	512.02
Resistance @ 40°C [mΩ]	7.2	7.2	7.2	7.2	7.2	7.2	7.2
Power [kW]	2.96	5.70	1.90	5.27	0.98	0.03	1,90
Voltage drop [V]	4.63	6.42	3.70	6.17	2.66	0.43	3.70
Coil weight [lb]	200.00	150.00	150.00	200.00	200.00	200.00	300.00
Number of water circuits	2 @ 0.6 gpm	2 @ 0.6 gpm	2 @ 0.6 gpm	2 @ 0.6 gpm	2 @ 0.6 gpm	2 @ 0.6 gpm	2 @ 0.6 gpm
Water flow rate, total [gpm]	1.20	2.40	1.20	1.20	1.20	1.20	1.20
Water pressure drop [psi]	100	100	100	100	100	100	100
Temperature rise [°C]	9.4	9.0	6.0	16.7	3.1	0.1	6.0
Total power (magnets and buss) [kW]	593.3	22.8	7.6	10.5	1.0	0.0	7.6
Total voltage (magnets and buss) [V]	1014.6	35.7	24.8	19.8	7.7	5.4	24.8
Total system water requirements (gpm)	230.4	9.6	4.8	2.4	1.2	1.2	4.8

Laminations will be rotated after stacking each (approximately) 4-in. segment of the core. In this way, errors due to the slight variation in the thickness of the laminations will be eliminated. (This thickness error, referred to as "crowning," is well-known to occur in flat rolled sheet due to curvature in the rollers caused by forces generated during the production of the sheet.) The precise number of laminations that are stacked before performing such a rotation, which can only be determined when the number of heats is known, will be sufficient to ensure that the regular periodicity of the witness marks is retained.

The magnets run at low fields, well below saturation, and thus are more sensitive to core length than to the density of the lamination packing. Therefore, to maximize magnet-to-magnet reproducibility, particular attention will be paid to the length of the core (rather than its packing factor).

The magnet end-plates will be manufactured by numerically controlled mills and will contain the necessary holes for mounting coil retainers and other such devices. Angle plates welded to both the end-plates and the laminations will provide the torsional rigidity necessary to stabilize the cores and prevent twisting or bending.

Magnet coils will be of water-cooled aluminum, extruded from billets using porthole dies to provide continuous lengths up to several thousand feet. This technique obviates the need to make joints in the coil, thus eliminating the possibility of leaks. The length of a typical coil is about 150 ft, so there will be minimal waste at the end of each reel of conductor. The estimated weight of one dipole, including coils, is 2200 lb.

5.1.2.2 Quadrupoles. The standard LER quadrupole has a length of 20.0 in. and a bore diameter of 3.937 in.; its physical dimensions are shown in Fig. 5-5. The electrical properties of the quadrupoles corresponding to the nominal energy are summarized in Table 5-5.

The LER quadrupoles will be constructed, and the laminations handled, in the same manner described for the dipole magnets, except that they will use four-piece construction. The anticipated weight of steel is larger than that for the dipoles, about 550 tons, thus requiring more heats (about eight rather than five).

The design will include numerically machined end-plates with predrilled holes to mount the beam position monitors. These end-plates will be used to sandwich the laminations together. As with the dipoles, angles welded to the corners of the laminations will provide the required torsional rigidity and stiffness. Four cores, fitted with water-cooled aluminum coils approximately 180 ft long and extruded by the same technique as used for the bending magnets, will be bolted together to form one quadrupole weighing an estimated 2000 lb.

5.1.2.3 Sextupoles. The LER sextupole physical dimensions are shown in Fig. 5-6. These magnets have a length of 8.071 in. and a bore of 4.724 in. Their electrical properties, corresponding to the nominal energy are summarized in Table 5-6.

The LER sextupoles will be identical to the present PEP short (8 in.) sextupoles. This will permit us to interchange magnets between the LER and HER, if necessary, and minimizes the required number of spares. Manufacturing techniques will be the same as those described above for the LER dipoles and quadrupoles, although the anticipated steel requirement of about 50 tons will come from only a single heat. For this reason, witness

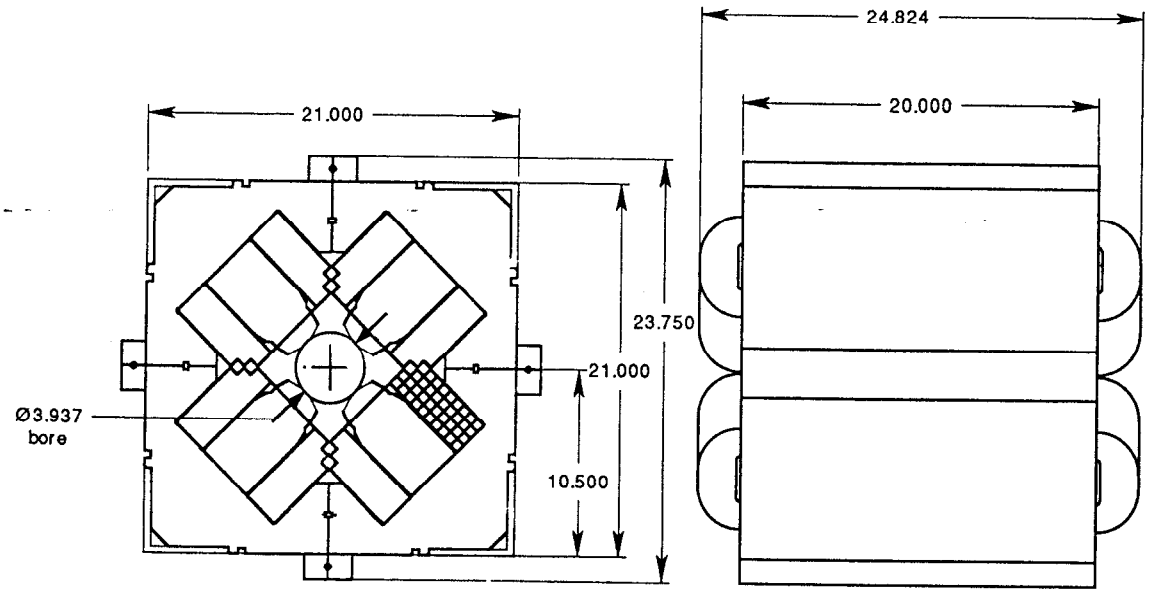

Fig. 5-5. End and side views of an LER quadrupole magnet. Dimensions are given in inches.

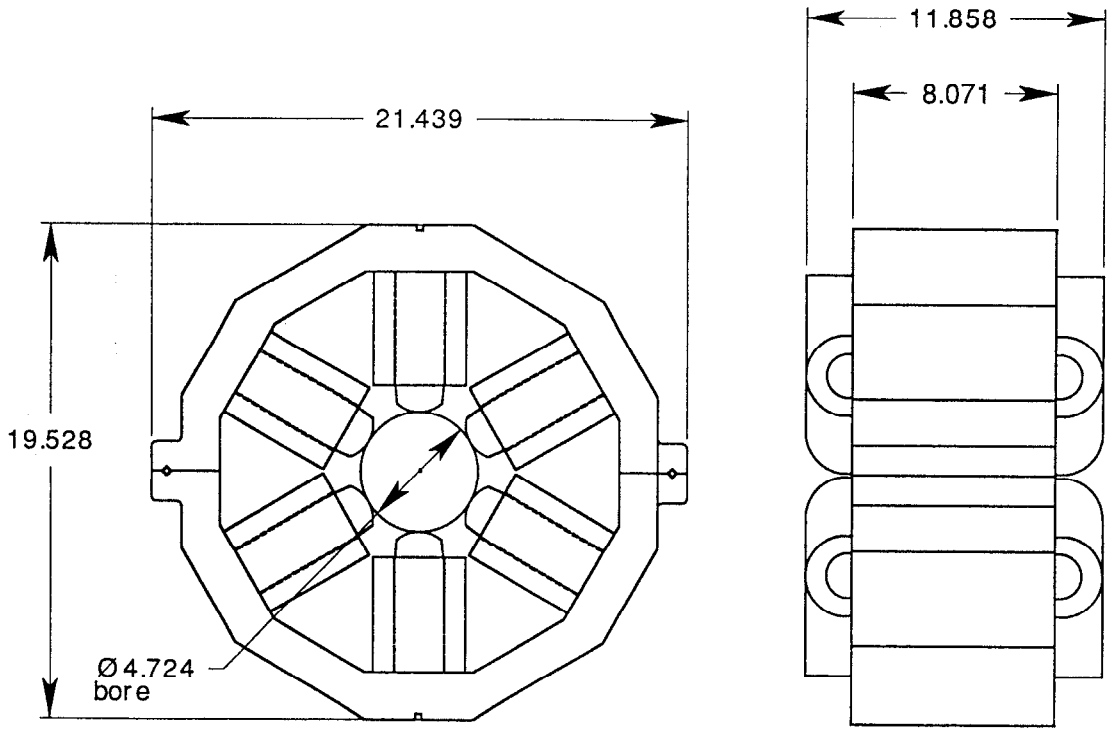

Fig. 5-6. End and side views of the LER sextupole magnet. Dimensions are given in inches.

Table 5-5. LER quadrupole parameters.

Magnet designation	4Q20	4Q13	4Q28	4Q40	4Q21	4Q21	4Q21
Location in ring	Arc & SS	IR	IR	IR	IR	IR	Wiggler
Number of magnets	264	4	4	6	12	4	6
Operating gradient [T/m]	2.499	10.340	8.980	8.980	11.350	3.410	4.500
Pole tip field @ operating gradient [T]	125	0.517	0.449	0.449	0.568	0.171	0.225
Gradient length product [T]	1.36	3.10	6.91	8.98	6.13	0.92	1.21
Inscribed radius [in.]	1.968	1.968	1.968	1.968	1.968	1.968	1.968
Minimum gap [in.]	1.457	1.457	1.457	1.457	1.457	1.457	1.457
Core length [in.]	20	10.354	28.8579	37.913	19.8028	9.1729	9.1729
Magnetic length [in.]	21.457	11.811	30.315	39.37	21.2598	10.6299	10.6299
Lamination height [in.]	10.5	10.5	10.5	10.5	1.968	1.968	1.968
Lamination width [in.]	10.5	10.5	10.5	10.5	1.457	1.457	1.457
Packing factor, minimum [%]	98	98	98	98	98	98	98
Core weight [lb]	1800	932	2597	3412	1782	826	826
Amp turns per pole	2484	10279	8927	8927	11283	3390	4473
Turns per pole	37	37	37	37	37	37	37
Pancakes per pole	1	1	1	1	1	1	1
Conductor cross-sectional area [in.^{2}]	0.197	0.197	0.197	0.197	0.197	0.197	0.197
Cooling hole diameter [in.]	0.25	0.25	0.25	0.25	0.25	0.25	0.25
Conductor dimensions [in.]	0.5 × 0.5	0.5× 0.5	0.5× 0.5	0.5× 0.5	0.5× 0.5	0.5× 0.5	0.5× 0.5
Conductor length/pole [ft]	180	180	180	180	180	180	180
Current [A]	67	278	241	241	305	92	121
Resistance @ 40°C [mΩ]	52.6	52.6	52.6	52.6	52.6	52.6	52.6
Power [kW]	0.237	4.06	3.06	3.1	4.9	0.4	0.8
Voltage drop [V]	3.5	14.6	12.7	12.7	16.0	4.8	6.4
Coil weight [lb]	151	151	151	151	151	151	151
Number of water circuits	1 @ 1 gpm	1 @ 1 gpm	1 @ 1 gpm	1 @ 1 gpm	1 @ 1 gpm	1 @ 1 gpm	1 @ 1 gpm
Water flow rate [gpm]	0.5	0.5	0.5	0.5	0.5	0.5	0.5
Water pressure drop [psi]	150	150	150	150	150	150	150
Temperature rise [°C]	0.00	0.03	0.02	0.02	0.04	0.00	0.01
Total magnet power [kW]	62.6	16.2	12.3	0.0	0.1	0.0	0.0
Total magnet water requirements [gpm]	132	2	2	3	6	2	3

Table 5-6. LER sextupole parameters.

Magnet designation	4.5S10
Number of magnets	144
Operating gradient [T/m^2]	36.07
Pole tip field @ operating gradient [T]	0.065
Integrated strength [T/m]	9.20
Aperture inscribed radius [in.]	2.362
Core length [in.]	8.071
Magnetic length [in.]	10.041
Core weight [lb]	170.
Amp turns per pole	1027.64
Turns per pole	24
Pancakes per pole	2
Conductor cross-sectional area [in.^{2}]	0.127
Cooling hole diameter [in.]	0.125
Conductor dimension [in.]	0.375×0.375
Current [A]	43.5
Resistance @ 40°C [mΩ]	62
Power [kW]	0.1
Voltage drop [V]	2.69
Coil weight [lb]	200
Number of water circuits	2 @ 0.125 gpm
Water flow rate [gpm]	0.25
Water pressure drop [psi]	150
Temperature rise [°C]	1.8
Total magnet power [kW]	16.9
Total system water requirements [gpm]	36.0

marks will not be needed for the sextupoles. Laminations will still be reversed periodically, however, to account for the crowning referred to above.

5.1.3 Interaction Region Magnets and Supports

5.1.3.1 Permanent Magnets. The final triplet of focusing quadrupoles, Q1, Q2, and Q3, and the magnetic separation dipoles B1 are located within 2 m of the IP. At these close distances, they will be inside the detector and immersed in its solenoidal magnetic field. The only viable magnet technologies for such an environment are superconducting or permanent magnets. A conventional electromagnet with iron pole tips would have its field distorted by the detector field. For the IR magnets, required field strengths and apertures are within the reach of modern rare-earth–cobalt (REC) alloys, and superconducting technology is not demanded. For the B Factory, the choice of a permanent magnet design was based on the following characteristics of such magnets:

- They avoid the complexity, cost, and reliability problems inherent in cryogenic operation.
- They are compact and avoid cryogenic plumbing and cryostats, both of which would significantly reduce the detector acceptance solid angle.
- They are nearly free of fringe fields that could otherwise complicate particle tracking.
- They avoid the safety aspects of superconducting systems; they will not quench—a possible advantage in a high-current storage ring.

There are also drawbacks to our choice of permanent magnet technology. Foremost among these is the fact that permanent magnets offer only a limited adjustment capability. In our design, we have added trim windings on all four pairs of permanent magnets in the IR to alleviate this lack of flexibility. Other issues include the following:

- The field quality of a REC magnet depends on accurate magnetization of its constituent blocks; special techniques and equipment must be developed to measure block magnetization, and to assemble and adjust blocks.
- Strong demagnetizing external fields and high temperatures must be avoided if field quality is to be preserved. Quadrupole and dipole fields are assembled from sector-shaped REC blocks arrayed in a circle around the magnet aperture [Halbach, 1981]. Each block is magnetized in an appropriate direction so that the magnetic field varies approximately as $\cos N\theta$ around the bore, where $N = 1$ for dipoles, $N = 2$ for quadrupoles, etc. The optimal compromise between the number of blocks, M, and the field quality is to use $M = 16$ for a quadrupole and $M = 8$ for a dipole. These configurations are shown in Fig. 5-7.

The magnetic and mechanical properties of the B Factory IR magnets are summarized in Table 5-7.

For quadrupoles ($N = 2$) the magnetic field at the aperture radius, $B(r_1)$, is related to the inner and outer radii, r_1 and r_2, by

$$B(r_1) = 2C_N B_r \left(1 - \frac{r_1}{r_2}\right) \tag{5-1}$$

where B_r is the remanent field of the permanent magnet material and

$$C_N = \frac{\cos^N\left(\frac{\pi}{M}\right) \sin\left(\frac{N\pi}{M}\right)}{\frac{N\pi}{M}} \tag{5-2}$$

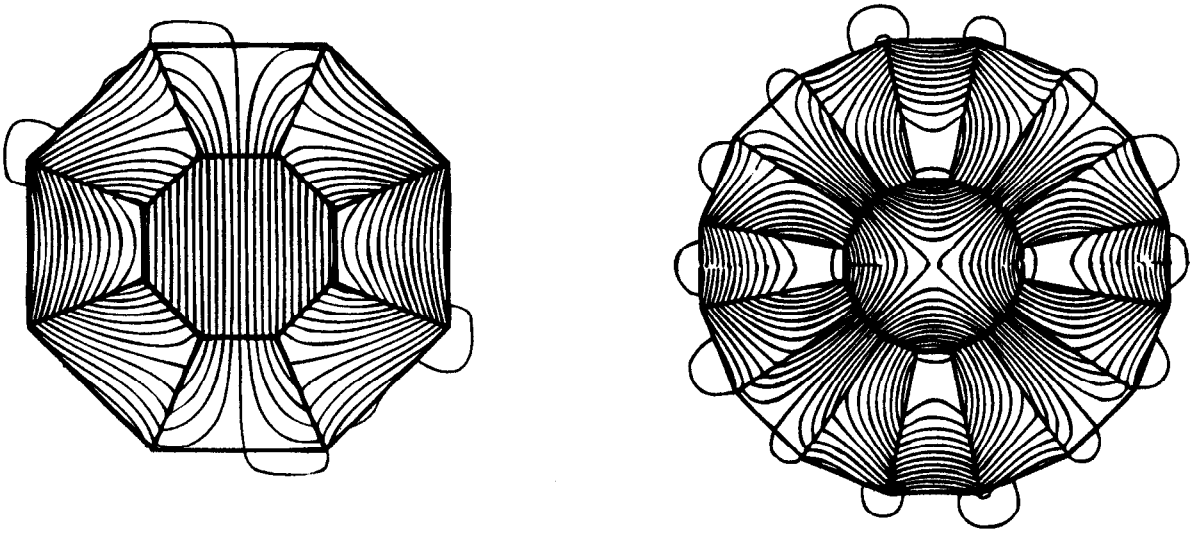

Fig. 5-7. Field lines for an 8-block permanent magnet dipole (left) and a 16-block quadrupole (right).

Table 5-7. Magnetic and mechanical dimensions for the IP permanent magnets.

	$B(r_1)$ [T]	Gradient [T/m]	r_1 [cm]	r_2 [cm]	L [cm]	Weight [kg]
B1	0.75	—	2.4	5.3	16.0	9.4
Q1	1.47	38.84	3.8	15.1	64.2	362.0
Q2	1.35	30.70	4.4	14.0	51.6	240.5
Q3	0.97	14.04	6.9	13.6	24.0	87.0

Choice of Material. The B Factory magnets will be assembled from Sm_2Co_{17}, a material having a high remanent field ($B_r = 1.05$ T). Figure 5-8 shows the B-H curves of some of these materials. Commercial grades of Sm_2Co_{17} are available.

The B-H relation for a candidate material, R26HS (see Table 5-8), shows a linear $\mu_r \approx 1$ for the entire second quadrant. An external demagnetizing H field must actually exceed B_r/μ_0 of the material before nonlinearities and hysteresis develop, causing permanent demagnetization of the material. For lower external fields, simple linear superposition of fields holds. Since the detector axial solenoidal field is nearly orthogonal to the transverse field of the beamline magnets, the two fields are not expected to interact. The high Curie temperature of Sm_2Co_{17} allows this material to be used at temperatures up to 500°C, and its low temperature coefficient should preserve field quality. Lastly, the chosen material has good radiation-resistance properties, so its performance is not expected to degrade in the relatively harsh environment of the B Factory IR.

Permanent Magnet Assembly. Taken together, fabrication of the IR magnets will involve thousands of precisely machined and magnetized blocks of Sm_2Co_{17}. The field quality of the resulting magnets depends critically on their precise magnetization. The magnitude, direction, and uniformity of the magnetization **M** will therefore be held to tight tolerances inside each block. In addition, variations can, to some degree, be accommodated by selective assembly and adjustment of final block positions. In any case, block magnetization will be measured before assembly. Even perfectly magnetized blocks do not produce simple, uniform **B** fields. Figure 5-9 shows the **B** field pattern for two typical uniform magnetizations of a block. The **B** field is related to block magnetization by

$$\mathbf{B}(\mathbf{r}) = \mu_0 \mathbf{M}(\mathbf{r}) + \frac{\mu_0}{4\pi}\left[\int_S \mathbf{M}\cdot\mathbf{n}\frac{(\mathbf{r}-\mathbf{r}')}{|\mathbf{r}-\mathbf{r}'|^3}da' - \int_V \nabla\mathbf{M}\frac{(\mathbf{r}-\mathbf{r}')}{|\mathbf{r}-\mathbf{r}'|^3}dV\right] \qquad (5\text{-}3)$$

If the block has perfectly uniform magnetization ($\nabla\mathbf{M} = 0$), then **B** and **M** differ only by a surface integral over the shape of the block. Using the above relation, the internal magnetization field of a block can be inspected by making measurements of **B** over its surface. Figure 5-10 illustrates this inspection procedure.

Table 5-8. Properties of R26HS magnetic material.

Material	B_r [T]	Temperature coefficient [%/°C]	Curie temperature [°C]	Density [g/cm^3]
R26HS	1.05	–0.03	820	8.4

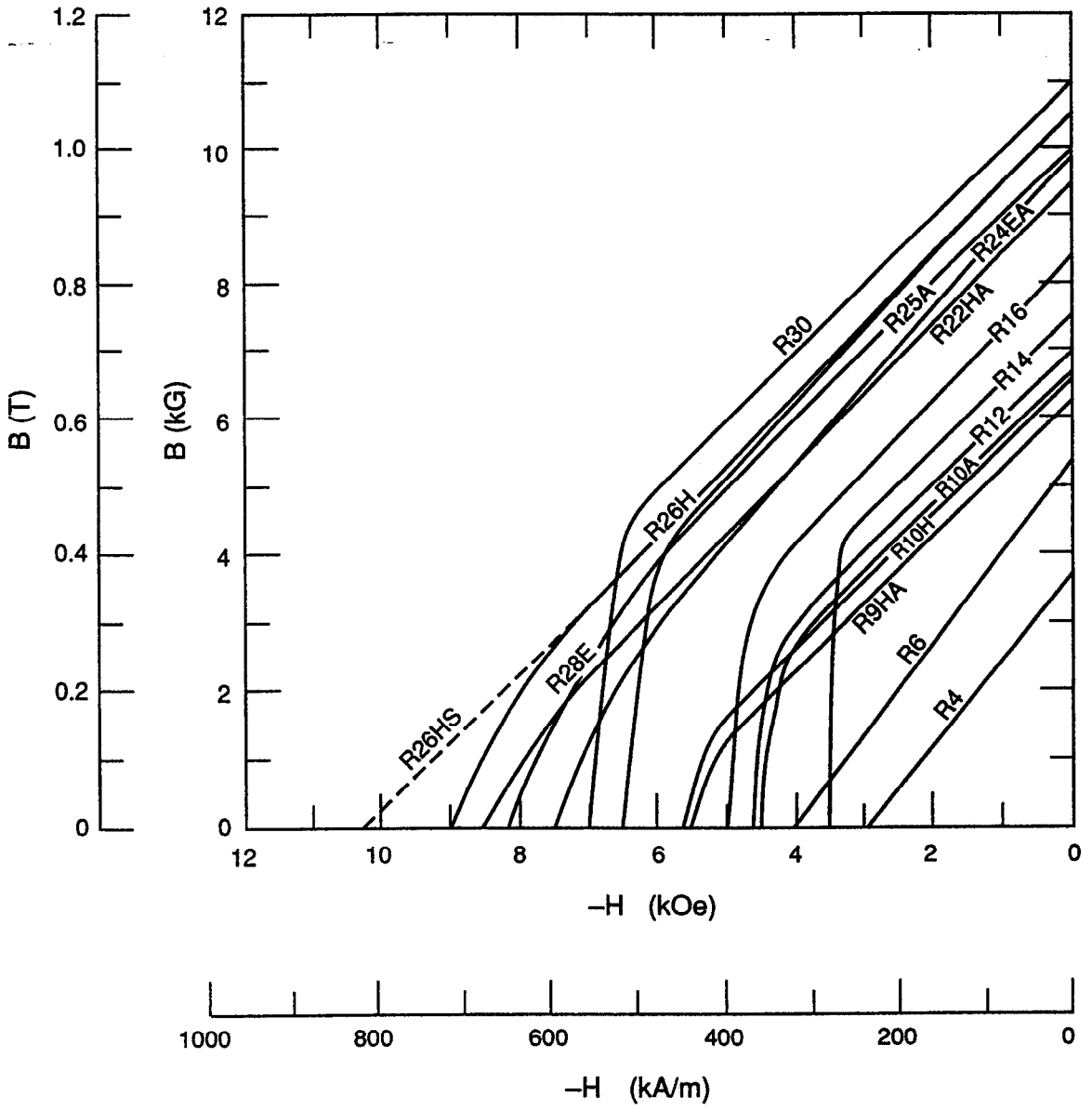

Fig. 5-8. B-H curves for various permanent magnet materials.

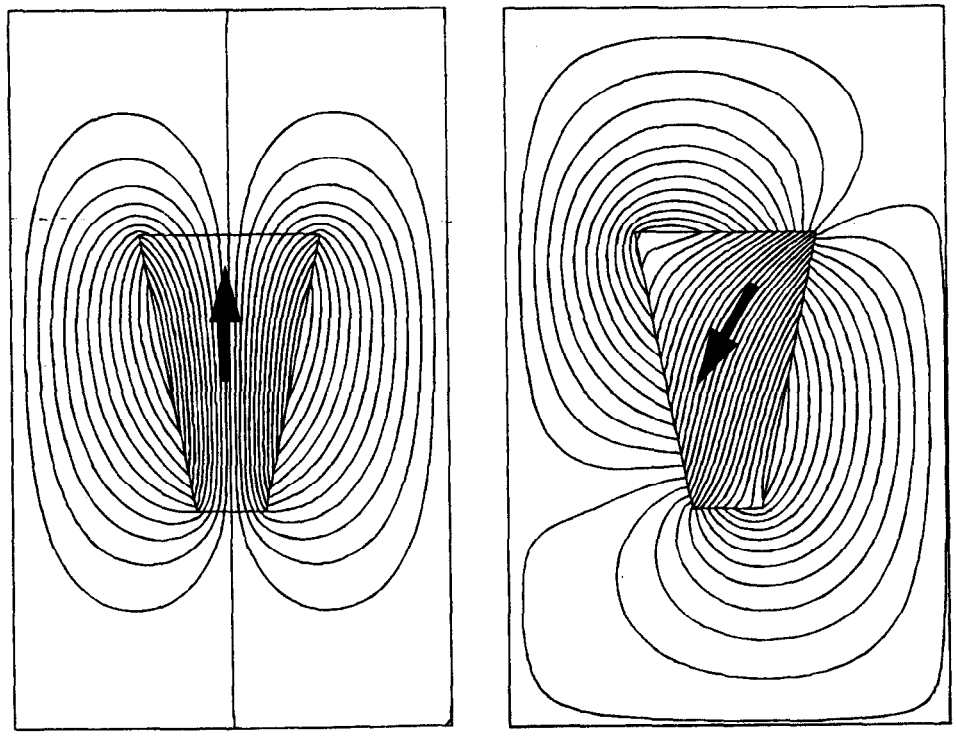

Fig. 5-9. Field patterns for two typical uniform magnetizations of permanent magnet material blocks.

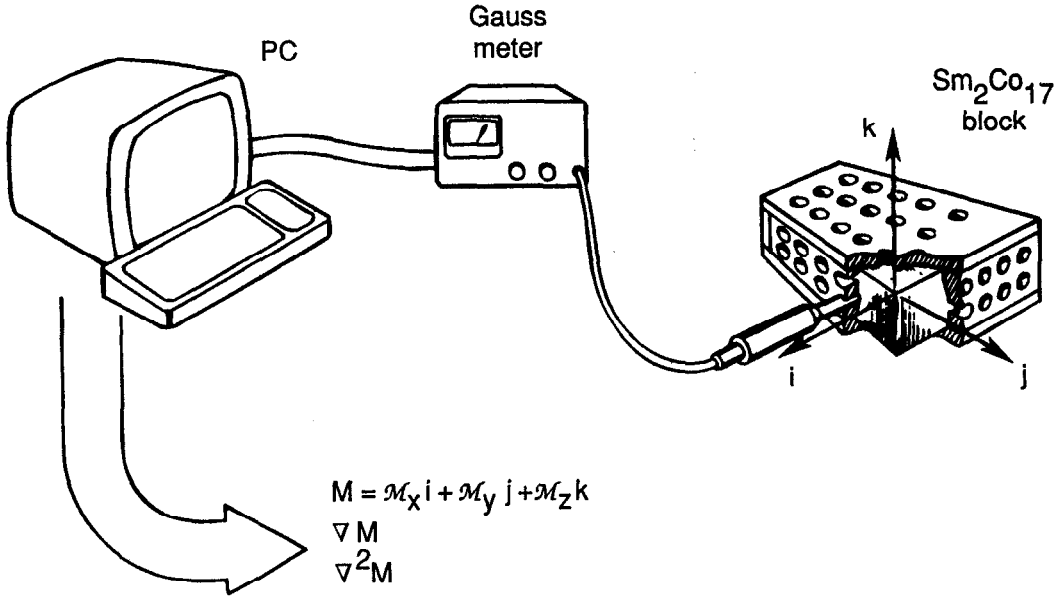

Fig. 5-10. Schematic representation of a procedure to inspect permanent magnet blocks before assembly.

A simple jig will be used to determine the coordinate frame and measurement points on the surface at which the normal component of **B** is measured. These data will then be used to calculate the magnitude and direction of **M** inside the block. Estimates of the uniformity of **M** can also be computed. If magnetic tolerances can be tightly held by this inspection procedure, it may be possible to avoid adjustment of individual block positions in the finished magnets. This would greatly reduce the time involved in this labor-intensive fabrication step.

Permanent magnets have already been successfully applied to storage rings at SLAC [Spencer, 1985] and elsewhere [Herb, 1987]. We consider the technology to be a mature one, well-suited to this application.

5.1.3.2 IP Support Barrel. The B Factory poses difficult support and alignment problems for the final magnetic elements near the interaction point (IP). Bunch spacing is only 1.26 m and requires magnetic separation of the two beams to begin at ±20 cm from the collision point. The final quadrupole triplets are completely buried inside the detector. Previous storage rings have placed the equivalent magnets on separate individual supports, cantilevered in from the detector entrance. Unfortunately, such a support is difficult to make rigid, and the relative alignment of the magnets is not easily measurable once they are installed.

As shown in Fig. 5-11, for the B Factory we intend to avoid this limitation by using a single support "barrel" through the detector, from one end to the other, to carry all magnets. In addition to carrying the beam separation dipoles B1 and the final permanent magnet quadrupole triplets, Q1, Q2, and Q3, the support barrel carries the central vertex detector. Other equipment carried inside the barrel includes the water-cooled masks AB and CD (see Sections 4.2 and 5.2.7), radial ion pumps, and BPMs. Plumbing and cabling

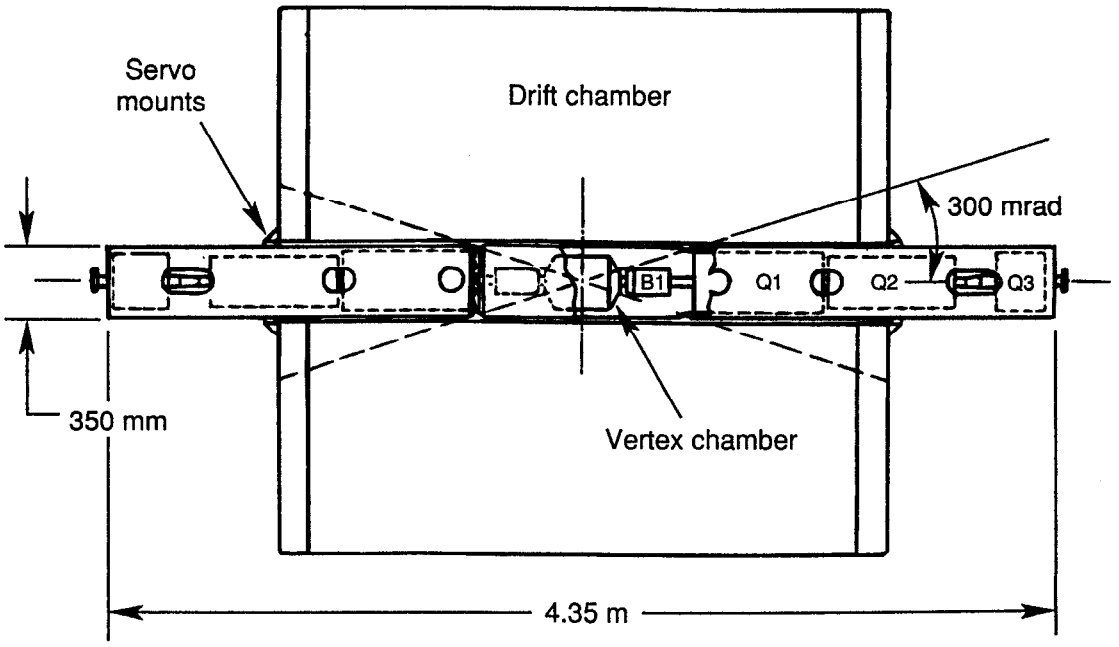

Fig. 5-11. Tube or barrel to support the permanent magnets, beam pipe, and vertex detector inside the drift chamber.

for this equipment passes through the barrel, while vertex detector cabling is carried on the outside.

Our choice of a single support barrel has two important advantages over previous designs:

- Magnetic elements on each side of the IP are directly connected by a rigid structure that maintains their relative alignment.
- All components can be preassembled and aligned in the barrel outside the detector, where precise and effective survey techniques can be employed.

Barrel Mounts. The barrel is supported from the detector drift chamber end-plates. These support locations are approximately at the quarter points of the barrel, thus balancing end and midpoint deflections. This reduces deflection by nearly 50-fold compared with a simple end support, and raises the natural frequency of the structure by a factor of 7. The barrel rests on roller cams (consisting of a spherical roller that bears on a shaft with 1.5-mm eccentric journals; see Fig. 5-12) at each end of the drift chamber. Two roller cams locate the barrel axis at one end, and three roller cams fix the axis and roll at the other end, as shown in Fig. 5-13. During operation, only the eccentric shaft rotates, displacing the outer bearing race. The race remains in fixed contact with its barrel support pad, so no sliding motions are involved; only rolling motion occurs. All five roller cams are driven by stepper motors through gear reducers, allowing five-axis remote positioning of the barrel; that is, the barrel position can be adjusted by ±1.5 mm in x and y, along with pitch, roll, and yaw, during beam operation.

With this technique, positioning of the support barrel to an accuracy of a few micrometers is practical. Because excursions are cyclic and naturally limited by cam lift, no limit switches are needed to protect against damage. Except for a fixed z restraint at

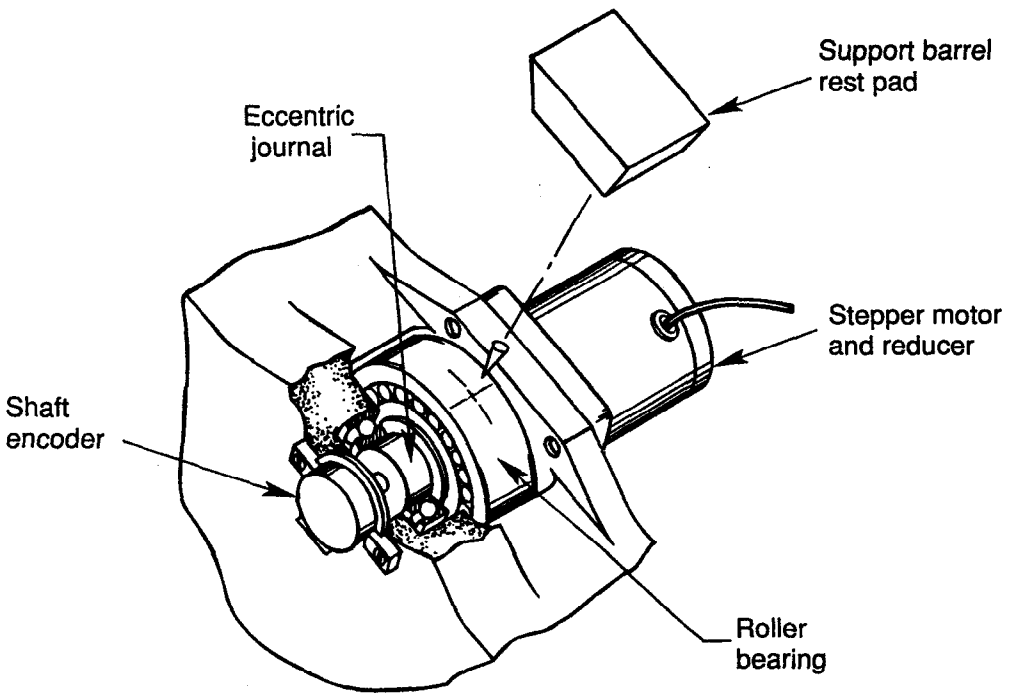

Fig. 5-12. Detail of roller cam for supporting and adjusting the support barrel.

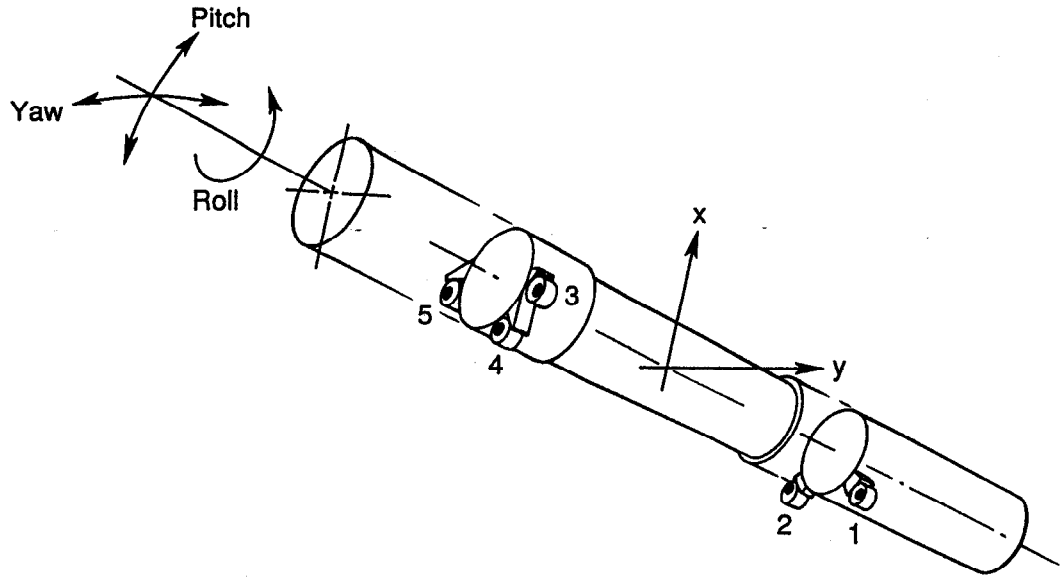

Fig. 5-13. View of the support barrel, showing its five remotely adjusted roller cams.

one end, the barrel mount is fully kinematic and free of any over-constraints that might distort internal alignment. A similar remote-positioning mount design is being used successfully for the final triplets in the SLC interaction region [Bowden and Putallaz, 1985].

Barrel Construction. The support barrel consists of three separable sections. The two outboard ends, which carry the heavy quadrupole triplets, are made from 0.75-in.-wall aluminum pipe. Access ports and magnet mounting points will be machined into the walls. The middle barrel section is of sandwich construction, with carbon-fiber facings and a foam core. This section must be nearly transparent to radiation and insensitive to thermal distortion, while supporting the peak mid-span bending moments (87.3×10^3 in. lb). Figure 5-14 shows the barrel construction details.

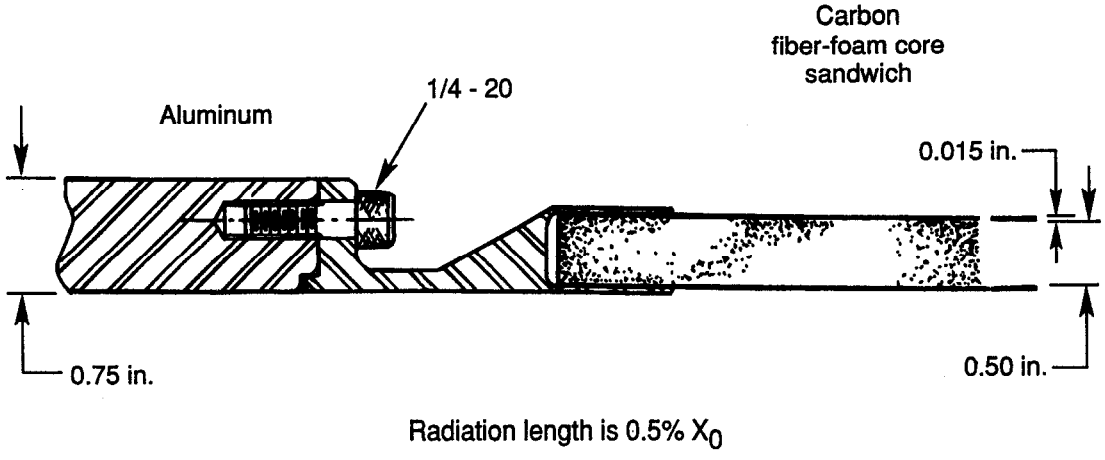

Fig. 5-14. Detail of joint between the thin inner section of the support barrel and the outer aluminum section.

The most damaging thermal distortion is bending of the barrel due to transverse temperature gradients. Expansion of the warmer top of the barrel and contraction of the cooler bottom would cause the barrel to arch upward, as shown in Fig. 5-15. Because carbon fibers shorten slightly with increasing temperature (see Table 5-9), the center barrel section can be compensated to approximately zero expansion, either by balancing the fiber pitch helix angle against the high expansion coefficient of the resin matrix, or by cladding the fiber layers (which have a negative expansion coefficient) with a thin (say, 10 μm) layer of a material having a positive expansion coefficient, such as aluminum. Because the two outer aluminum ends of the barrel are only about one-third of the total length L, it should be possible to hold the total distortion δ (defined in Fig. 5-15), below 25 μm per °C. In addition to the protection afforded by our fabrication method and materials, the barrel will be well-sealed from natural convection by the detector, and water cooling of local heat sources will prevent asymmetric heating from causing temperature differences greater than 1°C.

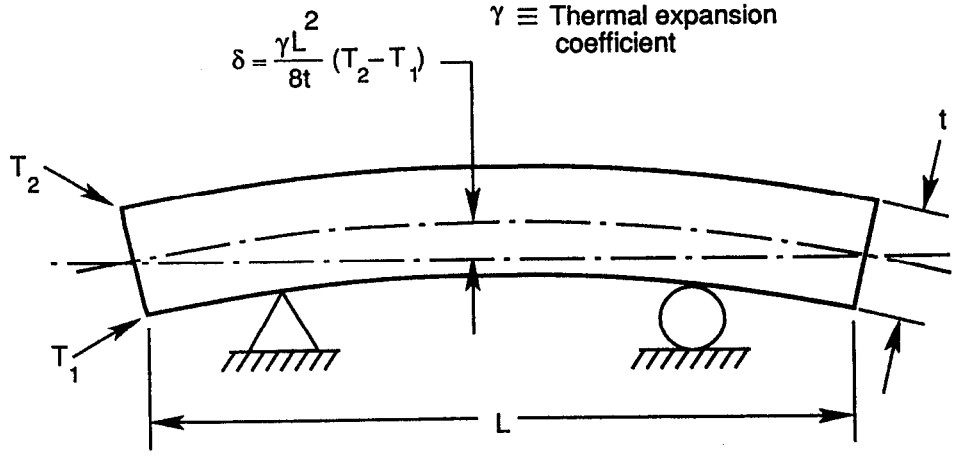

Fig. 5-15. Curvature of support barrel resulting from a temperature difference between its top and bottom.

Table 5-9. Thermal expansion coefficients and deflection of the materials that make up the 4.35-m barrel.

Material	γ [$\Delta L/L$ per °C]	δ [μm per °C]
Aluminum	2.3×10^{-5}	153.0
Carbon fiber 0°	-5.6×10^{-7}	−3.7
Carbon fiber 90°	3.6×10^{-5}	235.0

Ground Motion. Because the B Factory consists of two independent storage rings, microseismic ground motion could possibly interfere with beam collisions. The spectrum of ground motion measured at SLAC [Bowden, 1985] is shown in Fig. 5-16, along with its amplitude distribution. Most ground motion is found in the 1- to 10-Hz band, whereas the barrel resonant frequency is about 30 Hz; therefore, no strong coupling will occur. The vertical beam-spot size is 7 μm in the B Factory, about 100 times the amplitude of the average microseismic noise. Quadrupole amplification will use up some, but not all of the available margin. Further, because the barrel ensures a smooth fundamental-mode response to the vibration modes, the relative motions of the quadrupoles will be much smaller than the vibration amplitude of the barrel itself. Previous measurements at SLAC of mechanical noise from cooling-water flow have shown that this source usually does not make a significant contribution. Thus, we conclude that mechanical vibration will not be a serious problem for the barrel support.

Barrel Assembly and Component Alignment. The technical difficulties of assembling 4 m of heavy and delicate beamline equipment in a close-fitting support barrel has already been solved for the SLC final triplets, as demonstrated in Fig. 5-17. A similar technique will be employed for the B Factory. All beamline components are built up and checked out on a tracked assembly stand. Each magnet is equipped with small wheels that roll on the assembly stand rails, which are linked to rails on the inner walls of the support barrel. The train of magnets, along with a preinstalled vacuum pipe, ion pumps, BPMs, cabling, etc., is then pulled off the assembly stand into the support barrel. Once in place, magnets are temporarily supported on bolts screwed up from the barrel bottom while the rails are removed.

Magnet mounts are installed and adjusted from the outside of the barrel. Magnets are clamped near their ends by shimmed bolts through the barrel wall, as shown in Fig. 5-18. Bolts work in four opposing pairs. The position of one bolt in each pair is fixed by a replaceable shim washer. The opposing bolt preloads the magnet mount through a spring-loaded pusher. The amount of preload is set by a second shim under this bolt. Adjustment of the alignment is made by changing shim thicknesses. Whenever a fixed bolt shim is changed, the corresponding preload shim is changed to maintain the nominal preload. In this way, forces and deflections are held constant during the alignment procedure. Adjustment of one magnet position does not affect another, and the tightening torque on the support bolts does not affect magnet position. When this technique was

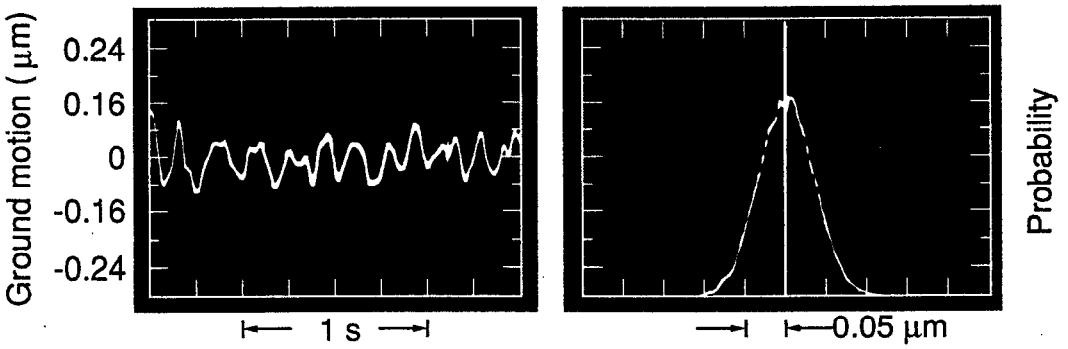

Fig. 5-16. Ground motion measured at SLAC.

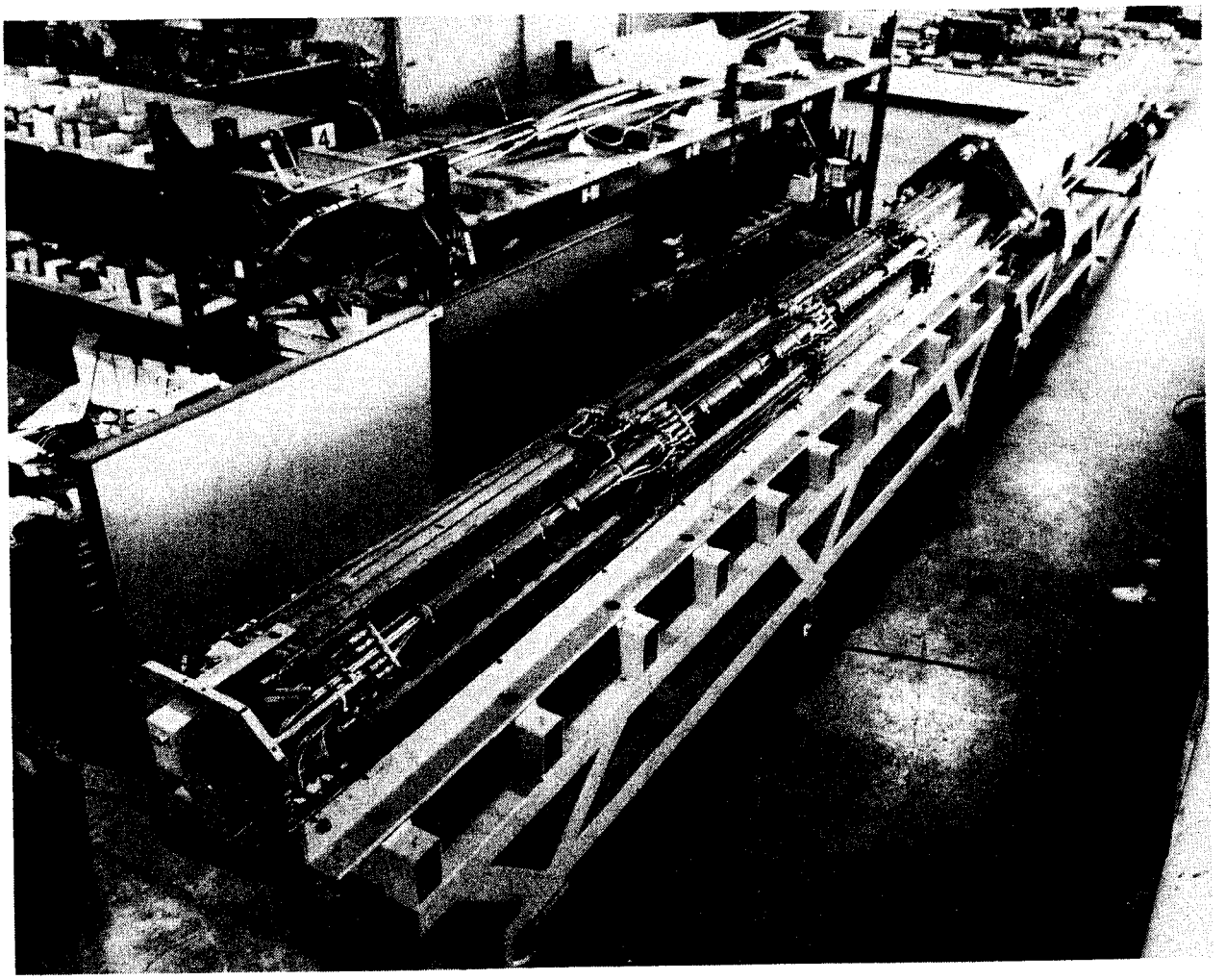

Fig. 5-17. Illustration showing the assembly technique for the SLC final focus triplet barrel.

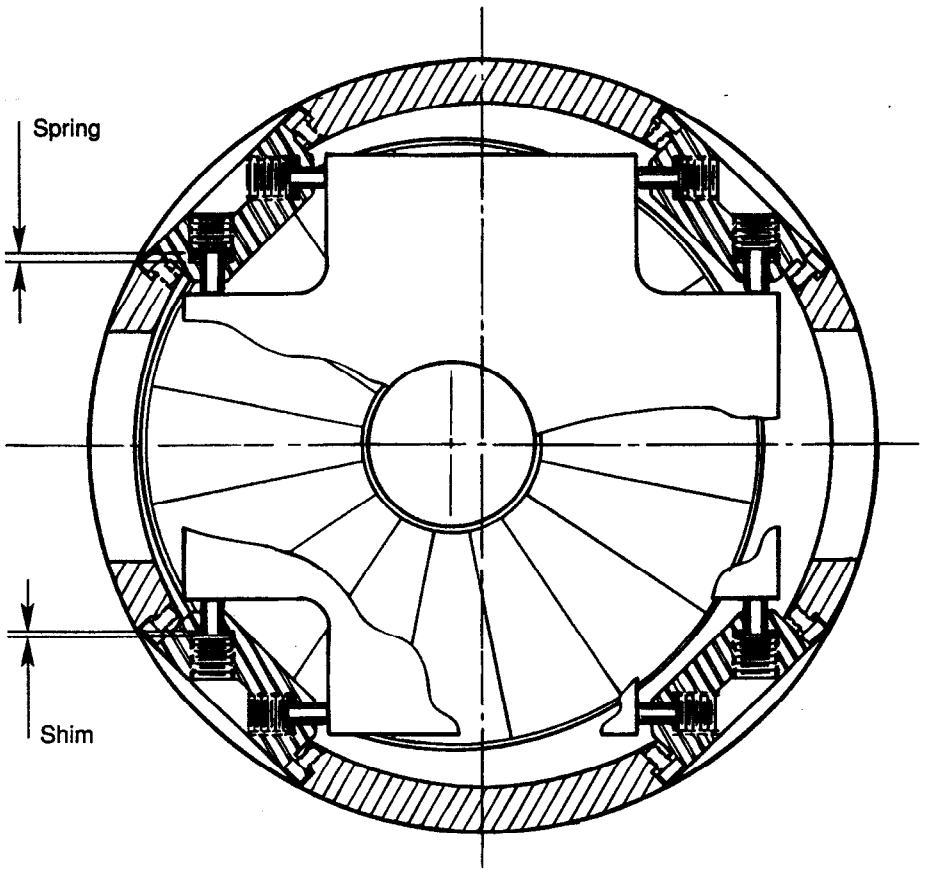

Fig. 5-18. Section through SLC final focus triplet barrel, showing magnet-positioning technique.

used on the SLC final triplets, alignment by shim changes converged in two iterations. This method is well-matched to modern survey procedures based on computer-linked theodolites and sophisticated survey software, of the type described in Section 5.3.

A major reason for building all IR components into a common support barrel is to allow prealignment of beamline components prior to assembly into the detector. Once hidden inside the detector, magnets cannot easily be surveyed from the outside. The support barrel allows this alignment to be done in the laboratory under optimal conditions; Fig. 5-19 illustrates the procedure.

During alignment the barrel will be supported in mounts identical to those to be used on the actual detector. In this way, all deflections are accurately reproduced. Access ports for either directly viewing magnet fiducials or attaching extended targets are provided on the support barrel. Magnet survey is done with computer-linked theodolites using many redundant observations to obtain a strongly over-constrained fit on the relative positions of all fiducials. A length standard is set in clear view of all theodolite locations. The raw survey data consist of precision-encoded angle measurements. All

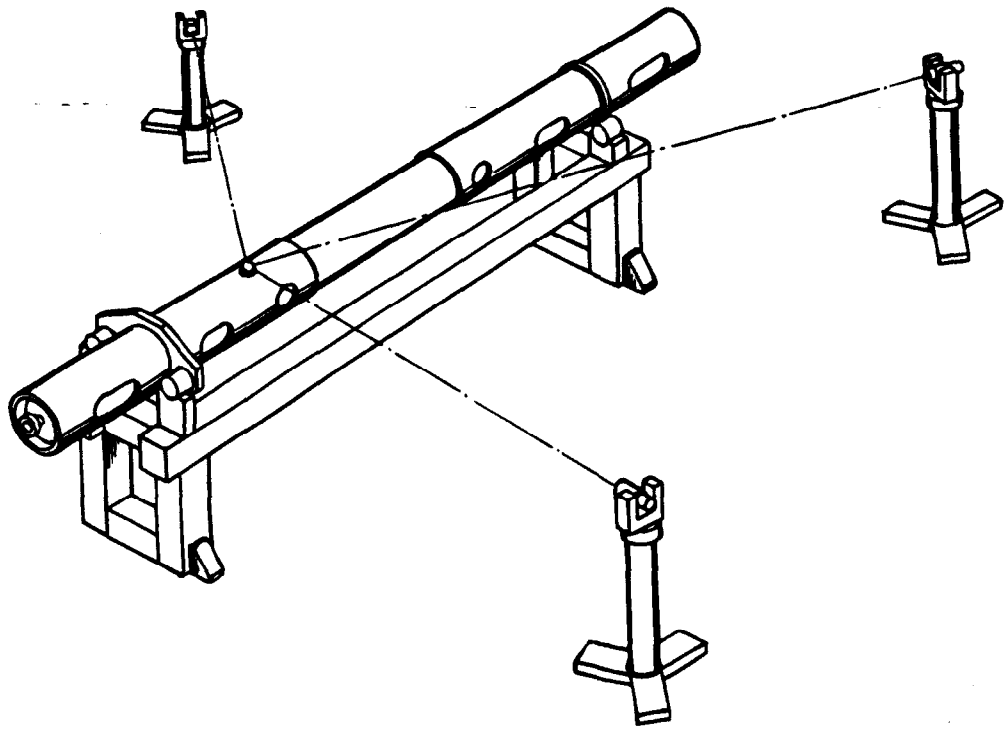

Fig. 5-19. Illustration of a method for prealigning elements inside the support barrel before installation in the detector.

measurements are then computer processed to reconstruct the relative magnet positions. The overall resolution of such a modern system is 25 μm over 5 m. Positioning the barrel components with respect to the rest of the storage ring is straightforward. After installation into the detector, barrel-end fiducials will be clearly visible from the standard survey stations used to align other external beamline components. Furthermore, the remote positioning mounts will allow fine adjustment of the barrel position during beam operation.

5.1.3.3 Permanent Magnet Trim Coils. To tune the collider beam optics and to permit shifting of the ring energies to reach different Υ resonances, Q1, Q2, Q3, and B1 will require trim coils with a 4% adjustment range. These coils, which line the bores of the permanent magnets, must be of compact design because the bore increases needed to accommodate them reduce the magnetic field strength. Moreover, small increases in the aperture of the inner bore require large increases in the outer diameter of the permanent magnet assembly to recover the lost strength.

Owing to the severe radial space limitations, conventional coils wound from hollow water-cooled conductor are not practical. Therefore, the trims will be single-layer coils

attached in good thermal contact to a highly conductive beam pipe made from high-strength GlidCop. The beam pipe will have single-pass water cooling coils brazed to it along the inner edges of each coil and will thus serve as a thermal sink to cool the coil. The layout we have adopted (see Fig. 5-20) allows parallel water channels for coil cooling. Dimensions shown are for Q1. The other magnets, B1, Q2, and Q3, have similar or more relaxed requirements.

Although an ideal quadrupole field requires a cos 2θ distribution of current density, this can be well approximated by a uniform coil subtending 0.5 rad (28.65°). For weak trim fields, the harmonic purity of this coil form is more than adequate.

For Q1 a 4% trim requires maximum fields of 0.055 T at the 35.3-mm mean trim-coil radius. Five turns of wire carrying 310 A will produce this field. The total power dissipated per coil is 1.4 kW (assuming that insulation and winding reduce the actual copper density in the coil to 80% of the overall cross section). Heat must be conducted from the middle of the coil to the cooled edge and then across the cooling-water boundary film. Conduction through the coil and to the beam pipe wall is reduced somewhat by electrical insulation. A worst-case estimate of this temperature rise gives $\Delta T = 20°C$ at full power. The multitube cooling channel carrying 1.2 gpm will have an outlet temperature rise of 4–5°C. The water film drop is 8°C using a film coefficient of 5 W/in.^{2} per °C. These temperature drops sum to 33°C, which is high but manageable.

5.1.3.4 Septum Quadrupole (Q4). The Q4 septum quadrupole is the last magnet in the HER before the high- and low-energy beam trajectories merge into a common vacuum pipe on their way to and from the IP. It is located about 4 m from the IP, and is the last storage ring magnet before the beamline "disappears" into the detector.

Although the two Q4 magnets focus only the incoming and outgoing high-energy beam (HEB), the low-energy beam (LEB) is separated from the HEB trajectory by only 6.5 cm at the front face of Q4. Figure 5-21 shows the dimensions of the beam-stay-clear envelopes, as well as the synchrotron radiation fans from the B1 bending magnets and from Q2, at the front face of Q4.

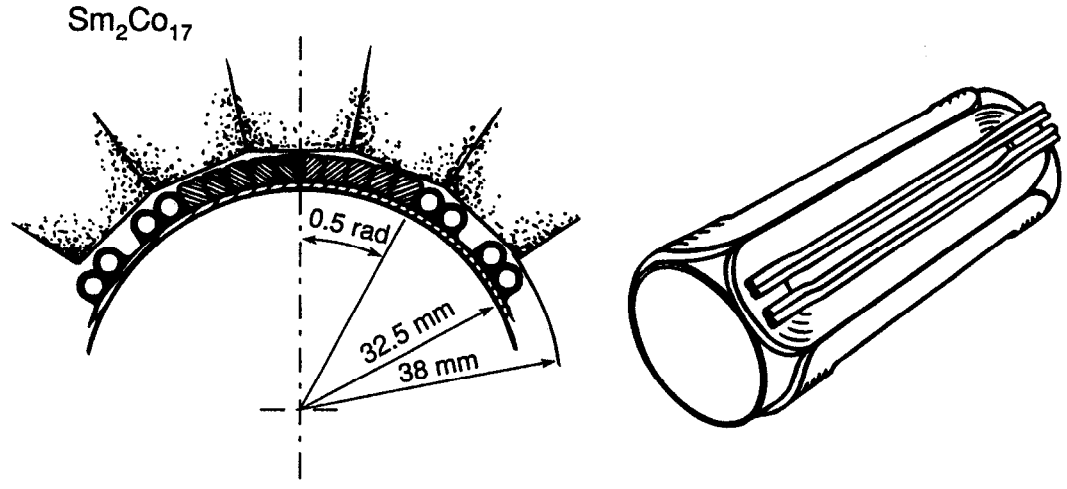

Fig. 5-20. Cross section and perspective view of the permanent magnet trim coils.

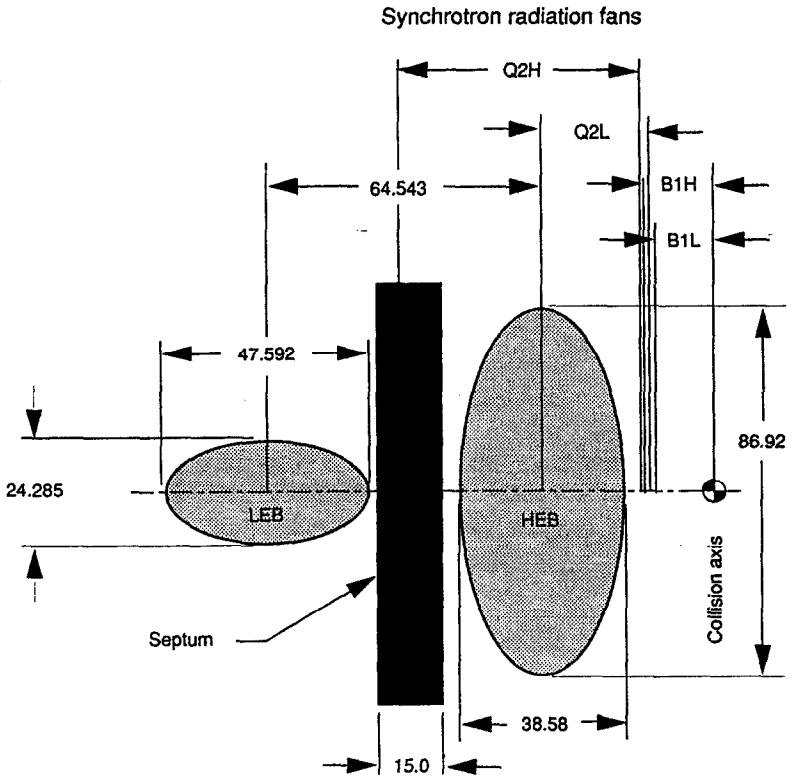

Fig. 5-21. Dimensions (in millimeters) of the beam-stay-clear envelopes and locations of the synchrotron radiation fans from the B1 and Q2 magnets.

Producing a pure quadrupole field centered on the HEB, while still leaving a clear field-free channel for the LEB only 6.5 cm to the side, is a formidable magnet design problem. (Only 21.4 mm of clearance exists between the two beam-stay-clear ellipses here.) The problem is compounded by the need to pass synchrotron light fans in the horizontal midplane. These fans carry 90 kW of radiation away from the region near the IP and, as shown in Fig. 5-21, extend in angle all the way out to the collision axis. Furthermore, the HEB requires a large, vertically elongated magnet aperture.

Ideally, the solution would be some type of septum quadrupole having a quadrupole field pattern sharply cut off by a septum separating the HEB from the LEB. Several designs have been considered.

The most obvious candidate is the Panofsky quadrupole, formed from a rectangular enclosure of current sheets. To pass the midplane synchrotron radiation fan, a large, nearly square aperture is required, with the quadrupole center offset to the side; in essence, this corresponds to a quadrupole with a superimposed dipole field. Panofsky quadrupoles are usually enclosed in an iron box to confine the external field, but their field shape is dominated by the current distribution rather than by the iron. By imbalancing the right-left symmetry of the currents, a dipole field can be created to shift the quadrupole magnetic axis. External iron is crucial in shielding the path of the low-energy beamline just outside the magnet. Magnetic flux in the midplane iron return path is large but tolerable. It is worth noting that pushing the quadrupole magnetic center toward this side of the aperture (by imposing a large dipole field) has the beneficial effect

of reducing this midplane flux.

Several estimates of a Panofsky style Q4 using conventional conductors have been made. The required gradient is about 15 T/m over an 80-cm length. Such a magnet requires high current densities, over 5 kA/cm^2, and would dissipate between 150 and 200 kW; cooling would therefore be a serious problem. Furthermore, conventional coils would be rather thick compared with the idealized current sheets required for pure quadrupole fields, which means that field quality would suffer. Designed as a superconducting magnet, these problems disappear. Such a design alternative is discussed below. We note here that Q5 must also be a nonstandard quadrupole, but its design is much less exacting than that of Q4, and it has not yet been studied at the same level of detail.

Superconducting Panofsky Quadrupole. A superconducting septum quadrupole Q4 consists of a square Panofsky quadrupole and a dipole, with the geometrical center of the magnet offset by 19 mm from the HEB center (Fig. 5-22). The dipole field is used to offset the quadrupole field such that the resulting quadrupole field is centered on the HEB.

The Q4 magnet has a gradient of 15.2 T/m and a magnetic length of 800 mm; the distance between the front face of the magnet and the IP is 3.96 m. The positions of the two beams, which lie in the same horizontal plane, are given in Table 5-10. As indicated in Fig. 5-22, the two beams diverge with an angle of 20 mrad.

The iron yoke is square and is everywhere 25 mm thick, except in the region between the two beams, where the thickness tapers to a minimum of about 2.3 mm near the end of the magnet closer to the IP. Because the magnet has a minimum distance between the inside of the two beam pipes of 13.55 mm (the "septum thickness"), the LEB vacuum pipe is supported by the same iron yoke. The bore tube inner radius is 45 mm for the HEB and 25 mm for the LEB. As mentioned, the dipole field strength is adjusted to offset the center of the quadrupole field by 19 mm from the center of the HEB bore tube.

The septum wall (Fig. 5-23) has the following elements:

- 1-mm-thick stainless-steel bore tube (HEB)
- 1.8-mm-thick multilayer insulation (MLI)
- 0.2-mm clearance
- 1.5-mm-thick stainless-steel vacuum pipe
- 3.25-mm-thick superconducting coils and electrical insulation
- 2.3-mm-thick iron
- 0.75-mm-thick stainless-steel vacuum pipe
- 1.8-mm-thick MLI
- 0.2-mm clearance
- 0.75-mm-thick stainless-steel bore tube (LEB)

The quadrupole coils are wound on four quadrants. These are then assembled around the outer diameter of a vacuum pipe that is separated from the bore tube by multilayer

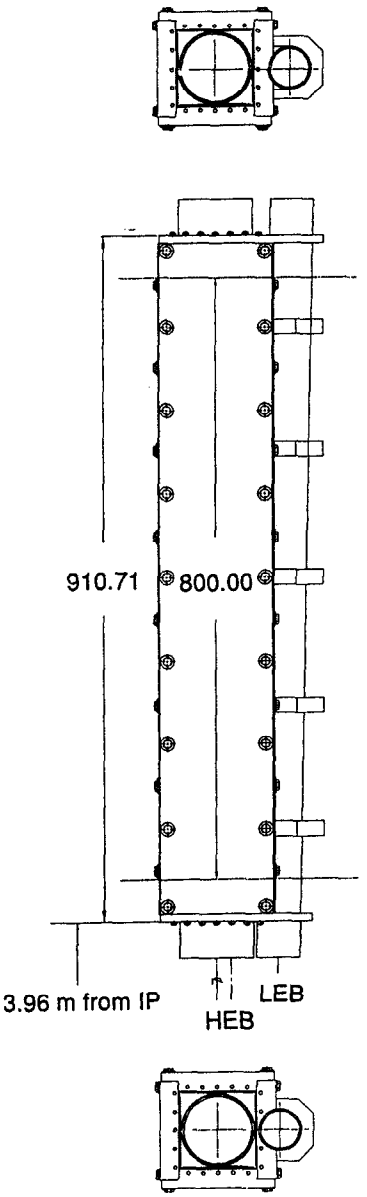

Fig. 5-22. Top and end views of the superconducting septum quadrupole Q4. Dimensions are in millimeters. The septum itself is shadowed with the Q4 crotch mask, described in Section 5.2.7.

Table 5-10. Positions of the beam along along the magnet.

Distance from IP (m)	HEB position (mm)	LEB position (mm)
3.96	40.29	104.84
4.76	51.95	132.69

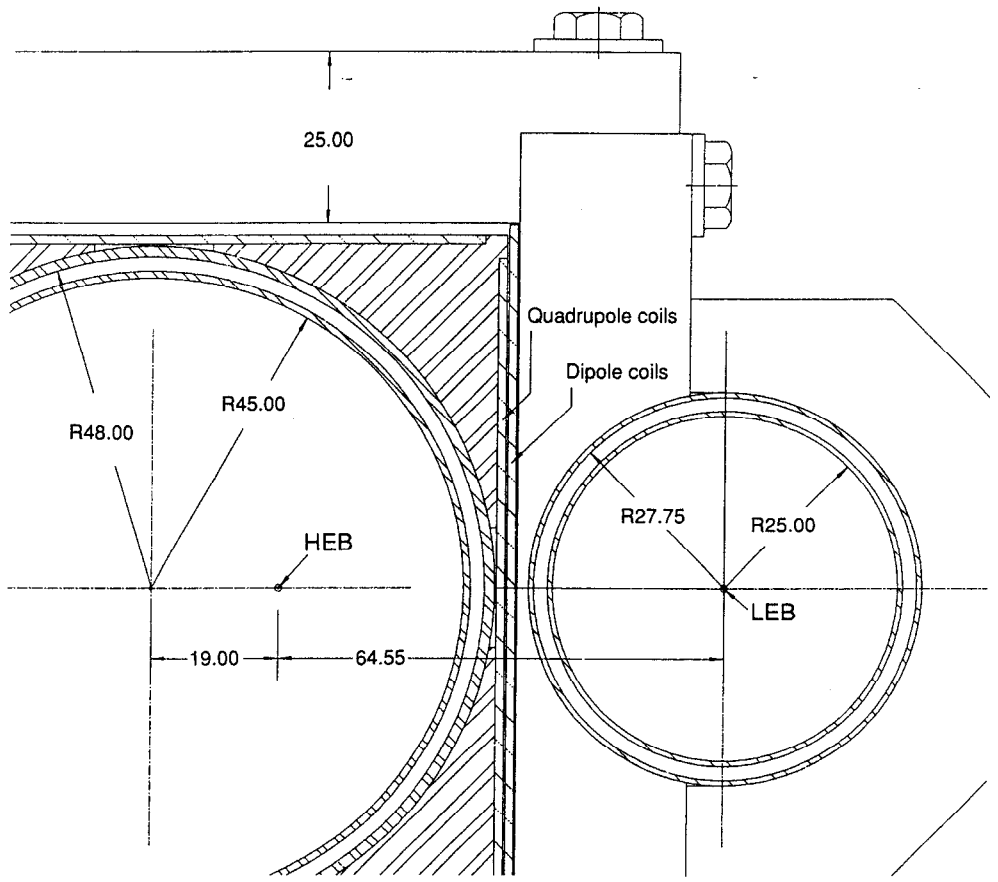

Fig. 5-23. Detail of the superconducting septum quadrupole Q4. Dimensions are in millimeters.

insulation. Next, the dipole coils are wound and assembled over the quadrupole coils. Finally, an iron yoke is put in place that completely covers the coils. The superconducting wire used in this magnet is a monolithic, square multifilamentary Nb-Ti superconductor in a copper matrix.

The Q4 field quality has been computed analytically considering the real coils and their images reflected in the iron yoke. The uniformity of the magnetic field is expressed in the usual multipole coefficients. The multipole coefficients of the magnetic field are shown in Tables 5-11, through 5-13; the coefficients are calculated at a radius of 10 mm centered around the bore tube ($x = 0$) and around the HEB axis ($x = 19$ mm). If need be, these multipole coefficients could be further reduced by using an appropriate nonuniform spacing of the wires in the coils.

A two-dimensional finite-element analysis using ANSYS and POISSON, and considering the real *B-H* curve for the iron (see Fig. 5-24), has confirmed that there is no saturation in the iron yoke and that the maximum field in the yoke is 1.37 T, as shown in

Table 5-11. Multipole coefficients for the Q4 quadrupole component only. A "unit" is $10^4 \times b_n(T/cm^{n-1})/b_2$.

	Multipoles at x = 0 mm	Multipoles at x = 19 mm
b1	0	–0.2884 T
b2	–0.1518 T/cm	–0.151807 T/cm
b3	0	0.50 units
b4	0	0.25 units
b5	0	0.05 units
b6	0.007 units	–0.002 units

Table 5-12. Multipole coefficients for the Q4 dipole component only.

	Multipoles at x = 0 mm	Multipoles at x = 19 mm
b1	0.288392 T	0.288527 T
b2	0	0.000148 T/cm
b3	–2.35 units	–2.9 units
b4	0	–0.16 units
b5	–0.035 units	0.008 units
b6	0	0.01 units

Table 5-13. Multipole coefficients for the combined Q4 quadrupole and dipole components.

	Multipoles at x = 0 mm	Multipoles at x = 19 mm
b1	0.288392 T	0.0001 T
b2	–0.1518 T/cm	–0.15166 T/cm
b3	–2.35 units	–2.4 units
b4	0	0.09 units
b5	–0.035 units	0.058 units
b6	0.007 units	0.008 units

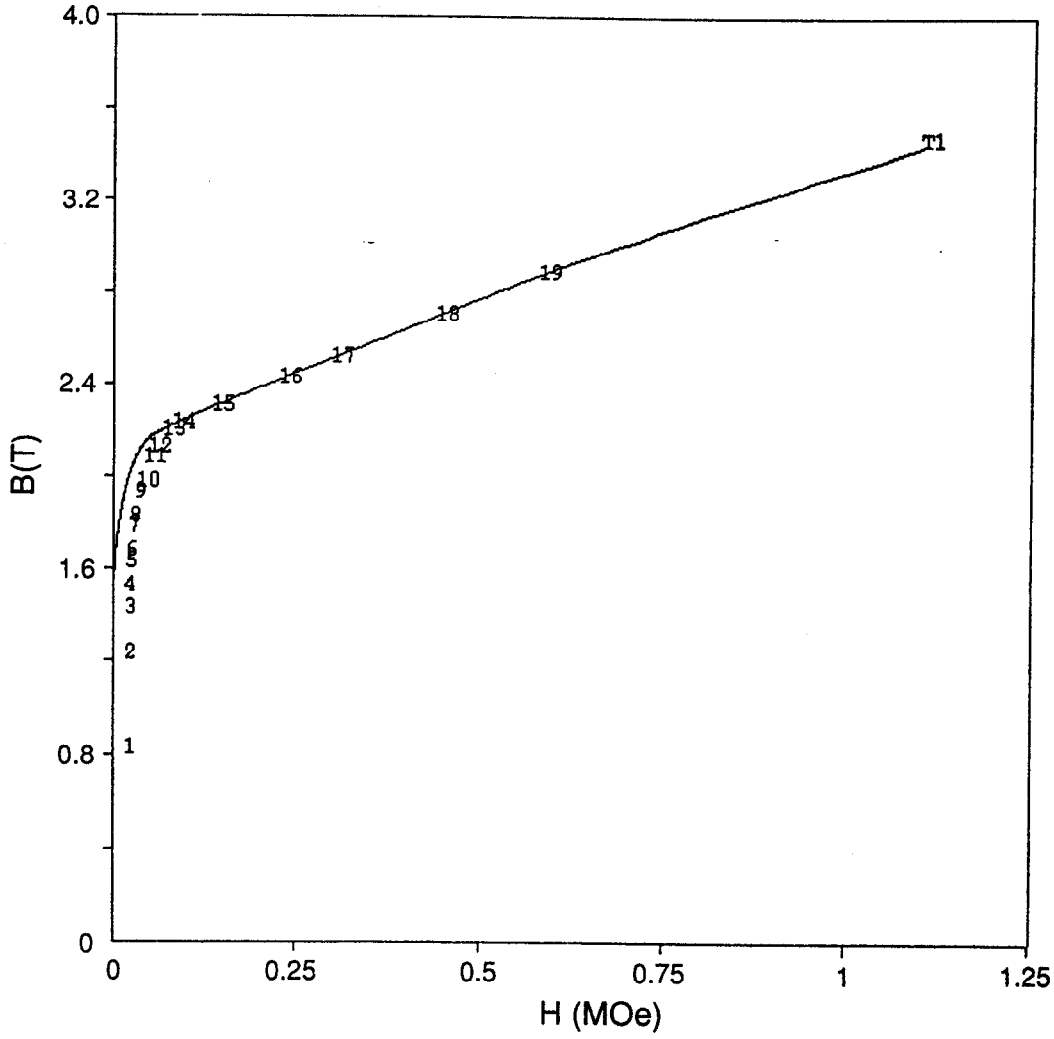

Fig. 5-24. B-H curve of the Q4 iron.

Fig. 5-25). This two-dimensional analysis was performed using the geometry of the magnet cross section at the magnetic center of the return end (that is, the end nearer the IP). Flux lines of the magnetic induction B are shown in Fig. 5-26. The maximum field in the coil region is at the quadrupole coil and is 1.253 T (see Fig. 5-27).

Because the magnet is required to have a wall thickness of 13.55 mm at the return end, the iron yoke has a circular cut to accommodate the beam pipe for the LEB. In this region the yoke thickness is reduced to 2.3 mm at the magnetic center of the return end (and to 1.6 mm at the physical end). However, in this region there is only a small magnetic flux because the dipole and quadrupole fluxes very nearly cancel each other. Nonetheless, this region of iron is required in order to close the magnetic flux and screen the LEB.

In Figs. 5-28 and 5-29, the Lorentz forces acting on the coils are shown; these values are summarized in Table 5-14. The Lorentz forces squeeze the quadrupole and dipole coils together and compress them along their main dimension. There is everywhere a force between the coils and the adjacent iron yoke face. The prestress required to maintain compressive loading of the coils during excitation is less than 8 N/mm^2. This

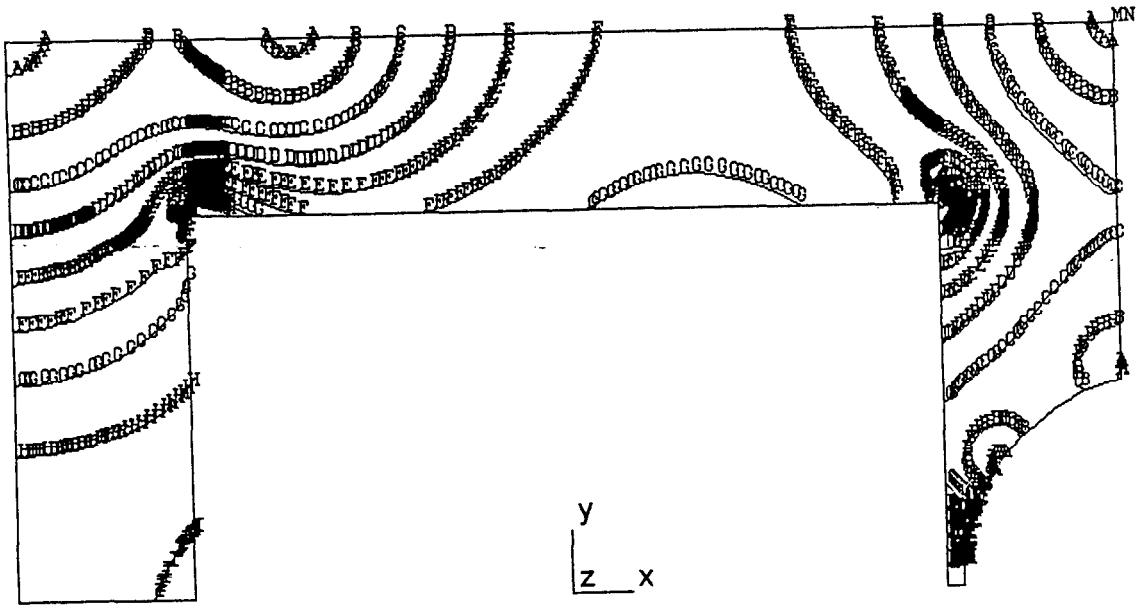

Fig. 5-25. Magnetic induction B in the Q4 iron yoke; B_{max} = 1.37 T.

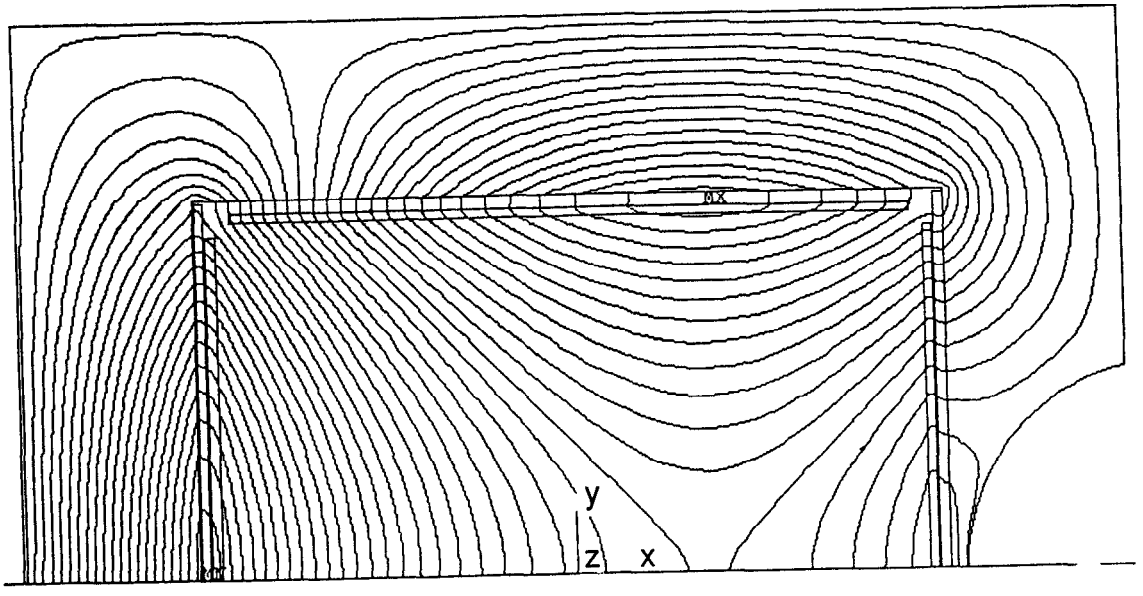

Fig. 5-26. Flux lines of the magnetic induction B for the Q4 quadrupole. Note the offset of the quadrupole center due to the superimposed dipole fold.

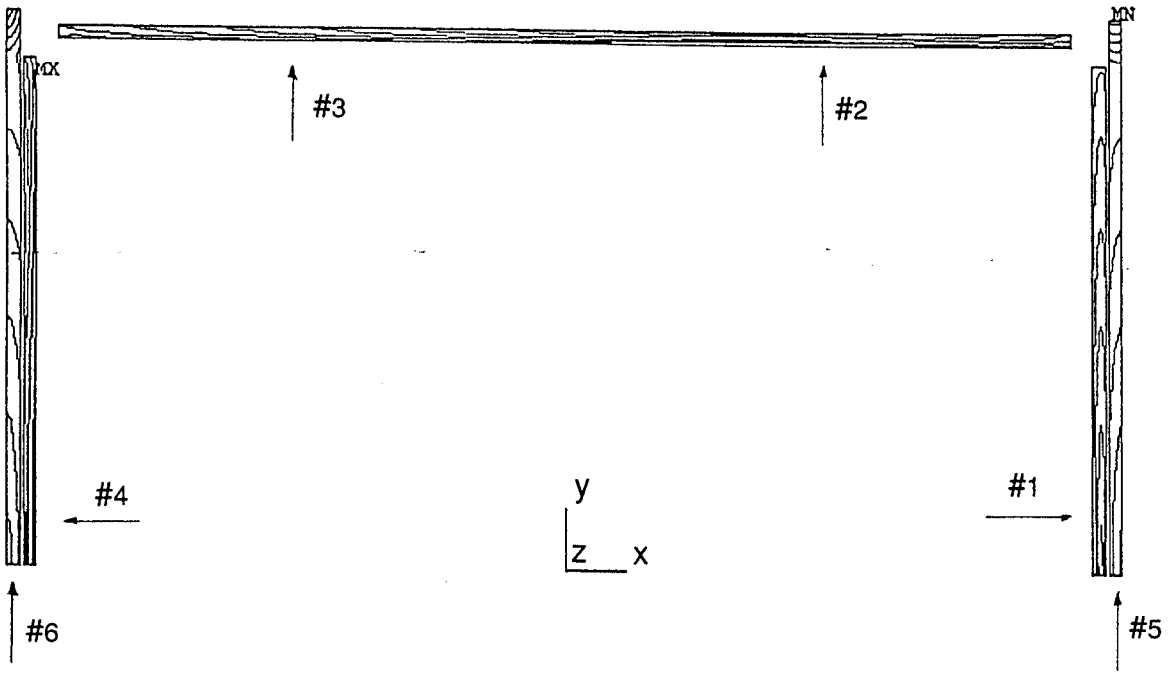

Fig. 5-27. Magnetic induction B in the Q4 coils; B_{max} = 1.253 T.

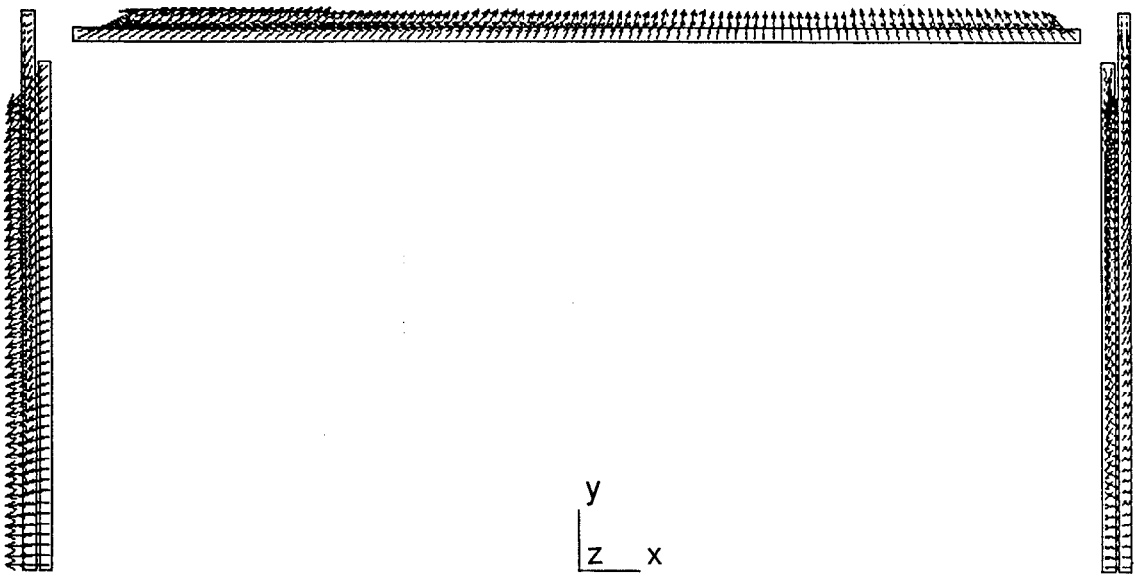

Fig. 5-28. Lorentz forces acting on the coils.

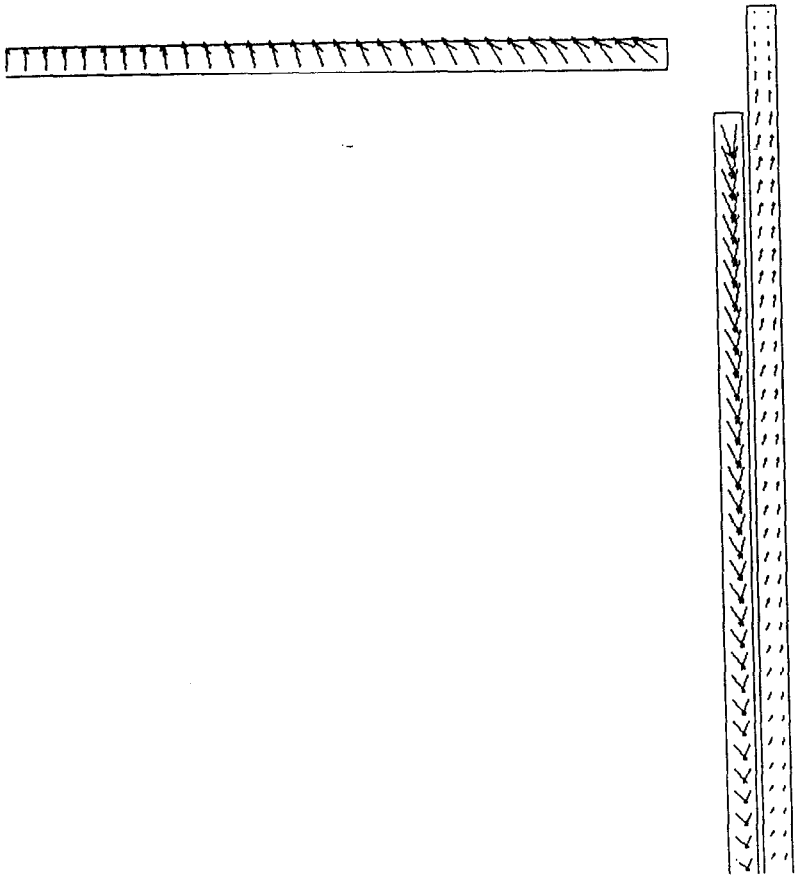

Fig. 5-29. Detail of the Lorentz forces acting on the coils.

Table 5-14. Lorentz forces acting on the coils.

Coil number[a]	F_x (N/mm)	F_y (N/mm)
1	2.5	–11.1
2	–2.7	11.1
3	19.7	11.1
4	–19.6	–11.3
5	1.7	4.3
6	–1.7	–4.3

[a]See Fig. 5-27.

prestress is applied during coil assembly by properly shimming the coils and assembling the four-piece iron yoke around the coils with an "interference" fit.

The overall current density in the dipole is $J_0 = 179$ A/mm^2, and in the quadrupole, it is $J_0 = 511$ A/mm^2. The critical curve B-J_{sc} for the superconducting material is obtained from the following expression:

$$J_{\text{sc-critical}}(T, B) = p_1\left(1 - \frac{T - T_0}{p_2 - p_3 B}\right)(1 + p_4 B) \tag{5-4}$$

with $p_2 = 7.81042$ K, $p_3 = 0.778448$ KT^{-1}, $p_4 = -0.0996643$ T^{-1}, and $T_0 = 4.22$ K. We assume a superconductor having J_{sc} ($T = 4.22$ K, $B = 5$ T) = 2750 A/mm^2, which gives $p_1 = 3192$ A/mm^2. The assumed packing factor of the conductor is 0.64 and the Cu:SC ratio is 3.0.

Because the operating current density is $J_{sc} = J_0(1 + 3)/0.64 = 3192$ A/mm^2 and the operating temperature is 4.22 K, then $J_{\text{sc-critical}} = 4513$ A/mm^2 and $B_{\text{critical}} = 1.77$ T. The operating margin, defined as $(J_{\text{sc-critical}} - J_{sc})/J_{sc}$ is 41% (Fig. 5-30).

The configuration used for the magnet ends is the "Lambertson" end [Laslett, et al., 1987], with an angle of 60° (see Figs. 5-31 and 5-32). These ends have the same integrated multipoles as found in the central cross section of the magnet, and this design eliminates the need for spacers between the wires. The physical length of the coils is 860 mm. Axial compression is obtained from the end-plates that are fixed to the iron yoke.

In the 1.8-mm space between the bore tube and the vacuum pipe, multilayer insulation is used. The assumed apparent conductivity is $k_a = 1 \times 10^{-4}$ W/m/K and the heat transfer from the two room-temperature bore tubes to the LHe-cooled vacuum pipes is ~7 W. The leads carry 800 A for the quadrupole and 280 A for the dipole. The heat flow into the helium is ~1 W/kA per lead; the four leads (two for the dipole and two for the quadrupole) contribute a heat load of about 2 W. The total heat to be extracted, then, is about 9 W; this is easily manageable.

The cryostat for the Q4 quadrupole, shown in Fig. 5-33, is a conventional assembly, typical of many others now in use with superconducting magnets (such as the three spin-rotator superconducting solenoid magnets now installed at SLAC). It has a diameter of about 46 cm and a length of 150 cm. The magnet cold mass is supported and aligned by vertical and horizontal fiberglass-reinforced plastic straps (similar to the designs used at DESY and SLAC). Both beam tubes are at room temperature and are shielded from the liquid-helium wall with superinsulation.

The cryostat has two dipole current leads (280 A each) and two quadrupole current leads (800 A each). Two bayonet connections, for liquid-helium supply and for liquid-nitrogen supply (to the heat shields), are indicated in Fig. 5-33. Static heat loads, including current leads, are estimated at 1.5–2 L/hr of liquid helium. A 50-L storage volume will provide 24-hour operation between liquid-helium fills. The liquid helium will be supplied by 500-L dewars fed from the SLAC central liquefiers (as is now done for the three spin-rotator solenoid cryostats).

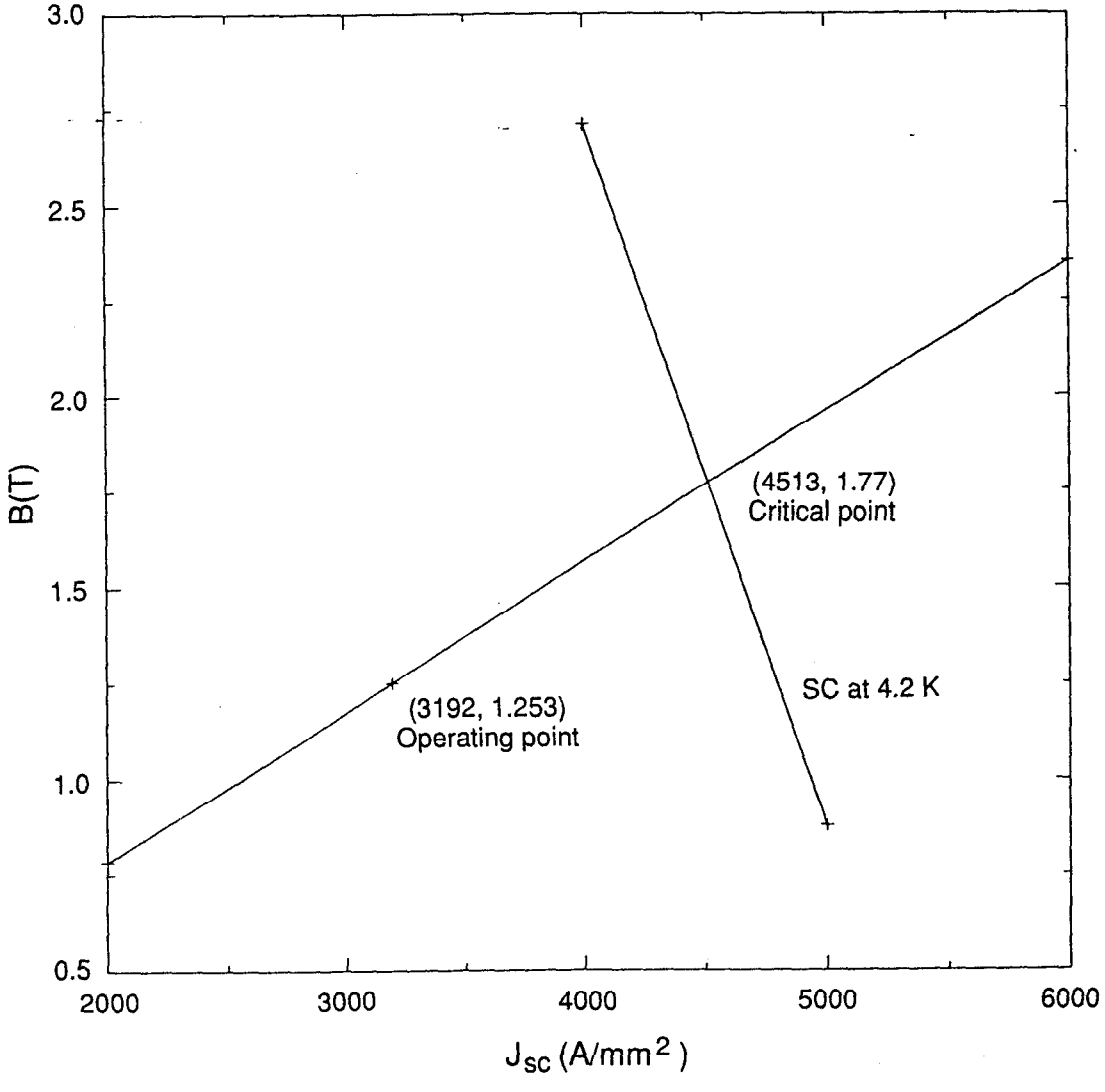

Fig. 5-30. Operating point of the magnet Q4 and critical curve B-J for the superconductor.

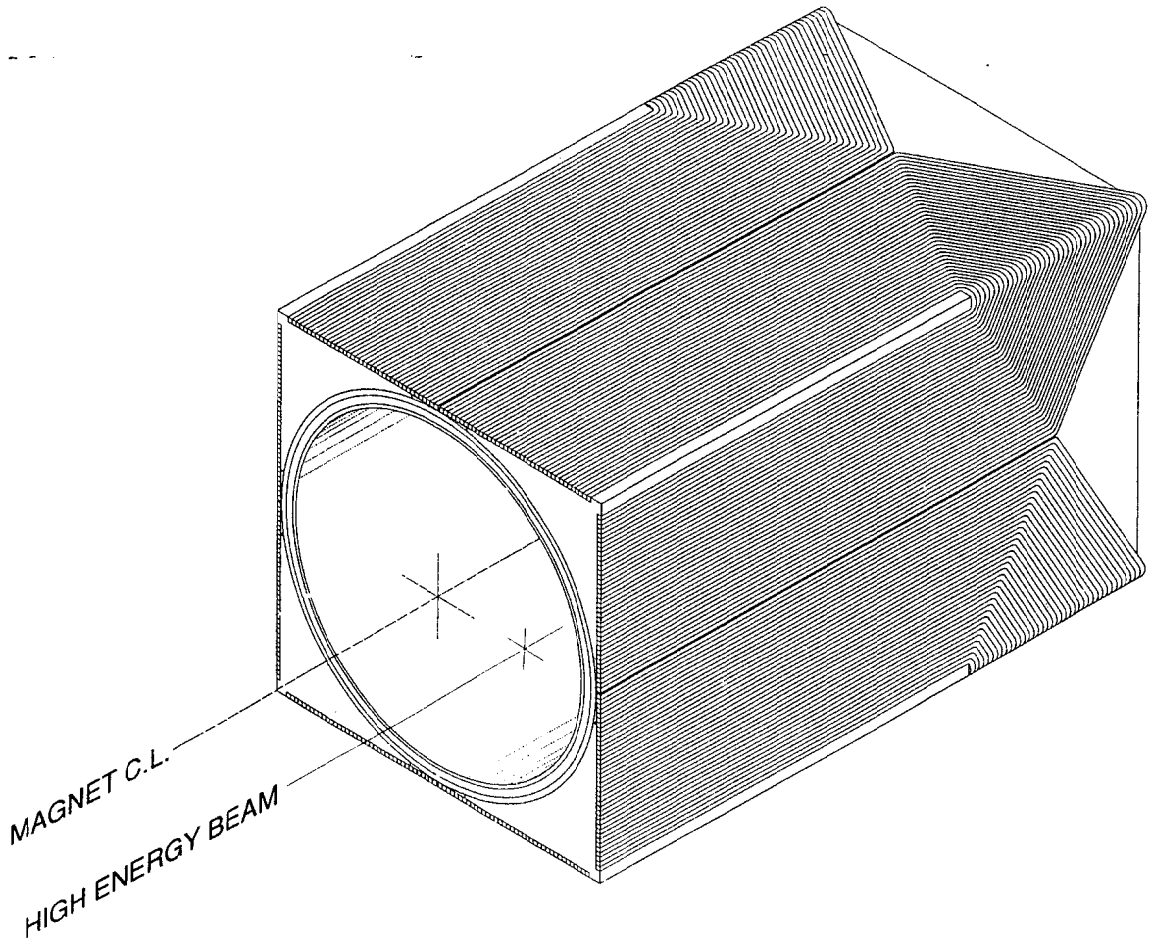

Fig. 5-31. View of the Lambertson end termination for the Q4 quadrupole coils.

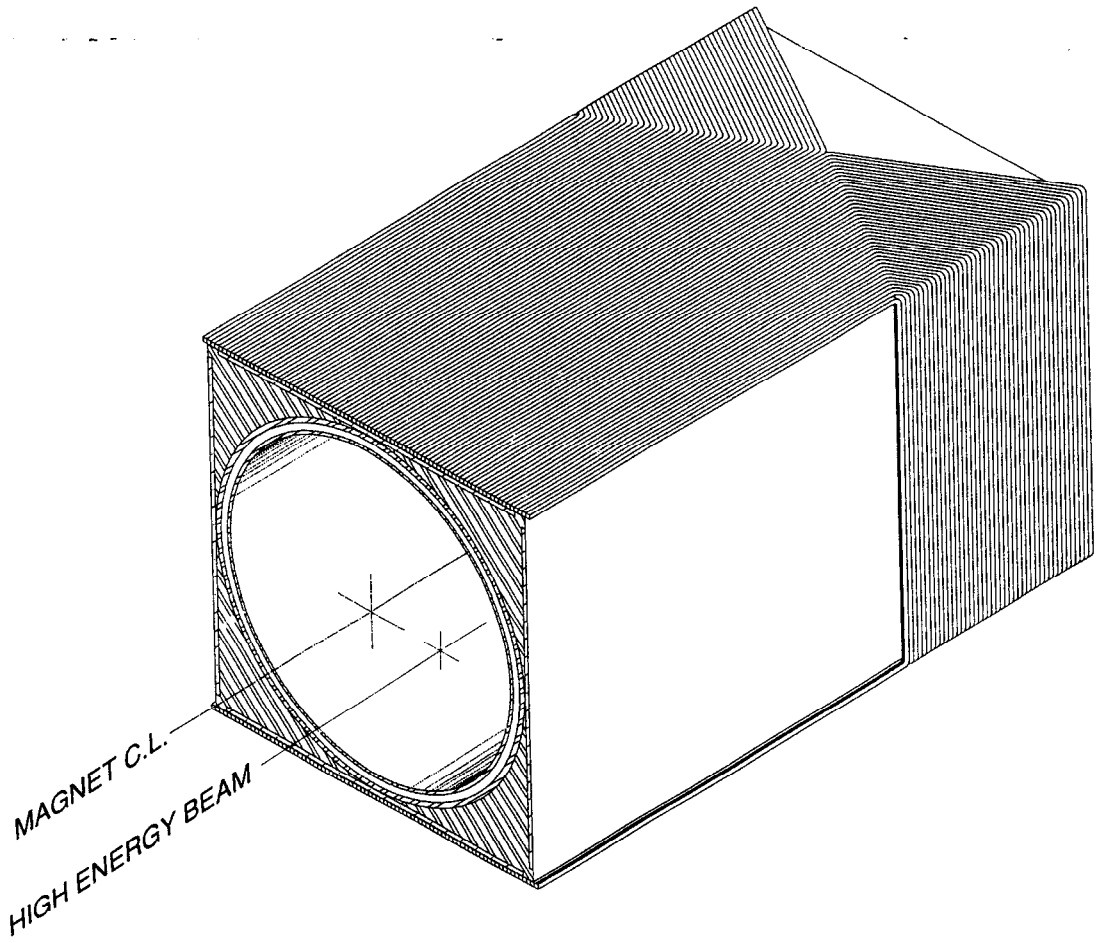

Fig. 5-32. View of the Lambertson end termination for the dipole coils.

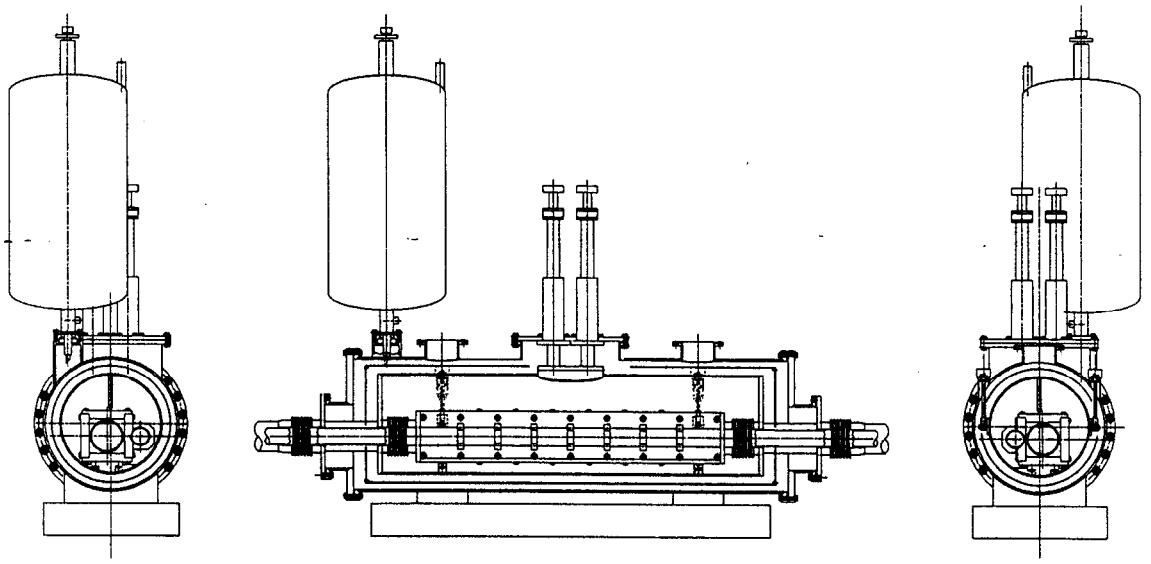

Fig. 5-33. End and cutaway views of Q4 cryostat.

Room-Temperature Alternative. Given the large amount of synchrotron radiation in this part of the lattice, it is clearly worthwhile to consider the possibility of a conventional, rather than a superconducting, Q4. An example of such an alternative concept would be to design a conventional quadrupole and then provide a flux-free channel for the LEB inside the magnet. A conventional quadrupole in the Collins form, with a figure-eight field pattern, has a natural coil-free midplane to pass the synchrotron light fan on one side. The low-energy beamline vacuum pipe is located in the midplane between the other two poles. An iron pipe of sufficiently high permeability and a sufficiently thick wall will screen out the field at the LEB beamline, but by itself would cause large distortions in the quadrupole field sampled by the HEB. A way around this difficulty has recently been discussed by Herrmann and Szyszko [1989]. A current sheet on the outer surface of the magnetic shield can, in principle, completely correct the external distortions introduced by the shield tube. Figure 5-34 shows the resultant field patterns.

On the left in Fig. 5-34 is the desired quadrupole field without a flux shield pipe. The center plot shows the distortion caused by the iron flux shield tube alone. The right-hand field plot shows the effect of the correcting current sheet. To match the original field pattern, the distribution of corrector currents must vary around the perimeter of the shield. The general rule for determining the required surface current elements *di* is

$$di = -\frac{\mathbf{B}\cdot\mathbf{ds}}{\mu_0} \quad [\mathrm{A}] \tag{5-5}$$

Here **ds** is a vector tangent to the outer surface of the iron shield and **B** is the undistorted magnetic field at that surface. In this approach, all magnetic flux that would otherwise have passed through the LEB beam-stay-clear aperture must now be channeled around in the iron beam pipe walls. The peak current densities in the corrector current

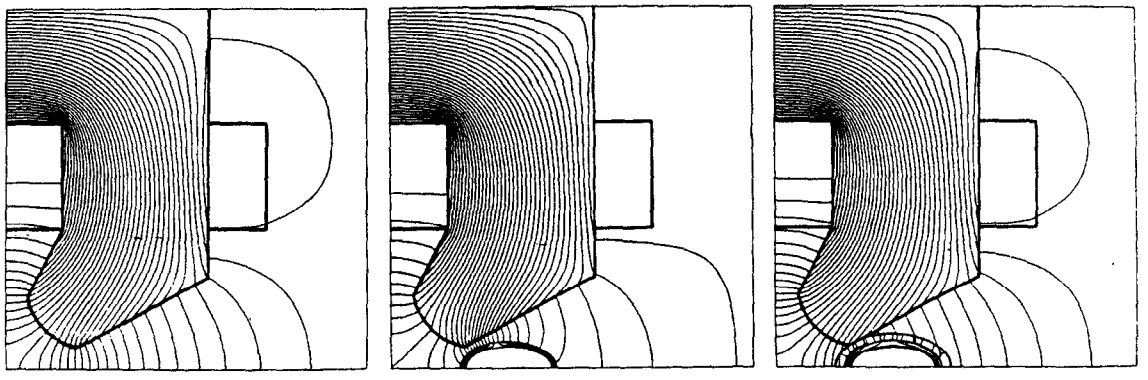

Fig. 5-34. Example of field lines for a Collins quadrupole design. The left picture is a single magnet, the center picture shows the field perturbations introduced when an iron pipe for the LEB is inserted, and the right picture shows the restored field when the proper current sheets are used to shield the LEB pipe.

sheath located at the midplane are 4–5 kA/cm^2, just as in the Panofsky septum designs. However, there are several important advantages to the design of a quadrupole with flux shield:

- Quadrupole magnet and flux shield are two distinct, decoupled design problems.
- No extra dipole field is required to offset the quadrupole center to create clearance for the synchrotron radiation fan. A gap for the fan is intrinsic to the standard quadrupole geometry. Total field energy is much lower for the flux shield approach.
- A conventional quadrupole can have standard low-current-density coils for low power consumption (10 kW or less).

Although a high current density (5 kA/cm^2) would still be required for a portion of the shield, the top and bottom surfaces of the elliptical flux shield, where the field strikes at almost normal incidence, would require only hundreds of A/cm of surface-current density. The total flux shield power could be as low as 10 kW.

The integrated current density around the perimeter of the flux shield is zero. Shaping the conductor cross sections or winding densities may make it possible to power the flux shield from a single supply. The wall thickness of the iron shield in any actual design would be adjusted around the perimeter to match the local flux and thus prevent saturation.

Simulations indicate that the remaining field inside the LEB beam pipe would be about 0.006 T. A second, floating magnetic-shield layer of high-permeability material lining the inner surface could reduce this further, if necessary. The particular Collins quadrupole design illustrated in Fig. 5-34 has a pole-tip bore radius of 3.12 cm and requires about 7000 A turns per coil to reach a field gradient of 17 T/m.

During the detailed design stage, studies will be carried out to see if the field quality expected from the superconducting design can also be achieved with a conventional magnet design. The design will ultimately depend on both performance and reliability considerations.

5.1.4 Magnetic Measurements

Five stations will be constructed for magnetic measurements, each having a computer. The computer will serve for data storage and data handling, and will also permit a comparison between the new magnetic measurements made on the refurbished PEP magnets and the original data taken at the time of their manufacture. A standardization procedure for each particular type of magnet will be stored in the computer so that it can be performed automatically prior to the commencement of measurements. The software will also prompt the operators to enter serial numbers, attach cables and water hoses, etc. Variables such as water flow, terminal voltage, and temperature rise will all become part of the database. This will ensure quality control and provide a complete pedigree for each magnet.

The choice of five stations will permit us to handle the five different types of magnets: HER dipoles, HER quadrupoles, LER dipoles, LER quadrupoles, and HER/LER sextupoles. This number of stations is perceived to be a minimum, based on the number of magnets to be tested and their different configurations. In particular, the HER dipoles present a challenge, owing to their 5.4-m length. The long coil required for these magnetic measurements will be unique. The LER bends are only 1 m long, so a relatively short coil can be used. Both HER and LER quadrupoles could be measured at a single station, but it is prudent to have a degree of redundancy and to avoid the possibility of bottlenecks. Because the HER and LER sextupoles are identical, the same station will be used, irrespective of the final destination of the magnet.

Magnetic measurements will be conducted using standard rotating–long-coil techniques. This method gives the integrated strength of the magnet, either $\int B\,dl$ or $\int G\,dl$, including end effects. In the case of quadrupoles, the rotating-coil measurement is a convenient way of determining the magnetic center, since a zero dipole signal occurs at this location. This measurement will provide a convenient check on the accuracy of the external fiducials built into the laminations at the time of stamping. Furthermore, the rotating-coil technique permits a determination of the higher-multipole content of the field, which is the true measure of magnet quality. Measurements will be conducted at different current settings, corresponding to the operating energies envisioned. This will provide a polynomial fit that will permit the magnets to be set accurately at any required field strength.

Magnetic tolerances for both the HER and the LER are similar to those for PEP and can be summarized as follows: The sum of all higher multipoles over the required beam-stay-clear region should be less than 0.1% of the main field component of the magnet over this same region.

5.1.5 Supports

Considerable thought has been given to the support and alignment of the two rings of the B Factory. Because of the large mass of the PEP components, which are to be reused in the HER, the HER will be mounted below the LER. A side elevation of the standard HER and LER cells and a cross-sectional view of the PEP tunnel are shown in Figs 5-35 and 5-36, respectively. An artist's conception of the overall layout of the two rings is shown in Fig 5-37.

Once the PEP tunnel has been emptied, a rough alignment procedure (see Section 5.3) will locate the anchors for the lower legs of the support structures. These support structures will be placed at the quarter-points of the HER dipole magnets, as was done in PEP, to maintain the alignment and minimize sag and twist of these long laminated magnets. The four feet necessary to adjust and maintain the alignment of the bending magnets will be mounted on these horizontal legs.

To facilitate installation, the quadrupole-sextupole pairs for the HER will be mounted on a rigid box-frame, or raft, and aligned in a temperature-controlled facility using high-precision optical benches. In this manner, component-to-component misalignment is kept to a minimum. The vacuum spool piece for this section will be installed along with the vacuum chamber support, which must be capable of locating and fixing the associated beam position monitor with an accuracy of about 0.1 mm with respect to the magnetic center of the adjacent quadrupole. This requirement justifies our plan to prealign the individual components on a monolithic, stress-relieved frame that will avoid costly in-field alignment (which historically has proved to be more expensive and less accurate than prealignment in the laboratory).

In the tunnel, precision alignment will locate the base support on which the doublet rests. The base will have dowel pins identical to those at the alignment stations. Thus, when the magnetic components and base are taken to the tunnel, these pins will enable us to place the doublet accurately. Although the base itself will be provided with adjustments having six degrees of freedom, we believe that it will be unnecessary to provide individual adjustment for all the raft components. The technique outlined here has been employed successfully at SLAC on several other projects, including the damping rings, the SLC arcs, and the final focus beamline.

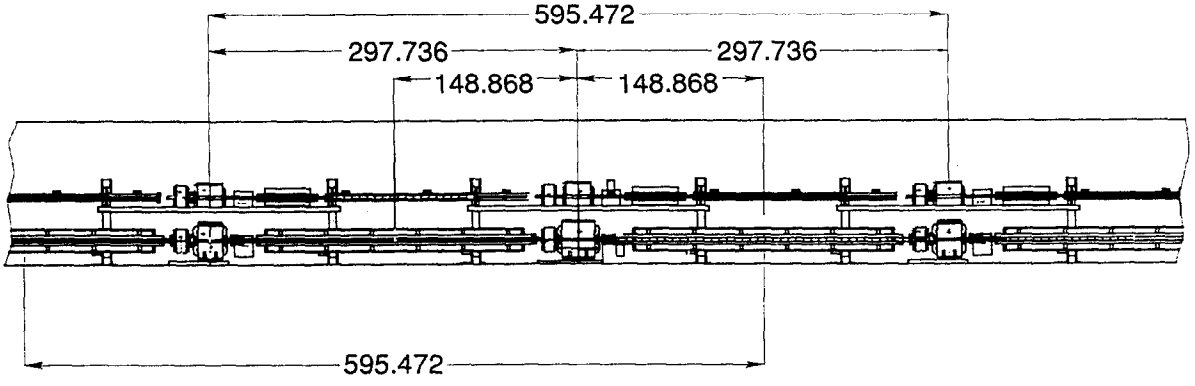

Fig. 5-35. Side elevation of a standard HER cell.

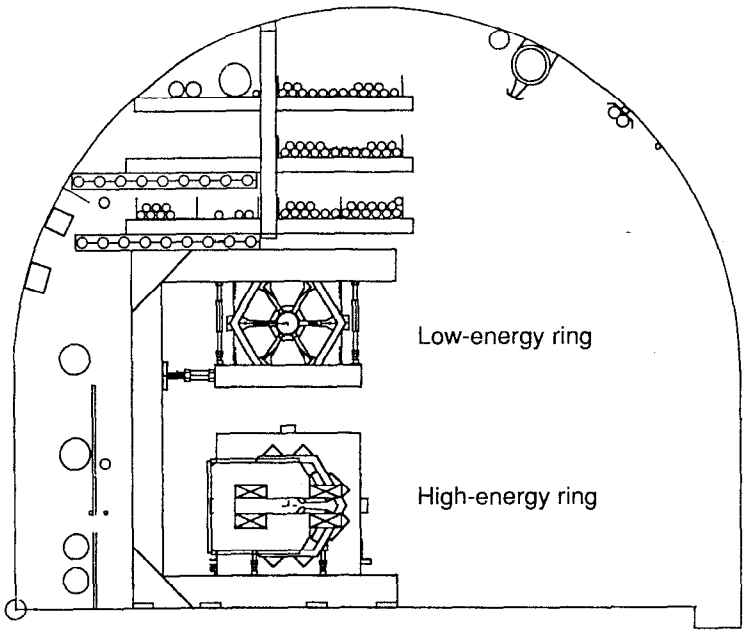

Fig. 5-36. Cross-sectional view of the PEP tunnel, showing the locations of utilities and the high- and low-energy rings.

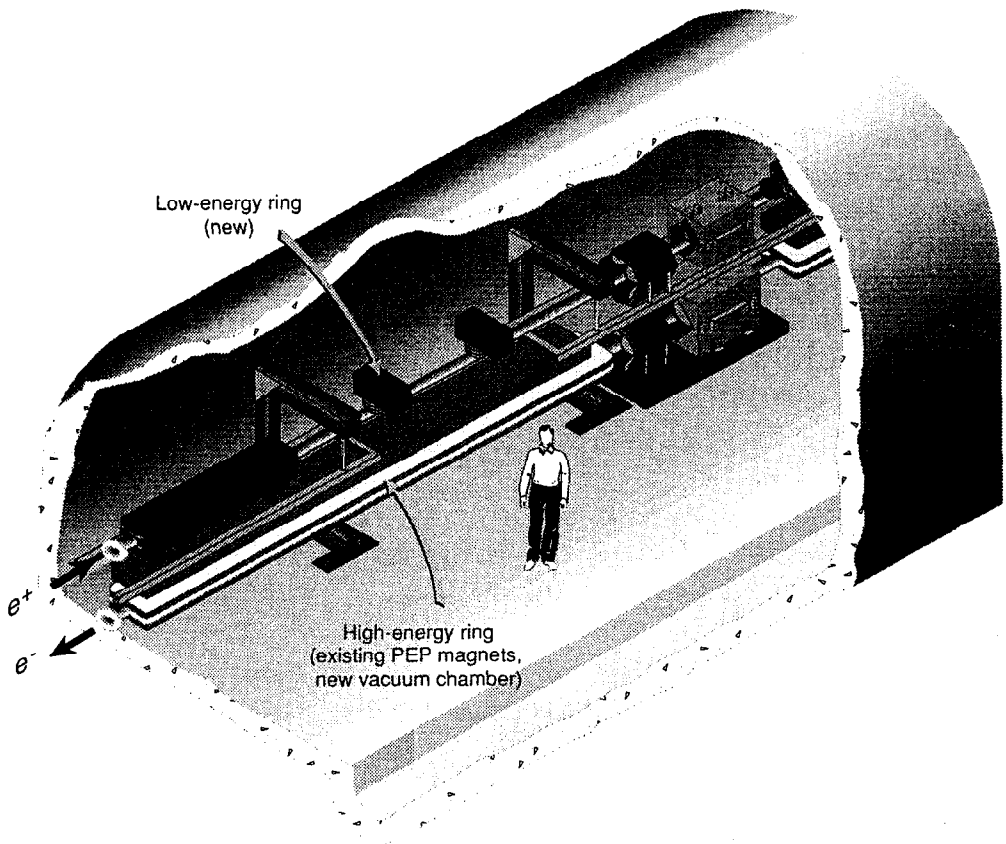

Fig. 5-37. Artist's conception of the high- and low-energy rings in the PEP tunnel.

After the main components of the HER ring are in place, the LER components will be installed above them. Once again, we will take the approach of using a raft or strong frame and prealigning the LER components in the laboratory. Because of their smaller size and lighter weight, we expect to be able to support and align the magnetic components of an entire half-cell (including a sextupole, a quadrupole, a bending magnet, and either a steering magnet or beam position monitor, together with the vacuum chamber and associated pumps) on one raft. As with the HER, the raft itself will be provided with six degrees of controlled freedom. We believe that it will be unnecessary to provide easy adjustments for individual raft components.

To facilitate alignment, the LER will be suspended above the HER such as to leave about an 8-in. component-free zone between the two rings for unobstructed line-of-sight. As discussed in Section 5.1.3, extensive ground-motion measurements were made at SLAC prior to building the SLC, since that accelerator was expected to be very sensitive to small, steady-state ground motions or noise. These measurements indicated which site-wide excitation frequencies are a problem. Our supports will be designed to avoid unwanted resonances.

Because the two rings are independently supported, at different heights in the tunnel, it is clear that changes in temperature within the tunnel can cause relative motion between them. Fortunately, time constants for such motion will be slow, of the order of hours, and steering corrections can be made in the IR to compensate for the resultant beam drifts.

5.2 VACUUM SYSTEM

The vacuum system of the B Factory collider presents a technical challenge beyond that of any existing electron-positron collider. Each technical subsystem must meet demanding design criteria to satisfy the overall system requirements. These subsystems for the high-energy (electron) and low-energy (positron) rings (HER and LER, respectively) include vacuum chambers, pumps, cooling, and special components, such as bellows, beam position monitors (BPMs), valves, etc.

In the case of the B Factory design, the high- and low-energy rings will have circulating beam currents of 1.48 and 2.14 A, respectively, to reach the design luminosity of 3×10^{33} cm^{-2} s^{-1}. We refer to these as the "nominal" or "design" currents. The nominal beam currents are at least an order of magnitude beyond the typical values for today's colliders and, as such, present an appreciable challenge to the vacuum system designer. To provide for possible upgrades, and for luminosity "breathing room," we also specify a *maximum allowable* current in each ring of 3 A. Because the vacuum system is generally difficult to upgrade after the collider is operating, we have chosen in some instances to allow for the 3-A capability from the outset. In cases where the initial configuration can be upgraded and does not require the extra capability, it is sufficient simply to provide the means for future upgrades—for example, by having unused ports to which additional pumps could be attached later.

Note that, in this section, we will use the term "electrons" in its generic sense, that is, to refer to either electrons or positrons.

5.2.1 General Issues and System Requirements

A well-designed vacuum chamber is the key to providing a suitable beam environment. In particular, the chamber design should have the following attributes:

- Adequate beam-stay-clear aperture for injection and for stored-beam lifetime
- Low impedance to avoid beam instabilities and to minimize higher-order-mode (HOM) power dissipation
- Sufficient pumping speed to maintain a low pressure in the face of substantial synchrotron-radiation-induced gas desorption
- Sufficient cooling to safely dissipate the heat load associated with both synchrotron radiation and HOM losses
- Capability to shield external ring components from synchrotron radiation

Most of these requirements are fairly obvious and do not differ from those of existing colliders. The main distinction in the case of the B Factory is associated with the required beam currents, which are much higher than those in present-day colliders.

Depending on the magnitude of the dynamic gas load due to photodesorption, the chamber could have a conventional elliptical shape or it could exploit differential pumping via an antechamber arrangement. In the B Factory parameter regime, use of a conventional chamber shape is acceptable, provided that the material is chosen to have a low photodesorption coefficient. If the chamber material is suitably chosen, the chamber walls will also serve as the primary shield for the synchrotron radiation that would otherwise damage magnets and other beamline components. Basically, this consideration implies the use of a high-Z material such as copper or stainless steel, rather than the more easily fabricated aluminum. (If aluminum were chosen, the shielding would have to be provided by an additional layer of material—for example, lead—to absorb the radiation passing through the chamber walls. While this is possible, it is an undesirable complication.)

Included as integral parts of the chamber are several special sections and components, such as cross-section transitions, pumping ports, bellows, and BPMs. The high peak and average beam currents in the B Factory demand that the electromagnetic environment presented by the vacuum chamber and its special components satisfy a strict impedance budget for the ring. It is known that the present PEP vacuum chamber provides a sufficiently low broadband impedance ($|Z/n| \approx 1\ \Omega$) to be acceptable for the B Factory [Rivkin, 1987; Zisman, 1990b]. Thus, we are assured that standard care in the design of the vacuum chamber will permit us to reach our impedance goal.

The pumping subsystem of the collider must maintain the specified operating vacuum under conditions of a large dynamic photodesorption gas load caused by the intense synchrotron radiation bombardment of the chamber walls. In high-energy, high-current electron rings, thermal outgassing is generally a small contribution to the gas load that mainly determines the base pressure in the absence of beam. In addition to handling the gas load during routine operation, the pumping must also be sufficient to allow for rapid initial commissioning (cleaning) of the vacuum chamber. The *system requirements* for the vacuum system during collider operation are as follows:

- ≤10 nTorr in the arcs
- ~3 nTorr in the straight sections
- ~1 nTorr in the two half straight sections upstream of the detector
- ~0.1 nTorr base pressure due to thermal outgassing under no-beam (static load) conditions

(Note that pressure requirements are quoted here as N_2-equivalent values.) We have generally designed the vacuum systems to reach these goals even at the maximum allowable beam current of 3 A. Thus, at the nominal operating currents, we expect to do better than the requirements listed above. In this sense, the design is conservative and should operate very reliably. Moreover, the additional pumping capability will be of great benefit in reducing the conditioning time for the system.

An electron beam circulating in a storage ring subjects the vacuum chamber walls to copious synchrotron radiation. As the spatial extent of the incident radiation is small, the associated thermal flux is generally high enough to require considerable cooling of the chamber wall. The cooling subsystem is designed to remove the waste heat safely under conditions of high radiation flux. As is typical, cooling is accomplished by water flowing

in channels outside the chamber. In addition to ensuring the mechanical stability of the chamber under thermal loads that could reach 10 MW in the HER, maintaining the chamber wall at a relatively low temperature serves to reduce the gas load due to thermal desorption.

5.2.2 Determination of Vacuum Chamber Aperture

The size requirements of the beam chambers are determined by the beam emittances and energy spreads and by the optical functions of the HER and LER lattices. To ensure adequate quantum lifetime, the chamber was designed to accommodate the *uncoupled* horizontal emittance and the *fully coupled* vertical emittance. It is also desirable to keep the cross section of the chamber constant throughout the arc sections to minimize the impedance contribution from shape transitions. Consequently, we considered the maximum values of the beta functions in determining the chamber sizes.

For determining the required chamber aperture, we took the uncoupled emittance value for each ring to be twice the value required for the nominal operating configuration. This will provide considerable flexibility to adjust the ring parameters as dictated by operational needs. Thus, the chamber of the HER was designed for 100 nm·rad uncoupled horizontal emittance, and the LER chamber was designed for 200 nm·rad. In the absence of wigglers, the relative energy spread of the beam in the HER should be close to its natural value of 6.1×10^{-4}. To be conservative, we took a value of 1×10^{-3} for estimating the required chamber size. For the LER, we envision that the natural energy spread of 3.5×10^{-4} will be increased by means of wigglers to a value closer to 1×10^{-3}, which we again adopted as a design specification for evaluating aperture requirements. Since the HER optics are similar to PEP, the closed-orbit allowances were taken to be the same as those adopted for the original PEP design; these values were also assumed for the LER.

Emittance and beta function values used to evaluate the required apertures for the HER and LER are summarized in Table 5-15.

The horizontal beam-stay-clear half-aperture is evaluated as

$$\mathrm{BSC}_x = 10\sqrt{\varepsilon_{x0}\hat{\beta}_x + \hat{D}^2\left(\frac{\sigma_E}{E}\right)^2} + \mathrm{COD}_x \tag{5-6}$$

Similarly, the vertical beam-stay-clear is

$$\mathrm{BSC}_y = 10\sqrt{\varepsilon_{y0}\hat{\beta}_y} + \mathrm{COD}_y \tag{5-7}$$

Using the values in Table 5-15 and including allowances for fabrication and mechanical positioning errors, we obtain the minimum chamber (inner) half-apertures:

HER: $\mathrm{BSC}_x \times \mathrm{BSC}_y = 45\ \mathrm{mm} \times 25\ \mathrm{mm}$

LER: $\mathrm{BSC}_x \times \mathrm{BSC}_y = 40\ \mathrm{mm} \times 25\ \mathrm{mm}$

The HER chamber dimensions can be accommodated by the present PEP magnets.

Table 5-15. Parameters used to evaluate vacuum chamber dimensions for the high- and low-energy ring arcs.

Beam parameter	HER	LER
Max. uncoupled horizontal emittance, ε_{x0} [nm]	100	200
Max. fully coupled vertical emittance, ε_{y0} [nm]	50	100
Max. horizontal beta in arcs, $\widehat{\beta_x}$ [m]	25.6	26
Max. vertical beta in arcs, $\widehat{\beta_y}$ [m]	32.9	26
Max. dispersion, $\widehat{D}$ [m]	1.86	0.7
Max. energy spread, σ_E / E	1×10^{-3}	1×10^{-3}
Horizontal closed-orbit allowance, COD_x [mm]	10	10
Vertical closed-orbit allowance, COD_y [mm]	5	5

It is worth noting that the corresponding conductances of a section of beam pipe of the above dimensions are 35 L/s per meter and 30 L/s per meter for the high- and low-energy rings, respectively. These relatively small values have a considerable influence on the choice of pump sizes and locations, as discussed below.

5.2.3 Synchrotron Radiation and Vacuum

As mentioned earlier, two design issues follow from the copious production of synchrotron radiation in a high-intensity storage ring: (i) heating of the vacuum chamber walls owing to the high thermal flux density and (ii) radiation-induced gas desorption (both photodesorption and thermal desorption). In this section, we quantify these effects and evaluate their impact on collider performance. As we shall see, despite the difficulties associated with the high beam currents in the B Factory storage rings, handling the large synchrotron radiation power is amenable to standard engineering solutions in a beam chamber of elliptical cross section, without requiring a more exotic approach based on an antechamber design.

5.2.3.1 Wall Heating. At the design luminosity of $3 \times 10^{33}\ \mathrm{cm^{-2}\ s^{-1}}$, each ring will contain a beam current more than an order of magnitude higher than that typical in existing high-energy storage rings; the associated heat load is, therefore, quite high. The technical difficulty is not the total synchrotron radiation power per se, but rather the linear thermal flux. Thus, contrary to intuition, a small-circumference ring is more difficult to cool and pump than a large ring. Were a very small circumference to be chosen for the LER, thermal management would be considerably more difficult than in

the HER, despite the fact that the total synchrotron radiation power would be considerably lower in the LER. By adopting a design in which the LER has a circumference equal to that of the HER, such concerns are eliminated (except for the damping wiggler regions). For this reason, our estimates in this section will focus on the parameters of the HER. The wiggler section of the LER lattice is discussed in Section 5.2.6, below.

To estimate the heat load, we start from the well-known expression [Sands, 1970] for the synchrotron radiation power (in kW) emitted by an electron beam in uniform circular motion:

$$P_{SR} = \frac{88.5\, E^4 I}{\rho} \tag{5-8}$$

where E is the total energy (in GeV), I is the total beam current (in A), and ρ is the bend radius of the dipoles (in meters). The linear power density (in W/cm) radiated along the circumferential path length is given by

$$P_L = \frac{10 P_{SR}}{2\pi\rho} = \frac{885\, E^4 I}{2\pi\rho^2} \tag{5-9}$$

For a 9-GeV beam in the HER (ρ = 165 m) at the maximum allowable current of 3 A, we find from Eq. 5-9 a linear power density of P_L = 102 W/cm. At the nominal operating current of 1.48 A (corresponding to the design luminosity of 3×10^{33} cm^{-2} s^{-1}), the linear power density is reduced to 51 W/cm.

In reality, the arcs are not exactly circular in either ring—the dipoles in each cell are connected by short straight sections a few meters in length. These straight regions serve to spread out the radiation flux. Consequently, Eq. 5-9 gives the worst-case value of the linear power density anywhere in the ring. For the purposes of designing the cooling system, we have used this worst-case value at the maximum allowable current. Thus, we have ample reserve cooling capacity at the nominal operating current.

The vertical (half) angular spread (in radians) of the synchrotron radiation fan containing ~85% of the radiation is given approximately by

$$\psi \approx \frac{m_0 c^2}{E} = \frac{1}{\gamma} \tag{5-10}$$

which, for a 9-GeV beam, is ψ = 0.06 mrad. Although it is not strictly true (see Section 5.2.6), we assume the power to be uniformly distributed over this angular extent. Including the finite size and angular divergence of the electron beam, the height of the vertical band illuminated by the synchrotron radiation fan is

$$h = 2\left[\sigma_y^2 + d^2\left(\sigma_{y'}^2 + \psi^2\right)\right]^{1/2} \tag{5-11}$$

where σ_y is the rms beam height, $\sigma_{y'}$ is the rms angular spread, and d is the tangential distance from the beam orbit to the chamber wall. The value for d can be easily calculated from the geometry shown in Fig. 5-38, where $w/2$ is the transverse distance from the beam orbit to the outer wall of the vacuum chamber:

$$d = \sqrt{\left(\rho + \frac{w}{2}\right)^2 - \rho^2} \tag{5-12}$$

For the HER, with a chamber of half-width equal to 4.5 cm and a 165-m bending radius, we obtain $d = 3.85$ m, with a maximum angle of incidence given by $\alpha = d/\rho = 23$ mrad.

To be conservative in estimating the power density, we have ignored the contribution to the height of the synchrotron radiation fan from the finite beam emittance; that is, we take $\sigma_y = \sigma_{y'} = 0$ in Eq. 5-11, and we assume that all the radiation falls between $\pm\psi$. Thus, the height of the illuminated strip is $h = 2\psi d = 0.44$ mm. The corresponding maximum thermal flux density at a beam current of 3 A is then $P_A = P_L/h = 2.3$ kW/cm^2. If need be, this value could be reduced by a factor of two by inclining the wall at 30°.

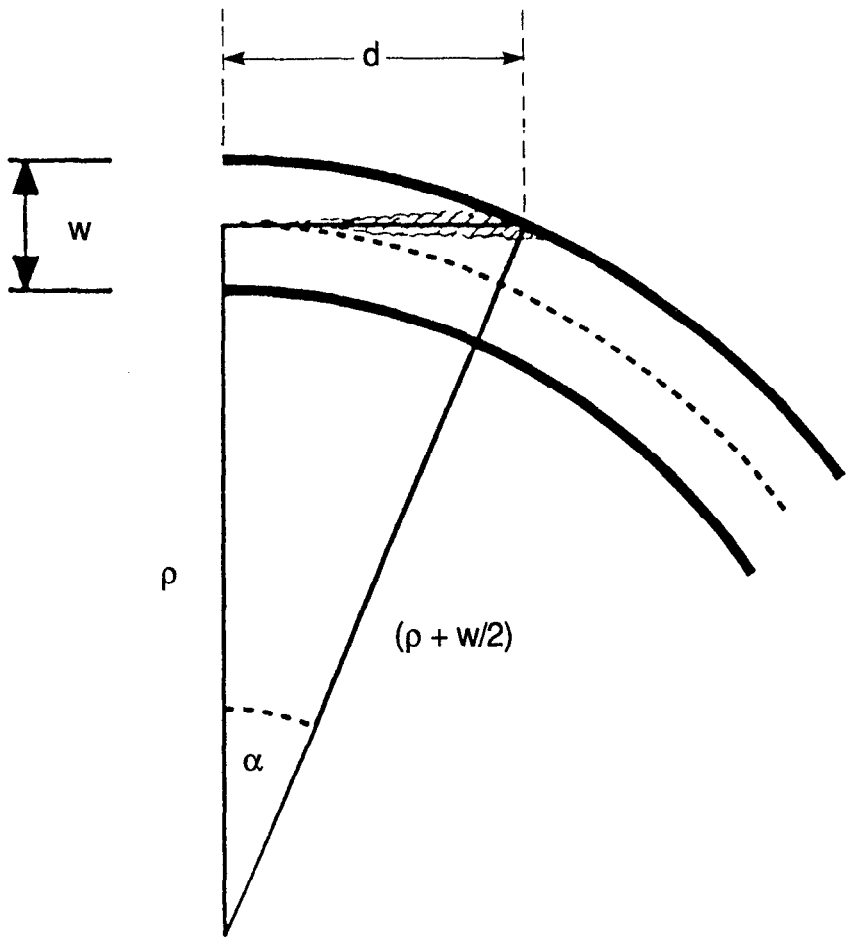

Fig. 5-38. Geometry of the synchrotron radiation fan hitting the vacuum chamber wall (not to scale).

The above estimate of power density applies to a photon beam incident on the HER vacuum chamber wall at a shallow angle ($\alpha = 23$ mrad). The worst case, however, is that of an object *normal* to the radiation fan, such as a flange or radiation mask, for which the density would increase in the ratio $\sin(\pi/2)/\sin\alpha \approx 43$, giving $P_A = 98$ kW/cm^2—a high value, but one still within the standard operating range for properly engineered masks.

Having calculated the thermal flux density produced by the synchrotron radiation, we can estimate the temperature drop ΔT across the vacuum chamber wall, using a thermal relaxation program. With this approach, it is possible to model the influence of wall thickness, fins, and cooling tubes to obtain an optimized design. Typical results for copper and aluminum chambers of simple geometry, with cooling water at 22°C, are shown in Fig. 5-39. Details of the thermal response of the HER chamber with a copper cooling bar are given in Section 5.2.4.

In addition to the synchrotron radiation heating, we must also consider the heat loads from HOM losses. These were estimated in Section 4.3.1.6 to be 400 and 800 kW for the HER and LER, respectively. This power will be distributed roughly uniformly around the ring, leading to an additional 1.8-W/cm thermal load for the HER and twice this for the LER. For the LER, this value is only about 20% of the peak synchrotron radiation load in the arcs, so HOM heating represents only a small additional burden for the cooling subsystem. In the HER, the additional heat load from HOM losses is only about 4% of that from synchrotron radiation.

Tables 5-16a and 5-16b summarize both the nominal-current and maximum-allowable-current cases for the LER and HER, respectively, compared with values from PEP. We see that the wall temperature is below the original design specification for the PEP chamber in all cases.

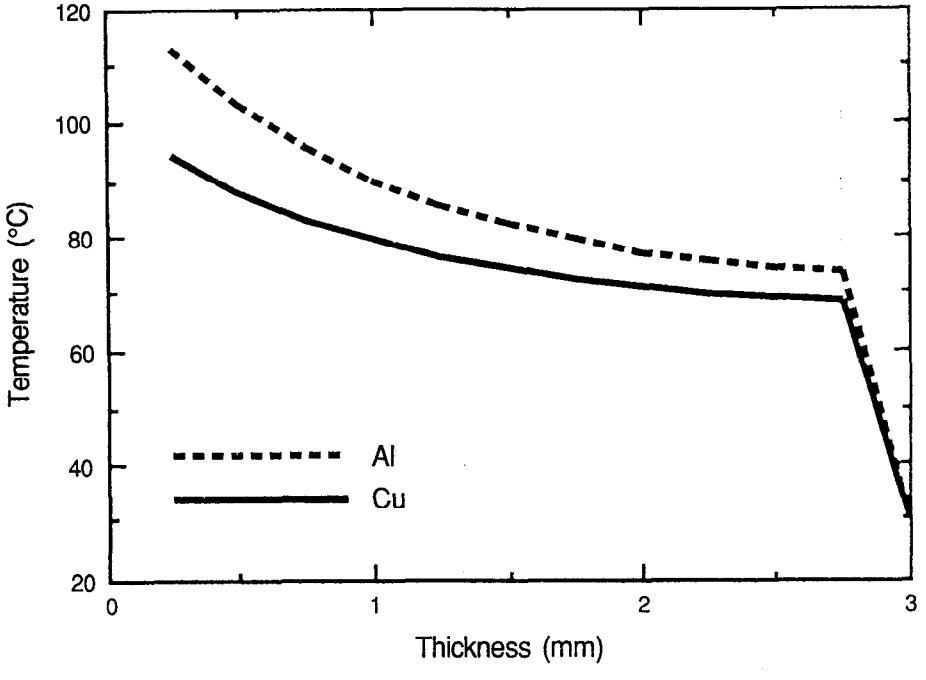

Fig. 5-39. Temperature distribution for the vacuum chamber wall, computed by a thermal relaxation code. Results for aluminum and copper are quite similar.

Table 5-16a. Comparison of radiation loads and heat fluxes in PEP and the B Factory LER. For PEP an aluminum chamber is used; the B Factory estimates assume a copper chamber and are computed as described by Alexandrov et al. [1990].

Parameter	PEP	B Factory	
		LER nominal current	LER maximum current
Magnetic radius [m]	165.00	30.56	30.56
Bending magnet field [T]	0.3033	0.3395	0.3395
Energy [GeV]	15.00	3.11	3.11
Current [mA]	200	2140	3000
Power [kW]	5,436	580	812
Peak chamber wall lin. flux [W cm^{-1}]	52	21	30
Beam divergence, 2θ [mrad]	0.07	0.33	0.33
Min. tangential distance, d [m]	4.06	1.35	1.35
Max. angle of incidence, α [mrad]	24.62	44.3	44.3
Minimum beam height [mm]	0.277	0.445	0.445
Linear flux on masks at 90° [W cm^{-1}]	2130	681	955
Wall heat load [kW cm^{-2}]	1.89	0.68	0.95
Heat load on masks at 90° [kW cm^{-2}]	77	15	21
Wall thickness [cm]	0.92	1.0	1.0
ΔT across wall [°C]	61	12	21
ΔT, chamber to water [°C]	35	14	24
ΔT, total, inner wall to water [°C]	96	26	45
Inlet water temperature [°C]	22	22	22
Water temperature rise [°C]	9	2	4

Table 5-16b. Comparison of radiation loads and heat fluxes in PEP and the B Factory HER. For PEP an aluminum chamber is used; the B Factory estimates assume a copper chamber. Temperatures are illustrative for a planar geometry. Actual values appear in Fig. 5-57.

Parameter	PEP	B Factory	
		HER nominal current	HER maximum current
Magnetic radius [m]	165.00	165.00	165.00
Bending magnet field [T]	0.3033	0.1820	0.1820
Energy [GeV]	15.00	9.00	9.00
Current [mA]	200	1500	3000
Power [kW]	5,436	5,424	10,567
Chamber wall linear flux [W cm^{-1}]	52.43	50.9	101.92
Beam divergence, 2θ [mrad]	0.07	0.11	0.11
Tangential distance, d [m]	4.06	3.85	3.85
Angle of incidence, α [mrad]	24.62	23.4	23.4
Beam height [mm]	0.277	0.44	0.44
Linear flux on masks at 90° [W cm^{-1}]	2130	2125	4140
Wall heat load [kW cm^{-2}]	1.89	1.14	2.29
Wall thickness [cm]	0.92	1.0[a]	1.0[a]
ΔT across wall [°C]	61	36	73
ΔT, chamber to water [°C]	35	31	62
ΔT, total, inner wall to water [°C]	96	67	135
Inlet water temperature [°C]	22	22	22
Water temperature rise [°C]	9	6	13

[a]Consists of 0.5 cm Cu-Sn wall, plus 0.5 cm pure Cu cooling bar.

5.2.3.2 Gas Desorption. The gas load in electron storage rings arises from two processes: thermal outgassing and synchrotron-radiation-induced photodesorption. Thermal outgassing is common to all vacuum systems and occurs in the absence of synchrotron radiation; that is, it contributes mainly to the base pressure of a ring in the absence of circulating beam. In all high-energy electron storage rings, thermal outgassing is negligible when compared with the dynamic gas load from photodesorption. Thus, the dynamic gas load due to synchrotron radiation actually determines the operating pressure of the ring.

To estimate the desorption rate, we follow the approach of Gröbner et al. [1983]. After taking the spectrum of the synchrotron radiation photons into account, we can express the photon flux in the spectral interval $(0, x)$ in the form

$$\dot{N}(x) = \frac{\sqrt{3}\, r_e}{e\hbar c} F(x)\, E\, I \tag{5-13}$$

where

$$x = \frac{\varepsilon}{\varepsilon_{\text{crit}}} = \frac{\varepsilon}{\left(\frac{3\hbar c}{2}\right)\left(\frac{\gamma^3}{\rho}\right)} \tag{5-14}$$

with ε being the photon energy and $\varepsilon_{\text{crit}}$ being the critical energy of the radiation in the dipoles. In practical units,

$$\varepsilon_{\text{crit}} = 2.218\, \frac{E^3}{\rho}\ [\text{keV}] \tag{5-15}$$

$F(x)$ is the integral over the modified Bessel function:

$$F(x) = \int_0^x \int_u^\infty K_{5/3}(y)\, dy\, du \tag{5-16}$$

For large values of x, $F(x) \rightarrow 5.23$. After rearranging terms and inserting appropriate values for the constants, we obtain a photon production rate of

$$\dot{N} = 8.08 \times 10^{20}\, E\, I\ [\text{photons/s}] \tag{5-17}$$

where E is in GeV and I is in A.

At the design current of 1.48 A, the synchrotron radiation load in the HER is 1.1×10^{22} photons per second, or a maximum of 1.0×10^{19} photons/s/m. As the height of the synchrotron radiation fan in the HER is only 0.44 mm, the maximum photon flux on

the walls is 2.4×10^{18} photons/cm^2/s. For later use in computing the photon dose on the chamber walls, we note that in the HER 1 A hr corresponds to 2.5×10^{22} photons/m.

Gas molecules are desorbed from the walls in proportion to the photon flux; that is, the number of molecules produced per incident photon is

$$\dot{N}_{\mathrm{Mol}} = 8.08 \times 10^{20}\, E\, I\, \eta \ \ [\mathrm{molecules/s}] \tag{5-18}$$

The ideal gas law relates the number of molecules to a gas load in Torr·L via a conversion factor of 3×10^{-20} Torr·L/molecule. In these units, the effective gas load due to photodesorption is found to be

$$Q_{\mathrm{gas}} = 24.2\ E\, I\, \eta\ [\mathrm{Torr \cdot L/s}] \tag{5-19}$$

The photodesorption coefficient η is a property of the chamber that depends on several factors:

- Chamber material
- Material fabrication and preparation
- Amount of prior exposure to radiation
- Photon angle of incidence
- Photon energy

In light of these complexities, it seems better to regard η as an effective engineering value that accounts for the differential illumination of the chamber walls by both direct (beam-produced) and diffusely scattered (secondary) photons, rather than considering the photodesorption coefficient to be a fundamental material property. Using a single value of η in Eq. 5-19 yields only a rough estimate of the actual dynamic gas load but one that is nonetheless useful in setting the scale of the engineering task, as well as in choosing the chamber material.

5.2.3.3 Choice of Chamber Material. Experimental measurements of η [Gröbner et al., 1983; Foerster et al., 1990; Ueda et al., 1990; Mathewson et al. 1990] for well-exposed samples of aluminum, stainless steel, and oxygen-free, high-conductivity copper indicate minimum values of η ranging from less than 2×10^{-6} for copper and stainless steel up to 2×10^{-5} for aluminum. Although the gas-scattering lifetimes in storage rings with lower critical photon energies than the B Factory suggest that aluminum chambers may eventually develop an effective $\eta \approx 10^{-6}$, we believe a more reliable design procedure is to adopt copper or stainless steel as the chamber material, despite their higher cost per kilogram. Because the data of Ueda et al. indicate that clean, machined, oxygen-free copper can attain $\eta = 2 \times 10^{-6}$, we have chosen this value as the design basis. Such a low photodesorption coefficient allows us to design the B Factory vacuum chamber with a conventional elliptical shape instead of being driven to adopt an antechamber design that is more difficult and expensive to fabricate. The apparent cost disadvantage of copper or stainless steel vis-à-vis aluminum is more than offset by the relative simplicity of the

chamber shape, by the reduction in the amount of pumping needed, and by the shortening of the vacuum commissioning time.

As shown below, copper and stainless steel also have the considerable advantage of being fully self-shielding and thus can protect the magnets and other hardware from radiation damage caused by the hard component of the synchrotron radiation. The need for lead shielding, which would be required to accompany an aluminum chamber, is completely eliminated. In that the chamber walls are subjected to very high thermal loads, copper, with its excellent thermal conductivity, appears to be the preferred material, despite the paucity of experience in building large copper vacuum chambers.

For a copper chamber with a desorption coefficient of $\eta = 2 \times 10^{-6}$, the dynamic gas load is

$$Q_{\text{gas}} = 4.84 \times 10^{-5} \; E\,I \; [\text{Torr·L/s}] \tag{5-20}$$

In Tables 5-17a and 5-17b, we use Eq. 5-20 to estimate the gas loads in the low- and high-energy rings. Maintaining a pressure of 10 nTorr in the LER requires a total

Table 5-17a. Comparison of vacuum loads and pumping speed requirements in PEP and the B Factory LER.

Parameter	PEP	B Factory LER nominal current	B Factory LER maximum current
Gas load [Torr·L s^{-1} mA^{-1}]	5.5×10^{-6}	1.5×10^{-7}	1.5×10^{-7}
Total photon gas load [Torr·L s^{-1}]	1.1×10^{-3}	3.2×10^{-4}	4.5×10^{-4}
Assumed desorption coefficient, η	1.5×10^{-5}	2.0×10^{-6}	2.0×10^{-6}
Photon gas load [Torr·L s^{-1} m^{-1}]	1.05×10^{-6}	1.68×10^{-6}	2.35×10^{-6}
Base pressure required [nTorr]	10	10	10
Distributed pumping [L m^{-1} s^{-1}]	105	–	–
Total distributed pumping [L s^{-1}]	109,080	–	–
Thermal desorption coef. [Torr·L cm^{-2}]	1.0×10^{-11}	1.0×10^{-11}	1.0×10^{-11}
Calculated wall temperature [°C]	123	89	115
Thermal desorption [Torr·L $°C^{-1}$ cm^{-2}]	8.2×10^{-11}	5.9×10^{-11}	7.7×10^{-11}
Total perimeter of ring [m]	2200	2200	2200
Calculated thermal load [Torr·L m^{-1}]	2.5×10^{-7}	1.8×10^{-7}	2.3×10^{-7}
Total calculated thermal load [Torr·L]	5.4×10^{-4}	3.9×10^{-4}	5.1×10^{-4}
Total gas load [Torr·L]	1.6×10^{-3}	7.1×10^{-4}	9.6×10^{-4}
Total pumping [L s^{-1}]	163,182	95,660	95,660

Table 5-17b. Comparison of vacuum loads and pumping speed requirements in PEP and the B Factory HER.

Parameter	PEP	B Factory HER nominal current	B Factory HER maximum current
Gas load [Torr·L s^{-1} mA^{-1}]	5.5×10^{-6}	4.3×10^{-7}	4.3×10^{-7}
Total photon gas load [Torr·L s^{-1}]	1.1×10^{-3}	6.6×10^{-4}	1.3×10^{-3}
Assumed desorption coefficient, η	1.5×10^{-5}	2.0×10^{-6}	2.0×10^{-6}
Photon gas load [Torr·L s^{-1} m^{-1}]	1.1×10^{-6}	6.3×10^{-7}	1.2×10^{-6}
Base pressure required [nTorr]	10	5	10
Distributed pumping [L m^{-1} s^{-1}]	105	125	125
Total distributed pumping [L s^{-1}]	109,080	1.3×10^{5}	1.3×10^{5}
Thermal desorption coef. [Torr·L cm^{-2}]	1.0×10^{-11}	1.0×10^{-11}	1.0×10^{-11}
Calculated wall temperature [°C]	130	67	109
Thermal desorption [Torr·L $°C^{-1}$ cm^{-2}]	8.7×10^{-11}	4.5×10^{-11}	6.0×10^{-11}
Total perimeter of ring [m]	2200	2200	2200
Calculated thermal load [Torr·L m^{-1}]	2.6×10^{-7}	1.3×10^{-7}	1.8×10^{-7}
Total calculated thermal load [Torr·L]	5.7×10^{-4}	2.9×10^{-4}	3.9×10^{-4}
Total gas load [Torr·L]	1.7×10^{-3}	5.3×10^{-3}	1.0×10^{-2}
Total pumping [L s^{-1}]	166,219	1.7×10^{5}	1.7×10^{5}

pumping speed of ~64,000 L/s at the maximum allowable current of 3 A. To put this requirement into perspective, we note that it is less than 1/15 of the pumping speed (per meter of ring circumference) being installed on the ALS ring at LBL [*1–2 GeV Synchrotron Radiation Source Conceptual Design Report,* 1986]. The HER requires about three times the pumping speed of the LER, which is still much less than the ALS specifications.

5.2.3.4 Evaluation of Gas Load Profile. To proceed beyond the estimates of the previous section to an engineering design of the vacuum system, it is necessary to specify the actual distribution of radiation along the arc, $\dot{N}(s)$, taking into account the presence of short straight sections between the dipoles. Following the prescription of Alexandrov et al. [1990], we computed the distributions shown in Figs. 5-40a and 5-40b for the HER and LER, respectively.

Naively, one might think to compute the distributed gas load in the arcs by applying Eq. 5-19 directly to the profiles given in Fig. 5-40, with the adopted value of η. This procedure would, however, neglect the strong variation in η with material exposure.

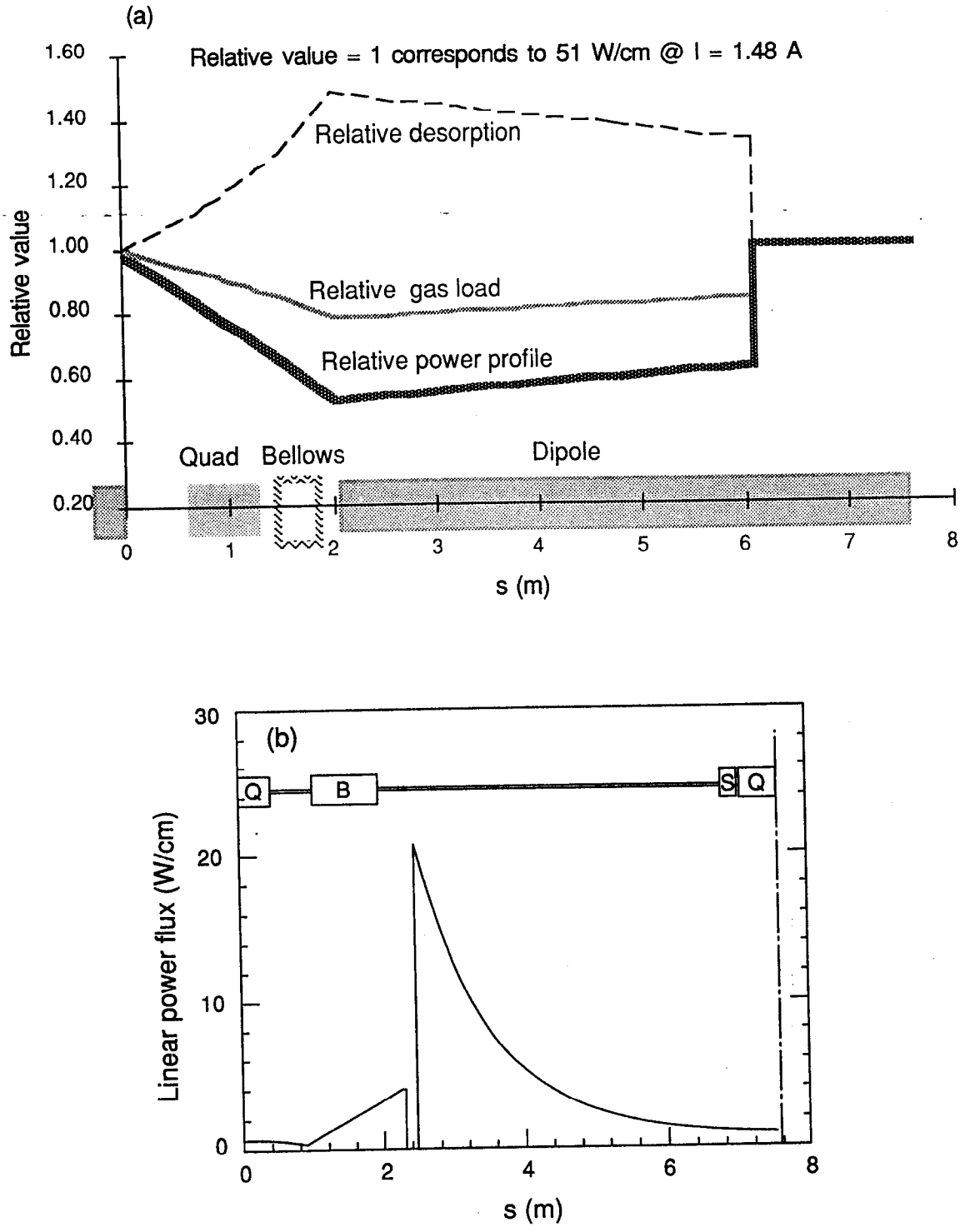

Fig. 5-40. (a) Radiation distribution along a half-cell of the HER arc at the design current of 1.48 A. (b) Radiation distribution along a half-cell of the LER arc at the design current of 2.14 A.

From a typical set of data, such as that reproduced in Fig. 5-41 [Foerster et al., 1990], we observe that, for large exposures, η tends to follow a power law dependence on dose; that is,

$$\eta \propto (It + t_0)^{-p} \tag{5-21}$$

where I is the beam current, t is the exposure time, and p is between 0.4 and 0.7 (depending on choice of material and preparation). The constant t_0 is chosen to yield the correct initial value of η. Assuming that $p = 0.6$ for copper, we can compute a local value of $\eta(s)$ along the beamline. Then the gas load at a position s is given by a generalization of Eq. 5-19:

$$Q_{\text{gas}}(s) = \eta(s)\dot{N}(s) \tag{5-22}$$

The effect of the differential exposure of the chamber is to level the gas load along the beamline and thus to require more pumping capacity than would be needed if Q_{gas} were a

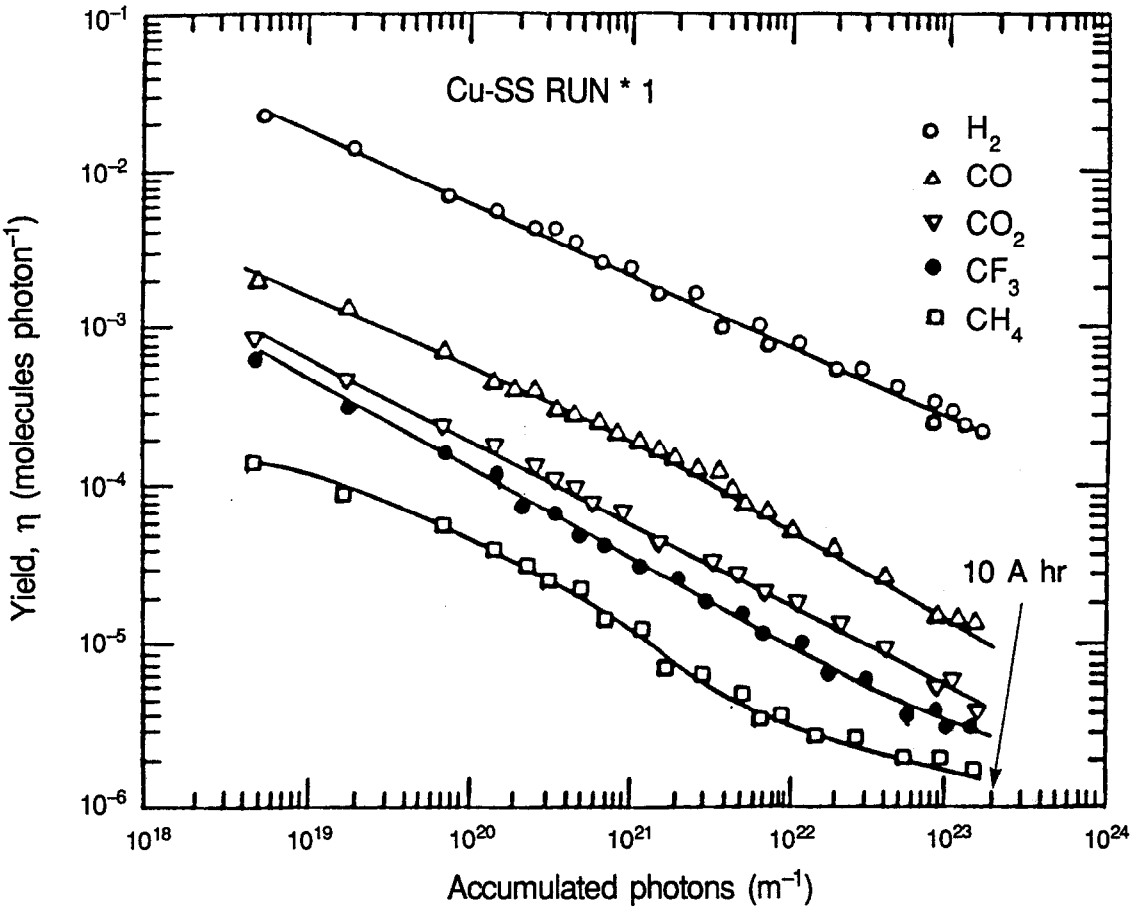

Fig. 5-41. Data from Foerster et al. [1990] showing the variation of the photodesorption coefficient η with material exposure.

constant multiple of the photon flux. By assuming that the value of η is 2×10^{-6} where $\dot{N}(s)$ assumes its *maximum* value, we compute the gas load along a half cell of the arc as shown in Fig. 5-42. This gas profile becomes a system specification for the vacuum engineer.

Using the data of Ueda et al. [1990], we have estimated that for copper with an initial desorption rate of 10^{-3} molecules/photon, the sections of the chamber will reach $\eta \approx 2 \times 10^{-6}$ after a photon exposure of about 100 A hr. Based on the pumping scheme described in Section 5.2.4 (which provides 125 L/s/m distributed in the dipoles), the vacuum-conditioning scenario can be computed as a function of the initial photodesorption rate. Such calculations are displayed in Fig. 5-43.

5.2.3.5 Validation Test Program. The data of Ueda et al., on which the above calculations are based, were taken with a photon beam incident normal to the surface and having $\varepsilon_{crit} = 4.5$ keV. In the HER, the critical energy is nearly 10 keV and photons will strike the surface at a shallow angle. The data of Foerster et al. [1990], though taken at a shallow angle, used a photon beam of $\varepsilon_{crit} = 500$ eV and were not generally carried to such large exposures as to actually observe photodesorption coefficients as low as 10^{-6}. Therefore, our design assumption of $\eta \approx 2 \times 10^{-6}$ must be viewed as an extrapolation of the experimental database. Although designing the pumping system to handle a photodesorption coefficient of roughly 2×10^{-6} from a copper chamber represents a reasonable extrapolation of that database, it is nonetheless prudent to carry out a series of validation experiments using the specific alloys, photon incidence angles, and preparation procedures that will actually be employed in the design. Fortunately, appropriate photon sources with which to make measurements on short sections of test chamber are available at several laboratories in the U.S., Europe, and Japan. We plan an experimental validation program as an essential component of the engineering design process. The experimental setup will follow closely the procedures that have been described extensively in the literature [Foerster et al., 1990; Ueda et al., 1990; Gröbner et al., 1983; Mathewson et al., 1990]. The primary quantity to be measured will be the specific pressure rise $\Delta P/I$, which is of most direct relevance to the engineering design of the B Factory vacuum system.

5.2.3.6 Shielding of Synchrotron Radiation. The HER of the B Factory, running at an energy of 9 GeV, generates the synchrotron radiation spectrum shown in Fig. 5-44a. It has been contemplated that the B Factory HER might also run at 12 GeV (though this is not part of the present design), in which case it would produce the harder spectrum shown in Fig. 5-44b. Depending upon beam pipe material and thickness, some of this radiation may escape and deposit energy in the surrounding material. This was originally pointed out during the design of PEP [Nelson et al., 1975] and subsequently verified by measurements both at PEP and at PETRA. Of most concern to the B Factory is magnet insulation, although other nearby materials, such as wire insulation and cooling-water hoses, are even more sensitive to radiation.

Radiation damage to magnets depends strongly on the type of material used in the potting compound. PEP magnets, which will be used for the HER of the B Factory, are insulated with an epoxy whose composition is given in Table 5-18 It is estimated that

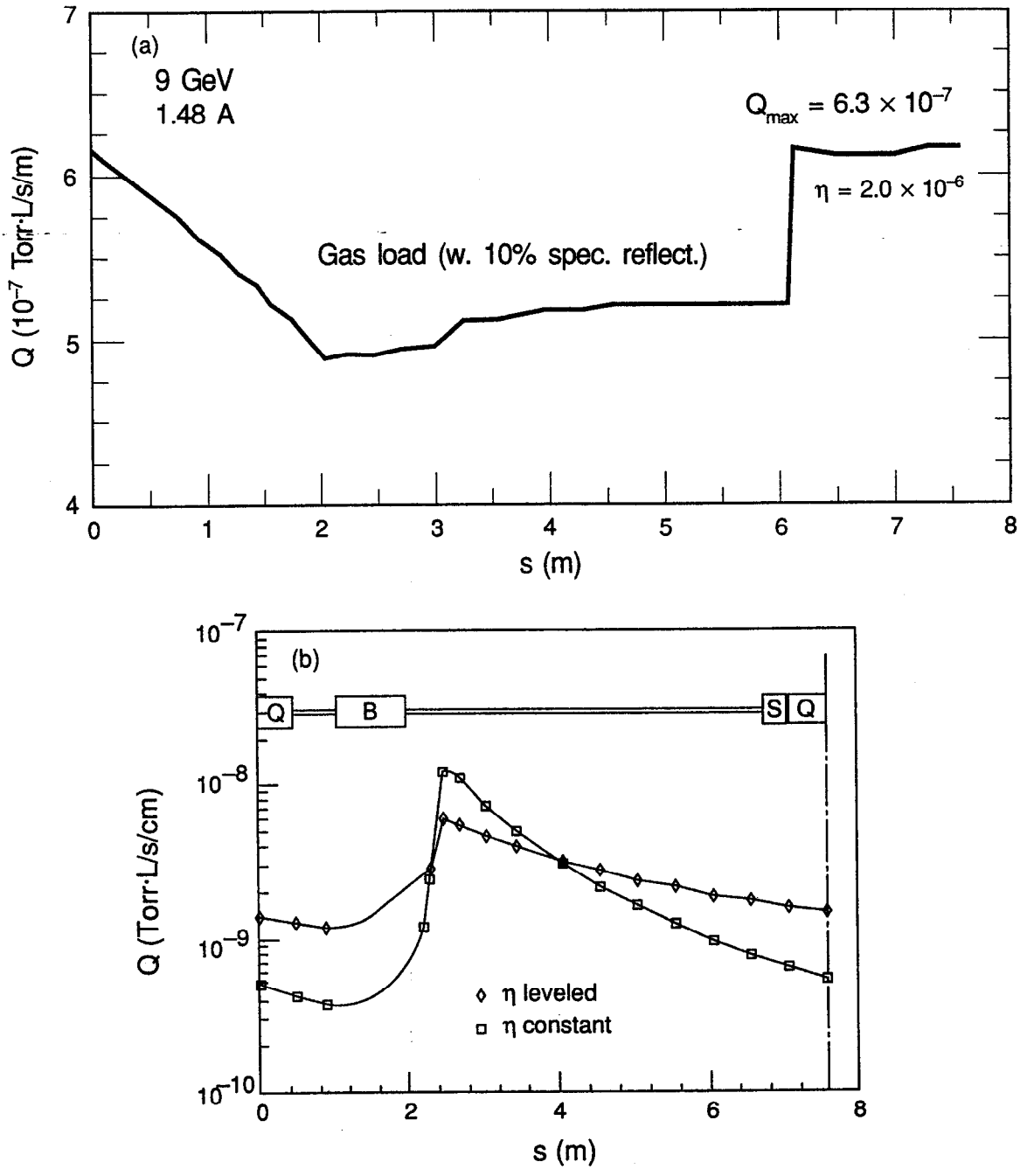

Fig. 5-42. (a) Gas load along a half cell of the arc in the HER at the design current of 1.48 A. The desorption coefficient was assumed to scale with the power profile and was normalized such that $\eta = 2 \times 10^{-6}$ molecules/photon at the location of maximum power. A contribution of 10% from reflected photons was included in the estimate of the gas load. (b) Gas load along an arc in the LER for two assumptions regarding the desorption coefficient: (i) constant value of $\eta = 2 \times 10^{-6}$ molecules/photon (squares), and (ii) "leveled" photodesorption accounting for the variation in exposure along the arc (diamonds). In the latter case, $\eta = 1 \times 10^{-6}$ at the peak power density.

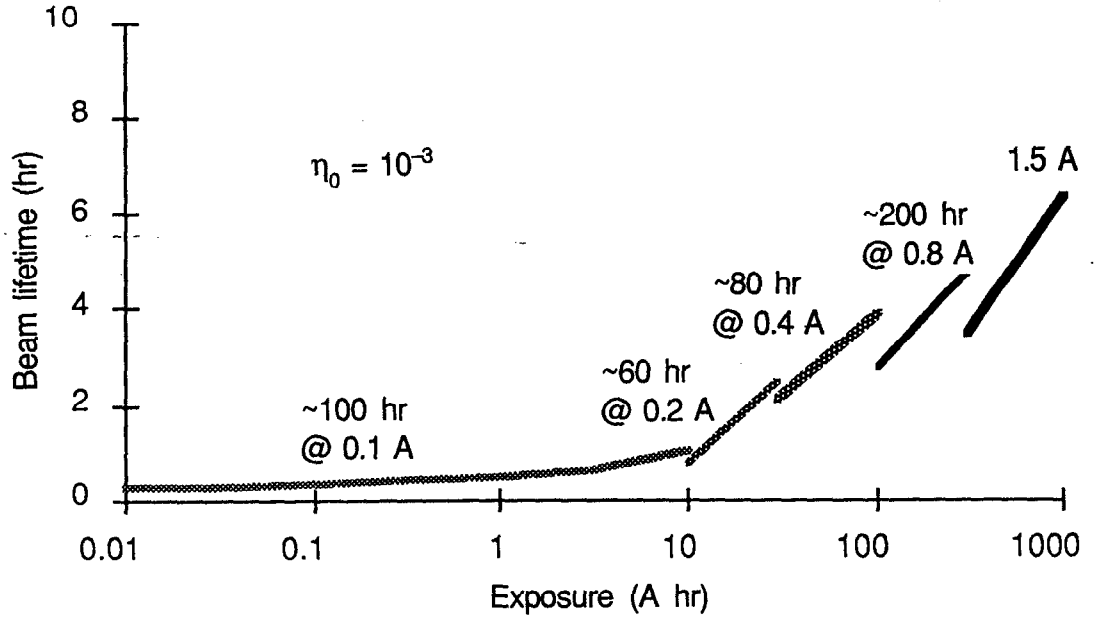

Fig. 5-43. Calculated beam lifetime in the HER as a function of exposure during initial commissioning of the collider.

this epoxy compound should tolerate doses of the order of 10^{10} rads without degradation of its properties. However, the exact damage threshold is not known, so we rely upon other sources to set a criterion. CERN used 3×10^9 rads as the dose criterion for the LEP magnets [CERN 85-02, 1985]. They note that using fiberglass insulation tape gives a factor of ten higher tolerance to radiation damage (up to the 10^{10}-rad region). To be conservative, we have elected to use 3×10^9 rads as a criterion for the B Factory magnet insulation. Stated another way, the criterion will be 10^8 rads/yr; this should give a magnet lifetime of 30 years or more. (Here, we ignore doses already received by the magnets from PEP running to date. These exposures are small compared with the doses expected from B Factory operation.)

To estimate the annual radiation dose, we take 1.48 A for a 6000-hr operating year, giving roughly 9000 A·hr/yr. The radiation strikes the wall at a 23-mrad angle of incidence. The absorbed dose D must remain below 4.9×10^{-19} rads/electron, corresponding to 10^8 rads/yr. This criterion is used when considering output from the program EGS4, which gives results *per incident electron*, either in terms of fluences, energy deposited, or rads (using appropriate conversion factors). Various user codes have been developed specifically to study such problems. These codes all generate the synchrotron radiation spectrum both analytically and from a sampling algorithm, with scoring done in the regions outside the beam pipe. A fluence-to-dose conversion, using the surface dose numbers of Rogers [1984], modified for the SLAC epoxy compound, is performed within the code each time the epoxy region is entered. Details of the calculations can be found in Jenkins et al. [1990].

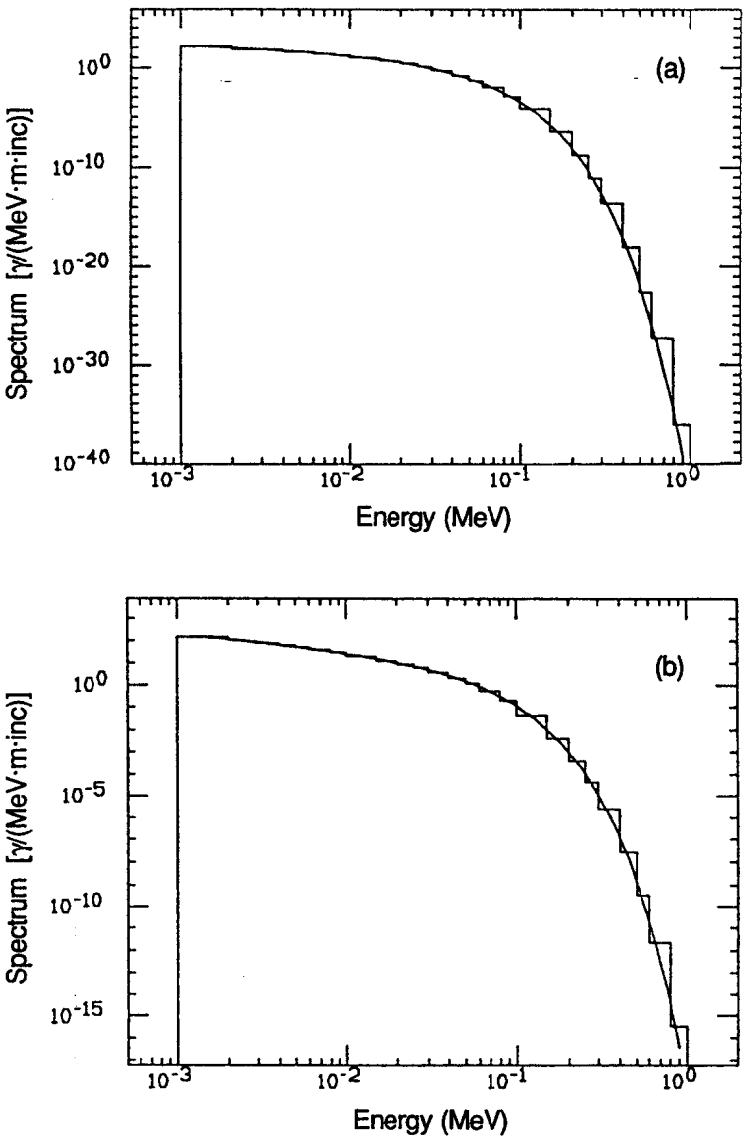

Fig. 5-44. Synchrotron radiation spectrum produced by (a) 9-GeV operation at PEP and (b) 12-GeV operation at PEP; solid line, analytic; histogram, EGS sampled spectrum.

Table 5-18. Chemical makeup and mass of the epoxy used in the PEP magnets.

Material	Composition	Mass[a] (g)
DER 332—epichlorohydrin + bisphenol A	$C_{21}H_{24}O_4$	851
DER 732—epichlorohydrin-polyglycol	$(C_3H_6O)_n\,C_6H_{10}O_3$	1049
NMA—nadic methyl anhydride	$C_9H_8O_3$	1832
Aluminum oxide	Al_2O_3	4252

[a]Weight fractions of the elements in the epoxy (for EGS4 purposes) are hydrogen, 2.6%; oxygen, 38.4%; carbon, 30.7%; aluminum, 28.3%.

Calculations are based on the configuration of the present PEP ring, assuming a maximum energy of 12 GeV and a nominal energy of 9 GeV. Only the HER is considered; synchrotron radiation will not penetrate the beam pipe of the LER, which runs at 3.1 GeV.

For this study, a new EGS4 data set was generated, including photon energies down to 1 keV and electron energies down to 10 keV (521-keV total energy). For most calculations, however, the actual cutoffs used were 10 keV (photons) and 1 MeV (electrons). Upper energies for both electrons and photons were 10 MeV, which is adequate because the spectra are essentially zero above a few MeV for both the 9- and 12-GeV electron energies. The photon spectrum was sampled uniformly within an energy range from $0.1\varepsilon_{crit}$ to $10\varepsilon_{crit}$. A weight was carried along with each photon (and its progeny) for scoring purposes. The final results were later normalized per incident beam electron.

The B Factory beam pipe geometry is similar to the existing PEP beam pipe, with some minor differences. First, the vacuum pumping channel is separate from the beam channel for most of the ring (the arc regions), with horizontal slots joining the two channels. Details of the chamber configuration are described in Section 5.2.4. The chamber material assumed for these calculations is copper; stainless steel would give essentially the same results.

A curve of the maximum dose versus copper thickness for an octagonal chamber cross section is shown in Fig. 5-45. Points for a chamber with a rectangular cross section are included for comparison. This figure shows the benefits of an octagonal geometry over a rectangular geometry, given the same wall thickness.

To summarize the results of our calculations, for an octagonal beam pipe, 0.7 cm of copper is needed at the point of maximum dose for 12-GeV operation to reach our dose criterion. For 9-GeV operation, an octagonal copper pipe need only be 0.25 cm thick. Clearly, with a copper chamber, a beam pipe 0.5 cm thick (required for structural reasons) is more than adequate, as shown in Fig. 5-46. By way of comparison, an

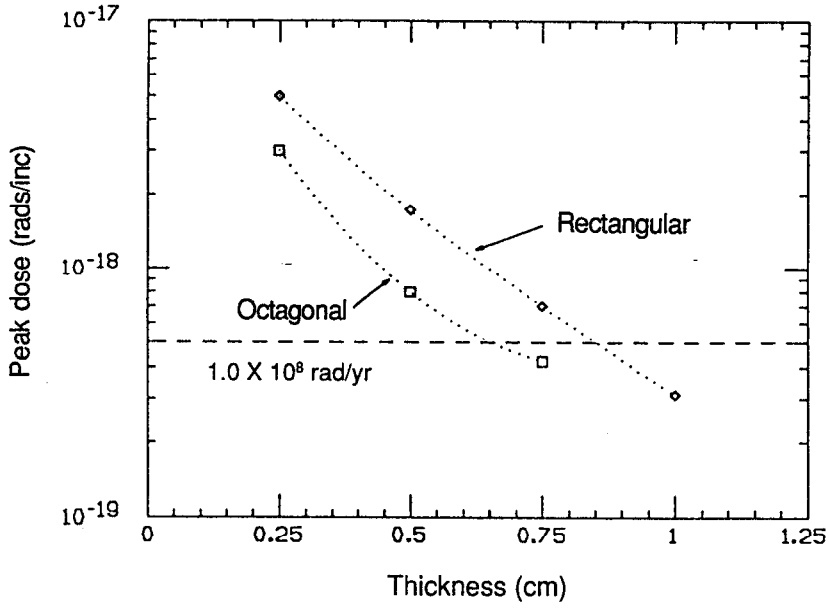

Fig. 5-45. Radiation dose to the magnet windings through a 0.5-cm-thick copper beam pipe having an octagonal cross section and a vacuum channel, computed for 12-GeV operation. A rectangular chamber of the same wall thickness does not provide as effective shielding. The dose corresponding to 1 $\times 10^8$ rads/yr is shown by the dashed line.

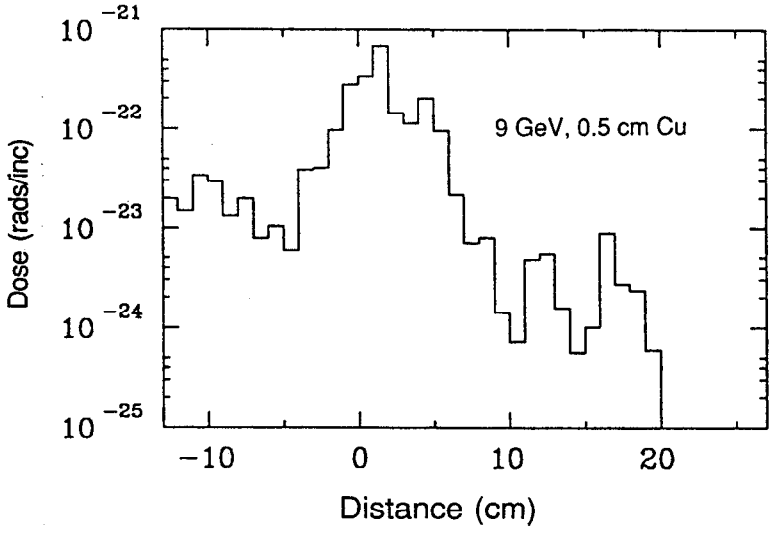

Fig. 5-46. Radiation dose to the magnet windings through a 0.5-cm-thick copper beam pipe with no liner, computed for 9-GeV operation. The radiation dose limit corresponds to 5 $\times 10^{-19}$ rads/inc electron, well above the calculated values.

octagonal aluminum chamber that is 0.5 cm thick would also need 0.3 cm of lead on the outside to reach the same dose criterion for 12-GeV operation. Even for 9-GeV operation, an aluminum pipe would require a lead liner. The liner would be needed only at the point of maximum dose (top and bottom of the beam pipe); the rest of the pipe could be thinner.

5.2.4 HER Vacuum Components

The configuration of the HER is shown schematically in Fig. 5-47. Figure 5-48 shows both the high- and low-energy rings in the tunnel, with the LER positioned above the HER. The overall circumference of the rings is 2200 m, and their geometries have been adjusted to fit in the existing PEP tunnel, as described in Section 4.1.

The vacuum system for the HER is designed to handle the large gas loads anticipated from photon-induced gas desorption and to carry away the large amount of power deposited on the outer chamber wall by the synchrotron radiation. The pressure requirements—quoted as N_2-equivalent values—were described in Section 5.2.3.

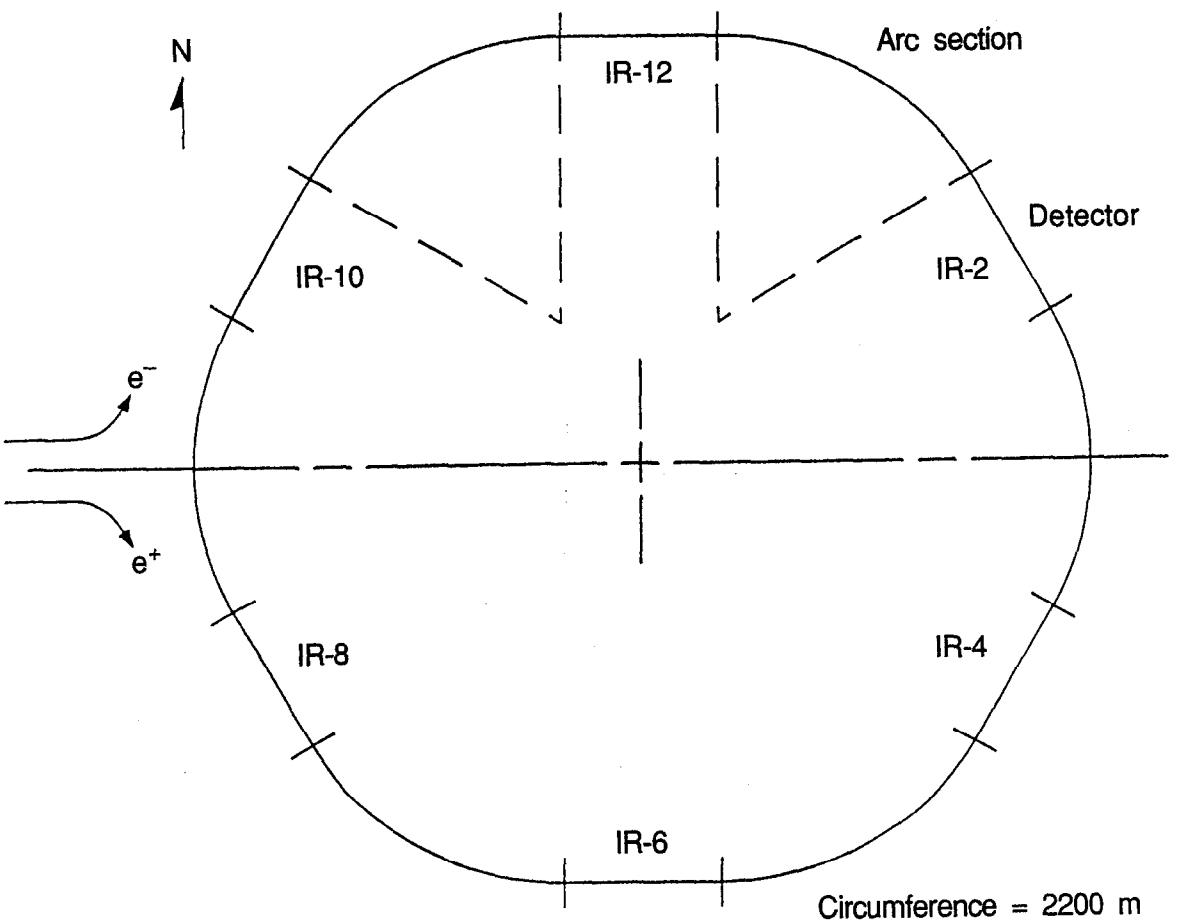

Fig. 5-47. Schematic of the B Factory storage ring layouts.

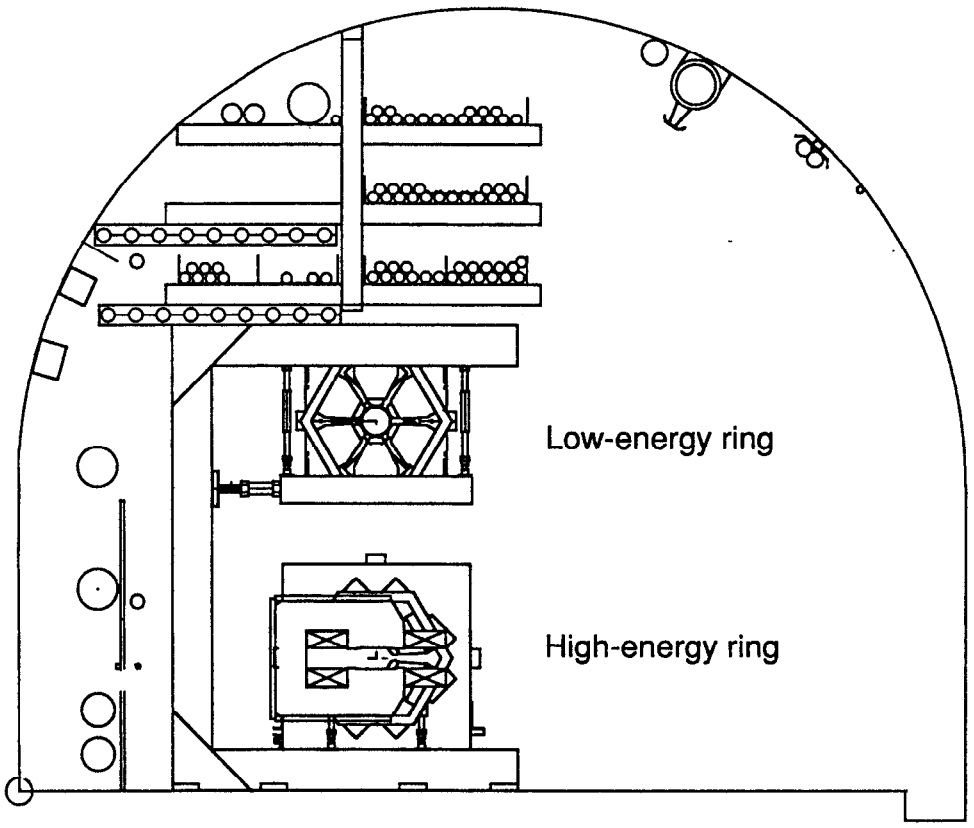

Fig. 5-48. Cross section of the PEP tunnel, showing the arrangement of the high- and low-energy rings of the B Factory.

The HER, illustrated in Fig. 5-49, contains 40 empty FODO cells grouped in 5 straight sections (the remaining straight section houses the interaction region) and 96 regular FODO cells in the arcs. As discussed above, copper was chosen for the vacuum chamber in the arcs because of its low photon-induced gas desorption coefficient, its high thermal conductivity, and its large absorption coefficient (which obviates the need for adding lead shielding). Vacuum chambers in the straight sections will be fabricated from stainless steel.

5.2.4.1 Arc Sections. Each arc section consists of 4 dispersion-suppressor cells of length 16.013 m and 12 regular cells of length 15.125 m, giving an overall arc length of 245.6 m. All-metal isolation valves are located at each end of the arc sections. The magnet arrangement in each of the regular cells consists of a defocusing quadrupole with sextupole, a dipole, a focusing quadrupole with sextupole, and finally a second dipole. The cell vacuum chamber will be constructed of extruded copper in four sections to facilitate fabrication and assembly in the PEP tunnel. Chamber sections are joined at the ends with 8-in., stainless-steel Conflat flanges; a bellows section is located in the vicinity of the focusing quadrupole.

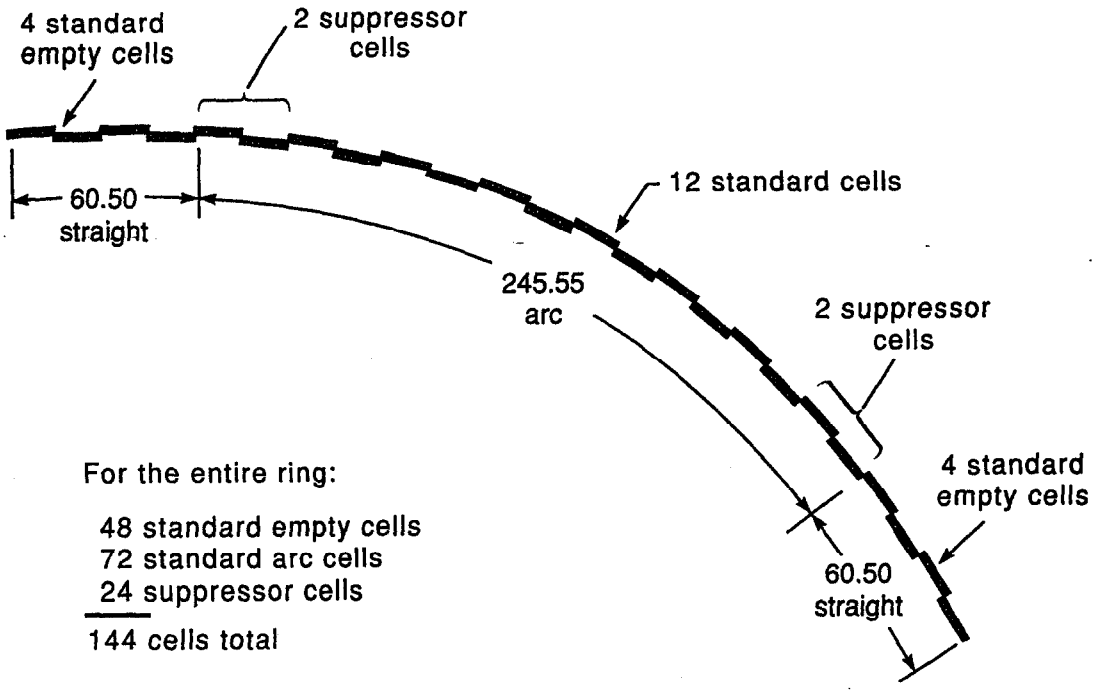

Fig. 5-49. Schematic of one sextant of the B Factory HER.

Cross sections of the vacuum chamber at the dipoles and quadrupoles are shown in Figs. 5-50 and 5-51, respectively. The beam tube of octagonal cross section is 100 mm wide (OD) by 60 mm high (OD), with a uniform wall thickness of 5 mm. The pumping channel for the distributed ion pumping has an inner size of 61 mm wide by 50 mm high. Slots in the septum between chambers are designed to provide a conductance of about 500 L/s/m. Both the beam tube and the pumping channel will be fabricated from a copper alloy having 2% tin (to maintain stiffness following an 800°C furnace braze). A cooling bar located on the outer wall of the beam tube carries away the heat produced by synchrotron radiation hitting the chamber wall. The bar will be fabricated from an oxygen-free copper alloy having a thermal conductivity of 93% International Annealed Copper Standard. Each of the quadrupoles in the arc cells has a pair of distributed ion pumps in stainless-steel housings, one located below and one to the side of the beam tube. The pumping slots between the beam tube and stainless-steel housing are arranged similarly to those in the dipoles. Lumped ion pumps are provided at each of the quadrupole spaces, as shown in Fig. 5-52; pressure gauges and pump-down connections are also located there.

5.2.4.2 Straight Sections. A standard cell in the straight sections is 15.125 m in length (as in the arcs) but contains no dipoles. The vacuum pipe is a 10-cm-diameter, stainless-steel tube of circular cross section, sized to clear the 100-mm bore of the quadrupole magnets. To produce an average pressure of less than 3 nTorr in the straight sections, lumped sputter-ion pumps rated at 230 L/s will be installed with a spacing of approximately 8 m. The pump size and spacing were calculated on the basis of a thermal

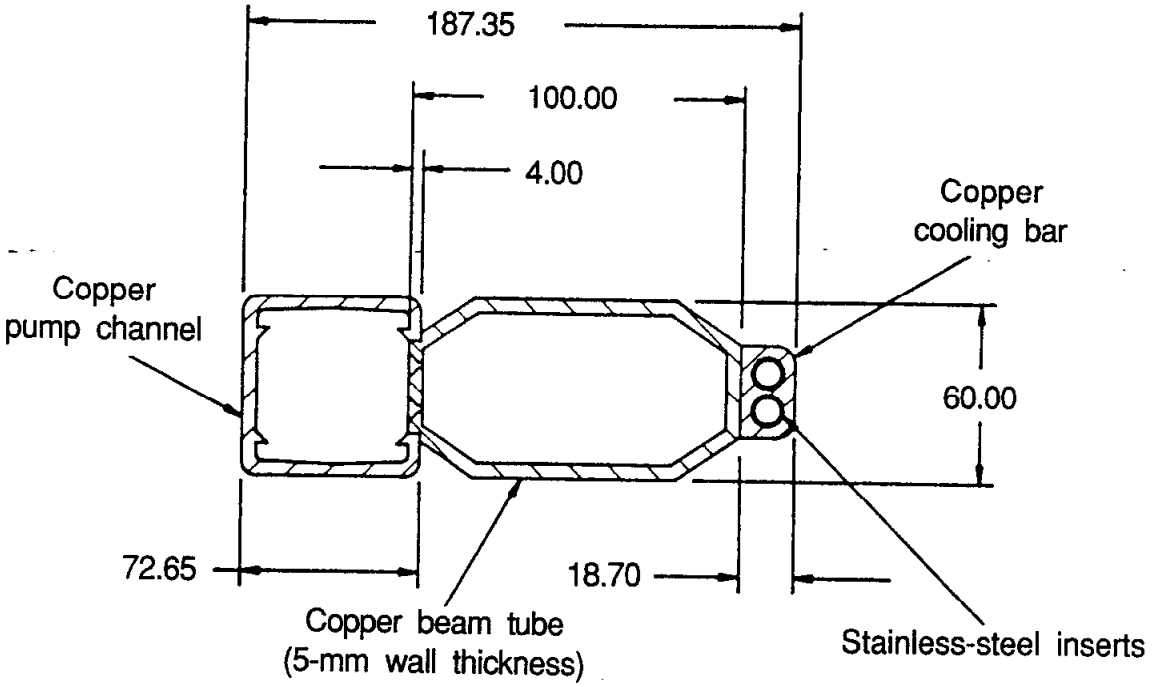

Fig. 5-50 Vacuum chamber cross section at a dipole; dimensions are in millimeters.

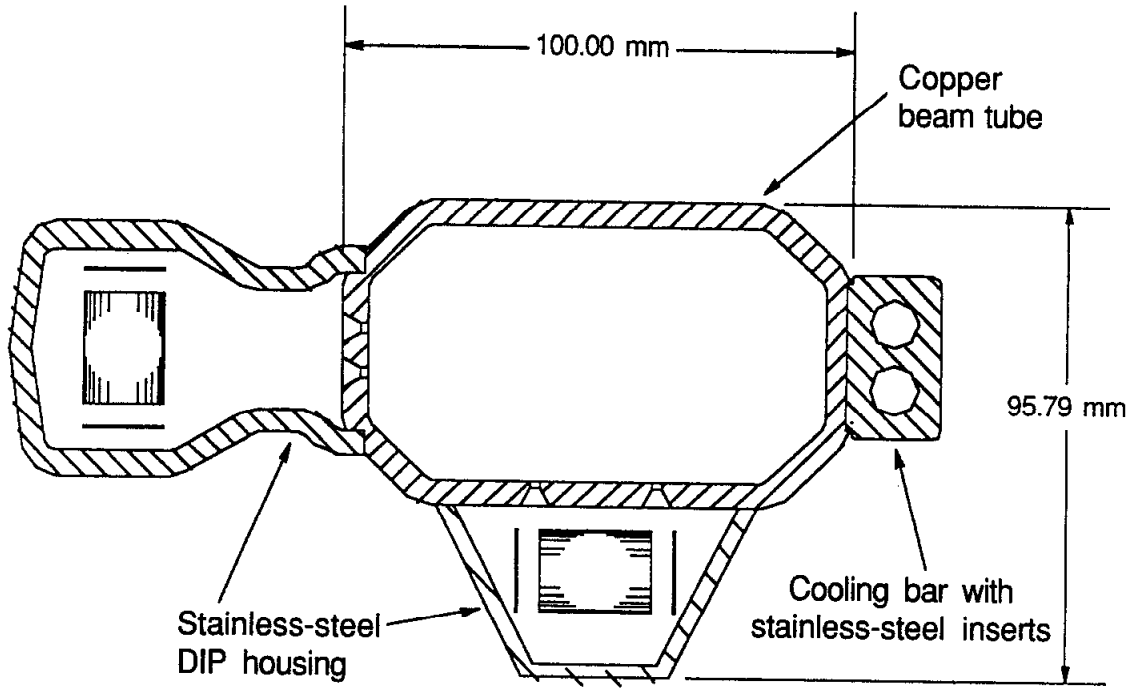

Fig. 5-51. Vacuum chamber cross section at a quadrupole (DIP, distributed ion pump).

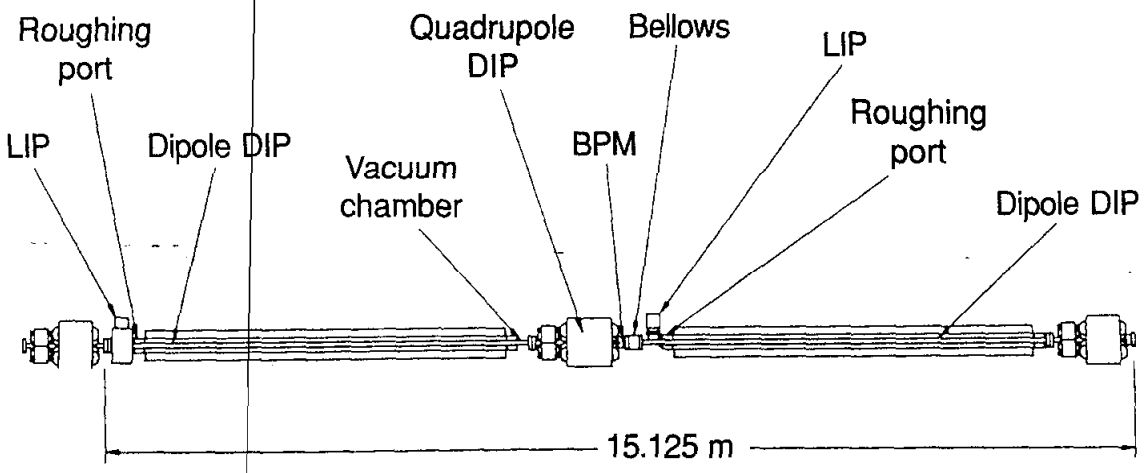

Fig. 5-52. Illustration showing locations of lumped ion pumps (LIPs) in the HER arc cells.

outgassing rate of 1×10^{-11} Torr·L cm^{-2} s^{-1} and a required base pressure in the beam tube of 0.5 nTorr. In situ baking compatibility to 300°C (150°C without opening the chambers) will be provided to reduce the initial outgassing rate and thus to allow for base pressures in the 0.1-nTorr range, should the need arise. A diagram of a straight-section cell is shown in Fig. 5-53.

5.2.4.3 Special Components. The bellows, which are designed to permit a 130°C thermal expansion, aid in the assembly of the ring. In their extended position (at room temperature), the bellows are 22.9 cm (9 in.) long, as shown in Fig. 5-54. They can compress about 4 cm at 150°C, the maximum temperature at which the ring can be baked in situ without disassembly. The inner bellows, which carries the surface currents, is fabricated as one piece, with formed convolutions in the plane of the beam tube flats; it has narrow slits at the intersecting corners to permit axial movement. To carry away the thermal load, a narrow slit at the outer beam tube wall permits synchrotron radiation to shine through to a thick-walled, water-cooled, copper absorber cantilevered from the bellows flanges.

Each arc cell contains a beam position monitor (BPM) located at, and anchored to, the defocusing quadrupole. The design chosen for the B Factory, shown in Fig. 5-55, follows the HERA design, with a few minor modifications. The housing will be accurately machined from a solid copper block. The block will have recesses on the end faces to index the beam tube ends for alignment during brazing. Cooling on both sides will preclude any temperature asymmetry.

Changes in cross section between the arc chambers of octagonal cross section and the straight section chambers of circular cross section are made with tapered transition elements. To keep the impedance contribution from the transitions low, the taper angle is less than 10°.

The system of supports for the arc cell vacuum chamber consists of a fixed support near the midpoint and flex supports at each end. Within the dipoles, slider supports are spaced at about 1.0-m intervals.

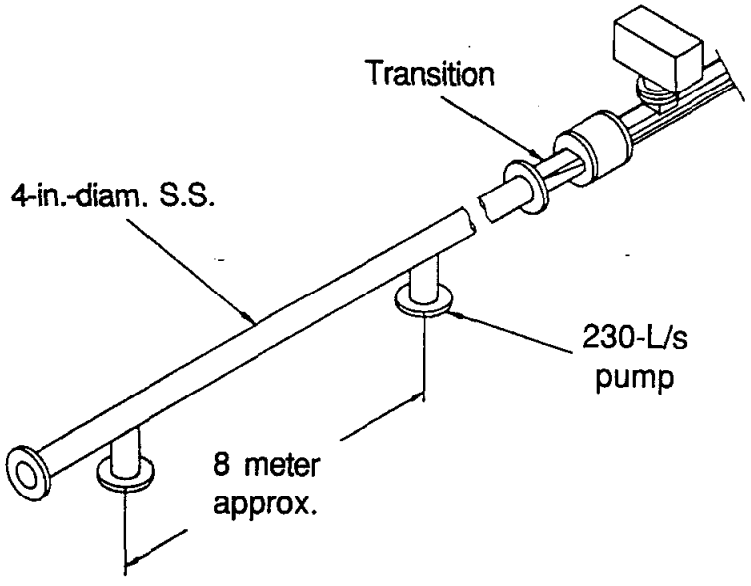

Fig. 5-53. Perspective view of straight-section vacuum chamber.

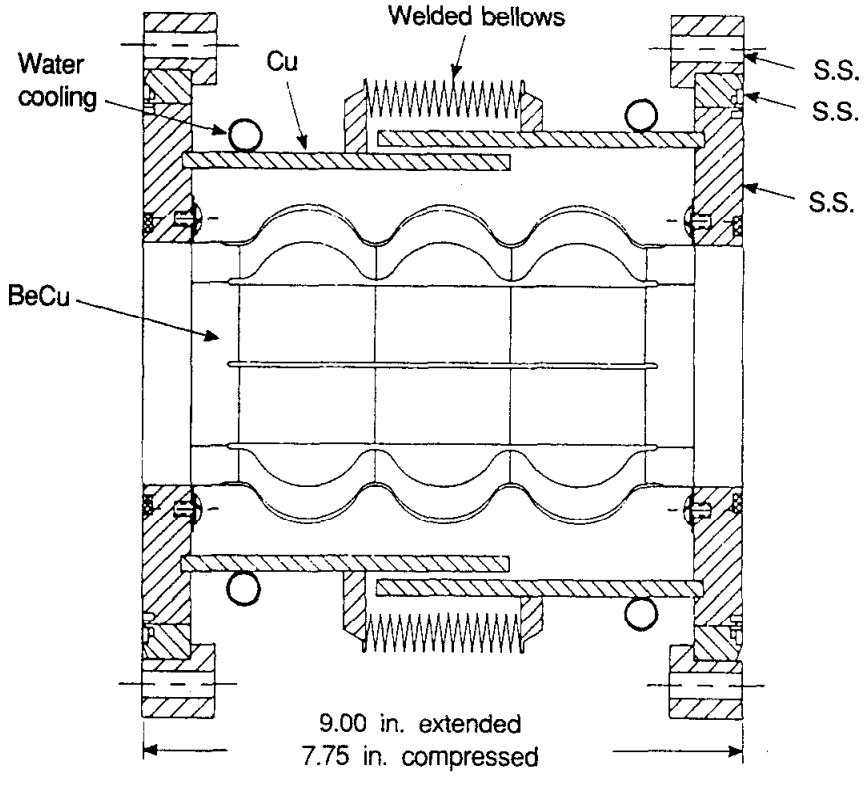

Fig. 5-54. Cross section of the vacuum chamber bellows.

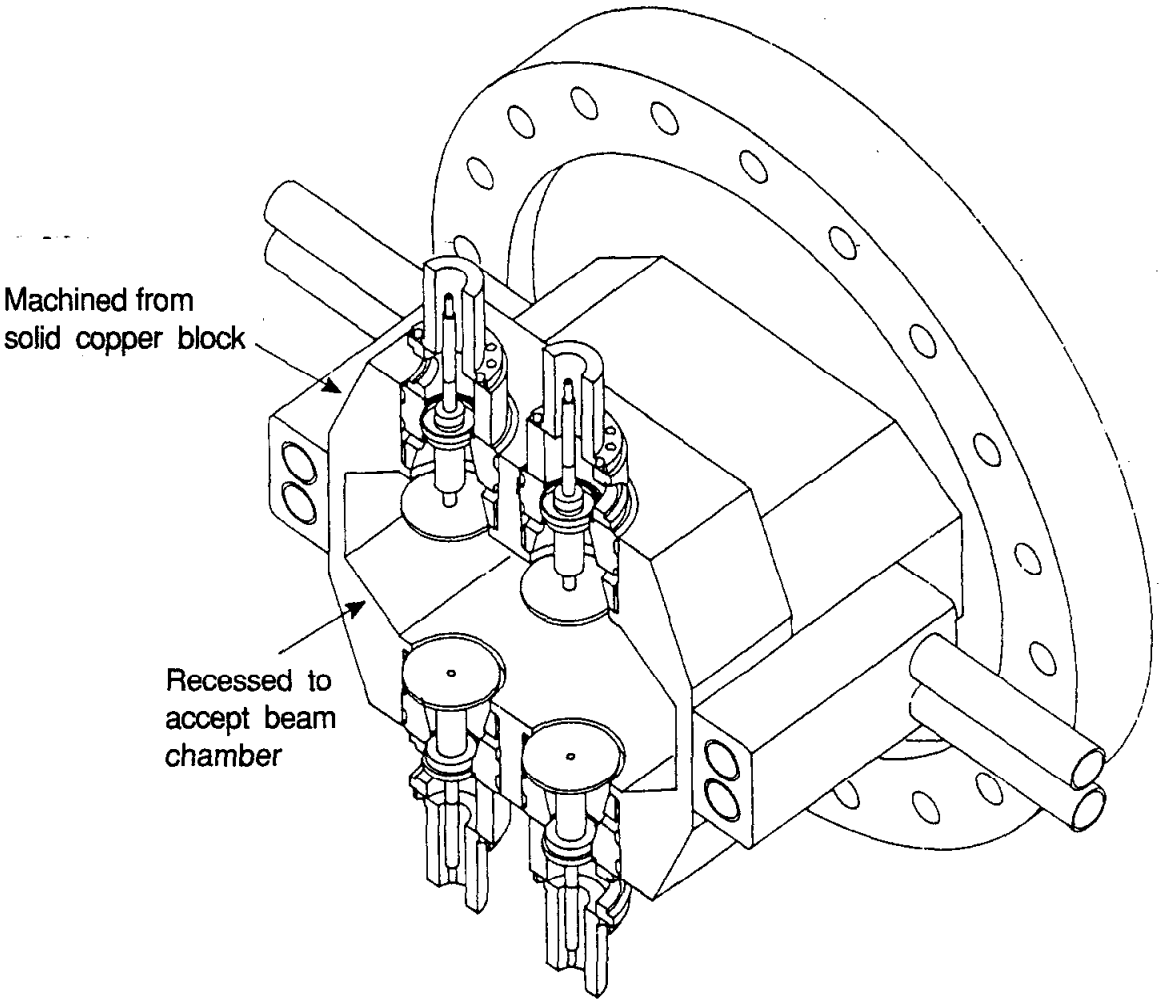

Fig. 5-55. Cutaway view of a B Factory beam position monitor.

5.2.4.4 Heat Load and Thermal Response. As described in Section 5.2.3, a maximum thermal load of 2.3 kW/cm^2 will be incident on a strip less than 0.5 mm high. A two-dimensional thermal analysis of the response of the vacuum chamber was performed using the output from EGS4 runs to specify the correct distribution of energy deposited along the interior walls of the beam tube. Examination of the EGS4 data shows that 99.9% of the energy is deposited locally at the radiation impact point. Figure 5-56 shows that the maximum temperature produced in the beam pipe wall is 160°C. In this calculation, the water in the cooling tubes enters at 30°C and flows with a velocity of 3 m/s. The two-dimensional stress analysis displayed in Fig. 5-57 shows a maximum thermal stress of 90 MPa, which exceeds the yield stress of the copper-tin alloy. We note that the major stress component occurs along the chamber length (perpendicular to the cross section), because in our calculation the thermal stress was not allowed to be

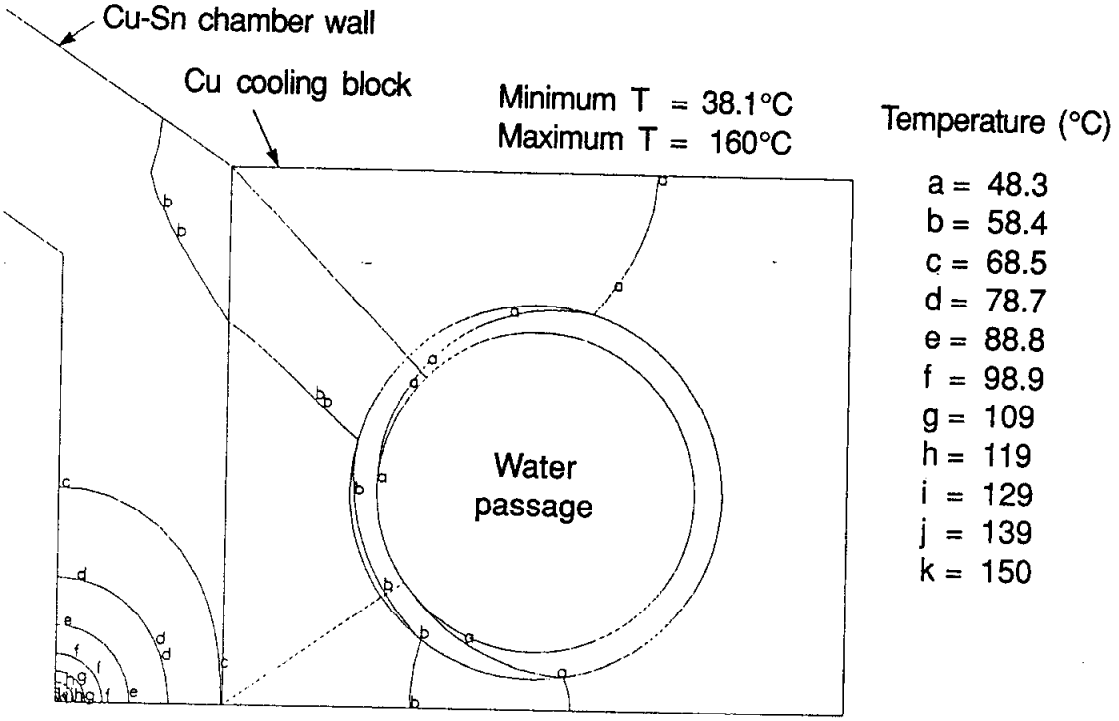

Fig. 5-56. Computed temperature distribution in the beam pipe wall and cooling bar of the B Factory HER.

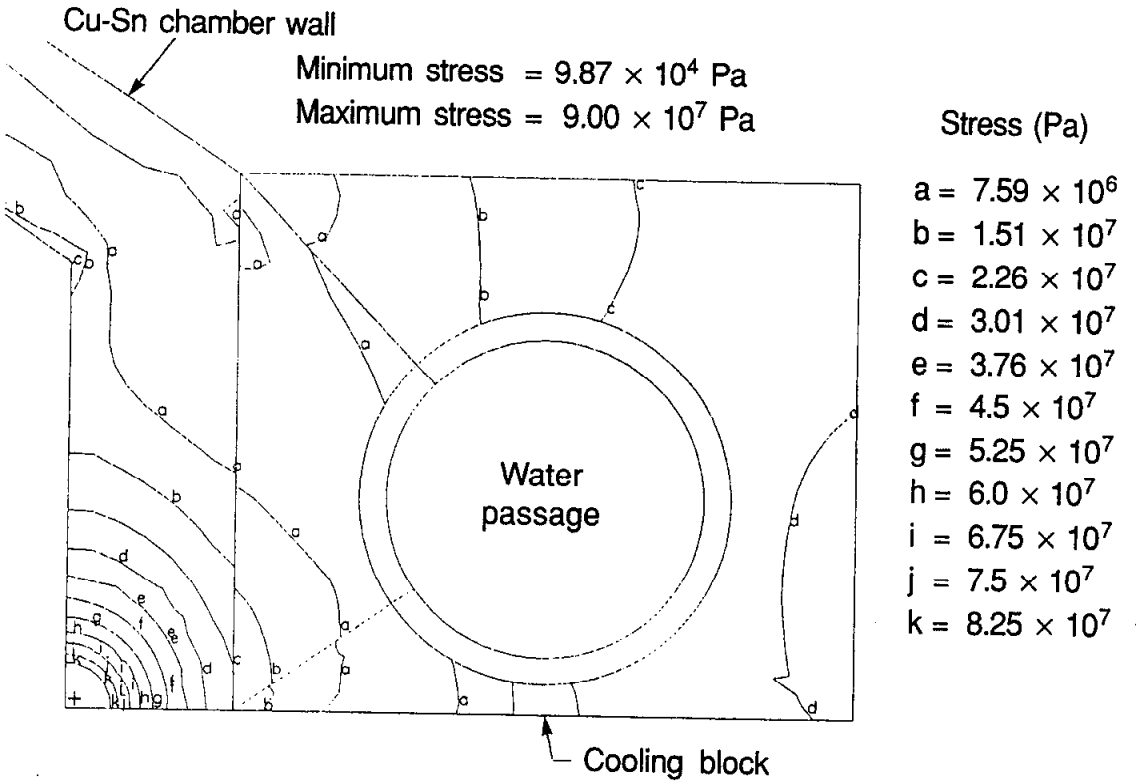

Fig. 5-57. Computed effective stress in the beam pipe wall and cooling bar of the B Factory HER.

relieved by expansion in that direction. Figure 5-58 shows that the maximum effective plastic strain is 0.1%. It is confined to the small area of synchrotron radiation impact and is not seen as a problem. Both these results were obtained using a two-dimensional plane-strain model with the thermal stress problem being started at the average steady-state cross section temperature. That is, the length was allowed to accommodate the average temperature of the cell because of the bellows. This calculation is overly conservative, since it does not account for the stress relief that will be obtained through bending. We therefore believe that the copper-tin alloy will actually have sufficient yield strength for the thermal load imposed by the radiation. Indeed, calculations done at CERN indicated that copper-tin alloy can tolerate more than twice the thermal stress to be encountered at the B Factory [Nakada, 1990].

A three-dimensional analysis is being made to evaluate the effects of bending. If the three-dimensional results also indicate that the material yields, a cyclic fatigue analysis will be made to determine if there is a structural problem. Examining the deflections of the structure in Fig. 5-59, we see that a maximum vertical deflection of 0.023 mm occurs in the horizontal flat faces of the beam tube, which is acceptable. Figure 5-60 shows the displaced shape, with vertical displacements multiplied by 100 for visibility.

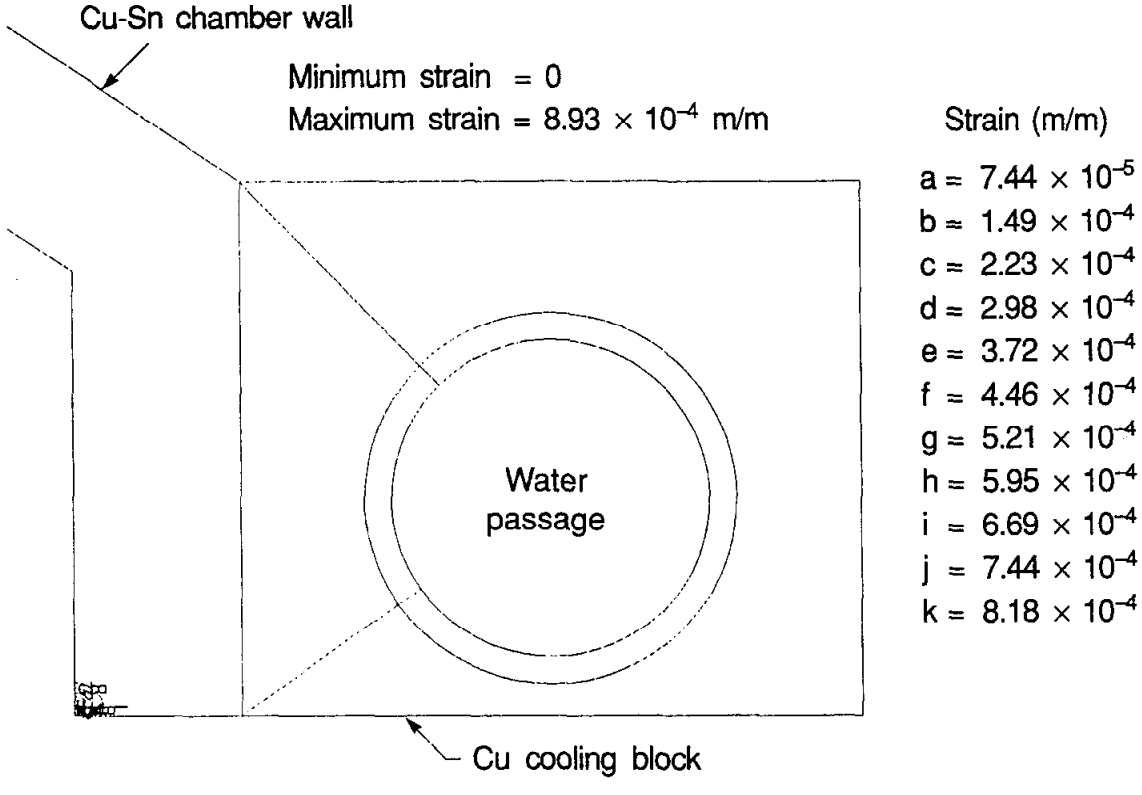

Fig. 5-58. Computed plastic strain in the beam pipe wall of the B Factory HER.

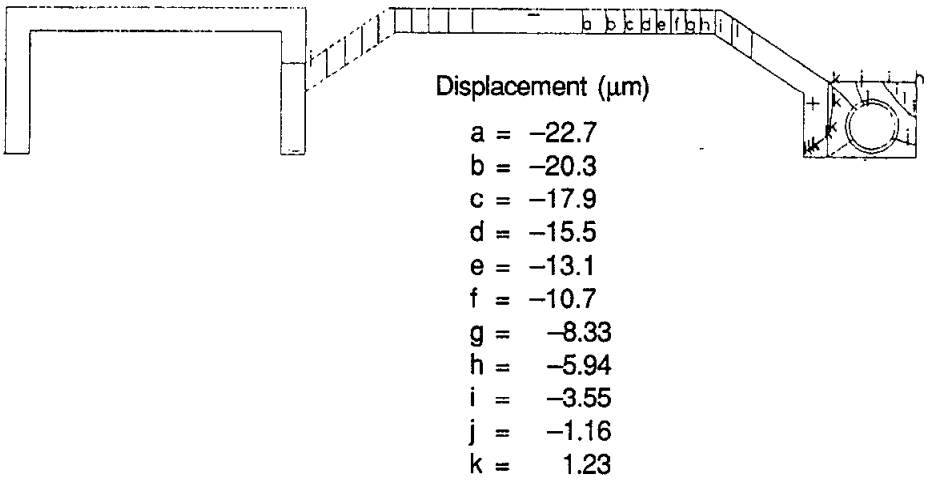

Fig. 5-59. Vertical deflections computed for the beam pipe wall and cooling bar of the HER, as a consequence of thermal stress.

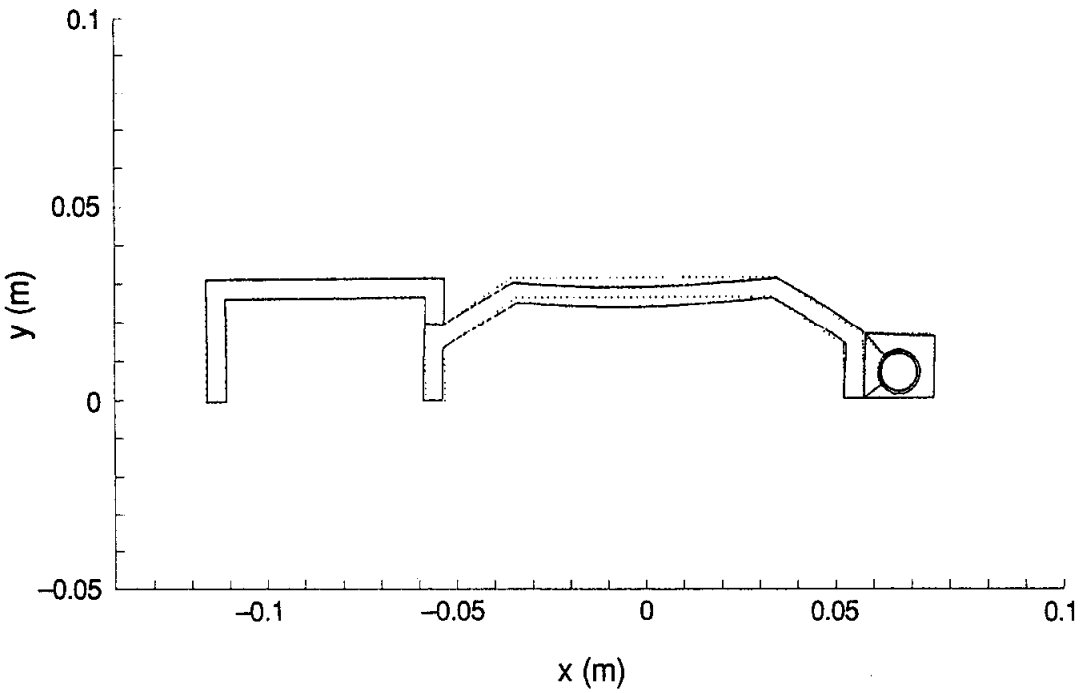

Fig. 5-60. Displaced shape computed for the beam pipe wall of the HER, as a consequence of thermal stress. The vertical scale is exaggerated by a factor of 100.

5.2.4.5 Vacuum Pumping Design. To satisfy the design criteria for adequate beam lifetime and low background rate, we chose to design the distributed pumping in the arcs to produce an average pressure of less than 5 nTorr at the nominal operating current of 1.48 A. The peak gas load corresponding to operation at the design luminosity has already been shown in Fig. 5-42.

We selected a design based entirely on sputter-ion pumps to handle this gas load. An inventory of pumping capacities for each pumping element in a typical cell is shown in Table 5-19. During 1.48-A operation, the desired average pressure (5 nTorr) can be maintained with distributed pumping of 125 L/s/m.

To achieve these pumping speeds, the distributed ion pumping in the dipoles was redesigned to operate in a 0.18-T field, about half of the 0.3-T field used normally in PEP. The anode diameter was maintained at 1.59 cm, but as seen in Fig. 5-61, an additional row has been added, increasing the number of anodes by about 50%, with a packing factor of about 90%. As mentioned, distributed ion pumping has also been included at the quadrupoles, located to one side of the beam tube and below, but not on the top, to preclude particles dropping into the beam chamber. Anode sizes for these pumps were scaled to fit into the very restrictive space available. The calculated pumping speed in the beam tube will be about 75 L/s/m from each of the stainless-steel housings shown in Fig. 5-62. However, the total pumping speeds for the defocusing and focusing quadrupoles will be different, owing to their differing magnetic lengths. To augment the distributed pumping, we have added 60-L/s lumped ion pumps in the spaces adjacent to each of the quadrupoles in the cells (see Fig. 5-52). Given the low conductance of the beam pipe, larger pumps would not improve system performance. In

Table 5-19. Available pumping in a typical cell.

2 dipole pumps at	800 L/s =	1600 L/s
1 quad pump at	110 L/s =	110 L/s
1 quad pump at	82 L/s =	82 L/s
2 LIP pumps at	60 L/s =	120 L/s
	Total =	1912 L/s
	or	125 L/s/m

For a gas load of 6.3×10^{-7} Torr·L/s/m,

P = 5.0 nTorr

For a gas load of 1.26×10^{-6} Torr·L/s/m,

P = 10 nTorr

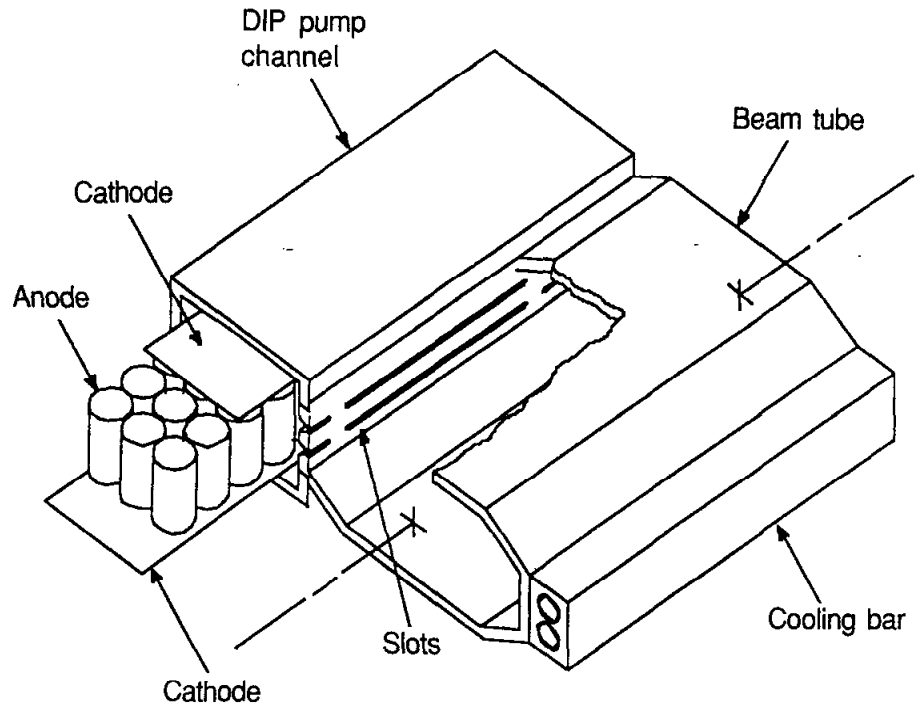

Fig. 5-61. Distributed ion pumping arrangement for the dipoles of the HER.

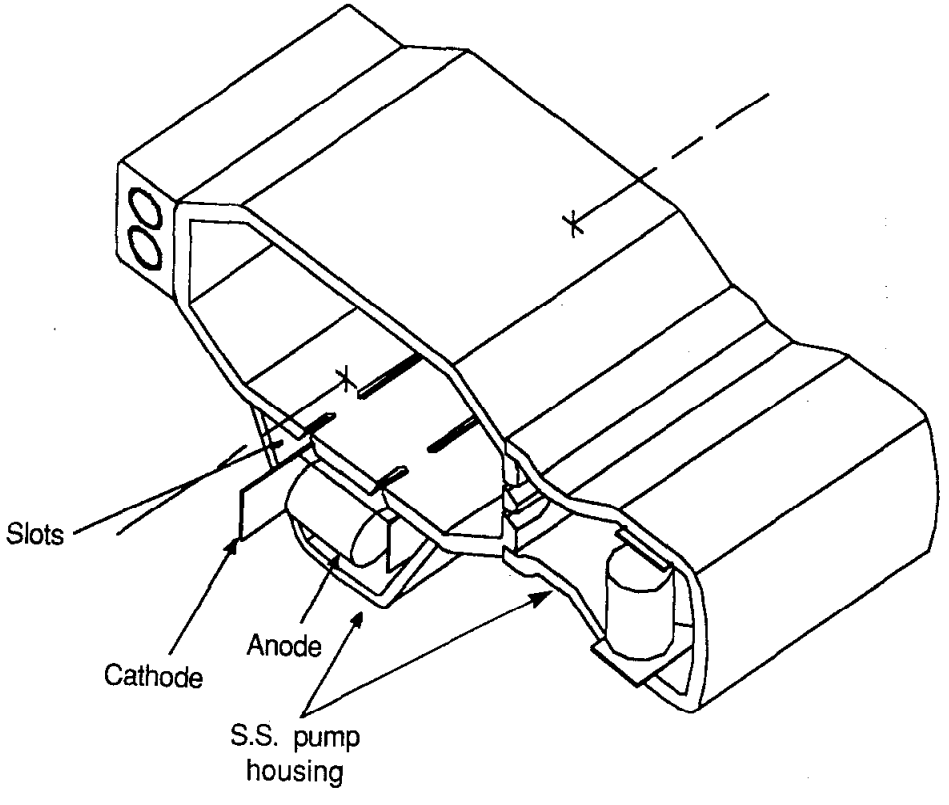

Fig. 5-62. Distributed ion pumping arrangement for the quadrupoles of the HER.

addition, the ports are designed to accommodate additional pumps, should the need arise. To keep the impedance contribution of the ports to a negligible level, they will be shielded with a perforated screen having longitudinal slots 10 cm in length.

The slots between the pumping chamber and beam tube are in rows, 9 cm long by about 0.2 cm wide, at a pitch of 10 cm, similar to the HERA machine; this gives a conductance of about 500 L/s/m. These slots contribute negligibly to the impedance.

The calculated pressure profile achieved with this configuration of pumps is shown in Fig. 5-63.

5.2.4.6 Fabrication. Several different fabrication methods will be utilized in the construction of the vacuum chambers for the HER. Vacuum chambers in the straight sections will be fabricated of stainless steel, using well-known and well-established welding methods to produce vacuum-tight assemblies. The copper vacuum chamber components in the arc sections will be joined almost entirely by brazing operations. Although long used for constructing small components, the brazing technique will, in this case, be applied to a much larger task, namely, producing approximately 400 vacuum chamber sections that vary in size from less than 2 m to approximately 6 m in length. Joints will also be required between stainless steel and copper.

For those B Factory fabrications involving copper components, we will use the same brazing steps, methods, and techniques established at DESY in constructing the vacuum chambers for HERA [Ballion et al., 1989]. This technology includes cleaning methods,

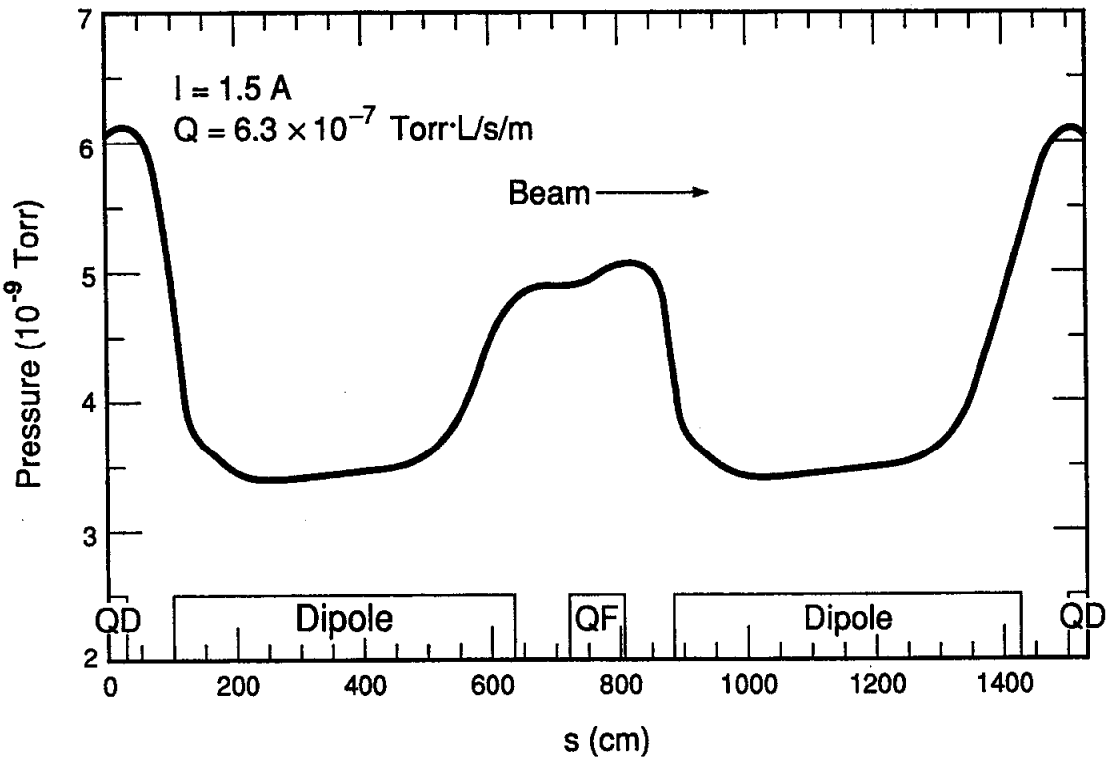

Fig. 5-63. Calculated beam pipe pressure profile of the B Factory HER.

fixturing, brazing alloys, furnace environments, heating schedules, and brazing steps at 1000°C and 800°C. Nonetheless, we recognize the necessity of prototyping these brazing processes in developing the required methods, materials, procedures, and specifications for our application, to ensure that appropriate fabrications can be made in a timely manner.

Cleaning. Techniques were developed at DESY to provide clean brazing surfaces and to obtain good vacuum properties on the chamber surfaces. The particular method chosen depends on the nature of the component being cleaned. Small stainless-steel parts are washed in an alkaline detergent and then rinsed in a dilute citric acid solution, followed by rinsing in distilled water at approximately 90°C. Small copper parts, following machining, are cleaned in the same manner, except that the detergent is only slightly alkaline and the process temperature is reduced to about 40°C. Large copper parts are assumed to be supplied by the vendor precleaned of production-process residues. Following machining, the parts are degreased in a slightly alkaline, 10% detergent bath, followed by rinsing in distilled water. Next, the parts are etched in a nonferrous-metal etch solution containing 83 parts water by volume, 10 parts concentrated sulfuric acid, 5 parts 35% hydrogen peroxide, and 2 parts stabilizer. After a rinse in distilled water, pickling is performed in warm water with 10% citric acid. Finally, the parts are rinsed in distilled water and dried.

Brazing. Brazing will be performed in two steps. The first step produces subassemblies of stainless-steel and copper parts. In the second step, only copper-to-copper brazing is performed. Brazing between stainless-steel and copper parts, which is required for the end-flanges, the lumped-pump ports, and the stainless-steel housings for distributed ion pumps in the quadrupoles, will be done in a small vacuum-furnace at 1000°C, using L-CuSn12 braze material. In the final braze assembly process, these subassemblies will be brought together with the beam tube, the pumping channel and cooling bar extrusions, the lumped-ion-pump manifolds, the BPM housings, and end-flanges, to form a complete chamber section that will be brazed at 800°C. For this brazing step, DESY used both brazing wire and a film of L-Ag72. We will use similar brazing alloys. This final brazing was made in a horizontal furnace in an atmosphere of 93% Ar and 7% H_2. This technique permitted rapid and uniform heating of the chamber assemblies and enabled 8-hour brazing cycles to be obtained. For the B Factory, leak checking will be performed after each brazing step, and completed chamber sections will be sealed and backfilled with dry nitrogen for storage and shipping to a preassembly site prior to installation.

Chamber Assembly. Assembly work on the vacuum chamber sections will include forming the chambers to contour; installing the dipole and quadrupole distributed ion pump hardware; making the vacuum seals for these chamber spaces; leak checking; installing the support-bracket plates, water connections, and BPM electrodes; performing mechanical and electrical checkouts (including dimensional checks); and carrying out a bakeout to 100°C above the ambient temperature. Completed assemblies will again be backfilled with dry nitrogen while awaiting installation. At this point, all necessary work will have been completed except for that required for actual installation in the tunnel.

5.2.5 LER Vacuum System

The operating pressure requirements for the LER are the same as those for the HER. In addition, the periodic layout of the lattice is similar: The cells of the two rings are the same length and stacked one atop the other. Major differences between the two rings, however, are the length and placement of the dipoles. The LER configuration, in the arcs, is shown in Fig. 5-64.

The synchrotron radiation photon flux in the LER will be four times that in PEP. Therefore, as already discussed, copper was chosen as the most suitable material for fabrication of the vacuum chambers in the arcs. In the straight sections, where the synchrotron radiation is minimal, the vacuum chambers will be fabricated from stainless steel.

5.2.5.1 Vacuum System Design. As shown in Fig. 5-65, the LER beam chamber cross section in the arc regions is identical to that of the HER, except for the omission of the pump channel. The inner dimensions accommodate the beam-stay-clear region required by beam dynamics and allow for the unavoidable errors in fabrication and mechanical positioning. A standard FODO cell contains the following elements: (i) defocusing sextupole, (ii) defocusing quadrupole, (iii) corrector, (iv) bending magnet, (v) drift, (vi) focusing sextupole, (vii) focusing quadrupole, (viii) bending magnet with corrector winding, and (ix) drift.

These two "sets" of magnets are grouped together on support rafts, with the bending magnet placed downstream of the other elements. The length of the bending magnet was chosen such that all of the synchrotron radiation it produces strikes the vacuum chamber

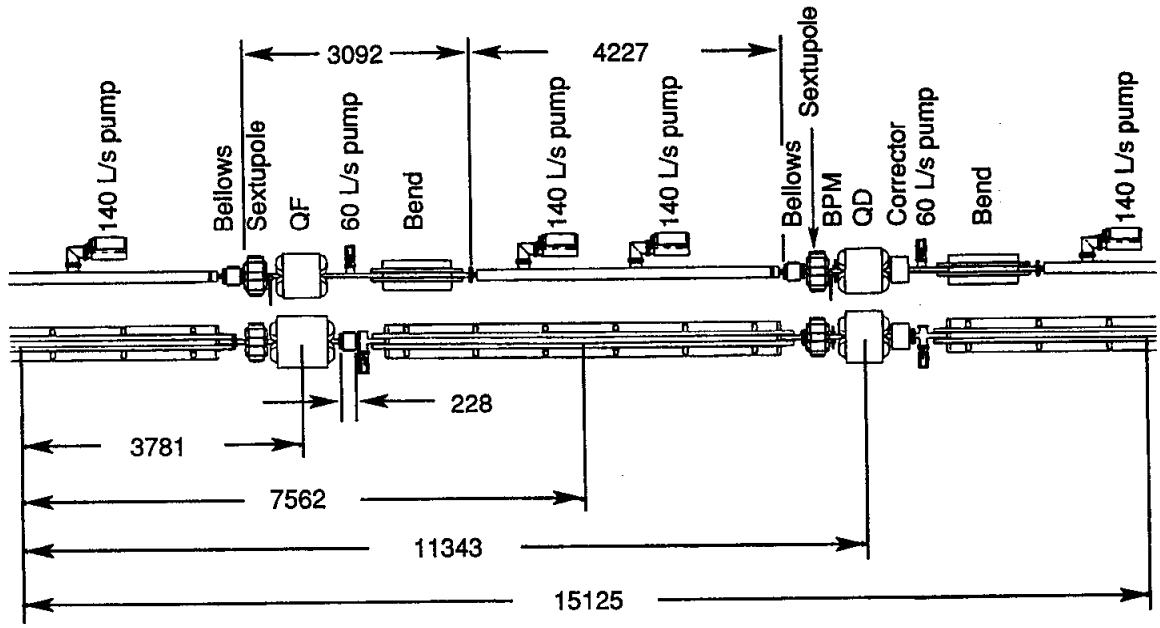

Fig. 5-64. Layout of a single arc cell of the LER of the B Factory; dimensions are in millimeters

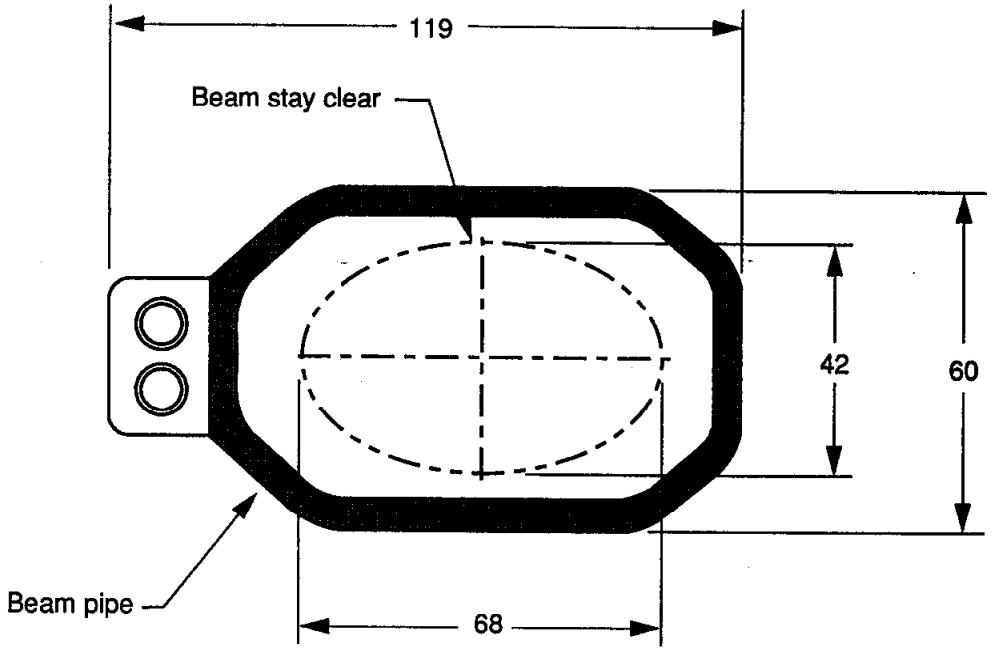

Fig. 5-65. Cross section of the LER vacuum chamber in the arcs; dimensions are in millimeters.

wall beyond the magnet (see Fig. 5-66), where vacuum pumps can be easily located to remove the desorbed gas. Distributed ion pumps inside the bending magnet are thus unnecessary. As is typical of storage rings, the beam chamber, which is of continuous cross section through the arc, is vacuum-conductance limited. Our solution for pumping the system (without using distributed ion pumps) is implemented in the sections of vacuum chamber downstream of the bending magnets. Here the conductance is doubled by enclosing the beam chamber itself within a tubular vacuum manifold.

Each of the six straight sections has a length corresponding to eight standard cells. Included in these sections are the RF cavities, the injection septa, beam pickups and kickers, horizontal and vertical beam scrapers, and BPMs. One of the straight sections houses the common interaction region for the B Factory and thus has a unique layout. There are also 28 empty FODO cells in the ring. The diameter for the beam pipe in the straight sections is 100 mm. Existing 152-mm-bore isolation valves from PEP will be used where possible; 100-mm-bore valves will be used elsewhere.

All pumping of the system is by means of lumped sputter-ion pumps. To provide stable argon pumping speed (in case of small air leaks), one pump in each cell will have "differential cathodes" (of titanium and tantalum). The pumping speed requirements are discussed below.

Experience from SPEAR and PEP has demonstrated the wisdom of installing a large vacuum system with flanged rather than welded interconnections. Standard stainless-steel Conflat flanges with copper gaskets will be used, as these have proved very reliable in the past.

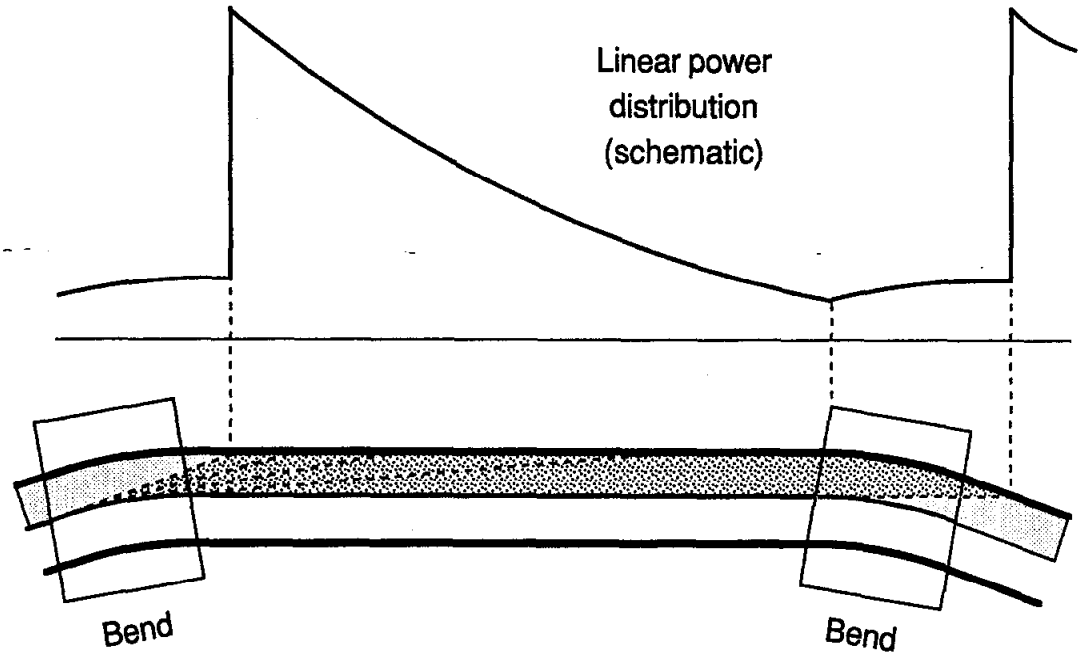

Fig. 5-66. Schematic illustration showing the distribution of synchrotron radiation power striking the LER vacuum chamber.

As in the HER, HOM losses will be kept to a minimum by keeping a uniform chamber cross section where possible. Tapered transitions smoothly blend the unavoidable changes in cross section. Ports on the beam chamber are shielded by screens. Copper rings between the flanges provide a smooth electrical path and will eliminate RF losses.

In the interest of reducing the number of different components, LER and HER vacuum systems will be standardized wherever possible. An example is the expansion bellows used to accommodate misalignment and to allow for thermal expansion of the vacuum chamber. Also interchangeable will be the isolation valves, pump-out valves, vacuum gauges, and ion pumps with their associated controls.

The vacuum system will be equipped to accommodate an in situ bakeout to 120°C. Thermal insulation of the bending magnet chamber will be provided by a permanently installed wrapping consisting of a powdered oxide pressed between glass fiber. Hot water circulated through the low-conductivity water (LCW) system will supply the heat.

5.2.5.2 Arcs. The layout of one standard cell is shown in Fig. 5-64. There are six beam chamber components per cell: bending magnet chamber, pumping chamber, bellows, bending magnet chamber with BPM, pumping chamber, and bellows.

The bending magnet chamber, shown in Fig. 5-67, is a 3.09-m-long, water-cooled copper brazement that passes through the sextupole, quadrupole, and bending magnets. It is rigidly attached to the support girder between the sextupole and quadrupole, at the location of the BPM. (Only alternate bending magnet chambers in the cell will require a BPM, namely, those near the defocusing quadrupole magnets.) Flex plates at the ends of

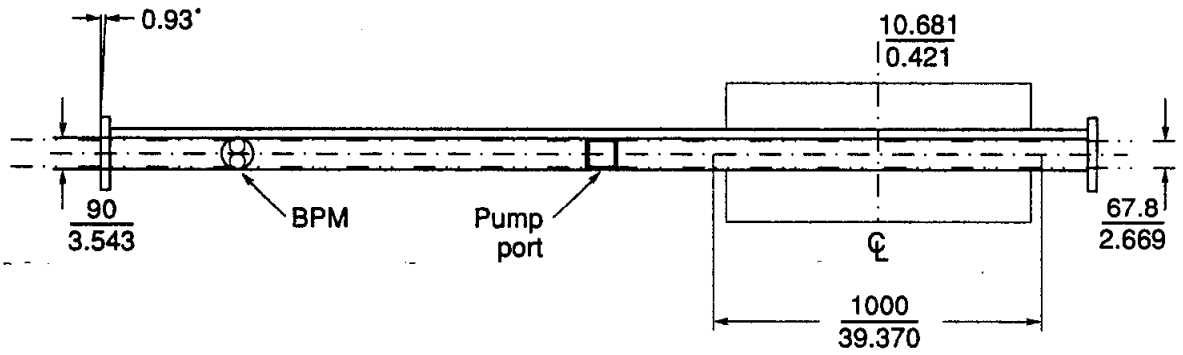

Fig. 5-67. Schematic of a bending magnet vacuum chamber for the LER.

the chamber will hold its lateral position while allowing thermal expansion. A pump port is provided between the quadrupole and bending magnets.

BPMs will be of the "button-electrode" type, modeled after the LEP design. They will be calibrated by a noninvasive technique, thus avoiding the threading of an antenna through the beam chamber and allowing the buttons to be located at any point along the beam pipe.

Most of the synchrotron radiation power is absorbed in the pumping chamber, which is 4.227 m long and is located immediately downstream of the bending magnet. The B Factory design, shown in Fig. 5-68, incorporates a water-cooled copper beam chamber,

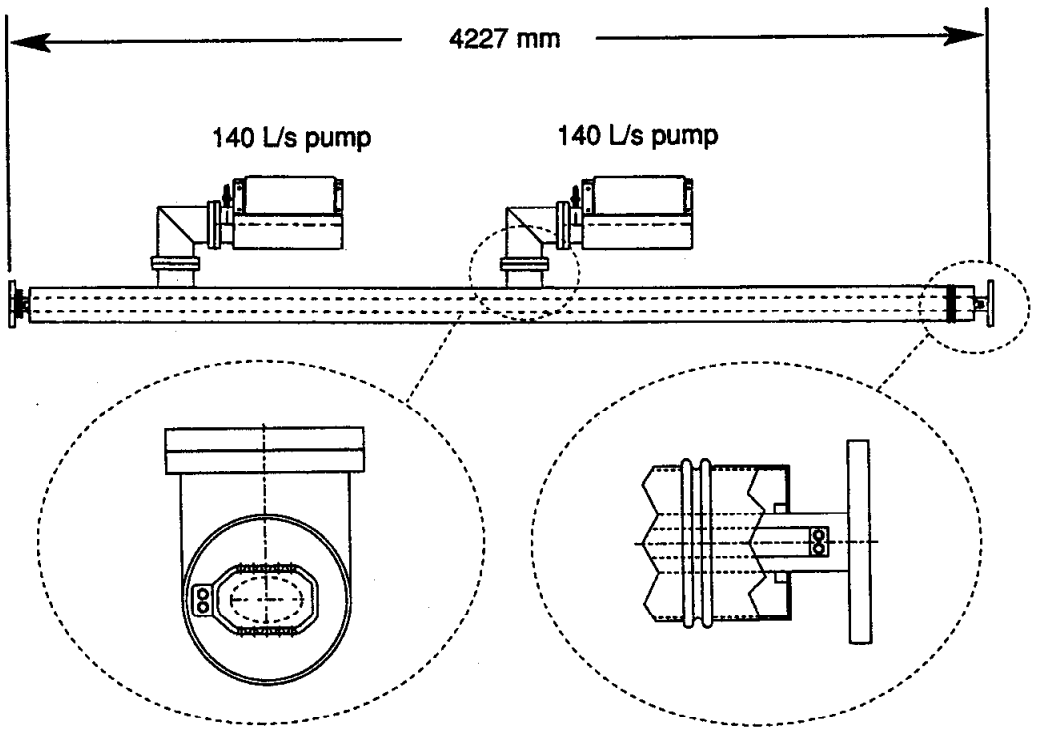

Fig. 5-68. Schematic of a pumping chamber for the LER.

with end flanges for interconnection. The chamber is slotted top and bottom over most of its length and surrounded by a 152-mm-diameter vacuum manifold. A short bellows at the end nearer the bending magnet allows the flexibility necessary for alignment. The longer bellows module at the downstream end of the pumping chamber provides the necessary space for installation and accommodates thermal expansion. Differential thermal expansion within the chamber is accommodated by a bellows on the manifold. Connections to the LCW system are external to the vacuum system, thus eliminating water-to-vacuum welds that might develop leaks.

5.2.5.3 Straight Sections. A typical straight section cell, fabricated from 100-mm-diameter stainless-steel tube, is shown in Fig. 5-69. Isolation valves are located in the straight sections at the end of each arc. To protect the RF cells in the event of an accidental vent to air and to facilitate their conditioning, additional valves are also provided to isolate them.

5.2.5.4 Synchrotron Radiation. At a beam energy of 3.1 GeV, the critical energy of the synchrotron radiation is 2.2 keV. In this photon energy regime, almost all the power is absorbed on the inside wall of the vacuum chamber. At 3.1 GeV, assuming 2.14 A of stored beam, the total power radiated in the arcs is 580 kW, giving 6.04 kW per cell. The power distribution is plotted in Fig. 5-40b. The peak power, 21 W/cm, is deposited approximately 40 cm beyond the bending magnet exit; thereafter, the power decreases rapidly along the cell.

Given this distribution of synchrotron radiation, the temperature differential across the water-cooled metal wall of the chamber is approximately 12°C; across the surface film in the water, it is 14°C. At the required flow rate of 10 gpm, the bulk temperature rise per cell is 2°C.

Within each cell, LCW from the supply header will flow out, in both directions, from the center of the cell through the LER bending magnet chambers. At the ends, the water will be directed to the HER chambers, through which it will flow back to the center. The two circuits then merge and pass into the return header through a flow switch that monitors for low flow (see Fig. 5-70). This design ensures that all cells are uniformly cooled.

A second consequence of synchrotron radiation is photodesorption. The gas load produced by this mechanism is plotted in Fig. 5-42b, assuming a value for the photodesorption coefficient equal to 1×10^{-6} molecules/photon at the maximum value of P_{SR}. The arrangement of sputter-ion pumps in the arc cells is shown in the layout of Fig.

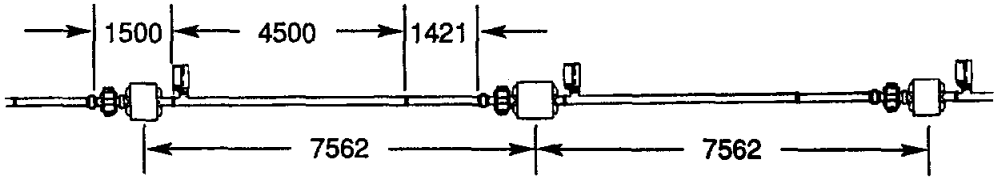

Fig. 5-69. Schematic of the vacuum chamber for an LER straight section. Dimensions are in millimeters.

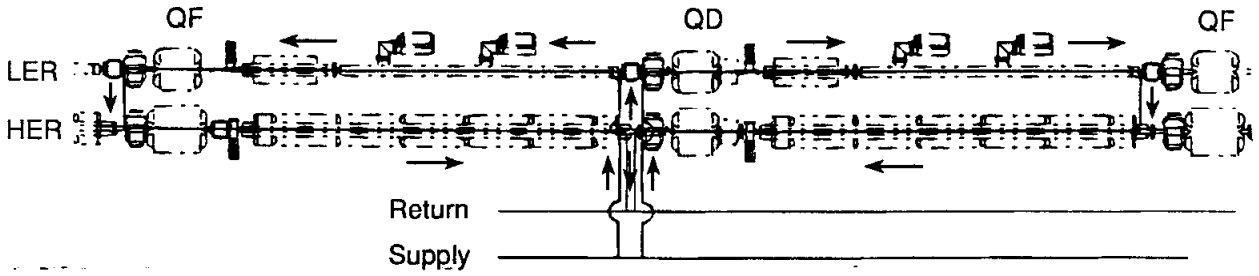

Fig. 5-70. Schematic of the cooling water system for the high- and low-energy-rings.

5-64. The total pumping speed per cell is 680 L/s. The pressure distribution calculated on this basis is shown in Fig. 5-71. Based on the above estimate of the desorption coefficient, the average pressure in the arcs during operation with a beam current of 2.14 A will be about 7.5 nTorr.

In the straight sections, the design pressure of 3 nTorr will be maintained by installing 220-L/s sputter-ion pumps at intervals of 7.56 m (that is, two per cell). Based on experience at SLAC, we have assumed a thermal outgassing rate of 1×10^{-11} Torr·L/s/cm^2. For the region immediately upstream of the interaction region, 220-L/s pumps will be installed at intervals of 3.8 m to obtain the operating pressure of 1 nTorr. With these values, the average pressure around the LER circumference is 6 nTorr. This pressure was used in the lifetime estimate discussed in Section 4.3.

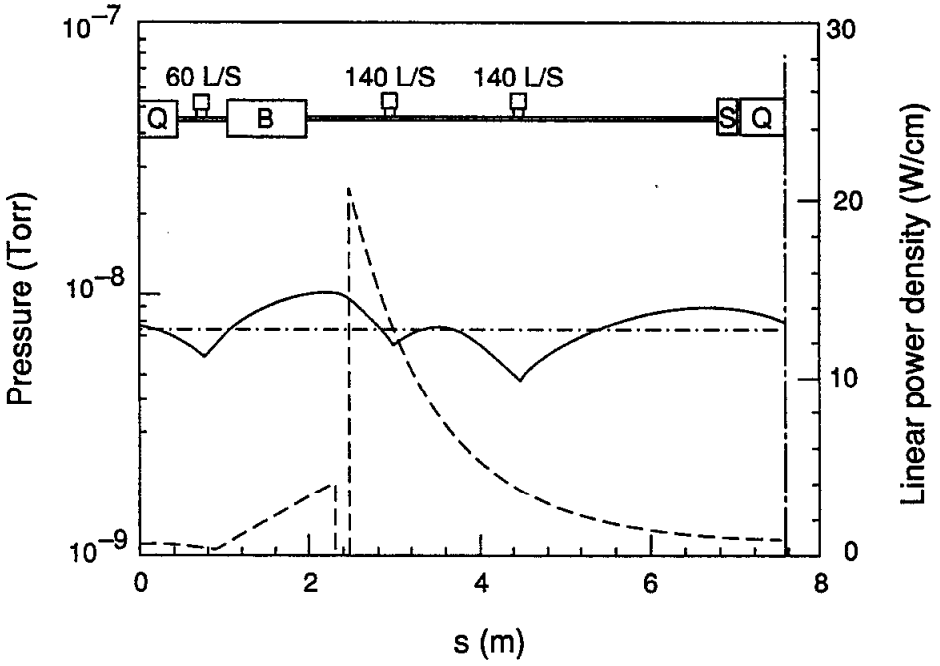

Fig. 5-71. Plot of the pressure distribution along an arc of the LER (solid line). The dashed line is the linear power density on the wall.

5.2.6 Radiation from Wigglers

To provide acceptable beam-beam tune shifts, the natural emittance of the LER must be increased considerably beyond that resulting from the arc dipoles alone. In addition, we have discussed in earlier reports [*Feasibility Study for an Asymmetric B Factory Based on PEP*, 1989; *Investigation of an Asymmetric B Factory in the PEP Tunnel*, 1990] the potential advantages of having equal damping decrements in the high- and low-energy rings to minimize the effects of the energy asymmetry on the beam-beam interaction. For these reasons, wigglers will be used to create additional energy loss in the LER.

The damping decrement for a storage ring can be written as

$$\lambda = \frac{T_0}{\tau_x} = \frac{U_0}{2E} \tag{5-23}$$

from which it is clear that, for equal damping decrements, the required synchrotron radiation energy loss per turn for the high- and low-energy rings must simply scale proportionately to the beam energy in the ring.

In the high-energy lattice (ρ = 165 m; E = 9 GeV), the total energy loss, which is dominated by the normal bends, is U_0 = 3.58 MeV/turn. For equal damping decrements, then, we need an energy loss in the LER of

$$U_{0,+} = U_{0,-}\frac{E_+}{E_-} = 3.58\left(\frac{3.1}{9.0}\right) = 1.24 \quad \text{[MeV/turn]} \tag{5-24}$$

In the LER, we have a bend radius of ρ = 30.6 m. The energy loss from the horizontal bends can be estimated as

$$U_0 = 0.0885\,\frac{E^4}{\rho} \quad \text{[MeV/turn]} \tag{5-25}$$

giving U_0 = 0.27 MeV/turn, that is, only about one-fifth of the requisite amount. (To create the matched damping decrement from the bending magnets alone would require a bend radius of 6.75 m, which would be, at best, inconvenient in terms of thermal power density.) In addition to the contribution from the horizontal bends, we must take account of the synchrotron radiation emission in the vertical bends used to steer the low-energy beam into the arc sections (which lie above the plane of the HER). The energy loss from the two sets of vertical separation magnets in the IR can be calculated from

$$U_{0,V} = 1.266 \times 10^{-3}\,E^2B^2L \quad \text{[MeV/turn]} \tag{5-26}$$

where E is in GeV, B is the dipole field in T, and L is the total bend length in meters. This gives a total contribution from the vertical bends of 0.014 MeV/turn. Thus, the lattice itself contributes a total energy loss of 0.28 MeV/turn from the bending and separation magnets.

To reach equal damping decrements, then, we must produce an additional energy loss of 0.96 MeV/turn. This will be accomplished by including wiggler magnets in two of the LER straight sections. As already mentioned, these wigglers also serve as a means of emittance adjustment for the LER; this adjustment works by creating a dispersion "bump" at the wiggler locations. By locating the wigglers in shallow chicanes off the principal axis of the straight section, the rms dispersion in the wiggler can be controlled externally to the wiggler. This additional degree of freedom extends the range of allowable wiggler characteristics. It also allows us to project the radiation into a distant photon dump. The bend magnets used to divert the beam into the chicanes contribute an additional 0.03 MeV/turn of energy loss.

Four wigglers, with nine periods of $\lambda_W = 0.67$ m, are included in each of two utility straight sections, as discussed in Section 4.1. The total length of wigglers is thus 48 m and the magnetic length is 28.8 m. A schematic drawing of the layout is shown in Fig. 5-72. For a wiggler composed of alternating-field dipoles, the total radiated power in MeV/turn is again given by Eq. 5-26. A wiggler field of $B = 1.63$ T is therefore needed to provide the additional 0.93 MeV/turn to fully equalize the damping decrements.

At the nominal current of 2.14 A, each wiggler will produce about 1 MW of synchrotron radiation power, with a critical energy of 10.4 keV. Most of this power will be dealt with externally to the ring vacuum chamber in specially designed photon beam dumps. However, some of the power will be deposited on the side walls of the vacuum chamber in the vicinity of the wiggler. To compute the power density at the dump and on the walls, we must estimate the angular distribution of the radiation. A precise description of radiation from a nonsinusoidally varying wiggler in the near field is not given in the literature, but we can modify the far-field description for standard wigglers given by Kim [1986] and apply it to segments of the wiggler to evaluate the resultant vacuum system requirements [Barletta and Garren, 1991].

Denoting the horizontal angle by θ and the vertical angle by ψ, we can write the power density in W/mrad^2 as

$$\frac{dP}{d\Omega}(\theta,\psi) = \frac{21\gamma^2}{16\pi K} U_{0,w}\, I\, N_W\, G(K)\, f_K(\gamma\theta,\gamma\psi) \tag{5-27}$$

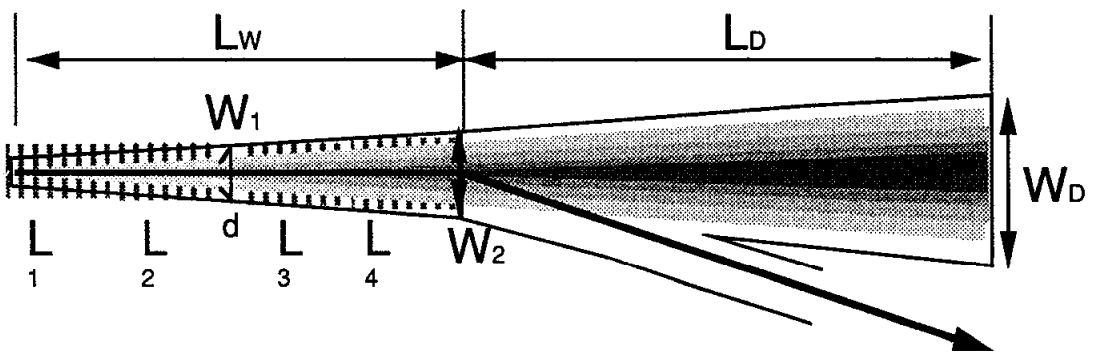

Figure 5-72. Schematic representation of the vacuum chamber in the region of the LER damping wigglers.

where $U_{0,w}$ is the synchrotron radiation loss in one wiggler period, I is the beam current in A, N_W is the number of wiggler periods, and G and f_K are universal functions. For the bend-drift configuration, $U_{0,w}$ is given by Eq. 5-26, where the wiggler magnetic length is substituted for L. For a standard wiggler, K is the usual wiggler parameter defined (for B in T and λ in cm) by

$$K = 0.934\ B_w \lambda_w \tag{5-28}$$

The normalization factor $G(K)$ is

$$G(K) = K \frac{\left(K^6 + \frac{24}{7}K^4 + \frac{16}{7}\right)}{\left(1 + K^2\right)^{7/2}} \tag{5-29}$$

For $K \gg 1$, $G(K) \rightarrow 1$; moreover, the angular distribution is sharply cut off in the wiggler bend plane. In the limit $K \rightarrow \infty$, the normalized angular distribution function $f_K(\gamma\theta, \gamma\psi)$ is given by

$$f_K(\gamma\theta, \gamma\psi) = \sqrt{1 - (\gamma\theta/K)^2}\ \left\{\frac{1}{\left[1 + (\gamma\psi)^2\right]^{5/2}} + \frac{5\,(\gamma\psi)^2}{7\left[1 + (\gamma\psi)^2\right]^{7/2}}\right\} \tag{5-30}$$

From Eq. 5-30 one sees that the radiation is spread over a horizontal angle $2\theta_w$, where

$$\theta_w = \frac{K}{\gamma} \tag{5-31}$$

For the bend-drift configuration, θ_w is the bend angle in a single dipole. In that case Eq. 5-31 becomes the defining relation for an effective K value, K_{eff}. Given this K_{eff}, we apply the formalism for the standard wiggler. In the nonbend (vertical) plane, the rms angle of the radiation is

$$\psi_w = \left(\frac{\varepsilon_y}{\beta_y} + \frac{0.63}{\gamma^2}\right)^{1/2} \tag{5-32}$$

At 3.1 GeV, the second term in Eq. 5-32 is dominant, and $\psi_w \approx 1/\gamma = 0.13$ mrad to a good approximation. At the nominal operating current of 2.14 A, each wiggler generates 42 kW/m. The opening half-angle of the radiation is 15.8 mrad. Therefore, if the vacuum chamber is to intercept less than 20% of the radiation generated (to avoid an impractically high power loading on the crotch and on the side walls), the enclosure needs to be quite wide. By integrating Eq. 5-27 over ψ for K_{eff}, one can determine the power density on the side walls of the enclosure.

With regard to pumping requirements, there is a weak trade-off between increasing the static load from widening the chamber and minimizing the dynamic load by avoiding

the photon fan. In the wiggler region, which occupies only 2% of the circumference of the ring, we have relaxed the required operating pressure to 10 nTorr.

As discussed in Section 4.1, we have opted for a quadrupole triplet located between wiggler segments L_2 and L_3 to provide flexibility to tune the lattice. This configuration suggests the use of a tapered stainless-steel chamber, as illustrated in Fig. 5-72. The photodesorption coefficient of the chamber is assumed to be 2×10^{-6}. The width W_1 should be as narrow as possible to maintain a practical quadrupole design. With this constraint in mind, the required pumping, which ranges from about 115 L/s/m in L_2 to about 160 L/s/m in L_4, is obtained for $W_1 = 24$ cm and $W_2 = 40$ cm. The corresponding thermal loads range from 3.2 to 5.1 kW/m, respectively, on each side wall of the wiggler enclosure.

From Eq. 5-27, we can estimate that, at 2.14 A, the power density in the forward direction will be 1.6×10^5 W/mrad^2. We also find that 80% of the radiation is emitted into 8.1 mrad^2. Hence, we can compute the distance from the end of the wiggler to the photon dump, such that the power density is limited to a maximum value of 1 kW/cm^2. The distance from the wiggler to the dump, L_D, can be foreshortened by tilting the dump at an angle of about 20° with respect to the vertical. For a tilted dump, L_D should be about 44 m. Although roughly 20% of the power will actually be deposited on the walls of the wiggler chamber, we estimate the gas load at the dump assuming that all the power is incident there. We find that, for a copper dump with a photodesorption coefficient of 2×10^{-6}, the gas load at the dump is $Q_{\text{dump}} = 1.1 \times 10^{-4}$ Torr·L/s.

By considering the flared vacuum chamber from the wiggler to the dump to be a long, differentially pumped manifold, we can allow the pressure at the dump to rise to a much higher value than that required in the beam pipe. At the dump, the maximum horizontal extent of the radiation fan is 2.15 m, whereas the vertical extent of the radiation is only 2.0 cm. To lower the conductance of the photon channel, we take the chamber height to be 8 cm; baffles will also be added as needed to reduce the vacuum conductance into the wiggler straight section to 250 Torr·L/s.

The minimum total pumping of the dump plus photon channel is obtained by choosing the pressure to be 60 nTorr. This pressure requires 2000 L/s of pumping at, or near, the dump. This could be provided, for example, by installing large cryopumps. At a distance $L_D/2$, 700 L/s of pumping will reduce the pressure to 45 nTorr. Distributed pumping of 50 L/s/m along the first third of the photon channel reduces the pressure to 10 nTorr at the exit of the wiggler. More novel approaches, such as having the radiation fan strike NEG panels, are under study [Halama and Guo, 1990].

A C-frame bending magnet 5 m downstream from the wiggler exit bends the positron beam out of the radiation fan and into the straight beamline. The crotch can thereby be located away from the radiation fan of the wiggler. The straight beam pipe leaving the crotch is a special section of stainless-steel pipe, with a restricted aperture of less than 3 cm. Lumped ion pumps, providing 100 L/s of pumping speed in the region starting 10 m beyond the crotch and extending 5 m downstream of it, will reduce the pressure to 3 nTorr. At this point, a transition section will match the beam pipe dimensions to the standard straight-section vacuum chamber cross section.

5.2.7 Interaction Region Considerations

The interaction region is the heart of the entire B Factory facility. Because the detector is located in the IR, and because the separation of the two beams takes place here, there are a number of special requirements and special constraints that must be accommodated by the hardware. The design issues that must be considered are mainly those associated with the need to protect the detector from backgrounds. As discussed in Section 4.2, various masks are used in this region to protect the detector components and other sensitive equipment from the synchrotron radiation emitted as the beams are being magnetically separated, and these masks perforce intercept some of the synchrotron radiation power. The issues that we consider here include:

- Local pumping to deal with the photodesorption from those mask surfaces hit by the synchrotron radiation fans
- Cooling of the detector beam pipe masks to remove the synchrotron radiation power
- Cooling of the so-called "crotch masks" that shield the septum quadrupole (Q4) from the high-power synchrotron radiation fans
- Cooling of the very thin beam pipe in the center of the detector to remove the power due to wall-current and HOM heating.

5.2.7.1 Local Pumping. The pressure requirements inside the detector in the region upstream of the permanent-magnet quadrupoles are set by beam-gas bremsstrahlung events leading to lost beam particles. Within about ±20 cm of the interaction point (IP), the limitation arises from electron-nucleus events leading to spurious triggers. For beam-gas interactions, we would like a pressure of 1 nTorr or lower outboard of the upstream Q2 magnet (for each beam). Near the IP, estimates based on calculations [Lightbody and O'Connel, 1988] indicate that some tens of nanotorrs should suffice, although measurements with MkII at PEP suggest a more stringent limit. For the B Factory, a precise calculation requires more knowledge of the detector and trigger design than is now available, so the simple estimates must suffice.

Pumping inside the detector is provided by radial ion pumps between the permanent magnets, for example, between B1 and Q1. These pumps utilize the 1-T field of the detector solenoid. It seems feasible to provide pumps with 150 L/s effective speed, including the conductance of the RF screen required to isolate the pump structure from the beam [Hartwig and Kouptsidis, 1974].

The principal gas load comes from photodesorption by the synchrotron radiation hitting masks AB and CD inside the B1 magnets. To estimate the magnitude of the gas load, we use a desorption coefficient of 2×10^{-6} molecules/photon and a thermal outgassing coefficient of 1×10^{-11} Torr·L/s/cm^2. With these parameters, it will be possible to achieve the desired pressures.

5.2.7.2 LEB Beam Pipe Mask (Mask AB). The vertex detector vacuum chamber must be protected from incident synchrotron radiation. Without a mask, portions of the synchrotron radiation fans generated by the incoming low-energy beam (LEB) as it

passes through BV1–, Q3, and Q1 would be incident on the vertex detector vacuum chamber. With our geometry (see Fig. 4-41), a mask that shields the vertex detector chamber from this radiation protrudes sufficiently into the beam pipe to intercept on its inboard (B) face some synchrotron radiation generated by the incoming high-energy beam (HEB) as it passes through B3 and B2. Characteristics of those portions of the synchrotron radiation fans that hit the mask are listed in Table 5-20.

As this table shows, the total heat deposited in the mask is 1273 W; this value was used in calculating the water temperature rise. A thermal analysis was performed only for the outboard (A) side of the mask, since the heat input and linear flux on the inboard side are very low. Because it is a small part of the total heat input, and because the source is so far away (making the fan very diffuse), the BV1– linear flux was also ignored in the analysis. As shown in Fig. 5-73, synchrotron radiation fans from Q1 and Q3 do not overlap; the two fans form a single continuous fan with a normal linear flux of 55 W/mm (although the σ_y values of the two fans differ by a factor of three). To reduce the synchrotron radiation background (see Section 4.2.1.1), the outboard side of the mask is sloped at 3.2:1, thereby reducing the surface linear flux to 17 W/mm. Using the lower σ_y value to be conservative, the peak heat flux normal to the surface is calculated to be 35 W/mm^2.

Two-dimensional spread-sheet analyses were carried out to determine the peak mask temperature and the maximum metal-to-water surface temperature for various distances between heated surface and cooling passage. Thermal stress was then estimated from the peak temperature results. Peak metal temperature, thermal stress, and cooling-surface maximum temperature are shown as functions of thickness, for the two σ_y values of interest, in Figs. 5-74, 5-75, and 5-76, respectively. As is true for the HEB crotch mask (see below), there is a trade-off between maximum cooling-surface temperature (peak heat flux) and thermal stress.

Furnace brazing the mask will subject it to a temperature of the order of 800°C. The yield strength of a dispersion-strengthened copper such as GlidCop, after being subjected

Table 5-20. Synchrotron radiation power on the AB mask.

	Source	Power (W)	Normal linear flux (W/mm)	σ_y[a] (mm)
	Side A (outboard; from LEB radiation)			
1	BV1–	106	8	—
2	Q3	901	55	0.5
3	Q1	138	55	15
	Side B (inboard; from HEB radiation)			
4	B3	29	2	—
5	B2	99	8	—

[a]Normal to radiation fan

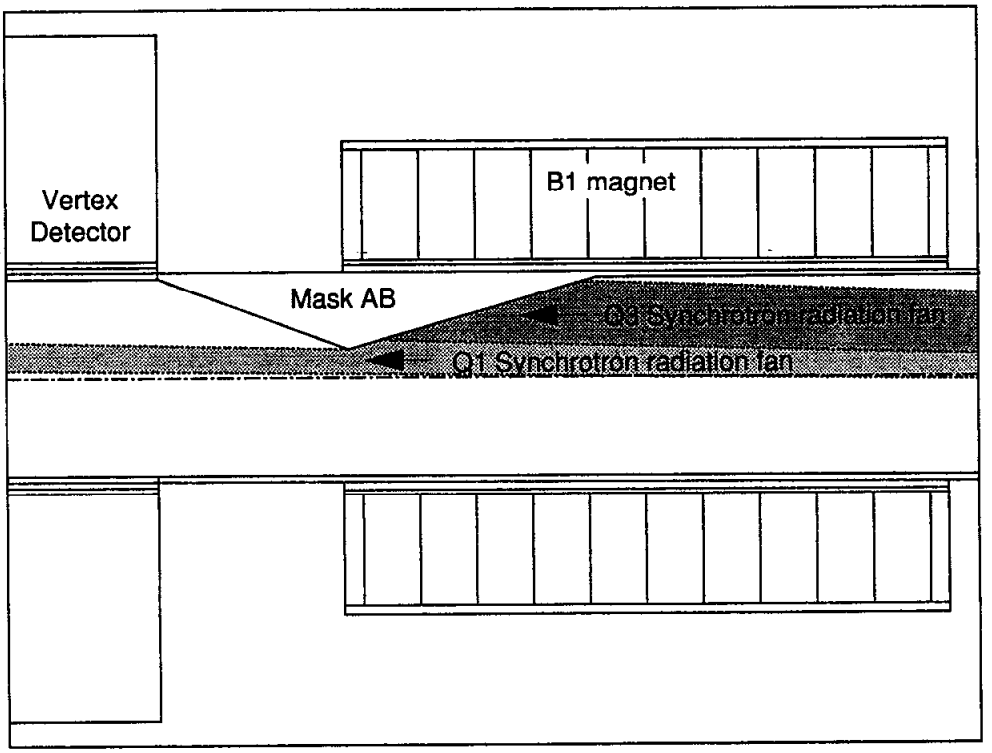

Fig. 5-73 Synchrotron radiation fans incident on the outboard side of the AB mask.

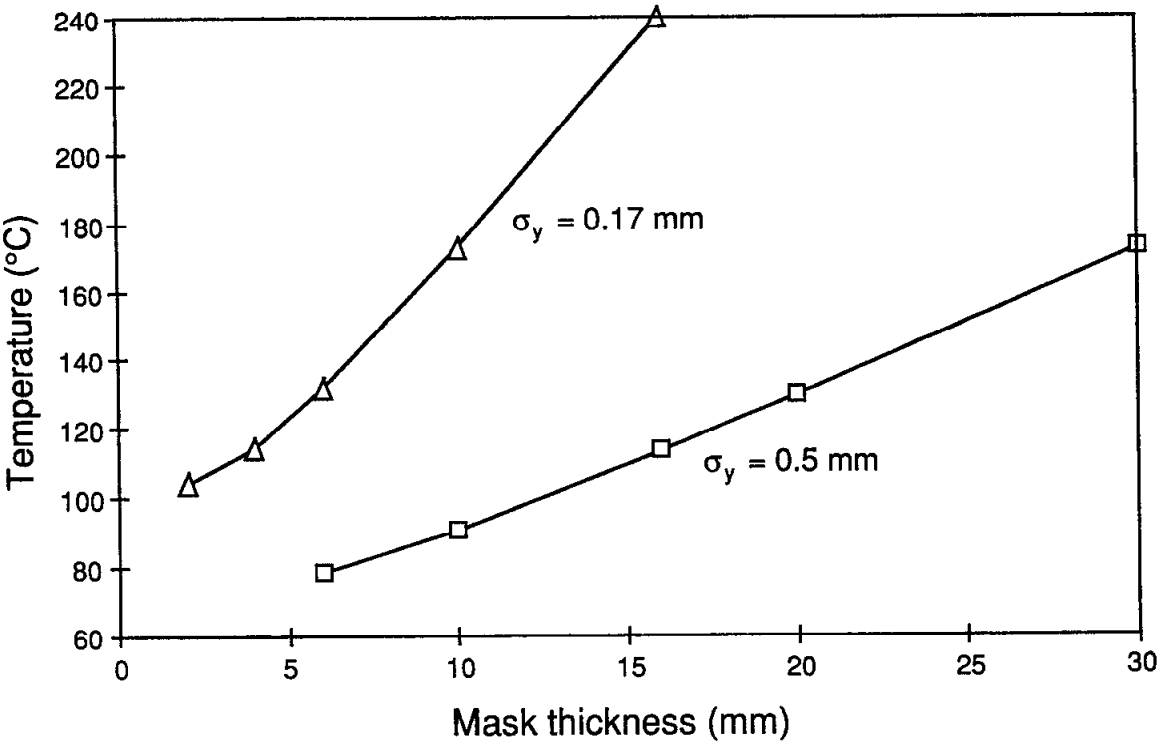

Fig. 5-74. Peak metal temperature on the AB mask as a function of thickness, for two values of σ_y.

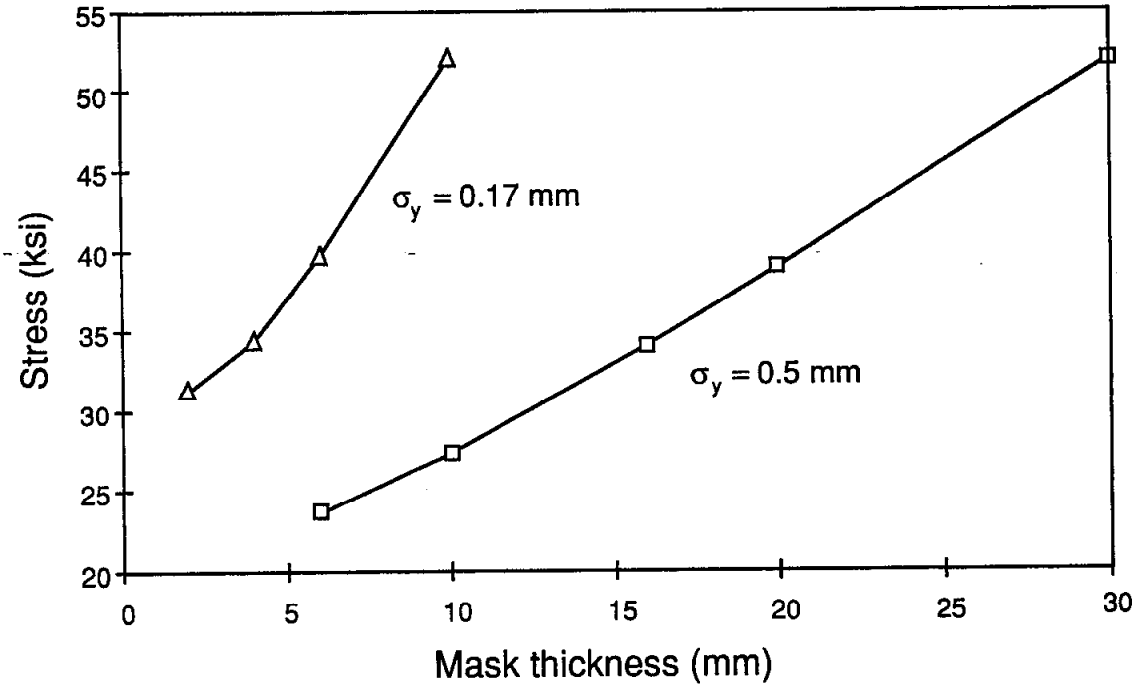

Fig. 5-75. Thermal stress at the AB mask as a function of thickness, for two values of σ_y.

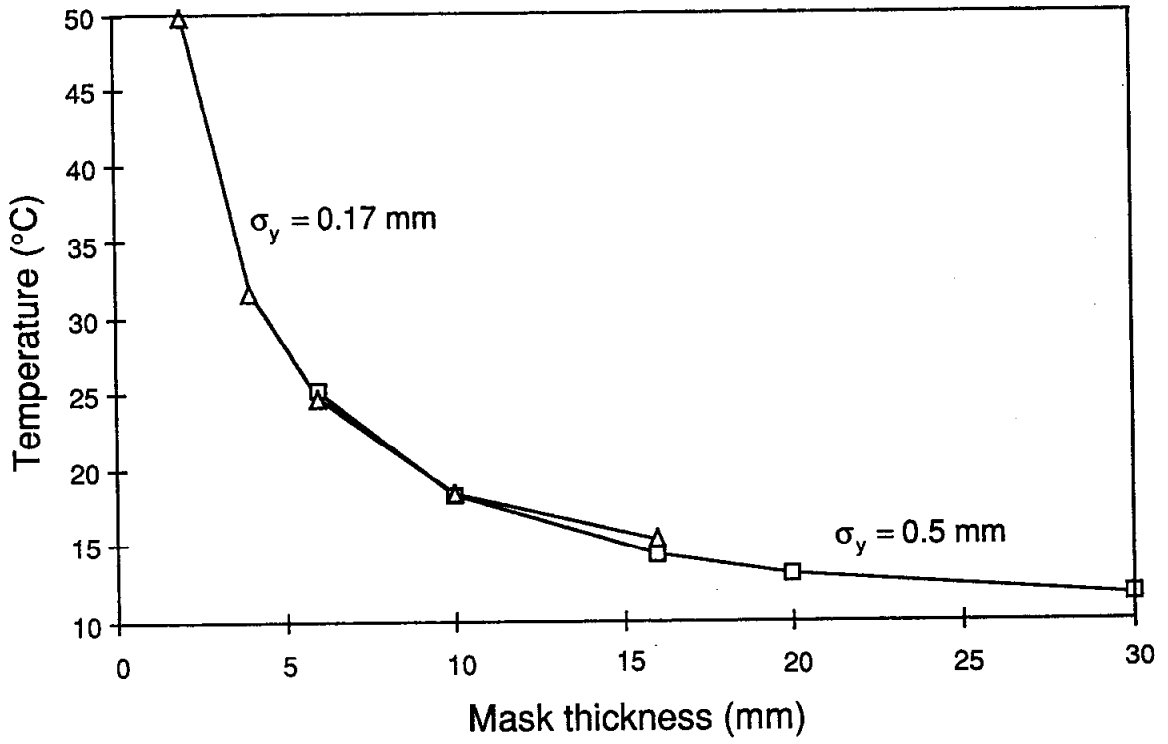

Fig. 5-76. Maximum cooling-surface temperature at the AB mask as a function of thickness, for two values of σ_y.

to such a temperature, is around 49,000 psi (see Fig. 5-77). If we desire to keep the peak stress to 75% of the yield strength, or 37,000 psi, then the distance from heated surface to water surface should not exceed 17 mm for the case of $\sigma_y = 0.5$ mm. For $\sigma_y = 0.17$ mm, the material thickness should not exceed 5 mm. In both cases, the maximum cooled-surface temperature is sufficiently low to avoid boiling. For long-term reliability, the vacuum-to-water wall thickness should not be less than 2 mm, and even at this thickness, the cooled-surface temperature is sufficiently low to avoid boiling (see Fig. 5-76).

Based on the two-dimensional analysis, the design shown in Fig. 5-78 will work well. During the detailed design phase, a three-dimensional analysis will be performed to verify these two-dimensional results for temperatures and stresses. The portion of the mask that forms the vacuum envelope is made of a single piece of GlidCop. As is normal practice, there will be no water-to-vacuum joints. Coolant passages will be drilled or milled from the outside (air side) of the mask. Covers that form the water-to-air seals will be brazed in place. Water is fed to the mask in a slot running from the outboard end

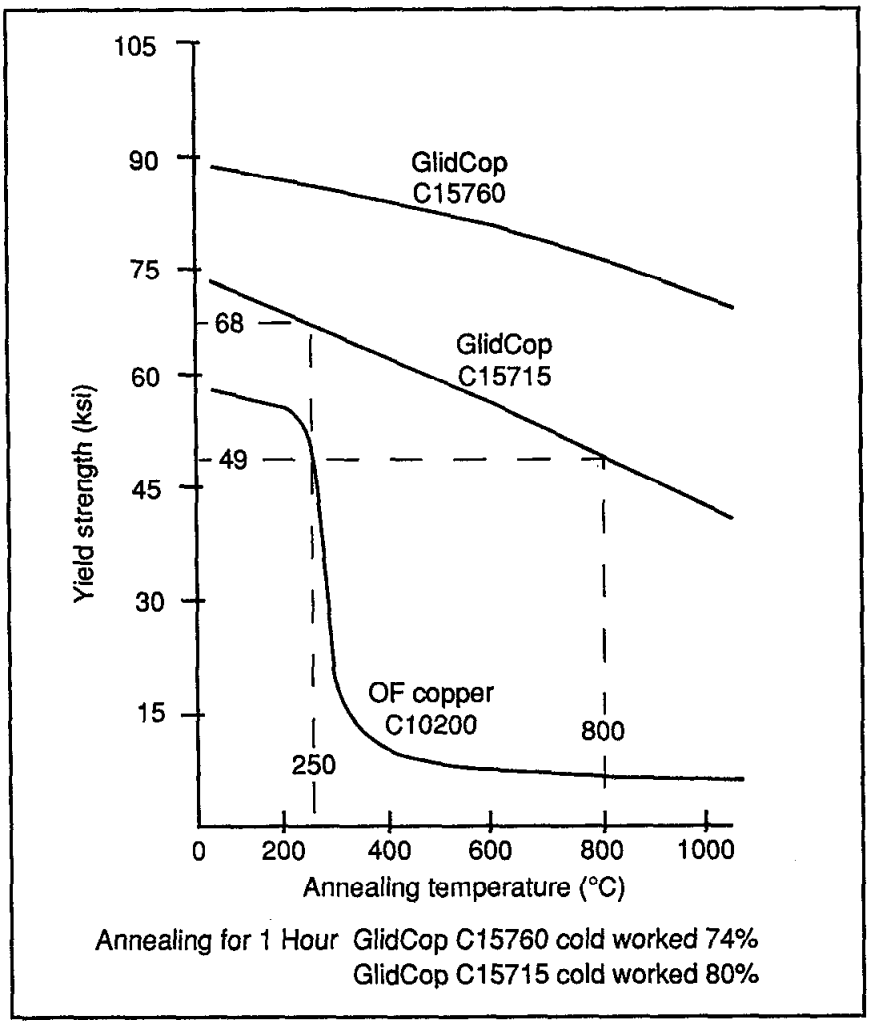

Fig. 5-77. Plot of the yield strength of a dispersion-strengthened copper, as a function of annealing temperature.

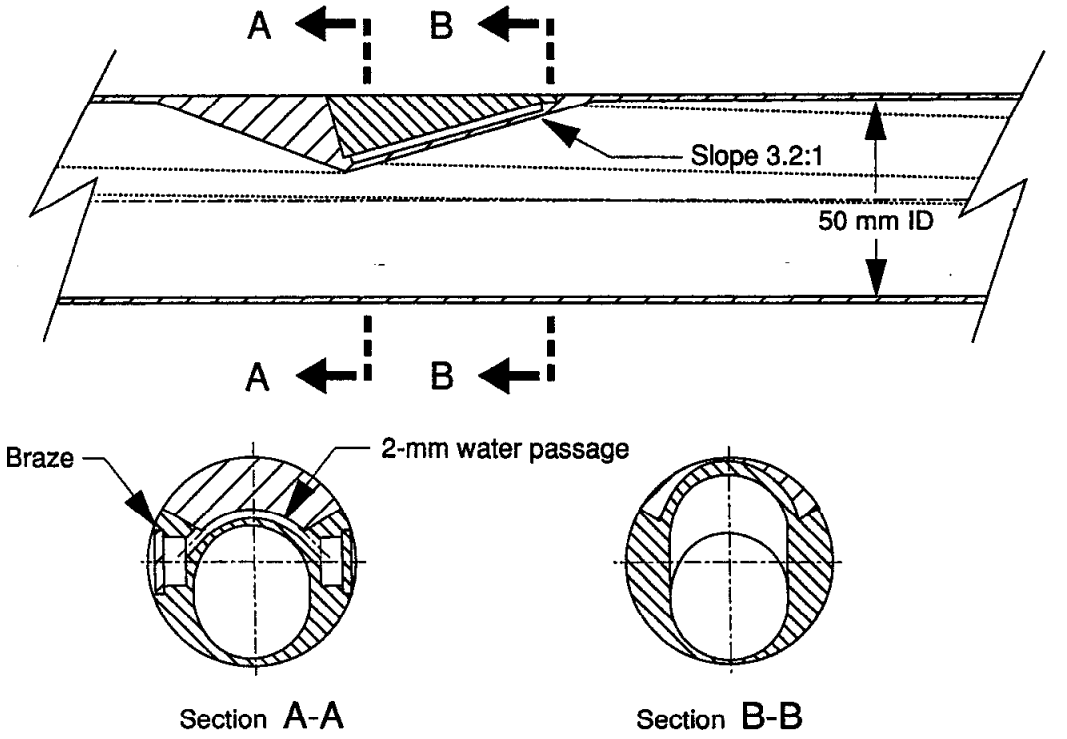

Fig. 5-78. Schematic showing the design of mask AB.

of B1; it returns via a similar slot on the other side of the mask body. With a total water flow rate of 1 gpm, the water-temperature rise will be 4.8°C.

5.2.7.3 HEB Beam Pipe Mask (Mask CD). Synchrotron radiation heat fluxes incident on both sides of mask CD (located on the incoming HEB side) are extremely low. Synchrotron radiation fan sources and their characteristics are listed in Table 5-21 The total heat deposition is only 36 W. With a surface slope of 6:1, the highest normal synchrotron radiation flux density is just 1 W/mm. Furthermore, σ_y values here are large, of the order of 3 mm or more. Thus, this mask will not present any thermal or stress problems.

5.2.7.4 High-Energy Beam Crotch Mask. The vacuum wall at the Q4 crotch must be protected from HEB synchrotron radiation by a mask, which we refer to as the HEB crotch mask. This crotch mask, located just ahead of Q4 on the incoming low-energy beam side of the IR, intercepts very strong synchrotron radiation generated by the HEB as it passes through the Q2 and B2 magnets, both on the incoming HEB side. Characteristics of the synchrotron radiation fans that hit the mask are summarized in Table 5-22.

The total power deposited in the mask is 4429 W. The fan from Q2 covers 7.6 mm of the 11-mm-wide mask; the B2 fan covers this same area plus another 0.3 mm. For the thermal and stress analyses, we assumed a total power input of 4430 W over a 7.6-mm width of the mask, giving a linear power density of 580 W/mm. The σ_y values in Table

Table 5-21. Synchrotron radiation power on the CD mask.

	Source	Power (W)	Normal linear flux (W/mm)
	Side C (inboard; from LEB radiation)		
1	BV1	11	6
	Side D (outboard; from HEB radiation)		
2	B3	9	2
3	Q4 + Q5	16	—

Table 5-22. Summary of synchrotron radiation power on the HEB crotch mask.

	Source	Power (W)	Normal linear flux (W/mm)	σ_y (mm)
1	Q2, incoming HEB side	4330	570	0.5
2	B2, incoming HEB side	99	13	>1.0

5-22 are for a zero-emittance beam, as this yields the most pessimistic result; the combined synchrotron radiation stripe was assumed to have σ_y = 0.5 mm. The vertical power distribution used in the analyses is shown in Fig. 5-79. The heat flux near the peak is 420 W/mm^2.

The above linear power density and heat flux are much too high for normal incidence, so the mask surface must be sloped relative to the incoming synchrotron radiation fan. Several slopes, ranging from 10:1 to 20:1 were investigated. A slope of 14:1 was ultimately selected and found to give reasonable temperatures and stresses. At a slope of 14:1, the linear power density becomes 42 W/mm, and the peak heat flux becomes 30 W/mm^2.

Initially, an uncooled tungsten mask was considered. However, it was found that the peak temperature on a mask that would fit into the available space was in excess of 2600°C. At that temperature, tungsten has a vapor pressure of about 10^{-4} Torr, and the evaporation rate is 0.6 μm/hr. Needless to say, radiation cooling was not considered further.

The mask design ultimately chosen and the synchrotron radiation orientation are shown in Fig. 5-80. Note that the leading edge (tip) of the mask must be tapered to avoid violating the beam-stay-clear region of the incoming low-energy beam. Because there is not room to locate the cooling water directly behind the heated surface, the mask must be edge cooled, with cooling tubes at the top and bottom. Figure 5-81 shows the mask in more detail. The mask will be fabricated of a dispersion-strengthened copper, such as GlidCop C15715. This material was selected because it has a high yield strength, while retaining a high thermal conductivity—only 7% lower than that of OFE copper. Yield

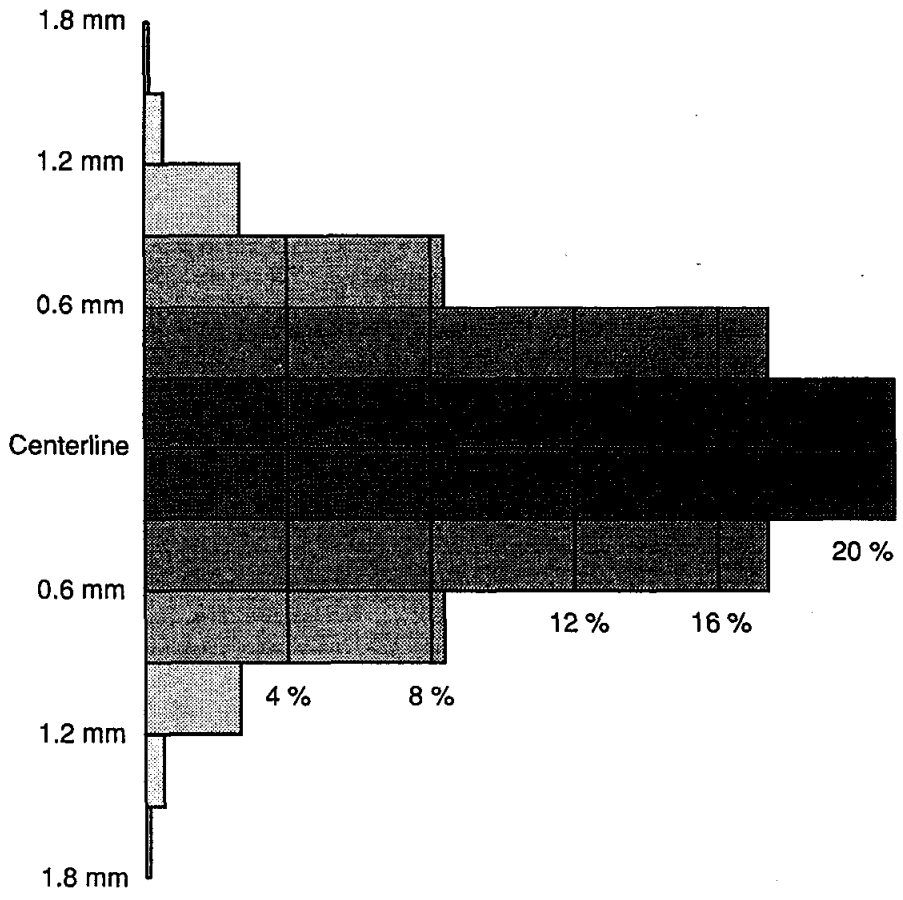

Fig. 5-79. Vertical synchrotron radiation power distribution assumed in thermal and stress analyses of HEB crotch mask.

strength is shown as a function of annealing, or operating, temperature in Fig. 5-77. Although the GlidCop yield strength is not as strong a function of temperature as is that for copper, its strength is somewhat (adversely) affected by temperature. Therefore, we plan to fabricate the mask from "as worked" material, without exposing the bulk of the material to brazing temperatures.

The mask and cooling passages will be machined from a single block of work-hardened GlidCop. Openings required to drill the cooling passages will be plugged, and cooling supply and return lines attached, by TIG brazing with an alloy such as Nicoro80. Using a TIG torch to braze allows the application of heat very locally at the braze joint, without subjecting the entire part to brazing temperatures. Sample TIG brazes have been made and found to be strong and vacuum leak tight. As mentioned above, double joints have been designed so that each vacuum joint has air rather than water on the outside. A second joint then separates water from air.

Two-dimensional spread-sheet analyses of mask temperatures were carried out to determine the feasibility of edge cooling. Various mask thicknesses and cooling-tube separations were studied. It was found that the maximum temperature dropped sharply

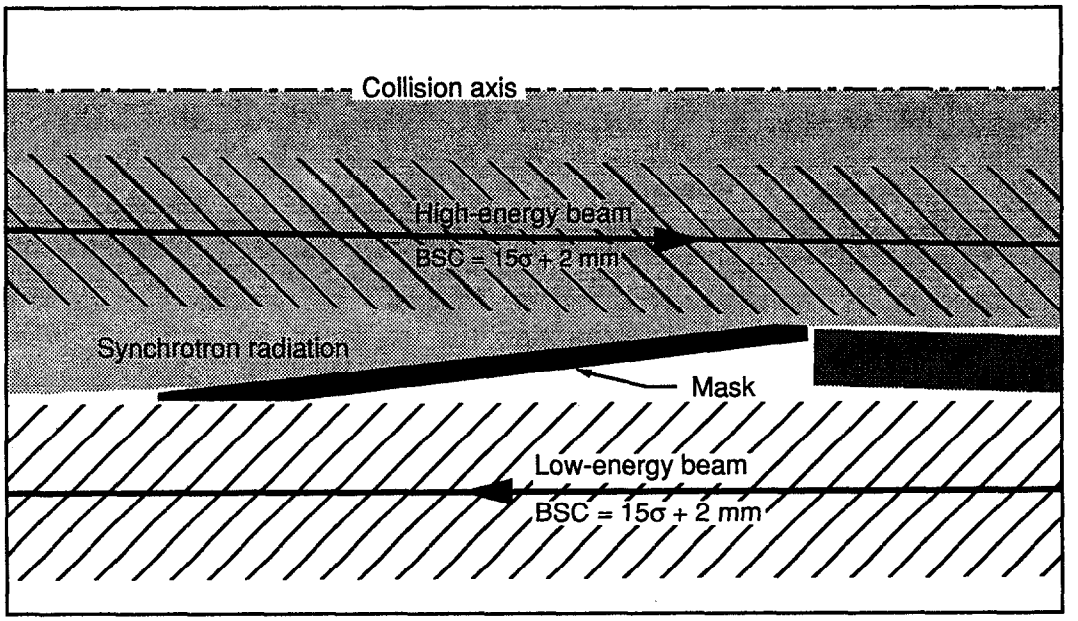

Fig. 5-80 Position of HEB crotch mask relative to impinging fan of synchrotron radiation. Beam-stay-clear areas are indicated by cross-hatching.

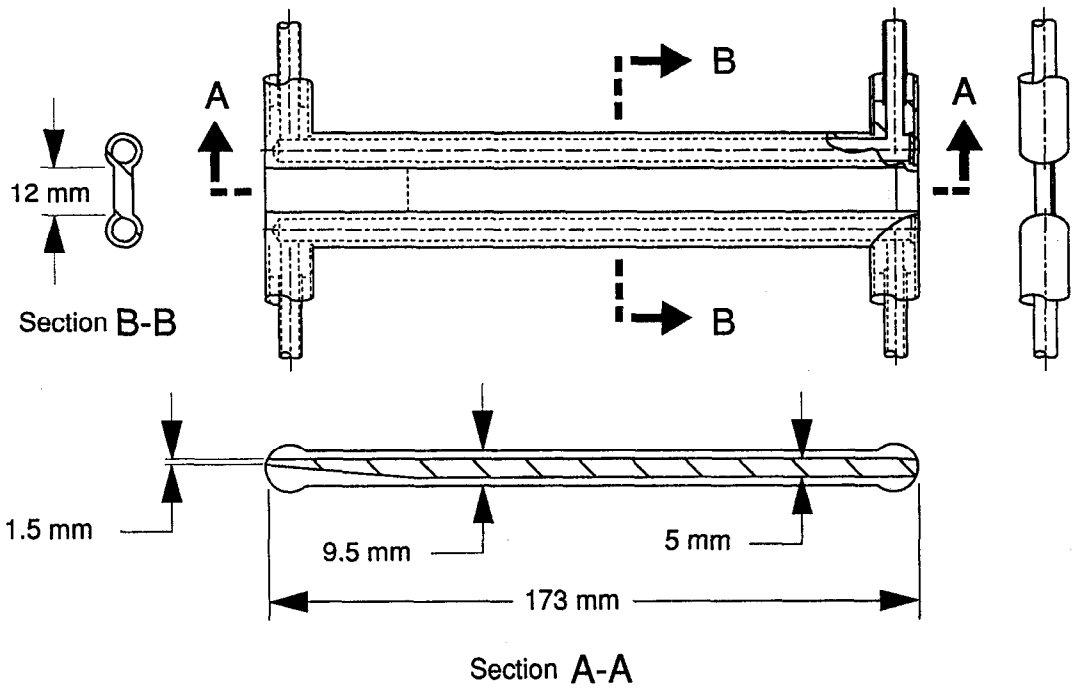

Fig. 5-81. Detail of HEB crotch mask.

with increasing mask thickness at thicknesses below 2 mm. Above 5 mm, however, added thickness actually increases the maximum temperature gradually. The results are plotted in Fig. 5-82. A 5-mm thickness gives both a maximum surface temperature that is near the minimum possible, and a reasonable interface temperature. Cooling-tube separation needs to be ±6 mm or greater to provide adequate clearance for the electron and positron beam-stay-clear regions.

A mask thickness of 5 mm and a distance of ±6 mm from beam centerline to water-cooling surface were chosen for a three-dimensional analysis using ANSYS. These results (see Fig. 5-83) show a maximum temperature of 253°C, which occurs on the beam centerline, approximately 9 mm beyond the edge of the synchrotron radiation fan, where the mask tapers to about a 3-mm thickness. Figures 5-83 and 5-84 show the geometry of the top half of the front portion of the mask used in the three-dimensional analysis. The top and bottom halves are mirror images, with the symmetry plane at the midplane of the synchrotron radiation fan. Highest temperatures and stresses occur in the tapered portion of the mask, near the front edge. The maximum stress is a compressive stress of 48,900 psi. It occurs on the beam centerline, approximately 11 mm from the fan edge. A maximum tensile stress of 18,400 psi occurs on the outside surface of the cooling channel at the end of the tapered section. The stress distribution is shown in Fig. 5-84.

The proposed design should be straightforward to fabricate. The vapor pressure of copper at 250°C is negligible, and the GlidCop yield strength at 250°C is 68,000 psi, well above what is required.

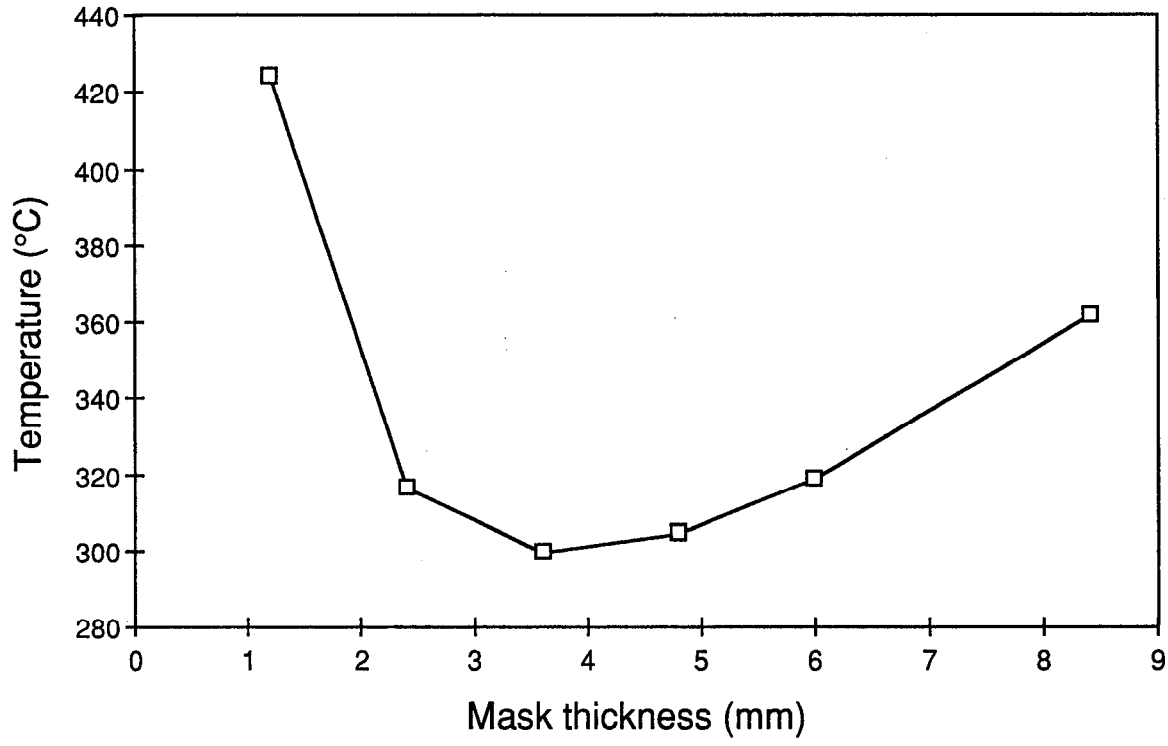

Fig. 5-82. Maximum HEB crotch mask temperature as a function of metal thickness.

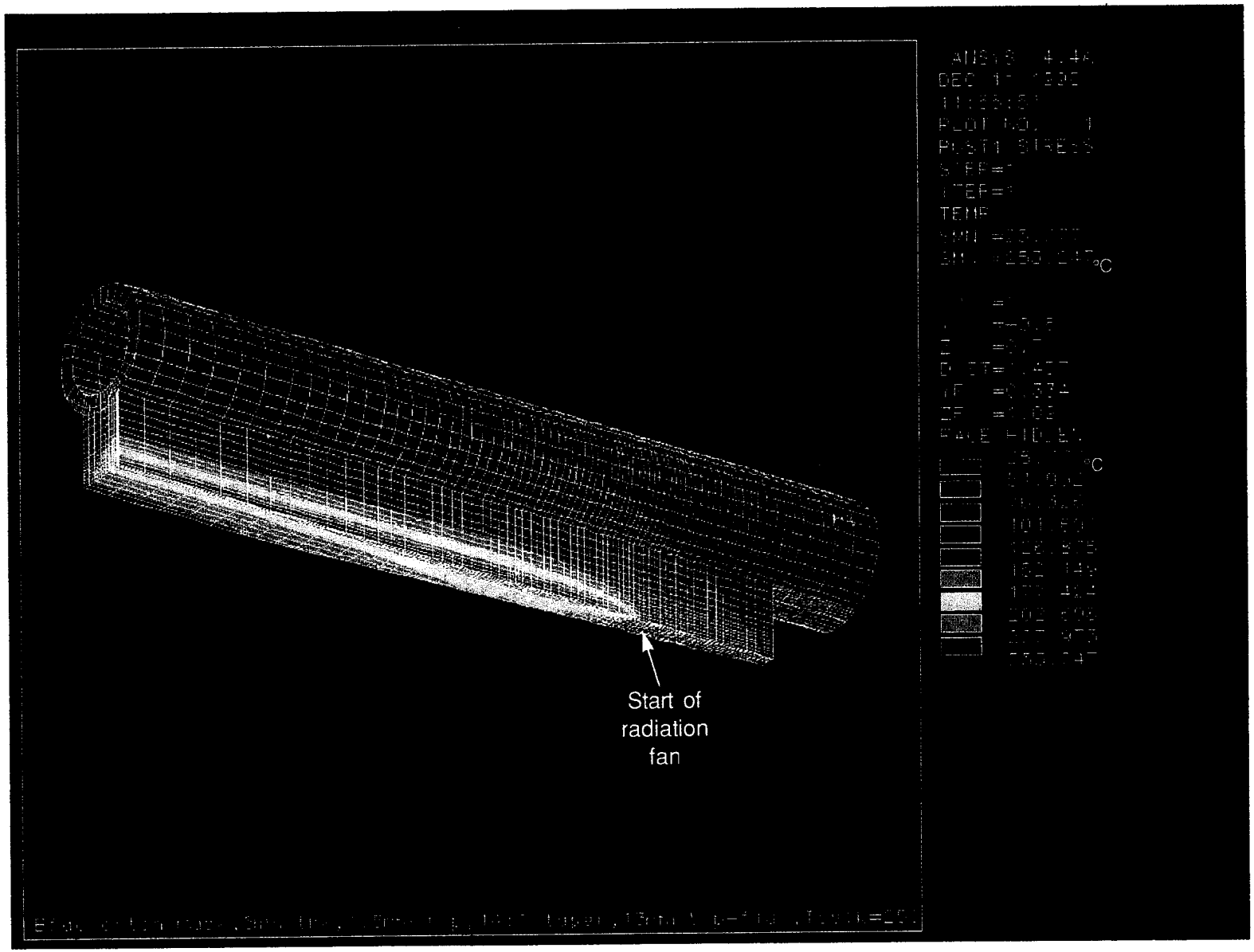

Fig. 5-83. Temperature distribution on HEB crotch mask from 3-D finite-element analysis.

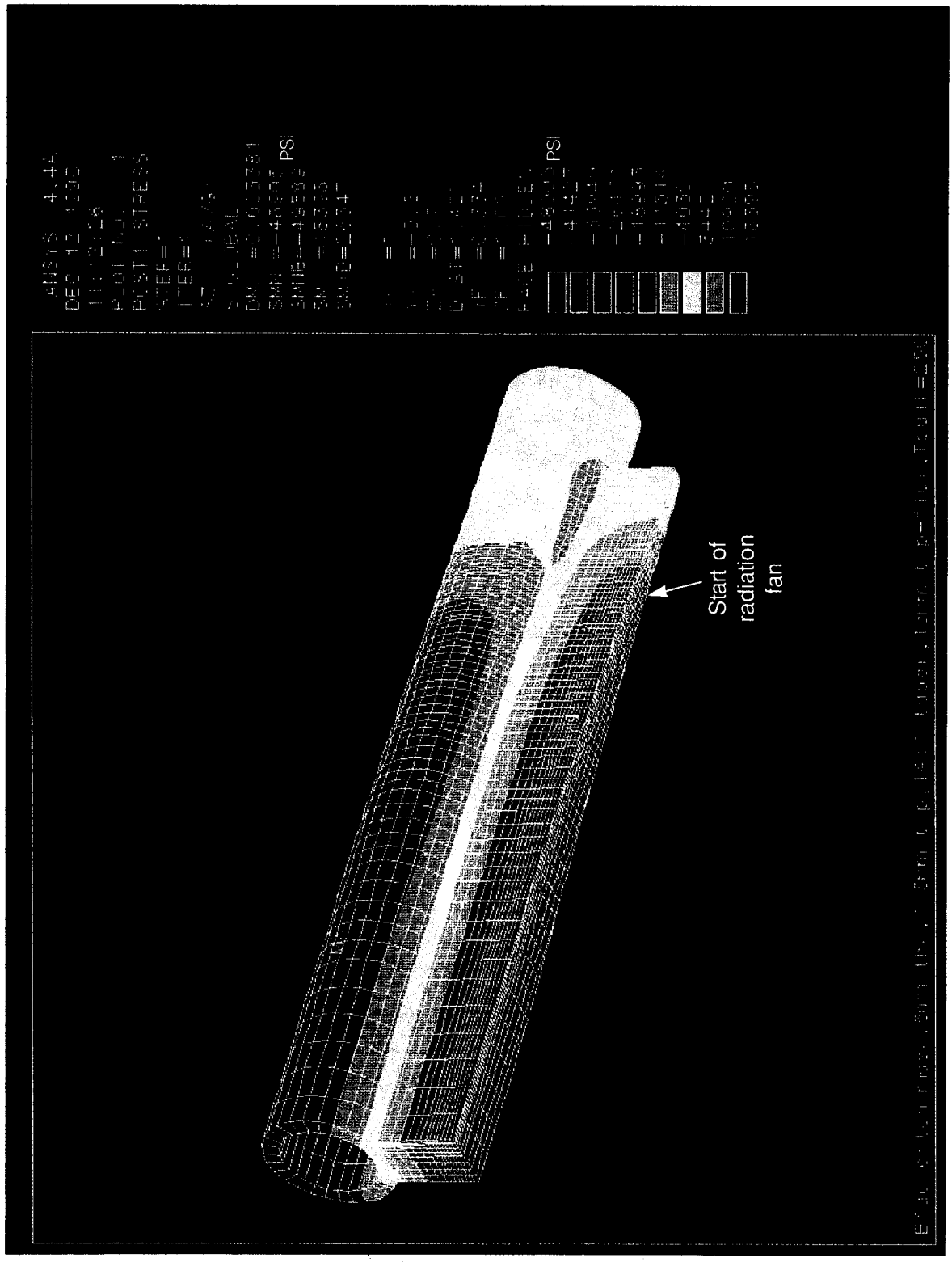

Fig. 5-84. Stress distribution on HEB crotch mask from 3-D finite-element analysis.

It is important to remember that the maximum temperature, and therefore the stress, rise rapidly with decreasing thickness below 2 mm (see Fig. 5-82). Therefore, the synchrotron radiation fan must not be allowed to strike too near the tip of the tapered portion of the mask (where the mask is thinner). In particular, the tip of the mask must be out of the radiation fan. A temperature-sensor located in the tip of the mask and connected to a beam abort system is provided to protect the mask from overheating.

A convection conductance h of 0.028 W/mm^2 per °C was used in all the analyses. A relatively high water velocity, 12 ft/s, is needed to reach such a value. To attain this water velocity in the two 7-mm-diameter cooling passages requires a total flow of about 4 gpm. At this flow rate, the water temperature rise will be about 4°C.

5.2.7.5 Low-Energy Beam Crotch Mask. The crotch ahead of Q4 on the incoming HEB side of the IR sees synchrotron radiation generated by the LEB as it passes through the Q1 magnets on both sides of the IP. The vacuum chamber wall at the crotch must therefore be protected from synchrotron radiation. Characteristics of the portions of the synchrotron radiation fans that hit the mask are summarized in Table 5-23.

The total power deposited in the mask is 383 W. The synchrotron radiation fan from source 1 in Table 5-23 covers the entire crotch width. The synchrotron radiation fan from source 2 covers 3.1 mm of the 11-mm-wide crotch, and the fan from source 3 covers the remaining 7.9 mm. For thermal and stress analyses, we assumed the sum of sources 1 and 2 to be the worst case, and then applied this power across the entire mask width. On this basis, the linear flux density is 41 W/mm. To be conservative, we assumed also that the beam σ_y is 0.8 mm for both fans. This value is a worst-case estimate based upon the assumption of a zero-emittance positron beam.

The above linear power density is about the same as that normal to the surface of the HEB crotch mask (at a 14:1 slope). The rms beam size here is 1.6 times that on the HEB side. We conclude, therefore, that the LEB mask need not be sloped. Its face can be normal to the synchrotron radiation fan. The mask geometry is shown in Fig. 5-85. The mask material is a dispersion-strengthened copper, such as GlidCop, because thermal stress levels preclude the use of oxygen-free copper.

A two-dimensional spread-sheet analysis of mask temperatures indicates that the mask should be at least 8 mm thick to give a maximum temperature at the copper-water interface that will avoid any possibility of boiling. Thickness, in this case, refers to the

Table 5-23. Summary of synchrotron radiation power on LEB crotch mask.

	Source	Power (W)	Normal linear flux (W/mm)	σ_y (mm)
1	Q1, LEB side	186	17	1.14
2	1st half Q1, HEB side	75	24	0.8
3	2nd half Q1, HEB side	122	15	0.7

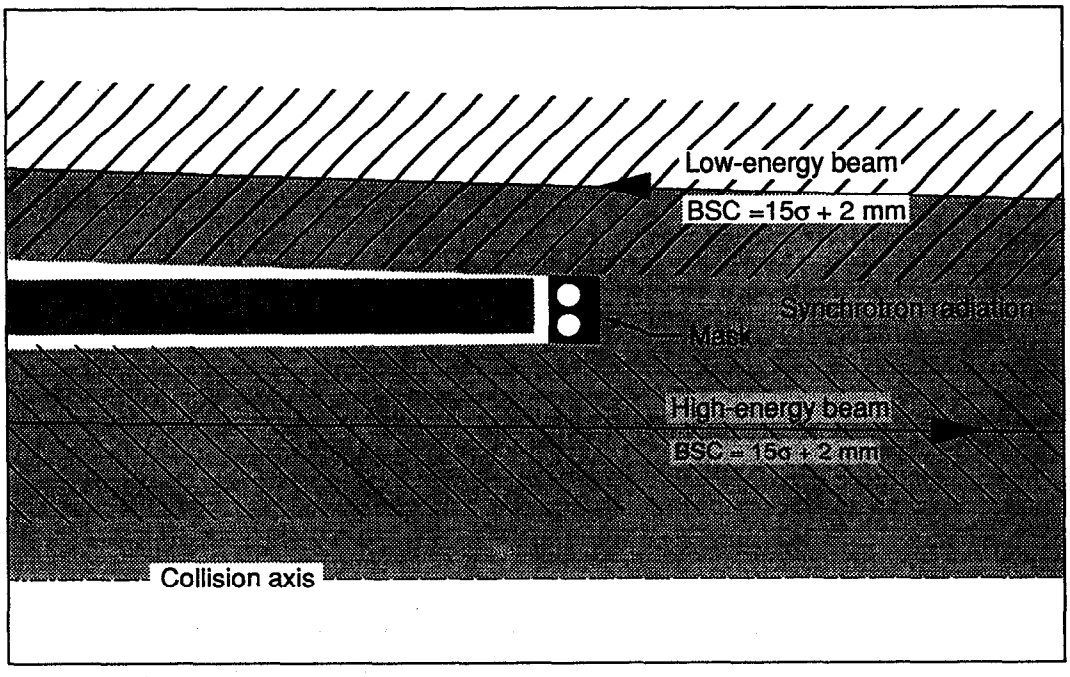

Fig. 5-85. Position of LEB crotch mask relative to impinging fan of synchrotron radiation. Beam-stay-clear areas are indicated by cross-hatching.

distance from the heat-absorbing face to the water-cooled face. The thicker the mask, the lower the maximum interface temperature, as can be seen in Fig. 5-86. However, as shown in Figs. 5-87 and 5-88, the thicker the mask, the higher the maximum temperature and therefore the stress. In this case, stress was determined by a simple calculation, assuming that $\sigma = E\alpha\Delta T$ at the maximum temperatures calculated above. Note that the above results are for oxygen-free copper; temperatures for GlidCop will be slightly higher and stresses about 5% higher.

The yield strength of GlidCop near 200°C (see Fig. 5-77) is about 69 ksi. If the stress is to be kept below 75% of yield, the thickness should not exceed about 10 mm. At 10 mm, the maximum temperature is about 170°C, and the stress is 50 ksi (72% of yield). To retain high yield strength, the mask will be fabricated from "as worked" material, and joints will be made by TIG brazing, as for the HEB crotch mask.

The peak heat flux is 1.5 W/mm^2. Such a value is manageable without boiling by maintaining a high water velocity (say, 12 ft/s) over the cooled surface. If the cooling passage inner diameter is 7 mm, a flow of 2 gpm is needed to attain this velocity. At such a flow, the water temperature will rise by only 0.7°C.

5.2.7.6 Vertex Detector Vacuum Chamber. The vertex detector vacuum chamber must be designed to be compatible with the detector requirements. This means that it must

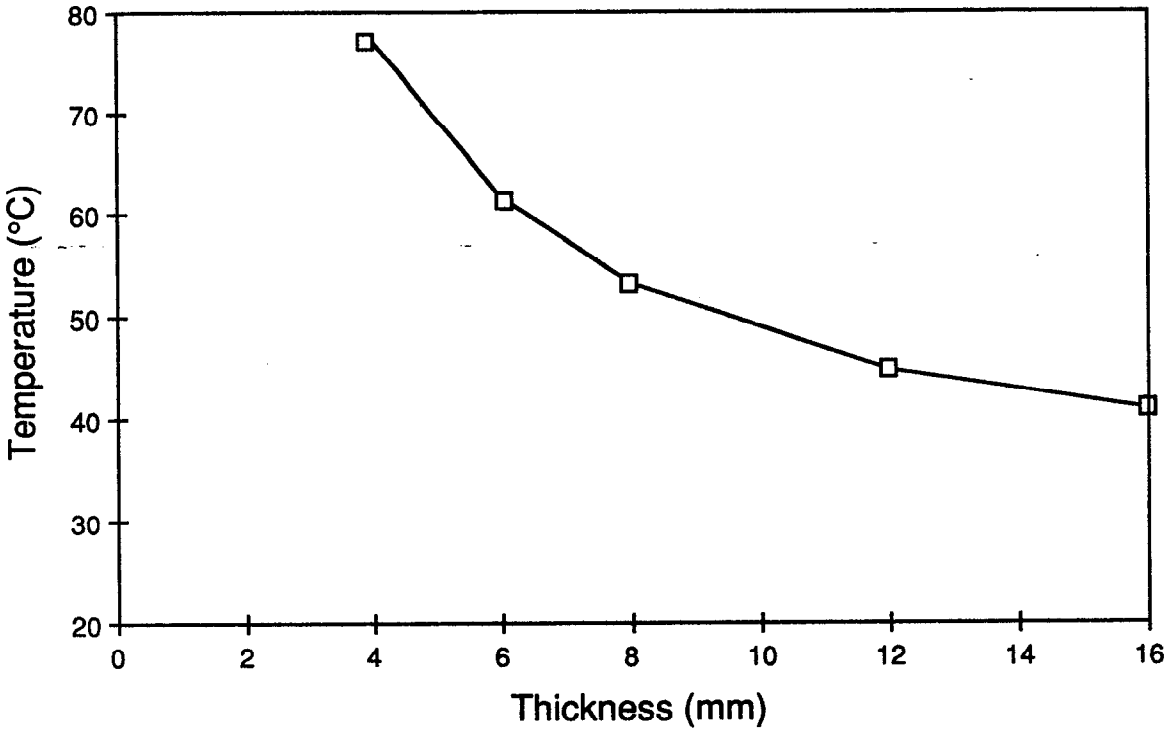

Fig. 5-86. Maximum cooling-surface temperature for the LEB crotch mask as a function of metal thickness.

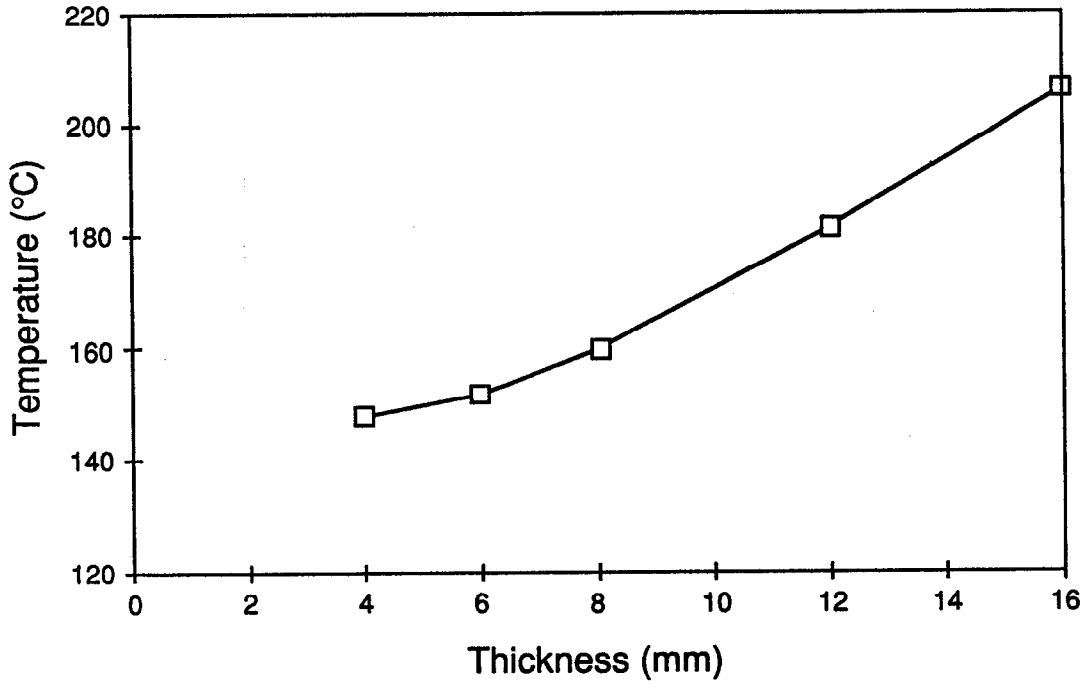

Fig. 5-87. Peak metal temperature on the LEB crotch mask as a function of metal thickness.

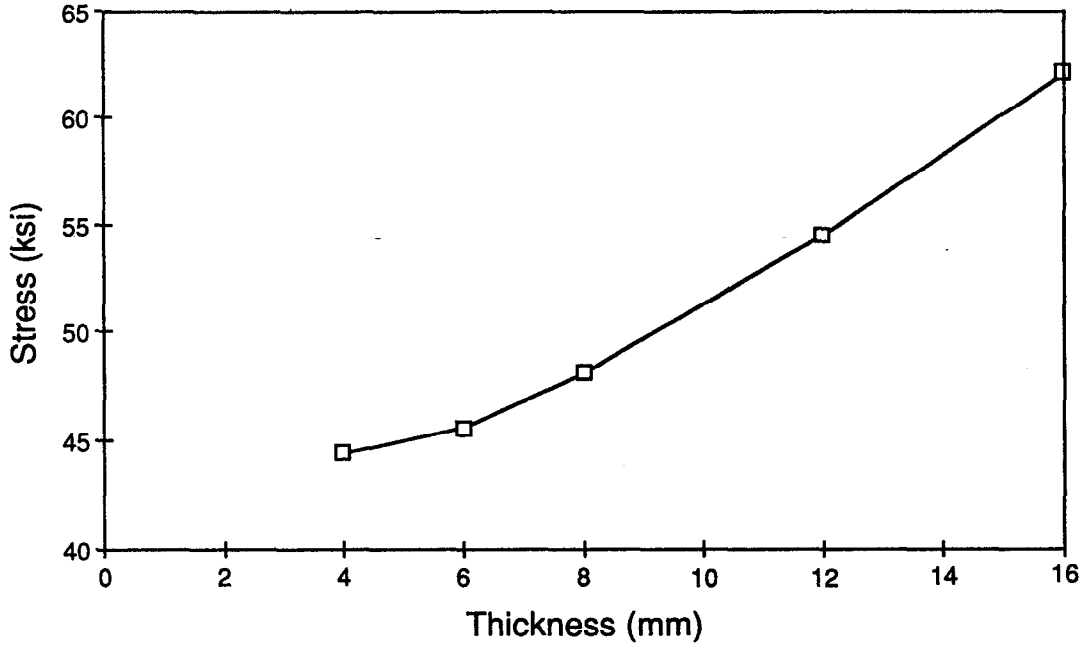

Fig. 5-88. Peak thermal stress on the LEB crotch mask as a function of metal thickness.

have the following features:

- It must be as transparent as possible to outgoing particles and photons from the collisions.
- It must have as small an outside diameter as possible.
- It must have an inside diameter of 50 mm or less.
- It must be approximately 300 mm long.

Because heat deposited in the chamber by HOM heating and resistive heating will be about 200 W, the vertex detector vacuum chamber must also be cooled.

Beryllium was chosen for the chamber wall material because of its low Z and relatively high strength. The possibility of a beryllium tube cooled only at its ends was considered, but a double-walled tube with a cooling fluid in the annular space was found to be a more transparent and more efficiently cooled design. An illustration of the chamber concept is shown in Fig. 5-89. The ends of the beryllium tubes are brazed to stainless-steel ends. A spacer ring between the inner and outer tubes at each end maintains concentricity between the tubes to form an annular cooling passage 2 mm wide. The stainless-steel ends are welded to the spacer ring to seal the ends of the passage. Stainless-steel-to-beryllium joining technology that was used in the construction of the SLD beryllium vertex chamber will be used. Figure 5-90 is a photograph of the SLD chamber.

The outer wall thickness of the vertex detector chamber pipe is 0.4 mm, and its inner wall has a thickness of 0.8 mm. Both will withstand a pressure of about 50 atm. Coolant pressure will be considerably lower than this, so the safety margin is substantial. Indeed,

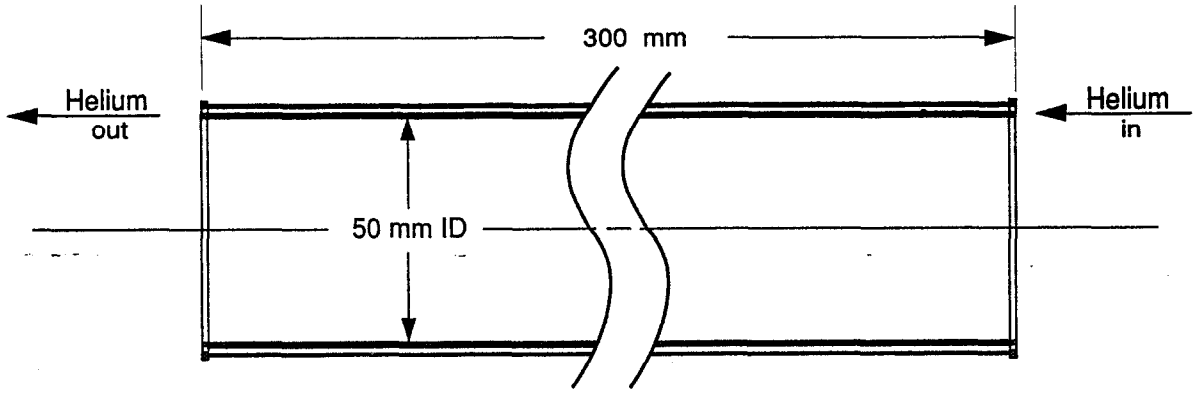

Overall length, 300 mm
Inner tube thickness, 0.8 mm
Outer tube thickness, 0.4 mm thick
Gap between tubes, 2 mm

Fig. 5-89. Design for the double-walled beryllium vacuum chamber for the vertex detector. Helium at 2 atm is used as the coolant.

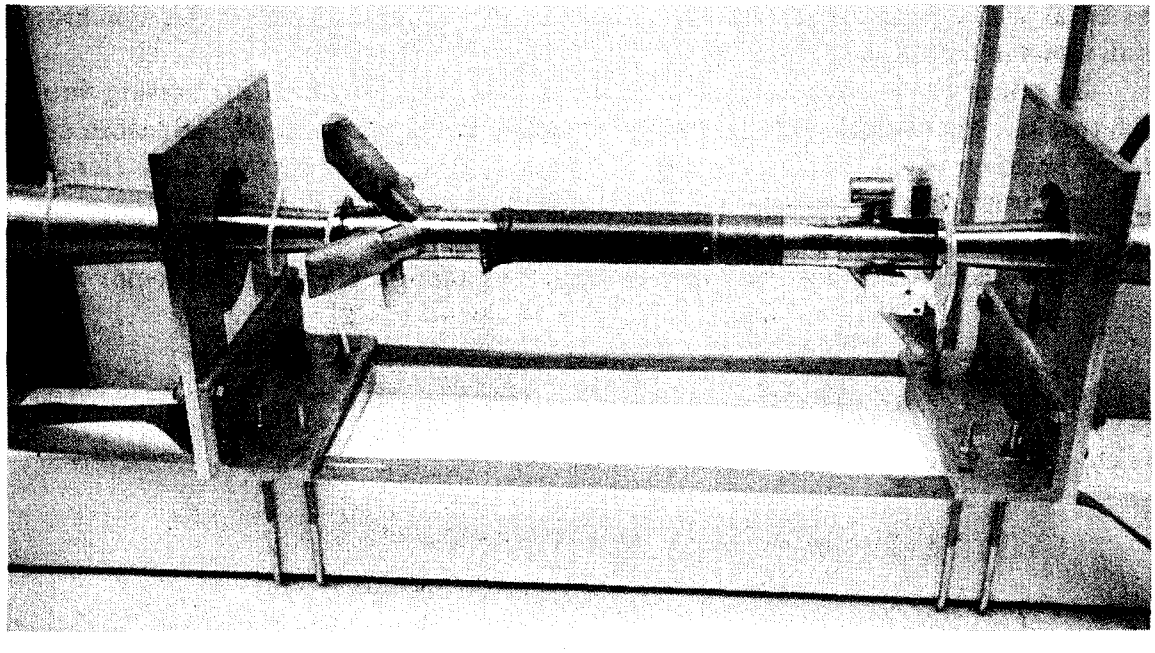

Fig. 5-90. Photograph of SLD vertex chamber.

the thickness was chosen primarily to make the chamber more rugged and to minimize chances of damage in handling.

Helium, hydrogen, and water were all considered as possible coolants. Although helium is not quite as good a coolant as either water or hydrogen, the fact that it is inert led to its being the coolant of choice. Beryllium and water appear to be compatible, but some beryllium would certainly enter the water and be carried by it. Concern about leaks and spills, and the resulting possibility of contamination, thus ruled out water. Hydrogen should be compatible with beryllium, but was ruled out because of its flammability.

Helium pressurized to 2 atm is quite adequate as a coolant. A flow of 22 g/s (Mach number = 0.2) gives a helium temperature rise of 1.1°C and a film temperature drop of 2°C for a 200-W heat input. Thermal stresses are quite low at these temperature differences. At least twice as much heat could be removed by the above flow should it prove necessary. Furthermore, the wall thicknesses adopted would allow the use of higher-pressure helium in the event that still more heat needed to be removed. Thus, the vertex chamber beam pipe is very reliably and conservatively designed for use in the B Factory.

5.2.7.7 Synchrotron Radiation Dumps. The synchrotron radiation fans created by the HEB passing through the two B1 and the two Q2 magnets carries some 80 kW of power. To keep IR backgrounds low and to allow the synchrotron radiation fans to spread, the bulk of the HEB synchrotron radiation fan is dumped at a location 12–15 m away from the IP. At 12 m, the synchrotron radiation fan linear power density from the two B1 magnets is 580 W/mm. The linear power density from the two Q2 magnets is only slightly lower. At 12 m from the IP, the fans have spread vertically to $\sigma_y = 1.2$ mm.

If the vacuum chamber wall has a slope of 11:1 relative to the fan, the radiation is absorbed over a length of about 2 m. The maximum linear power density is about 55 W/mm. This power is removed by a longitudinal cooling-water line that is brazed to the external wall of the copper vacuum chamber, just outside of where the synchrotron radiation fan strikes.

The power carried by synchrotron radiation fans created by the LEB passing through the two B1, the two Q1, and the two Q3 magnets is only about 8 kW. Because of the lower beam energy, vertical spreading will be even greater than for the HEB. Here also, the synchrotron radiation fans will be absorbed on the water-cooled vacuum chamber wall starting about 12 m from the IP.

Clearly, heat removal will not be a problem for either the HEB or LEB dump.

5.3 SURVEY AND ALIGNMENT

The primary goal of the survey and alignment activity for the Asymmetric B Factory is to align the lattice components along a "smooth" curve. This should be done in such a way that the rms deviations of components from this curve do not exceed 150 μm and that the resulting circumference is within 5 mm of its design value. Overall tolerances for the alignment of the various ring components are summarized in Table 5-24. As can be seen from this table, the most important alignment criterion is the *relative* accuracy requirement. Consequently, long-period systematic effects on the measurements and computations can be neglected. This means that we need not be concerned about effects like geoid undulations, deflections of the vertical, earth tides, site-wide water table changes, etc.

For the installation of the machine, modern computer-aided methods and procedures, which have been tested and proved at SLC, HERA, and LEP, will be applied to perform the alignment. The specific alignment tasks that are required include the following, each of which is taken up in a subsequent section:

- Support the component fiducialization effort
- Align modules and girder components in the alignment laboratory
- Perform "blue-line" survey of anchor bolt positions for supports
- Rough-align the supports
- Rough-align the components
- Final-align (smooth) the components
- Align the interaction region components
- Perform quality control surveys

5.3.1 Preliminary Considerations

Before expanding on specific tasks, some fundamental alignment requirements must be introduced.

5.3.1.1 Fiducialization. The virtual magnetic axis of each component must be related to external fiducial marks. Since the fiducialization error is budgeted as part of the overall alignment error, it should be kept very small. Otherwise, it will dominate the alignment error budget, thereby eliminating most of the allowable error margin for the positioning of the fiducial relative to the traverse monuments. In general, the fiducialization error should be kept below 50 μm to facilitate a successful alignment.

Because the low-energy ring (LER) is mounted above the high-energy ring (HER), there is inadequate space to mount alignment equipment on top of the HER magnets. Consequently, placement of permanent alignment fiducials on the tops of magnets is impractical. Therefore, we plan to incorporate reference grooves in the magnet

Table 5-24. B Factory alignment tolerances.

Global tolerances	
Horizontal and vertical positioning of quadrupoles (rms) [mm]	1.5
Horizontal and vertical positioning of sextupoles (rms) [mm]	1.5
Horizontal and vertical positioning of dipoles (rms) [mm]	4
Roll angle of quadrupoles (rms) [mrad]	1
Roll angle of sextupoles (rms) [mrad]	1
Roll angle of dipoles (rms) [mrad]	0.3
Circumference [mm]	5
Component-to-component tolerance	
Sextupole to quadrupole within a module (rms) [mm]	0.10
Horizontal and vertical position of quadrupoles and sextupoles in injection coast line [mm]	0.5
Smoothness tolerance	
Quadrupole-sextupole pair to quadrupole-sextupole pair (rms) [mm]	0.15

laminations that will allow alignment reference fixtures to be mounted on the aisle side of the components.

5.3.1.2 Coordinate System. Before performing the survey and alignment procedure, we must first define a coordinate system in which all measurements will be reported. For a machine of this size, the fact that the local shape of the earth is not planar, but somewhat spherical, must be taken into consideration. If the primary datum of the coordinate system is defined such that it coincides with the center of the ring, then, at least to a first approximation, the machine is built in a common tangential plane. This means that the horizontal direction with respect to gravity is also "horizontal" in the layout coordinate system, within the required accuracy. However, this horizontal plane is inclined with respect to the common SLAC coordinate system. With this in mind, the B Factory alignment coordinate system will have the following properties:

- Right-handed system
- Primary datum at the center of the ring
- Y-axis parallel to gravity at datum point
- Z-axis perpendicular to Y, along the SLAC linac axis, with the downstream direction of the linac defined as positive
- X-axis perpendicular both to Y and Z.

A rotation matrix will be defined to perform transformations between the local B Factory coordinate system, as defined above, and the global SLAC coordinate system.

5.3.1.3 Control Networks. Computer simulations have shown that the global tolerances for the positioning of the lattice components can be met without the supporting framework of a surface network. However, it was assumed that the tunnel control traverse can be measured all around the ring in one survey. The B Factory tunnel horizontal net will be established as a traverse with stations every 7.54 m, that is, adjacent to the middle of the HER bending-magnets. As floor marks, we will use a new design of three-dimensional "reference cups," a design adopted from the ALS now under construction at LBL. This design, combined with the new ALS "monopod" instrument stand, is highly efficient and accurate; it virtually eliminates the task of centering instruments and targets over monuments. Furthermore, the elevation of the instrument above the three-dimensional reference cup is known very accurately, which facilitates three-dimensional mapping with theodolites. The traverse layout will be modified as necessary to accommodate the bridging of interaction halls and to provide for the subsequent alignment of the interaction region components.

The fact that the PEP tunnel lies in a horizontal plane makes a liquid-leveling system practical and efficient. We will therefore refurbish and reinstall the existing PEP liquid-leveling system. The primary upgrade will involve replacing the present copper tubing with stainless steel. The tie to the linac and the SLAC-wide elevation datum will be made using differential-leveling procedures.

5.3.2 Survey and Alignment Tasks

5.3.2.1 Girder and Module Alignment in the Laboratory. The HER quadrupole-sextupole pairs will be aligned with each other in the laboratory and thereafter treated as a module; that is, their relative alignment will not be adjusted in the tunnel. The dipole-quadrupole-sextupole-BPM modules on each LER girder will also become a laboratory-aligned unit whose relative alignment will not be adjusted in the field. Traditional optical-tooling techniques can provide the 0.1-mm relative alignment required for this procedure.

5.3.2.2 Blue-Line Survey. In preparation for the installation of the support systems, a blue-line survey will be performed to lay out the anchor bolt positions. This will be done from the tunnel traverse points using intersection methods. An accuracy of 5 mm, which is more than sufficient, can be easily achieved.

5.3.2.3 Rough Alignment of Supports. After the blue-line survey, the anchors and support systems will be installed, but with the anchor bolt nuts only hand tight. At this point, the adjustment systems for the components are already mounted on the supports and adjusted to a midrange position. Using laser theodolites (set up on traverse points) and inclinometers as control instruments, the supports will be tapped into position to an accuracy of about 5 mm. This is especially important for the C-frame supports, because a small roll displacement will have a large correlated horizontal (x) effect for the LER components. If not controlled, this type of support misalignment could easily exceed the adjustment mechanism range of individual components.

5.3.2.4 Rough Alignment of Components. After the magnets are installed, they will be positioned relative to the traverse monuments to an accuracy of about 0.3 mm. This will be done with a two-step procedure:

- Bring the magnets to their ideal elevations and set their pitch and roll values to zero, using differential-leveling techniques
- Map the horizontal positions of quadrupole-sextupole pairs relative to the traverse points, using triangulation methods

The mapped positions will be compared with their ideal values to determine the required mechanical adjustments. The subsequent application of adjustments will be controlled using digital indicators. Two iterations should yield the desired accuracy. For the injection lines in the linac, traditional optical tooling techniques will be used. The linac tooling reference holes, after they have been mapped using the linac Fresnel lens alignment system, will provide the necessary tunnel control.

After the quadrupoles are aligned, the horizontal positions of the HER dipoles will be set using the HERA CCD-theodolite technique. Fixtures are attached to neighboring quadrupoles such that one supports a theodolite equipped with a CCD camera and the next a special target. The theodolite is aimed at the target, and another target is mounted on the dipole between the two quadrupoles. The surveyor then watches a video screen while moving the dipole to determine when it is properly aligned.

The alignment of the matching sections, the barrel, and the detector will lend itself to the standard rough alignment technique. Fiducials on the outermost magnets of the barrel will be visible from the aisle. These fiducials will be used to align the barrel.

5.3.2.5 Smoothing of Quadrupoles and Sextupoles. The "smoothness" of a beamline refers to the quality of the relative positioning of a number of adjacent beam-guiding components. The fact that smoothness is of the highest importance in terms of positioning magnets can be judged from the relative tolerances imposed by the beam optics (see Table 5-24). The benefits of the smoothing technique are that it eliminates the effects of unknown systematic errors and that it minimizes the number and size of magnet movements necessary to reach the final alignment criterion.

The observation plan best suited for this method is a three-dimensional traverse measured directly over the components to be smoothed. Unfortunately, for the B Factory design, there are constraints that make this scenario impossible. To have unobstructed lines-of-sight from one magnet to two adjacent ones in both directions, the measurements must be performed either on top of the magnets or on the side nearer the center of the ring. Because of the vertical arrangement of the two rings, there is no room on top, as mentioned above. In addition, the magnets are located near the wall closer to the center of the ring, so there is not enough room for measurements there either. Therefore, the observations must be carried out from the traverse stations on the aisle side.

From the aisle-side traverse stations, horizontal and vertical direction sets will be measured to the four nearest quadrupole-sextupole pairs. To strengthen the network, distances will be measured from station to station. One important difference from the rough positioning step described earlier is that the traverse stations will only be treated as tie points; that is, we will not introduce their known coordinates into the least-squares

adjustment, but rather treat them as unknowns. Repeated test smoothings carried out in the SLC arcs and Final Focus beamline have shown that 150-μm smoothness can be obtained in one iteration; a second iteration will improve this to better than 100 μm. (Note that we refer here to the rms value of the residual magnet fiducial displacement relative to a smooth curve, without including any fiducialization error.) The matching sections and the barrel will be included in the smoothing procedure, as will the NIT and SIT parts of the injection lines. The alignment tolerances of the injection bypass lines (the injection transport lines in the linac tunnel) do not warrant smoothing.

5.3.2.6 Quality Control. After completing the final smoothing step, the positions of all components will be mapped one more time to confirm that the alignment tolerances have been met.

5.4 POWER SUPPLIES

In this section we describe the power supplies required for the B Factory. For both the HER and LER, many of the supplies are very similar in function. These are described together in Section 5.4.1. In the common interaction region of the two rings, there are a number of special magnets that serve to focus and to separate the two beams. Power systems for these magnets are discussed in Section 5.4.2. Finally, in Section 5.4.3 we discuss the power supplies required for the injection system. Most of these supplies—along with the magnets they power—are already in existence. The primary exceptions to this are the supplies for the interaction region.

5.4.1 HER and LER Power Supplies

The HER and LER power supply systems are divided into a number of independent supply strings, as listed in Table 5-25 for the HER and Table 5-26 for the LER. Since the strings for the two rings are identical in most respects, save only their detailed electrical characteristics, they are described together in the following paragraphs.

5.4.1.1 Bending Magnet Strings. The HER utilizes a single bending magnet string of 192 dipoles, connected in series (see Fig. 5-91a) by existing water-cooled aluminum cables. The LER requires a similar string but, in this case, only 180 dipoles are on the main bus. One dipole at each end of each LER arc, denoted BL (left of straight, see Fig. 4-17) and BR (right of straight, see Fig. 4-18), is powered differently from the main string; these magnets are on independent busses as shown in Fig. 5-91b. The magnet connections consist of a supply cable and a return cable, with the turnarounds at IR-2 and the supplies at IR-8 (see Figs. 5-91a and 5-91b). Supply and return cables are arranged to cancel the residual field due to the high cable currents. Supply and return cable connections alternate every sector or half-sector to minimize the voltage to ground and to cancel current differences in the bending magnets that would otherwise develop as a result of current leakage to ground through cooling hoses or stray capacitance. The HER bending magnets require a maximum of 660 A, regulated to 0.01%; the main bending magnet string is supplied by two 500-V power supplies connected in series and located at IR-8. For the LER, the maximum current is 850 A, regulated to 0.01%; the main bending magnet string is supplied by four 500-V power supplies, also connected in series and located at IR-8. Two more supplies with the same rating are used for the offset dipole (BL and BR) strings. All these supplies will be refurbished PEP chopper-type supplies, upgraded with new power hardware and controls.

5.4.1.2 Quadrupole Magnet Strings. The quadrupole magnets of both rings fall into three main functional groups: arc quadrupoles; dispersion-suppressor quadrupoles; and straight-section quadrupoles. The straight-section quadrupoles further subdivide into quadrupoles for "normal" straights, injection straights, phase-trombone straights, wiggler straights and the collision straight.

Table 5-25. HER power supplies. In some cases the string voltage is dominated by cable voltage drop.

Magnet string name	Number of magnets	Current per magnet (A)	Voltage per magnet (V)	String voltage (V)	Number of supplies	Power supply rating
Bending magnets	192	660	3.63	457	2	500V/850A
Arc quadrupoles QF	60	100	9.1	280	2	500V/140A
Arc quadrupoles QD	66	140	9.9	338	2	500V/140A
Straight quadrupoles QF	16	110	8.7	70	2	80V/140A
Straight quadrupoles QD	14	110	8.7	62	2	80V/140A
Phase trombone quads QF	16	110	8.7	9	16	15V/140A
Phase trombone quads QD	14	110	8.7	9	14	15V/140A
Suppressor quadrupoles QF	36	95	11.6	17	36	15V/140A
Suppressor quadrupoles QD	36	129	9.4	9	36	15V/140A
Injection quadrupoles QF1	2	95	6.7	13	1	15V/140A
Injection quadrupoles QD2	2	106	7.7	15	1	15V/140A
Injection quadrupoles QF3	2	140	6.5	13	1	15V/140A
Injection quadrupoles QD4	2	500	35.8	99	1	500V/850A
Injection quadrupoles QF5	2	620	44.6	123	1	500V/850A
IR4-IR12 sextupoles SF	48	54	2.4	124	1	500V/140A
IR4-IR12 sextupoles SD	48	90	3.9	202	1	500V/140A
IR12-IR4 sextupoles SF	24	128	5.7	6	24	15V/140A
IR12-IR4 sextupoles SD	24	128	5.7	6	24	15V/140A
Dipole trims	96	12	25	25	96	40V/12A
Corrector vertical bends	144	6	20	20	144	±40V/6A
Corrector horizontal bends	48	6	20	20	48	±40V/6A
IR skew quadrupoles	8	12	25	27	8	40V/12A
Skew quadrupoles	12	12	25	26	12	40V/12A

Table 5-26. LER power supplies. In some cases the string voltage is dominated by cable voltage drop.

Magnet string name	Number of magnets	Current per magnet (A)	Voltage per magnet (V)	String voltage (V)	Number of supplies	Power supply rating
Bending magnets	180	822	6.0	335	4	500V/850A
Offset magnets BL	6	580	4.2	120	1	500V/850A
Offset magnets BR	6	1060	7.8	221	1	500V/1200A
Arc quadrupoles QF	60	87	4.6	290	1	500V/140A
Arc quadrupoles QD	54	87	4.6	263	1	500V/140A
Straight quadrupoles QF	32	87	4.6	161	1	500V/140A
Straight quadrupoles QD	28	87	4.6	143	1	500V/140A
Phase trombone quads QF	16	87	4.6	5	16	15V/140A
Phase trombone quads QD	14	87	4.6	5	14	15V/140A
Suppressor quadrupoles QF	36	87	4.6	5	36	15V/140A
Suppressor quadrupoles QD	48	87	4.6	5	48	15V/140A
Injection quadrupoles QF1	2	31	2.2	5	1	15V/140A
Injection quadrupoles QD2	2	35	2.6	6	1	15V/140A
Injection quadrupoles QF3	2	56	4	9	1	15V/140A
Injection quadrupoles QD4	2	164	11.9	26	1	30V/200A
Injection quadrupoles QF5	2	200	13	29	1	30V/200A
Wiggler quadrupoles QF	8	140	7.8	10	8	15V/140A
Wiggler quadrupoles QD	7	130	7	9	7	15V/140A
IR4-IR12 sextupoles SF	48	56	3.5	177	1	500V/140A
IR4-IR12 sextupoles SD	48	56	3.5	177	1	500V/140A
IR12-IR4 sextupoles SF	24	56	3.5	4	24	15V/140A
IR12-IR4 sextupoles SD	24	56	3.5	4	24	15V/140A
Wiggler magnets	4	1800	300	602	2	620V/1800A
Wiggler bend magnets	8	750	5.4	40	2	40V/800A
Dipole trims	96	12	25	26	96	40V/12A
Corrector vertical bends	144	6	20	22	144	±40V/6A
Corrector horizontal bends	48	6	20	22	48	±40V/6A
IR skew quadrupoles	8	12	25	26	8	40V/12A
Skew quadrupoles	12	12	25	26	12	40V/12A

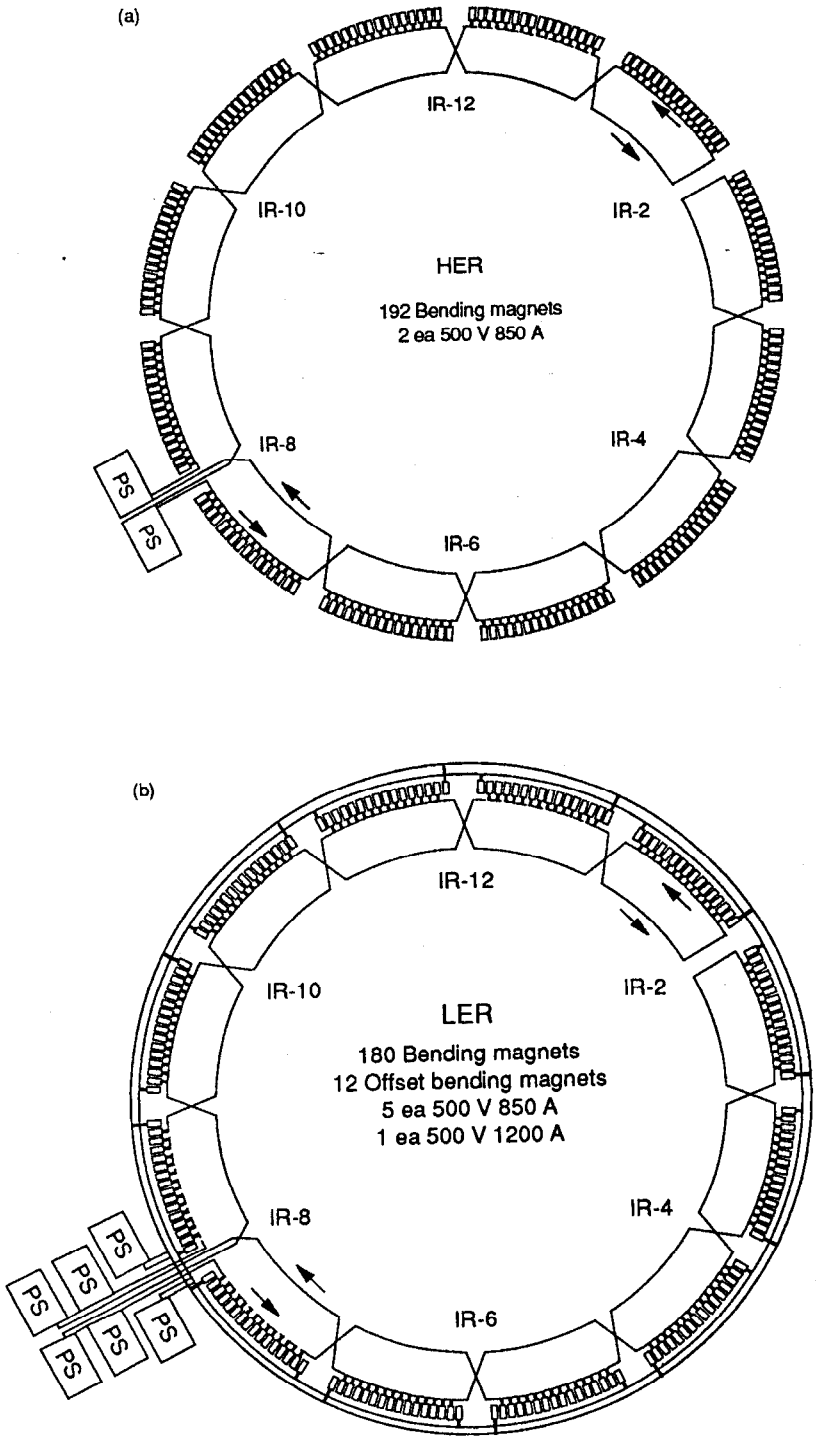

Fig. 5-91. Schematic of magnet and power supply connections for (a) the HER and (b) the LER bending magnet strings.

Arc Quadrupoles. The six arcs of each ring each have 12 horizontally focusing quadrupoles, QF, and 11 vertically focusing quadrupoles, QD, giving 72 QF and 66 QD quadrupoles in total. To help in tailoring the arc dispersion function in the HER, one QF quadrupole at each end of each arc needs to be independently powered. For similar reasons, in the LER there is one QF quadrupole and one QD quadrupole at each end of each arc that is independently powered. Figure 5-92a shows the circuits for the 60 QF and 66 QD magnets of the HER arc strings. Figure 5-92b shows the circuit powering the 60 QF and 54 QD quadrupoles of the LER that are on the main bus.

The main quadrupole busses for the two rings will use existing aluminum cables and do not require water cooling. The two cables will be powered with current flowing in opposite directions so as to help in cancellation of stray magnetic fields. The main arc quadrupoles require an operational current of 140 A (for the HER) and 90 A (for the LER), regulated to 0.01%, at a maximum of 350 V. These supplies will be refurbished PEP choppers, operating from the same DC supply as the bending magnet supplies. The independently powered quadrupoles at the ends of the arcs in the HER and LER are included in the dispersion-suppressor quadrupoles (see below).

Dispersion-Suppressor Quadrupoles. For the HER, the dispersion suppressors at both ends of each of the six arcs contain 6 quadrupoles, three vertically focusing and three horizontally focusing, giving 36 QD and 36 QF quadrupoles in all. Each of these magnets is powered by an independent 140-A power supply, regulated to 0.1%. The supplies are switching-type DC-to-DC converters, each locally mounted on the magnet girder and powered from a ring DC cable. Existing aluminum cables will be used for the DC source and will be powered from current-limiting regulated supplies (Fig. 5-93a) in buildings at IR-12, IR-8 and IR-4.

In the LER, the dispersion suppressors must occupy three full cells at each end of the arcs. (This is why the main LER quadrupole strings, QF and QD, have only 10 and 9 magnets per arc, respectively, or 60 and 54 magnets in all.) The LER dispersion suppressor quadrupoles, 36 QF and 48 QD magnets, have independent power supplies similar to those in the HER (see Fig. 5-93b).

Straight-Section Quadrupoles. The quadrupoles in the normal straight sections of the HER are arranged into FODO cells similar to those of the arcs (that is, they have the same cell length and phase advance, but the dipoles are absent). In the HER, normal straight sections are in regions 12 and 4 (these regions being where the RF for the HER will be located). The LER has no normal straights as such—every straight is required for some special purpose. The normal straight sections for the HER each utilize 8 QF and 7 QD quadrupoles (see Fig. 5-94a). The QF and QD magnets are connected in two strings, each powered in series from a supply having an operating current of 140 A, regulated to 0.01%, at a maximum of 70 V. These commercially procured, current-regulated supplies will be installed in the IR-12 and IR-4 support buildings.

The injection straight sections are in region 8 (for the LER, Fig. 5-94b) and region 10 (for the HER, Fig. 5-94a); they are configured identically for both rings. Each is symmetrical about its center, having a triplet structure (QF1, QD2, QF3) close to the arc and a doublet structure (QD4, QF5) nearer the center. Each of the five independent supplies for one ring feeds one pair of magnets located symmetrically on the two sides of

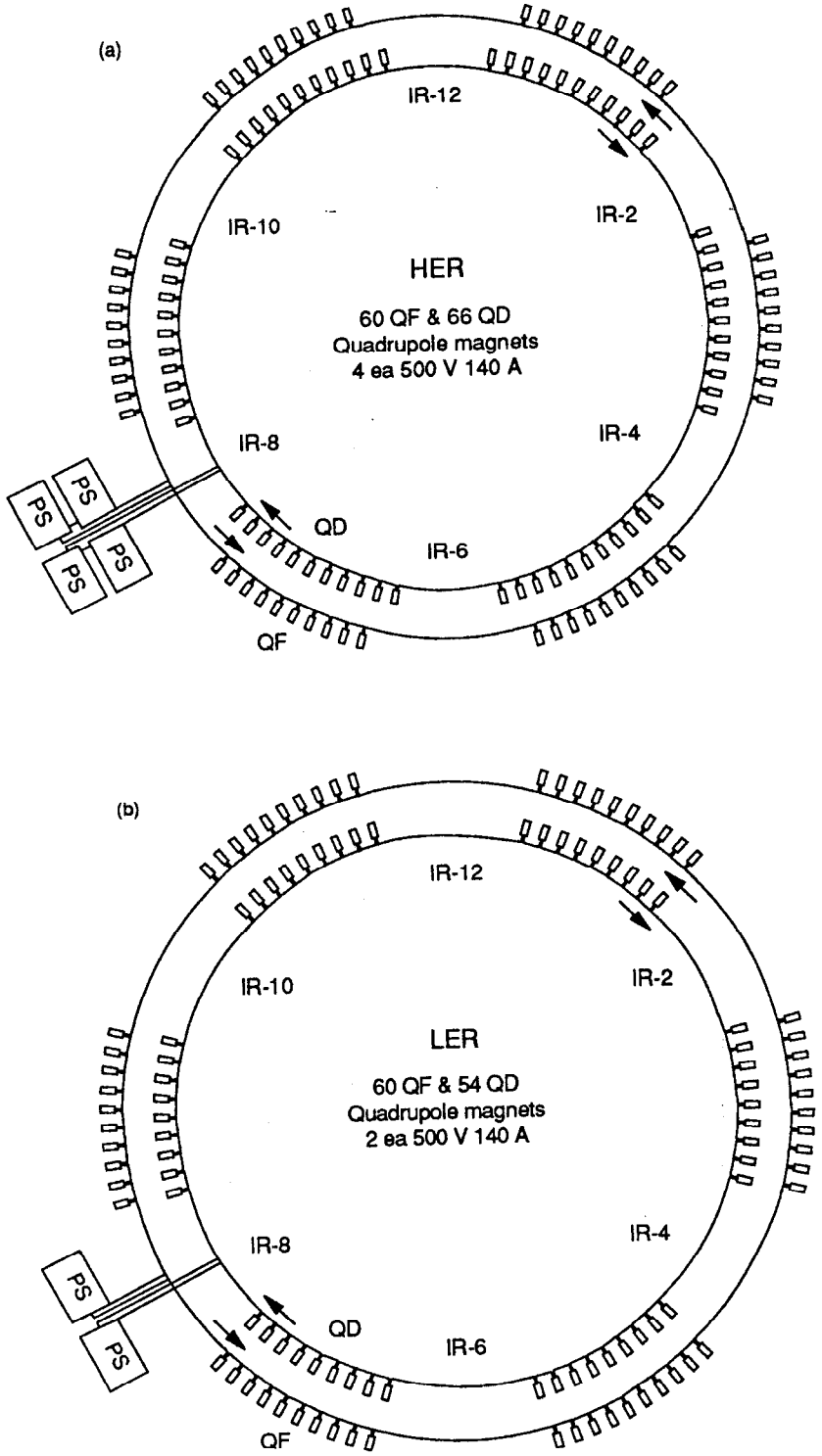

Fig. 5-92. Schematic of magnet and power supply connections for (a) the HER and (b) the LER arc quadrupole magnet strings.

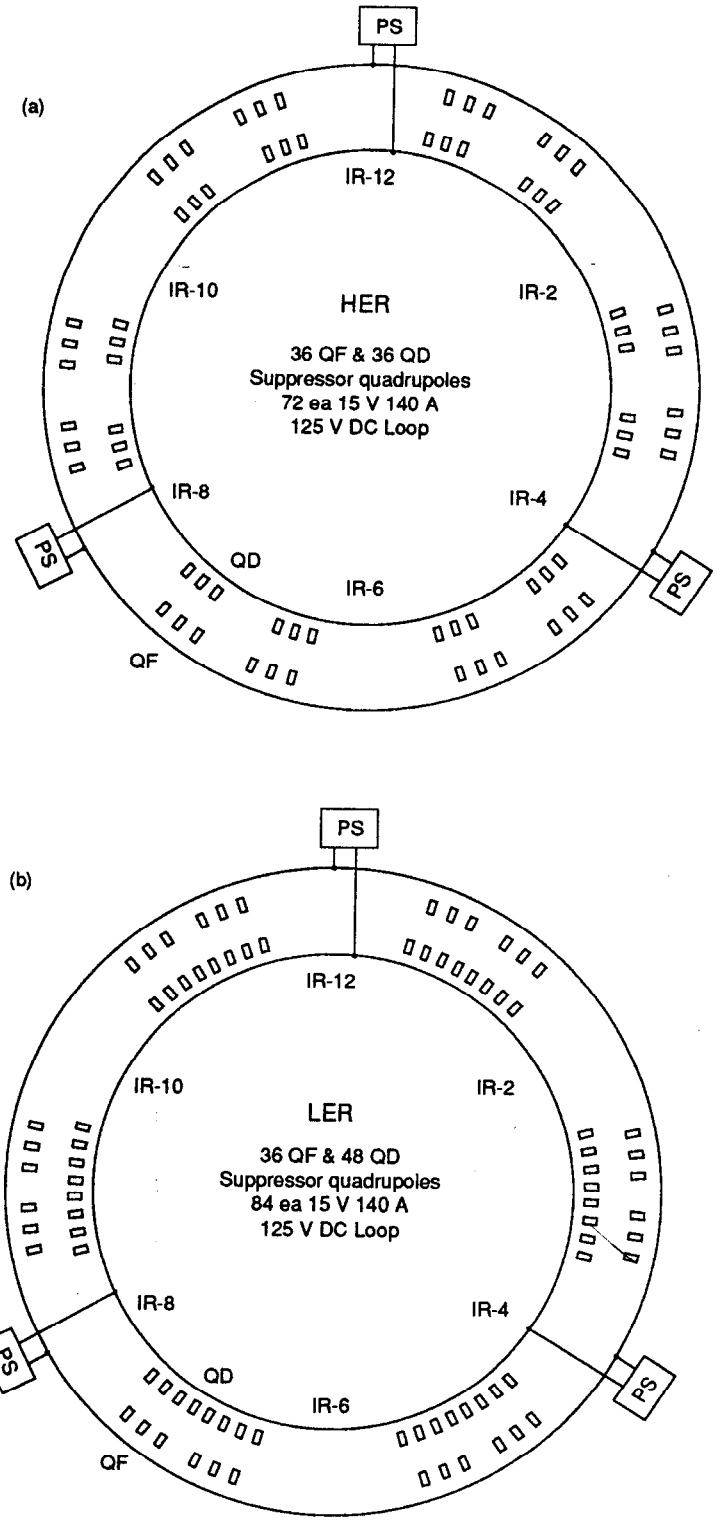

Fig. 5-93. Schematic of magnet and power supply connections for (a) the HER and (b) the LER suppressor quadrupole magnet strings.

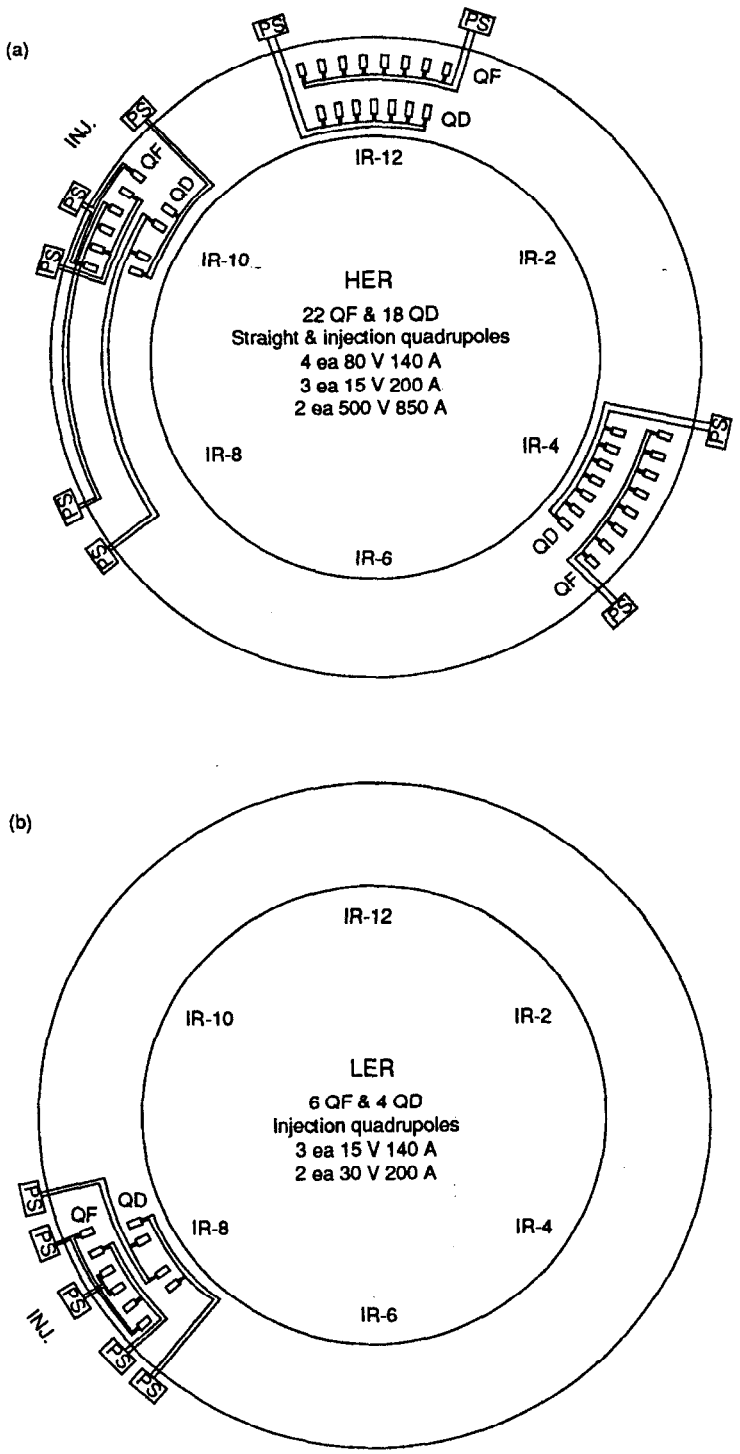

Fig. 5-94. Schematic of magnet and power supply connections for (a) the HER straight-section and injection quadrupole magnet strings and (b) the LER injection quadrupole strings.

the straight. The triplets will be powered by commercially procured, current-regulated supplies, regulated to 0.01%, that will be installed in their respective injection IR service buildings. The QD4 and QF5 quadrupoles will be connected to refurbished PEP chopper supplies (located in IR-8) in the same way as the arc quadrupoles. Existing cable (that will not need water cooling) between IR-8 and IR-10 will be used for the QD4 and QF5 quadrupoles in the HER injection straight section.

Each ring has two straight sections devoted to changing the betatron tunes of the machine. These "phase trombones" are located in regions 6 and 8 for the HER, and in regions 4 and 10 for the LER. (The LER RF cavities will share region 4 with the LER phase trombone.) The phase trombones consist of regularly spaced quadrupoles, as in the normal straights, but with each having an independent power supply identical to those for the dispersion-suppressor quadrupoles. There are then 15 power supplies for a total of 8 horizontally focusing and 7 vertically focusing quadrupoles in each region, as shown in Figs. 5-95a and 5-95b. Because one of the phase-trombone sections of the LER must coexist with the RF cavities, it is important to ensure smooth beta functions in this region.

In addition to the above functions, the LER has two straight sections (regions 6 and 12) devoted to control of beam emittance and damping via strings of wiggler magnets. A pair of dipoles on each side of the straight section, powered antisymmetrically about its center, provides the orbit dogleg and dispersion function for the emittance control (see Sections 4.1.2.5 and 5.2.6). Fifteen independently powered quadrupoles provide the necessary control of the beta functions (Fig. 5-96).

5.4.1.3 Sextupole Magnet Strings. The sextupoles of the HER comprise two sets, one between IR-4 and IR-12 and a second centered around the interaction region at IR-2. The first set of sextupoles is connected in two strings, one of 48 focusing sextupoles and a second of 48 defocusing sextupoles; these are shown in Fig. 5-97. The nominal operating current for these sextupole families is 130 A, regulated to 0.1%, at approximately 300 V per magnet string. The supplies will be refurbished PEP choppers operating from the same DC supply used for the bending magnets. The second set of sextupoles, which occupies arcs 1 and 3, includes 24 focusing and 24 defocusing magnets, each powered by an independent 140-A power supply (see Fig. 5-98). These supplies are switching-type DC-to-DC converters, each locally mounted and powered from a ring DC cable, just like those for the quadrupole DC-to-DC converters.

In particle tracking simulations done so far, the sextupoles of the LER have been grouped into just two families, consisting of 54 focusing and 54 defocusing sextupoles. To preserve flexibility, we plan to provide power supplies for the LER sextupoles just as described for the HER. For the LER, however, the nominal operating current of the sextupoles is only 60 A at 130 V.

5.4.1.4 Trim Magnet and Corrector Strings. Each bending magnet incorporates backleg windings, 96 of which are powered in each ring by backleg trim power supplies. The powering requirements for the backleg windings are less than 12 A, regulated to 0.1%, at approximately 25 V. There will be an induced voltage of not greater than 10 V on the backleg trim supplies when the bending magnets are energized or deenergized. The trim supplies are switching-type unipolar supplies, mounted in the tunnel in groups of eight or more independent supplies per cabinet. Control is supplied by way of a single

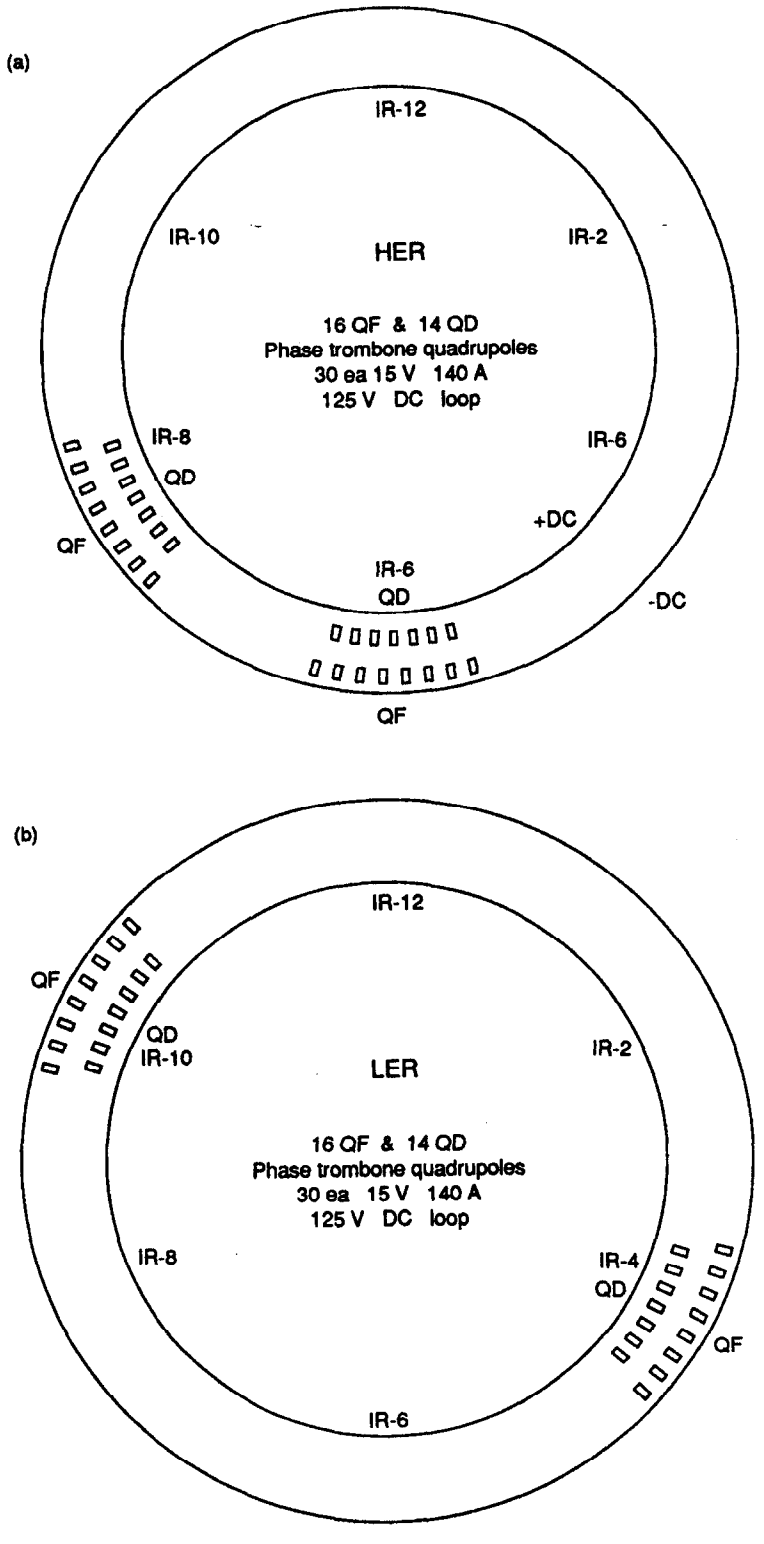

Fig. 5-95. Schematic of magnet and power supply connections for (a) the HER and (b) the LER phase trombone quadrupole magnet strings.

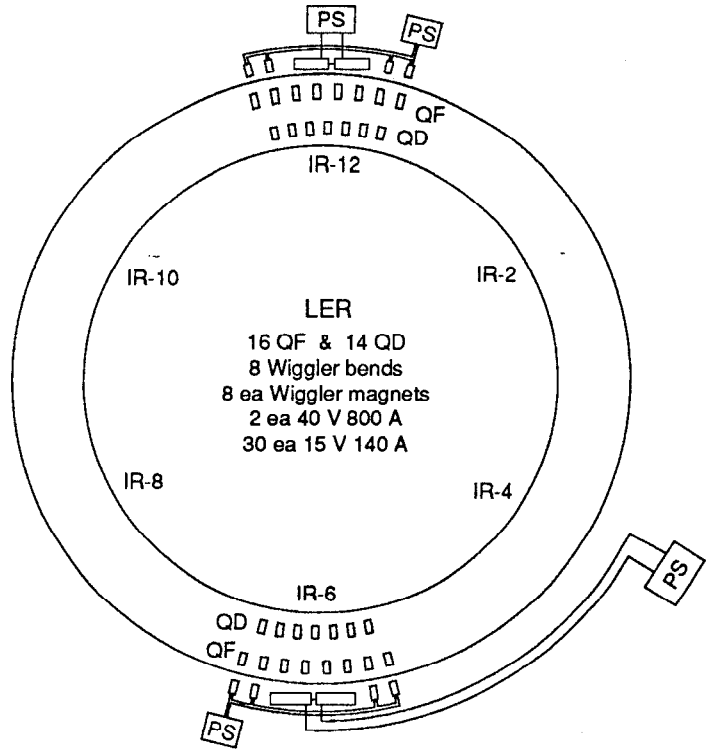

Fig. 5-96. Schematic of magnet and power supply connections for the LER wiggler, wiggler bending magnet, and wiggler quadrupole strings.

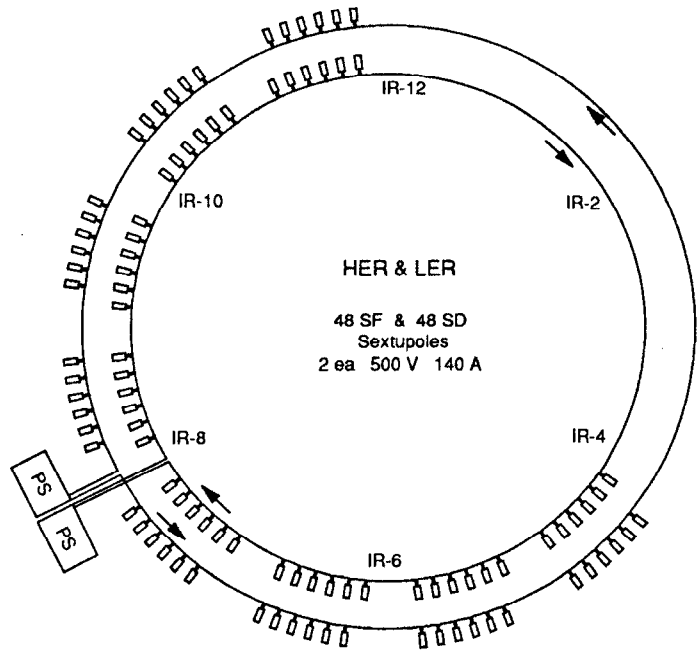

Fig. 5-97. Schematic of magnet and power supply connections for the normal sextupole magnet strings of both the HER and LER.

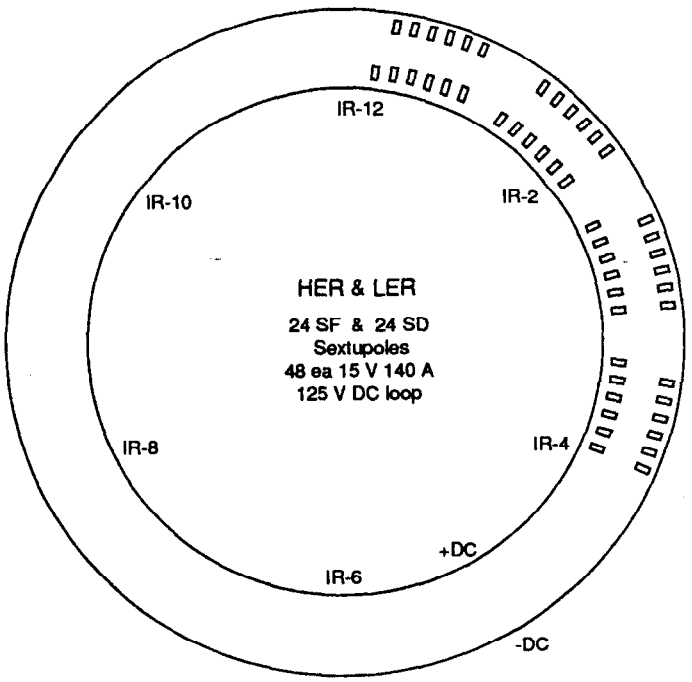

Fig. 5-98. Schematic of magnet and power supply connections for the sextupole magnet strings surrounding the IR, for both the HER and LER.

serial transmission line around the ring. The supplies are DC-to-DC converters, obtaining their power from a DC cable loop around the ring, powered in turn by current-limiting supplies in buildings at IR-12, IR-8, and IR-4 (see Fig. 5-99). Additional trim supplies are used to power 20 skew quadrupoles distributed around each ring.

There are also 144 vertical corrector magnets and 48 horizontal corrector magnets in each ring. The corrector supplies are switching-type, bipolar, two-quadrant supplies, powered from the same DC cable loop and mounted in the same enclosure as the trim supplies. The magnet requirements are ±6 A, regulated to 0.1%, at 20 V maximum. Control is as described for the trim supplies.

5.4.1.5 Wiggler Magnets. The LER will have four wiggler magnets located in IR-6 and IR-12. These magnets will require 1800 A at 300 V (Fig. 5-96). The two booster supplies for the PEP bending magnets will be reworked in the same way as the bulk supplies for the choppers and used to power the wiggler magnets. The supplies are located in IR-12 and IR-4. Existing water-cooled aluminum cables will be used to power the wigglers.

5.4.1.6 Refurbishing the PEP Chopper Supplies. The existing PEP chopper power system will be reworked for use in the B Factory. The 12-kV switchgear, rectifier transformers, and SCR-controlled DC converters will be reused, after being totally reconditioned. All equipment will be thoroughly inspected and cleaned, connections will be remade, and all parts subject to aging will be replaced. The controls of the DC supplies will be redesigned and rebuilt. The chopper supplies themselves will be redesigned and refurbished to make them more reliable and accessible, and where

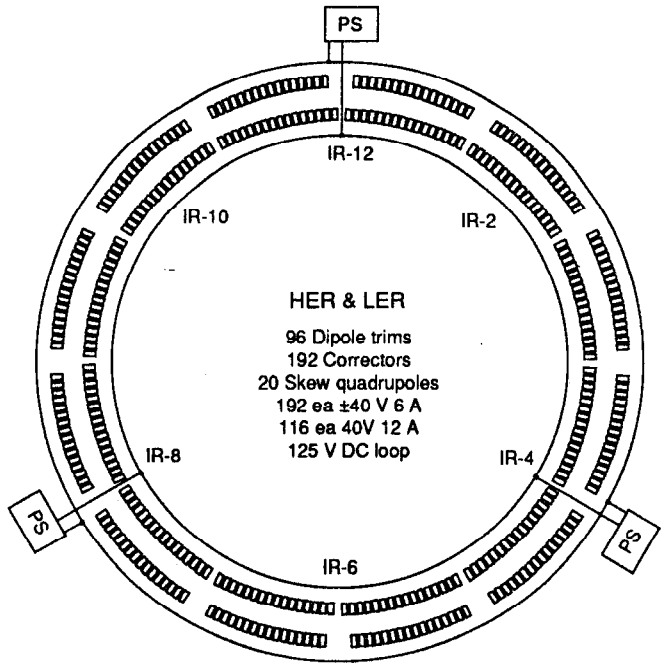

Fig. 5-99. Schematic of magnet and power supply connections for the trim dipole, skew quadrupole, and corrector strings for both the HER and LER.

practical they will be built with redundancy. The present SCR switches will be upgraded with modern switching devices, and the chopping frequency will be increased to improve the overall performance. Where practical, more than one chopper will be operated in parallel, designed and rated such that a single-point failure of power equipment or controls will not result in equipment shutdown.

The possibility of on-line replacement of failed equipment will be investigated to determine if it is practical and safe to incorporate this feature into the design, to improve the up-time of the supplies. Improved EMI filtering will be incorporated into the supplies to reduce noise. The choppers will be redesigned with all-digital computer controls to enhance performance and flexibility. The B Factory requires two sizes of chopper: one rated at 500 V (maximum) at 850 A (maximum) for the bending magnets and a second rated at 500 V (maximum) at 140 A (maximum) for the quadrupoles and sextupoles.

5.4.1.7 Quadrupole and Sextupole DC-to-DC Supplies. A DC-to-DC power supply will be developed for the quadrupoles and sextupoles that are to be operated individually. The supplies will be rated for 15 V at 140 A and will operate from a DC cable of approximately 120 V DC. The supplies will be designed to operate with a switching frequency greater than 20 kHz and will incorporate step-down transformers for magnet ground isolation and DC breakers for DC source isolation and protection. The supplies will be installed individually in the tunnel at locations adjacent to the magnets being supplied. There will be more than one switching system operating in parallel, such that in the event of a single-point failure the supply will continue to operate without interruption. The supplies will be designed to be readily replaceable, to reduce downtime. All-digital microcomputer controls will be connected in a serial transmission line running around the

tunnel for control and monitoring of the individual supplies. Each supply will have a local current monitor and regulator.

5.4.1.8 Trim and Corrector DC-to-DC Supplies. Trim and corrector DC-to-DC switching-type power supplies will also be developed (see Fig. 5-99). The trim supplies are unipolar, rated for 12 A at 40 V maximum. The bipolar, two-quadrant corrector supplies are rated for 6 A at 40 V. Both the trim and the corrector supplies operate from a DC cable of approximately 120 V DC. The supplies will be designed to operate with a switching frequency above 20 kHz and will incorporate an isolation step-down transformer for magnet ground isolation. The supplies will be installed in clusters of eight or more, and will be distributed around the tunnel at locations selected to minimize cabling costs. The supplies will be mounted in cabinets that will service both the HER and LER. Supply clusters will have DC breakers for DC source isolation and protection. The supplies will be plug-in types to allow easy replacement and thus reduce facility downtime. All-digital microcomputer controls will be connected to a single serial transmission line running around the tunnel for control and monitoring of the individual supplies.

5.4.2 Interaction Region Power Supplies

The magnetic devices at the heart of the interaction region are made of permanent magnet material and require no power supplies. To permit energy variations, however, there will be trim windings associated with these magnets (B1, Q1, Q2, Q3) that will require small supplies. The septum quadrupoles of the HER (QD4 and QF5), which focus the high-energy beam, are special magnets with special power supplies. The remaining IR power supply requirements for the HER are relatively straightforward. One supply powers the string of B2 weak bends on each side of the IP and another supply powers a similar string of B3 bends, each string (see Fig. 4-12) having four magnets. One supply powers the two B4 dipoles on each end of the straight, and two supplies are needed for the single QD6 and QF7 quadrupoles on each side of the IP (see Fig. 4-10).

The LER is much more complicated and power supplies are needed for many quadrupole and dipole magnets, including the vertical bending magnets and the horizontal magnets to align the collision axis. The complete list of power supplies for the interaction region is shown in Table 5-27. Supplies will all be installed in the existing IR-2 service building, where sufficient AC power is available. With the exception of those for the correctors and trims, all supplies will be commercially obtained and will be regulated to 0.01%. Supplies will be controlled remotely from the B Factory control system. The trim and corrector supplies will be of the type described in Section 5.4.1.8, and will be installed in the tunnel and controlled in the same manner.

5.4.3 Injection Power Supplies

The injection system for the B Factory utilizes the existing SLAC linac to produce positrons and electrons. We expect that no power supply modifications will be required to the present linac to accommodate the new injection system. Most of the linac power

Table 5-27. Interaction region power supplies. In some cases the string voltage is dominated by cable voltage drop.

Magnet string name	Number of magnets	Current per magnet (A)	Voltage per magnet (V)	String voltage (V)	Number of supplies	Power supply rating
HER dipoles B2	8	910	1.0	26	1	30V/1000A
HER dipoles B3	8	910	1.0	26	1	30V/1000A
HER dipoles B4	4	67	0.5	3	1	15V/140A
HER quadrupoles Q4	2	800	14	36	1	40V/800A
HER quadrupoles Q5	2	800	14	36	1	40V/800A
HER quadrupoles Q6	2	212	17	36	1	80V/250A
HER quadrupoles Q7	2	166	13.3	28	1	80V/250A
LER bend BV1	4	146	1.1	7	1	30V/200A
LER bend BV	4	731	5.3	36	1	40V/800A
LER bend B2	2	652	4.7	22	1	40V/800A
LER bend B3	2	139	1.0	5	1	15V/140A
LER bend B4	2	107	0.8	4	1	15V/140A
LER bend B5	2	25	0.2	2	1	15V/140A
LER bend B6	2	171	1.3	13	1	30V/200A
LER quadrupoles QF4	4	147	7.7	32	1	80V/250A
LER quadrupoles QVDD	4	158	12.7	52	1	80V/250A
LER quadrupoles QVF	4	219	17.5	72	1	80V/250A
LER quadrupoles QVD	4	219	17.5	72	1	80V/250A
LER quadrupoles QD8	2	164	8.5	19	1	30V/200A
LER quadrupoles QF9	2	164	13.2	27	1	30V/200A
LER quadrupoles QD10	2	105	9.7	20	1	30V/200A
LER quadrupoles QF11	2	76	4.5	9	1	15V/140A
LER quadrupoles QD12	2	116	5.1	11	1	15V/140A
LER quadrupoles QF13	2	105	5.6	12	1	15V/140A
Corrector vertical bend	16	6	20	20	16	±40V/6A
Corrector horizontal bend	16	6	20	20	16	±40V/6A
Quadrupole trims	11	12	25	18	15	40V/12A

supplies were either installed or upgraded during construction of the SLC. In addition, power supplies will be available from the SLC final focus and arc systems for the B Factory. The available supplies comply with SLC standards and are of the same age and condition as the rest of the SLC linac. We will therefore recondition and reuse as many of the SLC final focus and arc supplies as possible for the B Factory injection system. Power supply requirements for the injection system are listed in Table 5-28.

The B Factory injection power supply system can be divided into five parts: electron extraction, positron extraction, beam transport, NIT and SIT lines, and the kicker system. All of the power supplies except those for the kickers will be installed in the klystron gallery and will be controlled and operated by the SLC control system. Standard SLC equipment and procedures will be used throughout.

5.4.3.1 Electron Extraction System. The electron extraction system consists of two pulsed bending magnets connected in series, two bending magnets at the entrance to the NIT line, and 24 quadrupole magnets. The pulsed bending magnets require approximately 250 A at 750 V. The present SLC pulsed dump supplies are available for these magnets. The two-dipole string that directs the electron beam to the NIT line operates at 110 A; available SLC final focus supplies will be used for these magnets, along with existing SLC control interface equipment. There will be two strings of 8 quadrupoles, each operating from its own 6-A, 300-V supply. In addition, there will be two groups of 4 individually powered quadrupoles supplied by standard SLC power supplies (available from the final focus).

5.4.3.2 Positron Extraction System. The positron extraction system includes a bending magnet chicane composed of five bending magnets connected in series, a two-bending-magnet string, and 24 quadrupoles. The five-dipole string requires approximately 110 A at 120 V; the two-dipole string also operates at 110 A. For these strings, available SLC final focus supplies will be used with existing SLC control interface equipment. There will be two strings of 8 quadrupoles, each operating from its own 6-A, 300-V supply. In addition, there will be two groups of 4 individually powered quadrupoles supplied by standard SLC power supplies (available from the final focus).

5.4.3.3 Beam Transport. The positron beam transport system, consisting of two strings of 26 quadrupoles, connected in series, requires 6 A at 150 V per string. Available commercial power supplies, interfaced to the SLC control system, will be used. Requirements and provisions for the electron beam transport system, consisting of two strings of 22 quadrupoles, are identical. In addition, the beam transport systems include 120 individually controlled trim magnets, operating at 6 A maximum at approximately 12 V. The necessary supplies are available from the SLC final focus and are interfaced to the SLC control system.

5.4.3.4 NIT and SIT Lines. The NIT and SIT lines will be electrically connected as they were for PEP; however, all power supplies will be replaced by supplies available from the SLC final focus and arcs. A small number of the NIT supplies now located in Buildings 685 and 705 will be relocated to Sector 30, so that all of the NIT and SIT supplies can be easily controlled by the SLC control system.

Table 5-28. Injection power supplies.

Magnet string name	Number of magnets	Current per magnet (A)	Voltage per magnet (V)	String voltage (V)	Number of supplies	Power supply rating
Positron chicane bend magnets	5	110	23	127	1	150V/200A
Positron down bend magnets	2	110	23	51	1	80V/375A
Positron quadrupoles	16	6	10	100	2	300V/6A
Positron quadrupoles	8	6	10	11	8	SCOR6,25A
Electron pulsed bend magnets	2	250	750	1500	1	Dump pulser
Electron up and top bend magnets	2	110	22	48	1	80V/375A
Electron down bend magnets	2	110	23	51	1	80V/375A
Electron quadrupoles	16	6	10	100	2	300V/6A
Electron trims	8	6	10	11	8	SCOR6,25V
Bypass positron quadrupoles	52	6	5	143	2	250V/20A
Bypass electron quadrupoles	44	6	5	121	2	250V/20A
Bypass trim dipoles	120	6	10	11	120	HCOR12,35A
NIT electron bend magnets	11	570	5	12	5	30V/800A
NIT quadrupoles	24	62	7.1	62	3	100V/200A
NIT vertical bends	1	75	13	14	1	50V/200A
NIT dipole trims	16	14	16	18	16	HCOR12,35A
NIT new quadrupoles	4	62	7.1	8	4	20V/125A
NIT trim dipoles	4	6	12	13	4	SCOR6,25V
NIT septum	1	600	40	44	1	100V/600A
HER kicker magnets	2	1100	11 kV	11 kV	2	
HER pulsed septum	1	1100	18.2 kV	18.2 kV	1	
SIT positron bend magnets	10	230	2	4	5	45V/450A
SIT quadrupoles	24	25	2.8	25	3	30V/100A
SIT vertical bends	1	30	5.2	6	1	30V/100A
SIT dipole trims	16	5.8	6	7	16	SCOR6,25V
SIT new quadrupoles	4	25	2.8	3	4	20V/90A
SIT trim dipoles	4	6	12	13	4	SCOR6,25V
SIT septum	1	600	40	44	1	100V/600A
LER kicker magnets	2	600	5.8 kV	5.8 kV	2	
LER pulsed septum	1	600	9.7 kV	9.7 kV	1	

5.4.3.5 Injection Kicker System. The PEP kicker magnet modulator supplies will be redesigned and rebuilt at SLAC for the HER and LER. The kicker system for each ring consists of three kicker magnets. The current rise time for the magnet must be less than 200 ns, and the fall time less than 1.5 μs. Two of the kickers will operate at the same amplitude, while the third will be adjusted independently. Therefore, only two independent kicker modulators are required for each ring.

The kicker modulator design uses a capacitor that is pulse-charged to the required 10–20 kV, then discharged into the kicker magnet by use of a thyratron. A terminating resistor is provided to damp the discharge and thus avoid ringing in the magnet. The kicker modulator will be connected to the kicker magnets by coaxial cables with an impedance of approximately 12 Ω. This type of kicker modulator is currently being used in the SLC final focus dump system. The kickers will be controlled by the B Factory control system.